Plasma Physics Reports, Vol. 27, No. 1, 2001, pp. 1–17. Translated from Fizika Plazmy, Vol. 27, No. 1, 2001, pp. 3–18.

TOKAMAKS

Calculation of the Energy Confinement Time and Power Threshold for L–H Transitions in a Tokamak with Allowance for the Parameters of the Transport Barrier

M. V. Ossipenko and S. V. Tsaun

Russian Research Centre Kurchatov Institute, pl. Kurchatova 1, Moscow, 123182 Russia

Received February 17, 2000; in final form, May 18, 2000

Abstract—The ASTRA–ETL code is used to simulate L–H transition scenarios and calculate the energy confinement time and the threshold power of the L–H transition as functions of the averaged electron density $\langle n \rangle$, the averaged magnetic field B, the neutral density n_n, and the neutral temperature T_n, as well as the values of T_{Se}, T_{Si}, and n_S at the separatrix. It is shown that the linear dependence of the threshold power of the L–H transition on the averaged electron density, $Q_{\text{L–H}} \propto \langle n \rangle$, is associated with an increase in the viscosity of a poloidally rotating plasma due to charge exchange and is governed exclusively by an increase in the neutral density n_n. When the averaged electron density $\langle n \rangle$ is low, the threshold power rises because T_{Si} and T_{Se} increase. The accuracy of predictions for the power threshold of the L–H transition can be improved if the scaling of $Q_{\text{L–H}}$ versus $\langle n \rangle$ and B is derived by processing experimental data from discharges with close parameter values at the separatrix. The hysteresis effect during an L–H–L transition triggered by varying the input power is modeled. The global energy confinement time τ_E is shown to increase linearly with $\langle n \rangle$ in the range $\langle n \rangle < 3.6 \times 10^{19}$ m^{-3} and to saturate at higher electron densities; this behavior is found to be characteristic of the Ohmic, L-, and H-modes. The saturation is associated with the fact that losses via the ion channel (when the transport coefficients are density-independent) dominate over losses via the electron channel. The dependence of τ_E on the input power is determined from the calculated database and is found to be $\tau_E = 0.12\ Q_{\text{L–H}}^{-0.46}$ at a fixed averaged electron density $\langle n \rangle$. In the simulations of the L–H transition, the energy confinement time τ_E increases by a factor of 2 only if the thermal diffusivity inside the transport barrier is lower than that in the central plasma by a factor of more than 6. © *2001 MAIK "Nauka/Interperiodica".*

1. INTRODUCTION

The problem of predicting the global energy confinement time τ_E and the auxiliary heating power Q_{aux} required to trigger the transition to an improved confinement mode (the H-mode) is one of the key problems in designing present-day tokamaks. Experiments on the DIII-D [1, 2] and other tokamaks show that the power threshold of L–H transitions during which the energy confinement time τ_E changes depends sensitively on the plasma parameters at the separatrix and at the pedestal: the electron and ion temperatures, T_e and T_i; the electron density n; and the density n_n and temperature T_n of neutrals arriving from the wall and appearing due to recycling. These experiments spurred the development of a numerical code capable of describing the dynamics of plasma turbulence near the separatrix during L–H transitions and the effects of the edge turbulence on heat and particle transport in tokamaks. In the simplest formulation, this problem was solved in [3]. The ASTRA code developed in that paper was supplemented with the edge turbulent layer (ETL) model, which served to impose boundary conditions of the third kind. The combined ASTRA–ETL code made it possible to describe the formation of a transport barrier just inside the separatrix during the L–H transition in a tokamak. However, the two-field ETL model developed earlier turned out to be insufficiently adequate for interpreting the experimental data quantitatively, because it was constructed so that the mechanism for the formation of a transport barrier was only included in calculating the ion temperature profile. The two-field ETL model describes the formation of a transport barrier as a result of the suppression of convective cells by a sheared flow when the ion temperature gradient in a turbulent layer (TL) increases above a critical level, but no account was taken of the fluctuations of the electron density and temperature. The formation of a transport barrier on the electron temperature profile was modeled incorporating only the energy exchange between electrons and ions, while the electron density profile was taken from experiments. In our paper [4], the two-field ETL model was extended to describe turbulent convection excited in the separatrix region of a tokamak plasma by taking into account four types of interacting fluctuations, specifically, fluctuations of the electron and ion temperatures, plasma density, and electric potential at the plasma edge. It was shown that these

1063-780X/01/2701-0001$21.00

fluctuations can be described by the Braginskii four-field hydrodynamic equations, which can be reduced to three Lorentz-like sets of equations coupled through the equation for the kinetic energy of the fluctuations, i.e., to a four-field ETL model describing the nonlinear dynamics of convective cells in the presence of a sheared flow. The critical parameter for the onset of turbulent convection was shown to be the total plasma pressure gradient in the TL. For three coupled oscillators, the critical pressure gradient corresponding to transitions to both L- and H-modes was found to be much lower than that for an individual oscillator, which describes turbulent convection driven by one type of fluctuation. The four-field ETL model made it possible to calculate the heat and particle fluxes via the ion and electron channels; these fluxes were used as boundary conditions of the third kind in the transport problem for the main plasma. In this work, which is a continuation of paper [4], we further develop the ASTRA–ETL code in order to calculate the evolution of the profiles of the temperature and density of electrons and ions with allowance for turbulent convection. We can thus simulate L–H transition scenarios and evaluate the energy confinement time and the threshold auxiliary heating power required to trigger a transition to the H-mode as functions of the edge plasma parameters.

2. TRANSPORT MODEL FOR THE CENTRAL PLASMA

The profiles in the main plasma are calculated using the ASTRA balance transport code [5], in which the transport model is chosen to adequately describe the temperature and density profiles in the L-mode. The profiles of interest are calculated from the following one-dimensional transport equations, derived by averaging over the magnetic surfaces:

$$\frac{\partial n_e}{\partial t} + \mathrm{div}\,\Gamma = S, \tag{1}$$

$$\frac{3}{2}\frac{\partial}{\partial t}(n_e T_e) + \mathrm{div}\left(Q_e + \frac{3}{2}T_e\Gamma\right) = p_e, \tag{2}$$

$$\frac{3}{2}\frac{\partial}{\partial t}(n_i T_i) + \mathrm{div}\left(Q_i + \frac{3}{2}T_i\frac{\Gamma}{Z}\right) = P_i, \tag{3}$$

where $\Gamma = -D\dfrac{\partial n_e}{\partial r} + V_P n_e$, t is the time, r is the magnetic surface label, and $n_e = Zn_i = n$. Here and below, the linear dimensions are expressed in m, the time in s, the field in T, the current in MA, the density in units of 10^{19} m^{-3}, the temperature in keV, the particle mass in units of the proton mass, the particle charge Z in units of the electron charge, the power in MW, and the transport coefficients in m^2/s. We use the standard notation adopted in tokamak physics (see [4] for details):

$$D = D_u\chi_e^u + D_t\chi_e^t + C_{RB}\chi_{RB}, \tag{4}$$

where $\chi_e^u = 50(T_e/M_i)^{1/2}/(nqR)$ is the Ohkawa thermal diffusivity [6], $\chi_e^t = 7.36\varepsilon^{1/2}\sqrt{\dfrac{T_i}{T_e}}\dfrac{\rho}{qL_n}\dfrac{T_e}{B}$ is the thermal diffusivity due to trapped electrons [7] (ρ is the ion Larmor radius in terms of the electron temperature),

$$\chi_{RB} = 28q^2\rho C_S\frac{R}{a}\frac{\nu_e}{\Omega_e}\left|\frac{a}{L_n} + \frac{a}{L_T}\right| \tag{5}$$

is the thermal diffusivity due to resistive ballooning modes [8],

$$\frac{1}{L_n} = \frac{1}{n_e}\frac{\partial n_e}{\partial r}, \quad \frac{1}{L_T} = \frac{1}{T_i}\frac{\partial T_i}{\partial r};$$

and $V_P = \chi_e^t/(n_e L_n)$ is the coefficient describing the heat pinch effect at the density gradient due to trapped electrons [7] (for simplicity, we assume here that $V_P = 0$);

$$S = S_n + S_{\mathrm{NBI}},$$

where $S_n = \langle\sigma_{ei}v\rangle n_e n_n + \langle\sigma_{ii}v\rangle n_n n_i$ is the particle source related to the ionization of edge neutrals by electron and ion impacts and S_{NBI} is the particle source associated with neutral beam injection (NBI);

$$\begin{aligned} Q_e &= -1.602\times10^{-3}n_e\chi_e\frac{\partial T_e}{\partial r};\\ \chi_e &= C_u\chi_e^u + C_t\chi_e^t + C_{RB}\chi_{RB};\\ P_e &= P_J - P_{ei} - P_{en} + P_{e\mathrm{NBI}}, \end{aligned} \tag{6}$$

where P_J is the ohmic heating power,

$$P_{ei} = \frac{3}{\tau_{ei}}n_e(T_e - T_i)\frac{m_e}{M_i}, \quad \tau_{ei} = 7.3\times10^{-8}\frac{T_e^{3/2}}{Zn_e},$$

is the power transferred from electrons to ions due to Coulomb collisions, and $P_{en} = 2.08\times10^{-5}\langle\sigma v\rangle n_e n_n$ [MW/m^3] is the power lost by the electrons in ionizing cold neutrals;

$$\begin{aligned} Q_i &= -1.602\times10^{-3}n_i\chi_i\frac{\partial T_i}{\partial r},\\ \chi_i &= C_{dr}\chi_{dr} + C_{RB}\chi_{RB},\\ \chi_{dr} &= 0.25\rho C_S\frac{T_e}{T_i}\left|\frac{\rho}{L_n} + \frac{\rho}{L_T}\right|, \end{aligned} \tag{7}$$

where [7]

$$P_i = P_{ei} - P_{cx} + P_{in} + P_{i\mathrm{NBI}},$$

where $P_{cx} = 3/2\langle\sigma v\rangle_{cx}n_i n_n(T_i - T_n)$ is the power lost by the ions in charge-exchange collisions,

$P_{in} = 3/2 n_n T_n(\langle\sigma_e v\rangle n_e + \langle\sigma_i v\rangle n_i)$ is the energy acquired by the ions via the ionization of edge neutrals by electron and ion impacts, $P_{e\mathrm{NBI}}$ and $P_{i\mathrm{NBI}}$ are the fractions of NBI power distributed between electrons and ions according to the formulas [9]

$$P_{e\mathrm{NBI}} = S_{\mathrm{NBI}}\frac{m_b V_b^2}{2}[1-\xi],$$
$$P_{i\mathrm{NBI}} = S_{\mathrm{NBI}}\frac{m_b V_b^2}{2}\xi, \quad (8)$$

m_b is the mass of a beam ion (in units of the proton mass), $E_b = m_b V_b^2/2$ is the kinetic energy of the beam ions,

$$\xi = -\frac{1}{3}\frac{V_*^2}{V_b^2}\left[\ln\frac{V_*^2 - V_* V_b + V_b^2}{(V_* + V_b)^2} + 2\sqrt{3}\arctan\frac{2V_b - V_*}{\sqrt{3}V_*} + \frac{\pi}{\sqrt{3}}\right],$$

with $V_*^2 = \left(\frac{9\pi}{2}\right)^{1/3}\frac{T_e}{m_e^{1/3} m_b^{2/3}}$, and $S_{\mathrm{NBI}} = 3.1\times 10^{22}\times Q_{\mathrm{aux}}/E_b(1 - r/a)\exp(-r^2/(0.64a^2))$ [s^{-1}] is the NBI-related particle source normalized so that the integral of S_{NBI} over the entire plasma volume is equal to $624 Q_{\mathrm{aux}}/E_b$ (the beam power Q_{aux} and the beam kinetic energy E_b are expressed in MW and keV, respectively).

3. MATCHING OF THE ASTRA CODE WITH THE ETL MODEL

The temperature and density profiles are calculated by using boundary conditions of the third kind, i.e., by prescribing the fluxes at the inner boundary $R = R_B$ of the TL (transport barrier):

$$-D^{\mathrm{ASTRA}}\frac{\partial n}{\partial r} = \Gamma^{\mathrm{ETL}}, \quad \Gamma^{\mathrm{ETL}} = \Gamma^{\mathrm{turb}} + \Gamma^{\mathrm{dif}},$$
$$\Gamma^{\mathrm{turb}} = \frac{k_y}{k}C_S n_S X Y_n, \quad \Gamma^{\mathrm{dif}} = D\rho C_S\frac{n_B - n_S}{L},$$
$$-\chi_i^{\mathrm{ASTRA}} n^{\mathrm{ASTRA}}\frac{\partial T_i}{\partial r} - \frac{3}{2}D^{\mathrm{ASTRA}} T_i^{\mathrm{ASTRA}}\frac{\partial n}{\partial r} = \frac{n_B + n_S}{2}Q_i^{\mathrm{ETL}} + \frac{3}{2}\frac{T_{Bi} + T_{Si}}{2}\Gamma^{\mathrm{ETL}},$$
$$Q_i^{\mathrm{ETL}} = Q_i^{\mathrm{turb}} + Q_i^{\mathrm{dif}}, \quad Q_i^{\mathrm{turb}} = \frac{k_y}{k}C_S T_{Se} X Y_i,$$
$$Q_i^{\mathrm{dif}} = \chi_i\rho C_S\frac{T_{Bi} - T_{Si}}{L}, \quad (9)$$
$$-\chi_e^{\mathrm{ASTRA}} n^{\mathrm{ASTRA}}\frac{\partial T_e}{\partial r} - \frac{3}{2}D^{\mathrm{ASTRA}} T_e^{\mathrm{ASTRA}}\frac{\partial n}{\partial r} = \frac{n_B + n_S}{2}Q_e^{\mathrm{ETL}} + \frac{3}{2}\frac{T_{Be} + T_{Se}}{2}\Gamma^{\mathrm{ETL}},$$
$$Q_e^{\mathrm{ETL}} = Q_e^{\mathrm{turb}} + Q_e^{\mathrm{dif}}, \quad Q_e^{\mathrm{turb}} = \frac{k_y}{k}C_S T_{Se} X Y_e,$$
$$Q_e^{\mathrm{dif}} = \chi_e\rho C_S\frac{T_{Be} - T_{Se}}{L}.$$

Here, the diffusion coefficient D^{ASTRA} and the ion and electron thermal diffusivities, χ_i^{ASTRA} and χ_e^{ASTRA}, are defined in formulas (4)–(7); the electron density n^{ASTRA} and the electron and ion temperatures, T_i^{ASTRA} and T_e^{ASTRA}, are calculated by the ASTRA code at the magnetic surface $R = R_B - \Delta r/2$; Δr is the spatial step of the grid in the ASTRA code; Γ^{turb}, Q_i^{turb}, and Q_e^{turb} are the turbulent fluxes driven by the convective cells in a TL of width L (see Eqs. (29) and (35) in [4]); X is the dimensionless amplitude of the turbulent fluctuations of the electric potential; Y_n is the dimensionless amplitude of the electron density fluctuations; Y_i and Y_e are the amplitudes of the ion and electron temperature fluctuations (see definition (8) in [4]); the diffusive fluxes in the TL, Γ^{dif}, Q_i^{dif}, and Q_e^{dif}, are described by the seed transport coefficients $\chi_i = \chi_e = D = CD_B/\rho C_S$ in Eqs. (2)–(4) [4]; $D_B = \rho C_S/16$; and the numerical factor C is determined from the calibration of the ETL model. Note that, in the expressions for D^{ASTRA}, χ_i^{ASTRA}, and χ_e^{ASTRA}, the functional dependences and numerical factors, which are chosen so as to adjust the profiles calculated for the L-mode to the relevant experimental profiles, do not change during the L–H transition.

To include the boundary conditions (9) into the combined ASTRA–ETL code requires an implicit scheme. Since the profiles of T_e, T_i, and n_e are calculated with the help of similar algorithms for solving the boundary problem, we explain this scheme using as an example only the matching of the particle fluxes in the ASTRA code and in the ETL model. For all of the boundary conditions for matching fluxes (9), the transport coefficients in the main plasma and in the TL are calculated at the kth time step and the temperature and density gradients are calculated at the $(k+1)$th time step (here, k is the number of the time step in the ASTRA code). In the TL, the effective transport coefficient is defined as

$$D^{\mathrm{ETL}} = \Gamma^{\mathrm{ETL}}\left(\frac{n_B^k - n_S}{L}\right)^{-1},$$

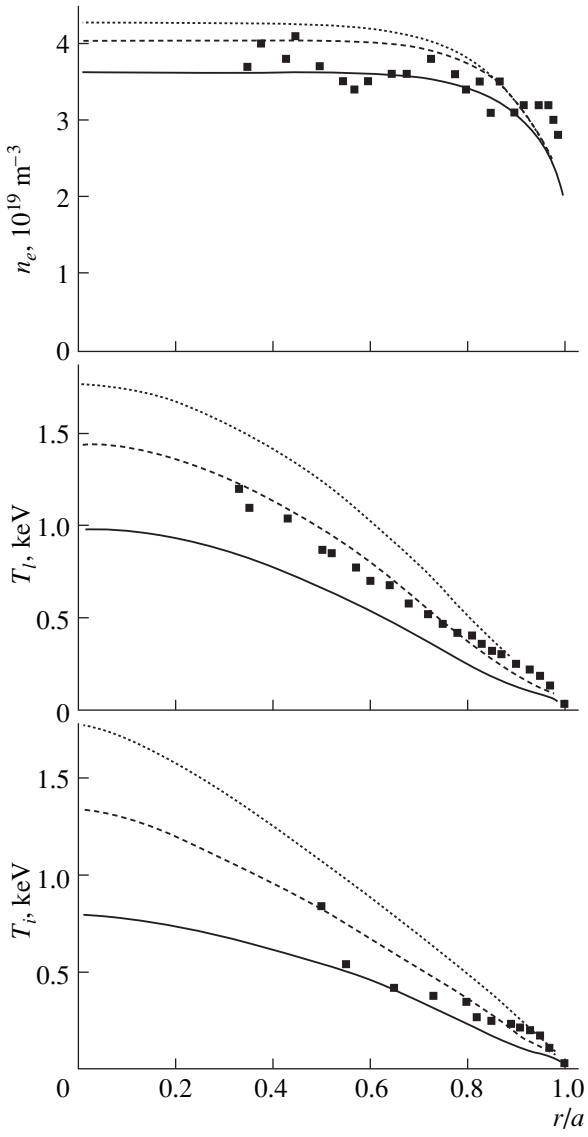

Fig. 1. Steady-state profiles of the electron density, electron temperature, and ion temperature in three confinement modes: the ohmic mode (solid curves), the H-mode with the NBI power Q_{aux} = 2.5 MW (dashed curves), and the H-mode with the NBI power Q_{aux} = 5 MW (dotted curves); closed squares are the experimental points.

where n_S = const, in which case the boundary condition has the form

$$D_N^{\mathrm{ASTRA}} \frac{n_{N-1}^{k+1} - n_N^{k+1}}{\Delta r} = D^{\mathrm{ETL}} \frac{n_N^{k+1} - n_S}{L}, \qquad (10)$$

where D_N^{ASTRA} and D^{ETL} are calculated at the kth time step. Consequently, relationship (10) serves as a boundary condition with which to solve the continuity equation by the sweep method. The ASTRA code was designed on a spatial grid consisting of N points, the grid size being Δr. The index N corresponds to the inner boundary $R = R_B$ of the TL.

The implicit scheme makes the iterative procedure stable at the inner boundary of the TL, at which the turbulent fluxes are matched; consequently, we can adopt a time step of 0.1 μs in the ETL model and a time step of 20 μs in the ASTRA code. In the ETL model, the characteristic time scale on which the plasma turbulence develops can be longer than the time step used in the ASTRA code; consequently, in calling up the ETL subroutine for the first time in each run of the ASTRA code, we must choose the number of iterations so that the plasma turbulence reaches saturation and ensures consistency between the turbulent fluxes and gradients in the TL. The amplitudes of the seed turbulent fluctuations are chosen to be two orders of magnitude smaller than the characteristic steady-state fluctuation amplitudes, which are independent of the initial conditions. At the first iteration step, the ETL subroutine adjusts the turbulent transport coefficients to the prescribed initial profiles. At subsequent iteration steps, it is run with the fluctuation amplitudes calculated at the preceding iteration step. Since the temperature and density profiles usually change much slower than the plasma turbulence, we may speak of the "evolution" of the ETL model, because it passes through a sequence of quasisteady states. In modeling L–H transitions, which occur on time scales of 5 to 20 μs, we must shorten the time step in the ASTRA code down to 1–5 μs.

4. SIMULATION OF THE L–H TRANSITION SCENARIOS

The L–H transition scenarios were simulated taking as an example DIII-D shot no. 82830, because, for this shot, the experimental data on the dynamics of turbulent fluctuations of the potential and density near the separatrix during the L–H transition were published in [10]. This information is required to test and calibrate the ETL model [4]. The auxiliary heating power input into a deuterium plasma with the effective charge number $Z_{\mathrm{eff}} \approx 1.5$ by injecting a neutral beam was Q_{aux} = 2.5 MW. As the initial conditions, we adopted the following parameters of the L-mode in DIII-D shot no. 82830:

$$R_{pl} = 1.67 \text{ m},\ a = 0.63 \text{ m},\ B = 2.17 \text{ T},$$
$$I_{pl} = 1.37 \text{ MA},\ q = 4.55,\ n_S = 1.5 \times 10^{19} \text{ m}^{-3}, \qquad (11)$$
$$T_{Se} = 30 \text{ eV},\ T_{Si} = 30 \text{ eV},$$

the ellipticity and triangularity being 1.8 and 0.3, respectively. The equilibrium configuration of the magnetic field was calculated initially and, in further simulations, was assumed to be fixed.

The calibration constants for the ETL model were calculated in accordance with [4] and were found to be equal to $V_1 = 0.08$, $C = 0.5$, and $\delta = 8$. In the ETL model, the numerical factors in the transport coefficients in (4), (6), and (7) were chosen so as to adjust the profiles cal-

culated for a steady-state confinement mode to the relevant experimental profiles. The numerical factors $D_u = C_u = 0.5$, $D_t = 3$, $D_{RB} = C_{RB} = 0.4$, and $C_t = C_{dr} = 5$ were calculated from the only available data on the steady-state H-mode ($Q_{\text{aux}} = 2.5$ MW). The profiles computed with these factors are shown in Fig. 1 and are seen to approximate the experimental points fairly well. The resulting transport coefficients are presented in Fig. 2. The centrally peaked Ohkawa thermal diffusivity χ_e^u made it possible to qualitatively account for enhanced transport in the central plasma due to sawtooth oscillations.

In the ASTRA–ETL code, either the experimental or calculated temperature and density profiles in the ohmic mode plasma ($Q_{\text{aux}} = 0$) can serve as the initial conditions. Since, for the shot under consideration, the data on the experimental profiles in the ohmic mode are unavailable, we determine the desired initial conditions by simulating an H-mode with subsequent switching-off of the auxiliary heating. With these initial conditions, the ASTRA–ETL code models the evolution of the plasma parameters during the L–H transition, the only control parameter being the input power. The ohmic power calculated at the initial instant is equal to $Q_{\text{Joule}} \approx 1.5$ MW. Below, the injected beam power will be assumed to be redistributed between ions and electrons according to formulas (8). The total input power is $Q_{\text{tot}} = Q_{\text{aux}} + Q_{\text{Joule}}$. A neutral beam with the power $Q_{\text{aux}} = 2.5$ MW begins to be injected at the time $t = 0$ ms. Figure 3 illustrates an L–H transition that starts 25 ms after the auxiliary neutral beam injection is switched on and lasts ~10 ms (the duration of the transition is determined from the time scale on which a poloidal sheared flow with a velocity V is generated). Figure 3a shows the time evolution of the heat flux Q_S through the TL (and, accordingly, through the separatrix). The turbulent heat flux is calculated from the following formula, which can be derived from the convective term in the Braginskii equation (1.23) in [11]:

$$(3/2)\langle n(T_e + T_i)V\rangle = (3/2)(\langle n\rangle(Q_i^{\text{turb}} + Q_e^{\text{turb}}) + \langle (T_e + T_i)\rangle\Gamma^{\text{turb}}),$$

where $Q^{\text{turb}} = \langle \tilde{T}\tilde{V}\rangle$, $\Gamma^{\text{turb}} = \langle \tilde{n}\tilde{V}\rangle$, the angular brackets $\langle\ldots\rangle$ stand for spatial averaging, $\tilde{T}$ and $\tilde{n}$ are temperature and density fluctuations, the velocity $\tilde{V}$ should be understood as the velocity field of the convective cells, and $\langle n\rangle = (n_B + n_S)/2$ and $\langle T\rangle = (T_B + T_S)/2$ are the averaged density and temperature inside the transport barrier. The power Q_S is expressed in MW and has the form

$$Q_S = Q^{\text{turb}} + Q^{\text{dif}}, \qquad (12)$$

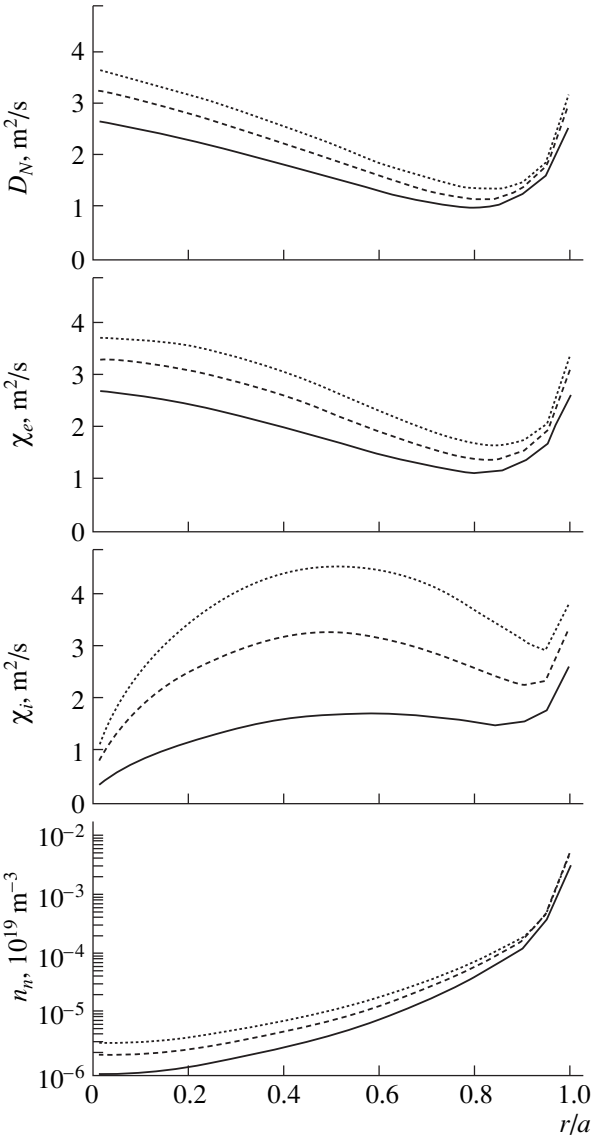

Fig. 2. Profiles of the transport coefficients and neutral density in accordance with the profiles shown in Fig. 1. The solid, dashed and dotted curves refer to the same confinement modes as in Fig. 1.

where

$$Q^{\text{turb}} = 1.6\times10^{-3}S\left\{\frac{3}{4}[(n_B + n_S)(Q_i^{\text{turb}} + Q_e^{\text{turb}}) + (T_{Bi} + T_{Si} + T_{Be} + T_{Se})\Gamma^{\text{turb}}]\right\},$$

$$Q^{\text{dif}} = 1.6\times10^{-3}S\left\{\frac{3}{4}[(n_B + n_S)(Q_i^{\text{dif}} + Q_e^{\text{dif}}) + (T_{Bi} + T_{Si} + T_{Be} + T_{Se})\Gamma^{\text{dif}}]\right\},$$

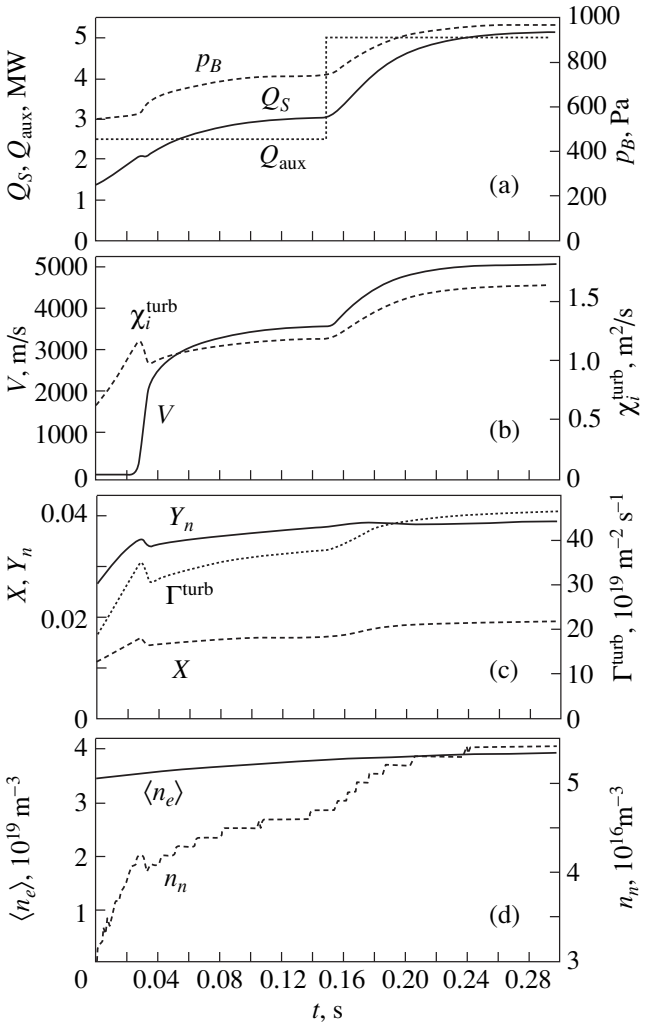

Fig. 3. Time evolutions of (a) the auxiliary heating power Q_{aux}, the power Q_S of the heat flux through the separatrix, and the pressure $p_B = (T_{Bi} + T_{Be})n_{Be}$ at the pedestal; (b) the velocity V of the poloidal sheared flow and the ion turbulent thermal diffusivity χ_i^{turb}; (c) the dimensionless amplitudes of potential and density fluctuations, X and Y_n, and the turbulent particle flux Γ^{turb}; and (d) the averaged electron density $\langle n_e \rangle$ and the neutral density n_n.

S is the area of the last closed magnetic surface in m^2; and T_B and n_B are expressed in keV and in units of 10^{19} m^{-3}, respectively.

The diffusive transport is assumed to be driven by small-scale ($\lambda \ll L$) plasma turbulence.

Figure 3b displays the time evolution of the ion turbulent thermal diffusivity $\chi_i^{turb} = Q_i^{turb} L/(T_{Bi} - T_{Si})$, which reaches its maximum value just before the L–H transition and then starts to decrease because the plasma turbulence is suppressed by the developing poloidal sheared flow. The power of the heat flux through the separatrix at the time at which the turbulent

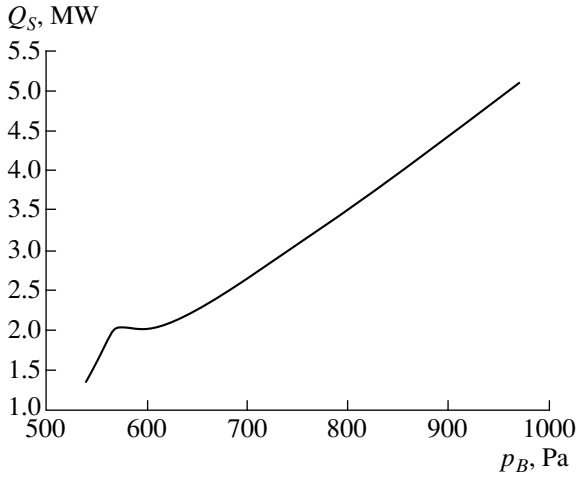

Fig. 4. Power Q_S of the heat flux through the separatrix as a function of the pressure at the pedestal for the L–H transition scenario illustrated in Fig. 3.

transport coefficients reach their maxima can naturally be regarded as a threshold power Q_{L-H} for the L–H transition.

For the averaged electron density $\langle n \rangle = 3.55 \times 10^{19}$ m^{-3}, the threshold power is $Q_{L-H} \approx 2.07$ MW. Since the input power exceeds the threshold power only slightly, the experimentally observed L–H transition occurs on a relatively long time scale (about 15 ms). The calculated velocity of the sheared $\mathbf{E} \times \mathbf{B}$ flow is equal to 3600 m/s (the measured poloidal flow velocity being 5000 m/s), and the turbulent transport coefficients decrease (Fig. 3b). Although, during the L–H transition, the temperature and density profiles in the central plasma change insignificantly (the only pronounced effect is the appearance of a pedestal), the plasma confinement actually improves. The confinement improvement is clearly seen in Fig. 4, which presents the heat power Q_S flowing through the separatrix as a function of the pressure $p_B = (T_{Be} + T_{Bi})n_B$ at the pedestal (since the pressure at the separatrix is constant, the pressure gradient inside the transport barrier is governed by the pressure at the pedestal). Here, the values of Q_S and p_B are taken from the time evolutions shown in Fig. 3a. The horizontal part of the profile (at $Q_S \approx Q_{L-H}$) corresponds to the L–H transition. A decrease in the slope angle of the profile at large pressure gradients provides evidence that the plasma confinement does improve. It is interesting to note that an increase in the input power of up to $Q_{aux} = 5$ MW at $t = 150$ ms after the L–H transition (Fig. 3a) does not further improve the confinement (the slope angle of the plot in Fig. 4 does not change), although the pressure p_B at the pedestal increases from 717 to 973 Pa ($p_S = 192$ Pa) and, accordingly, the profile shifts upward (see the profiles in Fig. 1). For $Q_S = 2.5$ MW in the steady state (Fig. 3c), the fluctuation amplitudes in the

Table 1

n_n, 10^{19} m^{-3}	L_n, m	$\langle n\rangle$, 10^{19} m^{-3}	$\frac{Q_{\mathrm{L-H}}}{\langle n\rangle}$	$Q_{\mathrm{L-H}}$, MW	T_{Bi}, keV	T_{Be}, keV	n_B, 10^{19} m^{-3}	ν/ω_c, 10^{-5}	ν_{cx}/ω_c, 10^{-5}
0.0014	0.025	2.98	0.70	2.09	0.085	0.09	2.19	1.24	0.55
0.0029	0.024	3.82	0.67	2.56	0.082	0.085	2.34	1.15	1.14
0.0044	0.023	4.36	0.67	2.92	0.08	0.081	2.45	1.09	1.68
0.0059	0.023	4.75	0.68	3.24	0.077	0.078	2.56	1.02	2.26

H-mode are close to those measured experimentally [10]: $e\varphi_{rms}/T = (L/\pi\rho)X \approx 10X = 0.16$ and $n_{rms}/n = 2Y_n = 0.08$.

Figure 3d shows the time evolution of the averaged electron density. In the ASTRA code, the averaged density is made close to the experimental one by automatically adjusting the neutral source power at the plasma edge. This algorithm models controlled gas puffing through a valve in real experiments. The neutral density n_n at the separatrix is computed from the preset initial and final values of $\langle n\rangle$ and from the desired evolution time. The neutral density, which is assumed, for simplicity, to be constant in the TL ($n_{nS} = n_{nB} = n_n$), usually varies in the range $10^{16} < n_n < 10^{17}$ m^{-3}. In order for the L–H transition scenario to agree with the shot under analysis, we calculated n_n by setting $\langle n\rangle$ (t = 0) = 3.45×10^{19} m^{-3} and $\langle n\rangle$ (t = 150 ms) = 4×10^{19} m^{-3}, the temperature of neutral particles at the separatrix being constant, T_n = 0.003 keV.

5. DEPENDENCE OF THE THRESHOLD POWER OF THE L–H TRANSITION ON THE AVERAGED ELECTRON DENSITY

To illustrate the dependence of the threshold power of the L–H transition on the averaged electron density, we use existence diagrams, in which the experimental points corresponding to the L- and H-modes are plotted in the "power flowing through the separatrix–averaged density" coordinates. The dependence of the threshold power on the averaged density is represented by the curve that separates the points referring to the L- and H-modes. In simulations, the threshold power $Q_{\mathrm{L-H}}$ is defined as the sum of the heat fluxes through the separatrix via the ion and electron channels just before the L–H transition, when the turbulent transport coefficients are maximum. Since, in simulations of the transition scenarios, the averaged electron density depends sensitively on the source of neutral particles, we first consider how the edge density and temperature of the neutral particles affect the parameters of the L–H transition.

In the combined ASTRA–ETL model, the neutrals, on the one hand, act to slow down the poloidal plasma rotation because of the momentum exchange with ions via the charge exchange mechanism and, on the other hand, serve as a particle source, which governs the electron density profile. In turn, the transport coefficients that depend on the density profile in the central plasma affect the parameters of the L–H transition. In order to determine the extent to which the power threshold and energy confinement time are influenced by neutral particles, we carried out a series of simulations of L–H transition scenarios at different neutral densities n_n, the other parameters in (11) being fixed [10]. The results of calculations with different neutral densities n_n are summarized in Table 1 and are illustrated by circles in Fig. 5.

In this series of simulations, the threshold power $Q_{\mathrm{L-H}}$ is a linear function of the averaged density $\langle n\rangle$, because the viscosity of a poloidally rotating plasma increases due to charge exchange. In the ETL model,

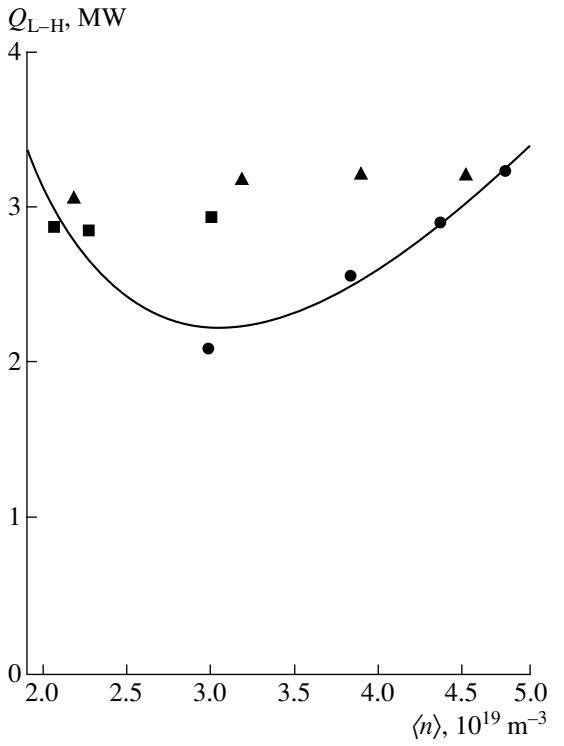

Fig. 5. Threshold power $Q_{\mathrm{L-H}}$ vs. the mean plasma density: the circles and triangles illustrate how the electron density changes at the expense of n_n and T_n, respectively, and the squares refer to a discharge with cryopumping (shot no. 89348).

the transition to the H-mode is associated with the onset of the poloidal sheared flow, which suppresses plasma turbulence. The sheared flow results from the interaction between the convective cells in the TL. The plasma starts to rotate in the poloidal direction only when the rate of the nonlinear generation of the sheared flow by the convective cells is higher than the rate of viscous damping; in other words, the rotation velocity in convective cells should exceed a critical value (see Eqs. (39) and (41) in [4]). The characteristic velocity of the plasma convection near the separatrix is governed by the pressure gradient. As the viscosity increases, the velocity of the poloidal sheared flow decreases and, consequently, the pressure gradient ∇p_B in the TL (i.e., the input power) required for the transition to the H-mode increases. According to Eq. (40) in [4], the criterion for the L–H transition in terms of the pressure gradient in the TL has the form

$$\nabla p_B > \nabla p_{\mathrm{L-H}}, \tag{13}$$

where

$$\nabla p_B \equiv [n_B(T_{Bi} + T_{Be}) - n_S(T_{Se} + T_{Si})]/L,$$

$$\nabla p_{\mathrm{L-H}} \approx \frac{n_S T_{Se}}{\rho}\left[0.074(\sigma k^{-2} + 0.037k^2)k^2\frac{R}{\rho}\left(1 + 5\frac{\nu + \nu_{cx}}{\omega_c k^2}\right)\right],$$

$k = 2\sqrt{2}\,\rho\pi/L$, $\rho = C_S/\omega_c$ is the ion Larmor radius in terms of the electron temperature, L is the width of the transport barrier, C_S is the speed of sound in terms of the electron temperature, ω_c is the ion gyrofrequency, R is the major radius of the plasma column, the quantity $\sigma = \sqrt{M_i/m_e}k_\parallel^2\rho\lambda_e$ is proportional to the Spitzer plasma conductivity, $k_\parallel = 1/qR$, and λ_e is the electron mean free path.

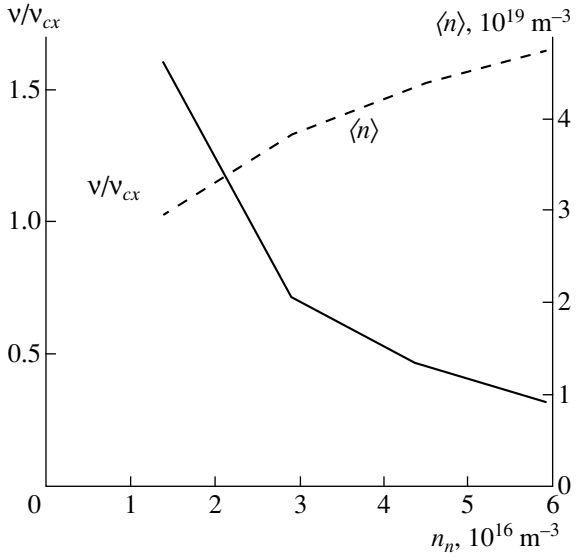

Fig. 6. Plots of ν_{cx}/ν and $\langle n\rangle$ vs. the neutral density n_n.

From (13), we can see that the critical pressure gradient $\nabla p_{\mathrm{L-H}}$ depends linearly on the ion viscosity $(\nu + \nu_{cx})$, where

$$\nu = \frac{\omega_T\nu_*}{(1 + \nu_*)(1 + \nu_*\varepsilon^{3/2})}, \quad \nu_{cx} = \langle v\sigma\rangle_{cx} n_n \tag{14}$$

are the simplest representations of the neoclassical viscosity and the friction coefficient due to the charge exchange of neutrals with a zero mean poloidal velocity on the bulk ions. In (14), the ion collisionality parameter has the form $\nu_* \equiv \nu_i/(\omega_T\varepsilon^{3/2})$, where ν_i is the ion collision frequency, $\omega_T = V_{Ti}/(qR)$ is the bounce frequency, V_{Ti} is the ion thermal velocity, q is the safety factor, and $\varepsilon = a/R$ is the inverse aspect ratio.

In the four-field ETL model, the generalized expression for the power carried away by the convective cells during the L–H transition has the form (cf. Eq. (22) in [3])

$$Q_{\mathrm{L-H}}^{\mathrm{turb}} \approx 3.2L(\nu + \nu_{cx})[n_B(T_{Bi} + T_{Be}) - n_S(T_{Si} + T_{Se})] = 3.2L^2(\nu + \nu_{cx})\nabla p_{\mathrm{L-H}} \tag{15}$$

so that the total threshold power of the L–H transition can be written as

$$Q_{\mathrm{L-H}} = Q_{\mathrm{L-H}}^{\mathrm{turb}} + Q_{\mathrm{L-H}}^{\mathrm{dif}} \approx (3.2L^2(\nu + \nu_{cx}) + CD_B)\nabla p_{\mathrm{L-H}}. \tag{16}$$

Estimate (15) was derived under the assumption that, in the ETL model, the dissipation coefficients in the equations for the temperature and density fluctuations are the same. Without this assumption, we cannot express $Q_{\mathrm{L-H}}^{\mathrm{turb}}$ through $\nabla p_{\mathrm{L-H}}$. In expression (16), $D_B = \rho C_S/16$ is the Bohm diffusion coefficient and the numerical factor $C = 0.5$ was determined from the calibration calculations. For simulations illustrated in Figs. 3 and 4, estimate (16) gives $Q_{\mathrm{L-H}} \approx 2.5$ MW, which is close to the computed level $Q_{\mathrm{L-H}} \approx 2.07$ MW. We substitute the critical pressure gradient (13) into formula (16) to arrive at the final expression for the threshold power:

$$Q_{\mathrm{L-H}} \approx 9.9\frac{(L^2(\nu + \nu_{cx}) + CD_B)\lambda_e}{q^2\rho R}n_S T_{Se} \propto \frac{L^2(\nu + \nu_{cx})BT_{Se}^{5/2}}{q^2 R}. \tag{17}$$

Formula (17) implies that, for $\nu < \nu_{cx}$, the threshold power $Q_{\mathrm{L-H}}$ is proportional to n_n and, accordingly, to $\langle n\rangle$. The dependence of $\langle n\rangle$ on n_n is presented in Fig. 6, which also shows the ratio of the neoclassical viscosity to the viscosity associated with charge exchange for different neutral densities. One can see that, in the

ranges $n_n > 2.5 \times 10^{16}$ m^{-3} and $\langle n \rangle > 3.5 \times 10^{19}$ m^{-3}, the charge exchange–related viscosity dominates over the neoclassical one, $\nu_{cx} > \nu$. In these ranges, an increase in the neutral density via neutral injection prevents the onset of the poloidal sheared flow, so that the transition to the H-mode requires high input powers.

The simulations under discussion were performed for a mixture of cold and warm neutrals, $n_n = n_C + n_W$, where the density n_W of warm neutrals (with the temperature $T_W = 20$ eV) was equal to 0.3 of the density n_C of cold neutrals (with the temperature $T_C = 2$ eV).

We also carried out a series of simulations in the range of low plasma densities for the discharge with cryopumping (shot no. 89348 [12], see the squares in Fig. 5). The input parameters were as follows:

$$R = 1.67 \text{ m},\ a = 0.63 \text{ m},\ B = 2.17 \text{ T},$$
$$I_{pl} = 1.37 \text{ MA},\ q = 4.55,\ b/a = 1.8,\ \delta = 0.3, \quad (18)$$
$$T_{Si} = 190 \text{ eV},\ T_{Se} = 55 \text{ eV},\ n_S = 0.8 \times 10^{19} \text{ m}^{-3}.$$

Since the plasma density in this discharge is low, the electron and ion temperatures at the separatrix may be different. A neutral beam with the power $Q_{\text{aux}} = 2$ MW begins to be injected at the time $t = 0$; at the time $t = 0.2$ ms, the neutral beam power is instantaneously increased to $Q_{\text{aux}} = 3$ MW. In order to determine how much the L–H transition is sensitive to the neutral density n_n and neutral temperature T_n, we simulated the following four L–H transition scenarios:

1. A scenario with n_n = const and T_n = const. This scenario refers to the point at which $Q_{\text{L–H}} = 2.87$ MW, $\langle n \rangle = 2.07 \times 10^{19}$ m^{-3}, and $n_n = 5.8 \times 10^{15}$ m^{-3} (the first square from the left in Fig. 5). During the injection of a neutral beam with the power $Q_{\text{aux}} = 2$ MW, the plasma is in the L-mode. After the beam power is instantaneously increased to $Q_{\text{aux}} = 3$ MW, the plasma evolves into the H-mode: pedestals form on the electron and ion temperature profiles (T_{Bi} and T_{Be} increase) and a sheared $\mathbf{E} \times \mathbf{B}$ flow with a rotation velocity of 8450 m/s is generated. The simulated scenario differs from the actual one in that the averaged electron density and the energy confinement time τ_E both decrease after the L–H transition, because, in calculations, the source of neutral particles was artificially fixed. The confinement deteriorates because transport coefficients increase with temperature.

2. The ASTRA code changes the averaged electron density by adjusting the neutral density profile n_n to the experimental one. This scenario refers to the point at which $Q_{\text{L–H}} = 2.85$ MW, $\langle n \rangle = 2.27 \times 10^{19}$ m^{-3}, and $n_n = 9.5 \times 10^{15}$ m^{-3} (the second square from the left in Fig. 5). According to Fig. 10a in [12], the time behavior of the averaged electron density $\langle n \rangle$ is prescribed as follows: first, the density $\langle n \rangle$ decreases from $\langle n \rangle (t = 0) = 2.37 \times 10^{19}$ m^{-3} to $\langle n \rangle (t = 0.21 \text{ s}) = 2.27 \times 10^{19}$ m^{-3}; then, at fixed $\langle n \rangle$, the plasma evolves from the L-mode to the H-mode; and, finally, starting from the time $t = 0.4$ s, the averaged electron density increases to $\langle n \rangle (t = 0.62 \text{ s}) = 2.92 \times 10^{19}$ m^{-3}. The velocity of the poloidal sheared flow is found to be about 3500 m/s, which is much lower than that in the first scenario, and the energy confinement time τ_E increases insignificantly. The confinement improves only slightly, because the appearance of a pedestal on the density profile leads to the disappearance of pedestals from the temperature profiles.

3. T_n increases at constant n_n. This scenario refers to the point at which $Q_{\text{L–H}} = 2.94$ MW, $\langle n \rangle = 3 \times 10^{19}$ m^{-3}, and $n_n = 6 \times 10^{15}$ m^{-3} (the first square from the right in Fig. 5). In the ohmic mode, we have $T_n = 30$ eV (as in the first and second scenarios). After a neutral beam with the power $Q_{\text{aux}} = 2$ MW begins to be injected at $t = 0$, the temperature T_n is found to increase to 60 eV ($T_{Bi} = 156$ eV). Because of the increase in T_n, the spatial scale L_n (on which the radial profile of the neutral density decreases) increases from 12.5 to 20 cm. After the time $t = 0.2$ s, at which the beam power is instantaneously raised to $Q_{\text{aux}} = 3$ MW, the temperature T_n is found to increase to 100 eV ($T_{Bi} = 175$ eV) and L_n becomes as long as 26 cm. As a result, a barrier forms on the density profile, thereby naturally increasing both the energy confinement time τ_E and the electron density $\langle n \rangle$ during the L–H transition. The assumption that the temperature of neutral particles increases proportionally to the edge ion temperature is justified by the fact that warm neutrals are produced from the recycling of ions escaping from the plasma.

4. A scenario with $n_C = 1.7 \times 10^{16}$ m^{-3}, $T_C = 2$ eV, $n_W = \eta_n \Gamma_n$ with $\eta_n = 2.7 \times 10^{-7}$, and $T_W = \eta_T T_{Bi}$ with $\eta_T = 0.3$. In this scenario, the feedback condition is introduced for the density and temperature of the warm neutrals produced by recycling. The time evolution of a discharge plasma with these parameters is illustrated in Fig. 7. The L–H transition corresponds to the point at which $Q_{\text{L–H}} = 3$ MW, $\langle n \rangle = 3.4 \times 10^{19}$ m^{-3}, and $n_n = 2.33 \times 10^{16}$ m^{-3}. Note that the experimentally observed increase in the averaged electron density after the L–H transition is well reproduced in this scenario.

A comparison between these four scenarios shows that, although the details of the L–H transitions are sensitive to the way in which the density evolves, the threshold powers for these transitions differ at most by 5%.

Combining the points calculated for a low-density plasma (the first and second scenarios) with the simulation results summarized in Table 1, we arrive at a U-shaped profile of the threshold power (Fig. 5):

$$Q_{\text{L–H}} \approx 1.7\langle n \rangle + 15.4/\langle n \rangle - 7.9, \quad (19)$$

where $Q_{\text{L–H}}$ is in MW and $\langle n \rangle$ is in units of 10^{19} m^{-3}.

When approximating experimental data, Carreras *et al.* [12] obtained a similar dependence (see Fig. 19 in

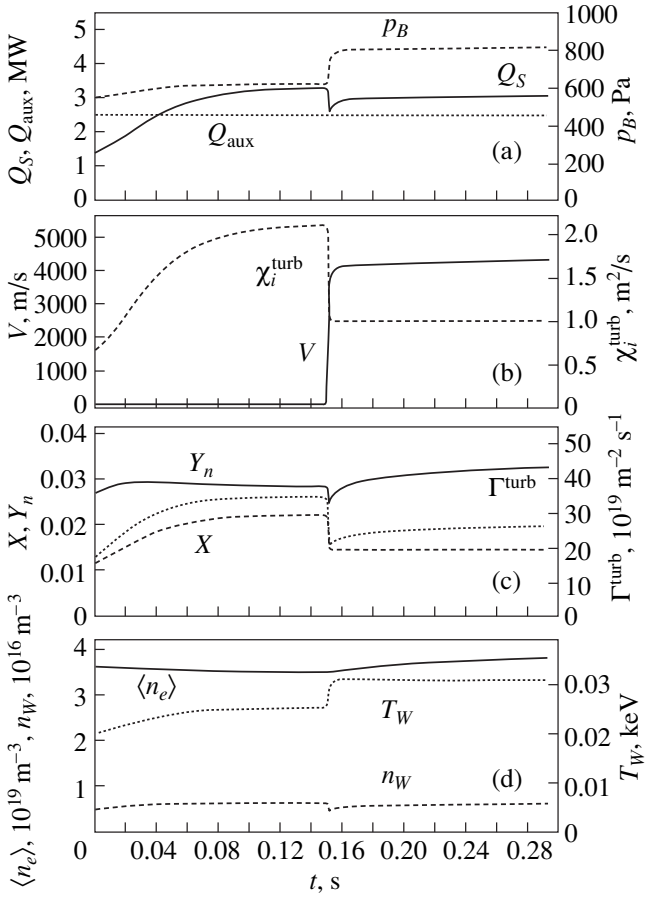

Fig. 7. L–H transition scenario analogous to that illustrated in Fig. 3, but when the density and temperature of warm neutrals serve as adjustable parameters: $n_W = \eta_n \Gamma_n$ and $T_W = \eta_T T_{Bi}$.

[12]). Our simulations show that such a specific U-shape can be explained by the fact that the profile is composed of two different parts: in the range $\langle n \rangle > 3 \times 10^{19}$ m^{-3}, in which $\nu_{cx} > \nu$, we have $Q_{L-H} \propto \langle n \rangle$ because of the friction of ions on neutrals, and, in the range of lower electron densities, in which $\nu_{cx} < \nu$, the profile becomes nonlinear and the threshold power increases because the electron and ion temperatures and electron density at the separatrix increase (see below). The points that do not lie on the U-shaped profile in Fig. 5 were calculated from the parameter values (18) at the separatrix for a discharge with cryopumping (shot no. 89348). However, because of the lack of experimental data on n_n and T_n, we had to vary these two parameters. For this reason, the averaged electron density in this series of simulations was higher than the measured one. We found that, for the same electron density ($\langle n \rangle \approx 3 \times 10^{19}$ m^{-3}) and same magnetic configuration, the threshold power in shot no. 89348 (a discharge with cryopumping) was higher than that in shot no. 82830. This result agrees with the experimental observations.

In order to show that the dependence $Q_{L-H} \propto \langle n \rangle$ results exclusively from an increase in n_n, we carried out a series of calculations in which $\langle n \rangle$ changed at the expense of the neutral temperature T_n, the neutral density n_n being fixed. The calculated results are shown by triangles in Fig. 5. The triangles refer to the temperatures T_n = 0.03, 0.06, 0.09, and 0.12 keV (from left to right). Since the neutral temperature enters only the formula for the spatial scale L_n, on which the radial profile of the neutral density decreases, varying T_n makes it possible to change solely the electron density $\langle n \rangle$, the remaining parameters being fixed. The threshold power Q_{L-H} calculated in such a manner was found to be independent of $\langle n \rangle$. Thus, we can conclude that, in the ASTRA–ETL model, the dependence $Q_{L-H} \propto \langle n \rangle$ is associated exclusively with an increase in the friction of ions on neutrals.

6. THRESHOLD POWER AS A FUNCTION OF THE PARAMETER VALUES AT THE SEPARATRIX

Since experimental observations show that the power threshold of the L–H transition depends on the temperatures T_{Se} and T_{Si} and density n_S at the separatrix (see Fig. 1a in [13]), we performed a series of calculations for DIII-D shot no. 82830 in order to clarify this dependence.

Figure 8 makes it possible to compare the power thresholds calculated at different electron densities for two different ion temperatures at the separatrix (Fig. 8a): T_{Si} = 0.055 keV (triangles with upward-oriented vertices) and T_{Si} = 0.03 keV (triangles with downward-oriented vertices). Both of these series of calculations were carried out for T_{Se} = 0.03 keV. The remaining parameter values were taken from (11). An increase in the threshold power with increasing ion temperature at the separatrix is attributed to the following two circumstances. First, to raise the ion temperature at the separatrix, higher input powers are required. Second, in the Pfirsch–Schlüter regime, in which the ion collisionality parameter lies in the range $\nu_* > \varepsilon^{-3/2}$ (in calculations, we used $\nu_* \approx 6$ and $\varepsilon^{-3/2} \approx 4.2$), the neoclassical viscosity increases with ion temperature, thereby slowing down the poloidal sheared rotation. The dependence of the neoclassical viscosity $\nu \approx \omega_T/(\varepsilon^{3/2}\nu_*) \propto T^{5/2}$ on the ion temperature at the separatrix manifests itself in the fact that the threshold power Q_{L-H} becomes almost independent of the averaged electron density $\langle n \rangle$ (triangles with downward-oriented vertices), because, at T_{Si} = 0.055 keV, the charge exchange–related viscosity is lower than the neoclassical viscosity, $\nu_{cx} < \nu$. In contrast, the value T_{Si} = 0.03 keV refers to the case $\nu_{cx} > \nu$.

In Fig. 8b, the dependence of Q_{L-H} on the parameter n_S at fixed n_n is illustrated by asterisks, which correspond to $n_S = 1.5 \times 10^{19}$, 2×10^{19}, and 2.5×10^{19} m^{-3}

(from left to right). As n_S increases, the threshold power decreases because of a decrease in the neoclassical viscosity.

Figure 8c illustrates the threshold power as a function of the electron temperature ($T_{Se} = T_{Si}$) at the separatrix for a fixed averaged electron density ($\langle n\rangle = 3 \times 10^{19}$ m^{-3}). The parameter T_{Se} is incorporated into the ETL model through the dissipation coefficient, which is proportional to the Spitzer conductivity ($\sigma \propto T_{Se}^{5/2}$), and through the normalization condition for the electron and ion temperatures. According to criterion (13), the threshold for the onset of turbulent convection and the threshold power (17) are both functions of σ. From Fig. 8c, we can see that the threshold power is very sensitive to T_{Se}: as the temperature $T_{Se} = T_{Si}$ increases by 20%, the threshold power increases by a factor of 2.5. As $T_{Se} = T_{Si}$ further increases, the plasma conductivity becomes higher, thereby completely stabilizing the interchange instability, in which case the ASTRA–ETL model implies that the plasma cannot evolve into the L-mode. As the electron temperature ($T_{Se} = T_{Si}$) decreases, the threshold power decreases, so that the Joule heating power becomes high enough for a plasma to evolve into the ohmic L- and H-modes.

The sensitivity of the results obtained with the ASTRA–ETL model to the parameter $T_{Se} = T_{Si}$ probably stems from the assumption that T_{Se} and T_{Si} are both fixed at the separatrix. In the experiment, the temperatures T_{Se} and T_{Si} evolve in a self-consistent fashion, so that the power fluxes through the TL and the scrape-off layer (SOL) are the same. For example, if T_{Se} is low, then an interchange instability develops and the turbulent flux causes the temperature profile to flatten, which leads to an increase in T_{Se}. Another restriction on the ASTRA–ETL model is associated with the fact that the seed dissipation coefficients, which stem from the truncation of Fourier expansions of the fluctuating quantities, are assumed to be constant. However, the dependence $\sigma \propto T_{Se}^{5/2}$ implies that the seed dissipation coefficients should change as time elapses. To remove these restrictions requires three-dimensional modeling of the TL.

Our simulations show that higher power thresholds of the L–H transition may lead to better energy confinement. In order to illustrate this conclusion, we compare the turbulent transport coefficients for two transition scenarios corresponding to the points $T_{Se} = T_{Si} = 0.033$ keV and $T_{Se} = T_{Si} = 0.029$ keV in Fig. 8c. In Table 2, we summarize the parameters of the transport barrier for the following cases:

(i) L–H transition at $Q_S = 3.69$ MW and $T_{Se} = T_{Si} = 0.033$ keV.

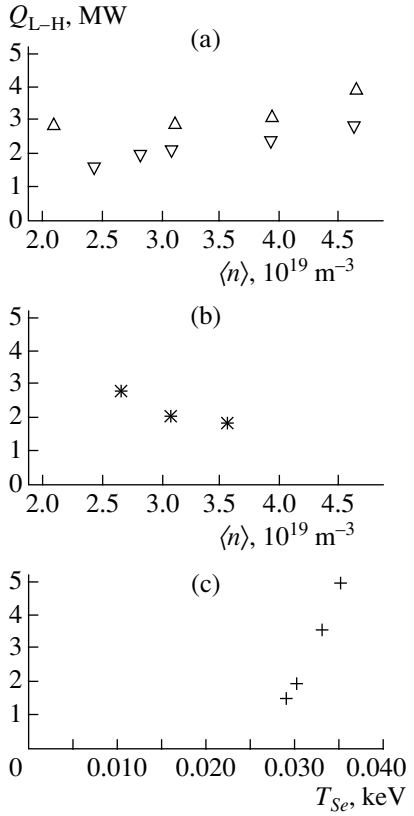

Fig. 8. (a) Threshold power $Q_{L–H}$ vs. the averaged electron density at $T_{Se} = 0.03$ keV for $T_{Si} = 0.055$ keV (triangles with upward-oriented vertices) and $T_{Si} = 0.03$ keV (triangles with downward-oriented vertices). (b) Threshold power $Q_{L–H}$ vs. the averaged electron density for different electron densities at the separatrix: $n_S = 1.5 \times 10^{19}$, 2×10^{19}, and 2.5×10^{19} m^{-3} (from left to right). (c) Threshold power $Q_{L–H}$ vs. the electron temperature at the separatrix ($T_{Si} = T_{Se}$) for $\langle n\rangle = 3 \times 10^{19}$ m^{-3}.

Table 2

No.	$T_{Se} = T_{Si}$, keV	Q_S, MW	$\langle n\rangle$, 10^{19} m^{-3}	T_{Bi}, keV	T_{Be}, keV	n_B, 10^{19} m^{-3}	V, m/s	χ_i^{turb}, m^2/s	χ_e^{turb}, m^2/s	D^{turb}, m^2/s	$e\phi_{rms}/T_{Se}$	n_{rms}/n_S	τ_E, s	Mode
1	0.033	3.69	3.12	0.11	0.11	2.3	370	1.67	1.4	1.45	0.2	0.036	0.07	H
2	0.033	1.50	3.23	0.08	0.08	2.5	0.24	0.35	0.31	0.32	0.1	0.034	0.12	L
3	0.029	1.53	3.12	0.07	0.07	2.4	1515	0.83	0.76	0.76	0.14	0.042	0.11	H

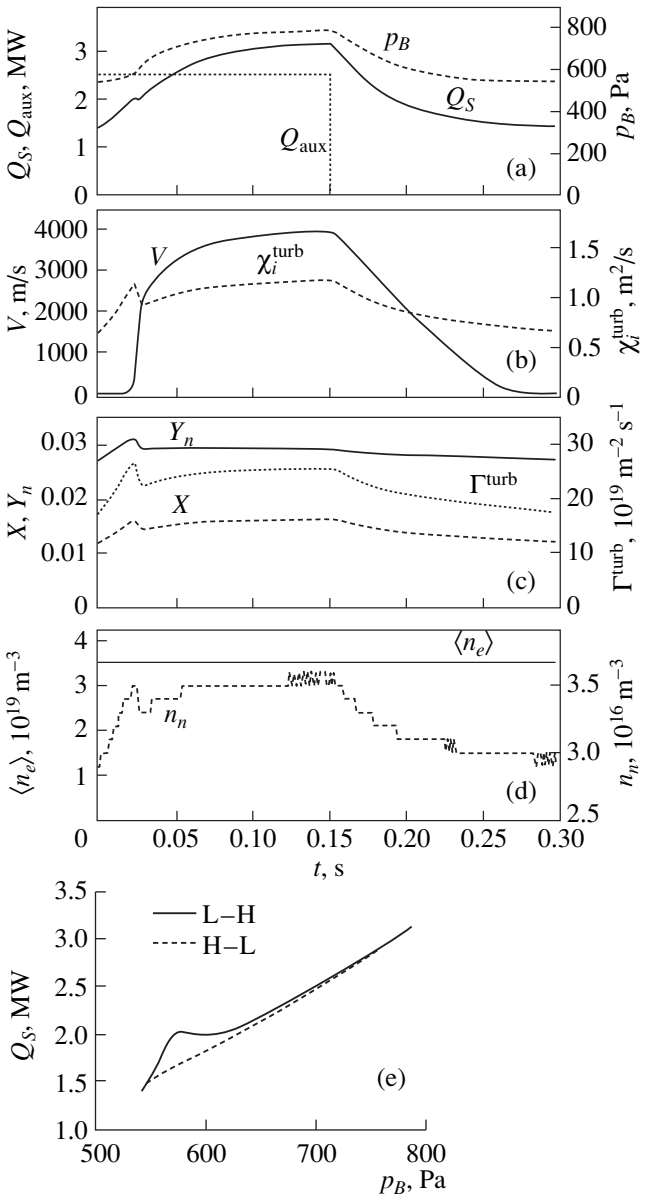

Fig. 9. L–H–L transition scenario in which the plasma evolves back into the L-mode after the neutral beam is switched off: (a) time evolutions of the auxiliary heating power Q_{aux}, the heat flux Q_S through the TL, and the pressure p_B at the pedestal; (b) time evolutions of the velocity V of the poloidal sheared flow and the turbulent thermal diffusivity χ_i^{turb}; (c) time evolutions of the fluctuation amplitudes X and Y_n and the turbulent particle flux Γ^{turb}; (d) time evolutions of the averaged electron density $\langle n_e \rangle$ and the neutral density n_n; and (e) the hysteresis curve $Q_S(p_B)$.

(ii) The transient L-mode in the same discharge at the time at which the power flux through the separatrix, $Q_S = 1.5$ MW, is close to the threshold power of the L–H transition in case (iii).

(iii) L–H transition at $Q_S = 1.53$ MW and $T_{Se} = T_{Si} = 0.029$ keV.

A comparison between the turbulent transport coefficients and τ_E in the second and third rows of Table 2 shows that, for essentially the same power Q_S, the energy confinement in the L-mode with a higher power threshold is no worse than that in the H-mode with a lower power threshold. Thus, we can conclude that, in discharges in which plasma turbulence is stabilized to a greater extent, the transition to the L-mode requires higher input powers.

7. MODELING OF THE H–L TRANSITION

In order to model the H–L transition scenarios, we also carried out two series of simulations for a discharge with the parameter values (11) and with $T_n = 0.003$ keV and $n_n = 3 \times 10^{16}$ m^{-3} (shot no. 82830). The calculated scenarios are illustrated in Figs. 9 and 10.

In the first series of simulations, the averaged plasma density was maintained at a constant level by automatically adjusting the model neutral source in the ASTRA code (Figs. 9d, 10d). The H–L transition illustrated in Fig. 9 was simulated by switching-off the neutral beam power, the averaged plasma density being constant (Fig. 9a). The plasma is seen to evolve in a quasi-steady fashion back into the ohmic mode on a time scale of about 80 ms, which is comparable with the energy confinement time. The L–H–L transitions show a pronounced hysteresis effect (Fig. 9e): at $Q_S = 1.5$ MW, the plasma remains in the H-mode, although the threshold power of the L–H transition is equal to 2 MW.

In the second series of simulations (Fig. 10), the H–L transition was driven by an increase in the plasma density via gas puffing, the NBI power being constant. The plasma eventually evolves into the L-mode, but, because of an increase in the plasma density (Fig. 10d), the turbulent fluxes are more intense than before the L–H transition (Fig. 10c). The time scales on which the plasma evolves into the H-mode and, then, back into the L-mode are close to one another and are approximately equal to 50 ms. From Fig. 10e, we can see that, after the transition back to the L-mode, the effective thermal diffusivity, proportional to Q_S/p_B, is much higher than that before the transition to the H-mode.

8. PARAMETRIC DEPENDENCES OF THE ENERGY CONFINEMENT TIME

We applied the ASTRA–ETL code to investigate the global energy confinement time τ_E as a function of the averaged plasma density. According to our simulations, the behavior of the energy confinement time can be described as follows (see Fig. 11a). In the range $\langle n \rangle < 3.6 \times 10^{19}$ m^{-3}, τ_E increases linearly with $\langle n \rangle$. In the ohmic mode, we have $\tau_E = \text{const}$, and, in the L-mode,

we have $\tau_E \propto \langle n \rangle^{0.6}$, which is close to the dependence $\tau_E \propto \langle n \rangle^{0.5} P^{-0.5}$ (where P is the input power) measured experimentally in DIII-D (see Eq. (4) in [14], p. 2–41). That the confinement improves as $\langle n \rangle$ increases is explained by the dependence $1/\langle n \rangle$ in the Ohkawa electron thermal diffusivity (4). The confinement saturation is caused by the transport via the ion channel dominating over that via the electron channel (in the core plasma, the ion transport coefficients are density-independent). The dependence of the energy confinement time on the threshold power (Fig. 11b) was evaluated from the database used in simulations and, at fixed values of $\langle n \rangle$, was found to be $\tau_E = 0.12\, Q_{\mathrm{L-H}}^{-0.46}$ (the power-law index in the measured dependence is –0.5).

Simulations with the ASTRA–ETL code showed that, during the L–H transition, τ_E increases insignificantly (Fig. 11a), although the turbulent transport coefficients decrease by at least a factor of 2. This result can be explained by the fact that, for the experimentally observed width of the transport barrier ($L \approx 2$ cm), τ_E is only slightly sensitive to the evolution of the transport coefficients inside the barrier, provided that the thermal diffusivity χ^{ETL} inside the barrier is close to the mean thermal diffusivity χ^{ASTRA} in the central plasma. In order for τ_E to increase by a factor of 2 during the L–H transition, it is necessary that the thermal diffusivity inside the barrier be lower than the mean thermal diffusivity in the central plasma by a factor of more than 6, $\chi^{\mathrm{ETL}}/\chi^{\mathrm{ASTRA}} < 1/6$ (Fig. 11c).

The calculated results make it possible to establish the temperature at the center of the plasma column as a function of the temperature at the top of the pedestal for different averaged plasma densities. In the steady-state H-mode, the central temperature decreases only slightly in a linear fashion as the averaged plasma density increases. At the pedestal, the temperature decreases according to the law $1/n$, so that the effect of the temperature-profile "stiffness" (T_0/T_B = const) is not observed.

The dependence of τ_E on the extent to which the radial input power profile is peaked was determined using as an example the profile $P \propto \exp(-(r/r_0)^2)$. In the range $r_0 > 1.5a$, τ_E is independent of r_0. Making the input power profile peaked (with $r_0 = 0.1a$) strongly affects the temperature profile (the ratio $T_i(0)/T_{Bi}$ increases by a factor of 3), but τ_E increases at most by 20%.

The energy confinement time computed as a function of the toroidal magnetic field B is illustrated in Fig. 11d. In the ohmic mode, τ_E increases almost linearly with B. In the L-mode, we obtained the dependence $\tau_E \propto B^{0.69}$, which is steeper than the dependence that follows from the ITER-89P statistical scaling: $\tau_E \propto B^{0.2}$. We still lack the experimental data that would allow us to compare the calculated dependence $\tau_E(B)$ with that measured in DIII-D, because the scaling of the energy confinement time in terms of q for the L-mode in DIII-D is unavailable (see [14], p. 2–41).

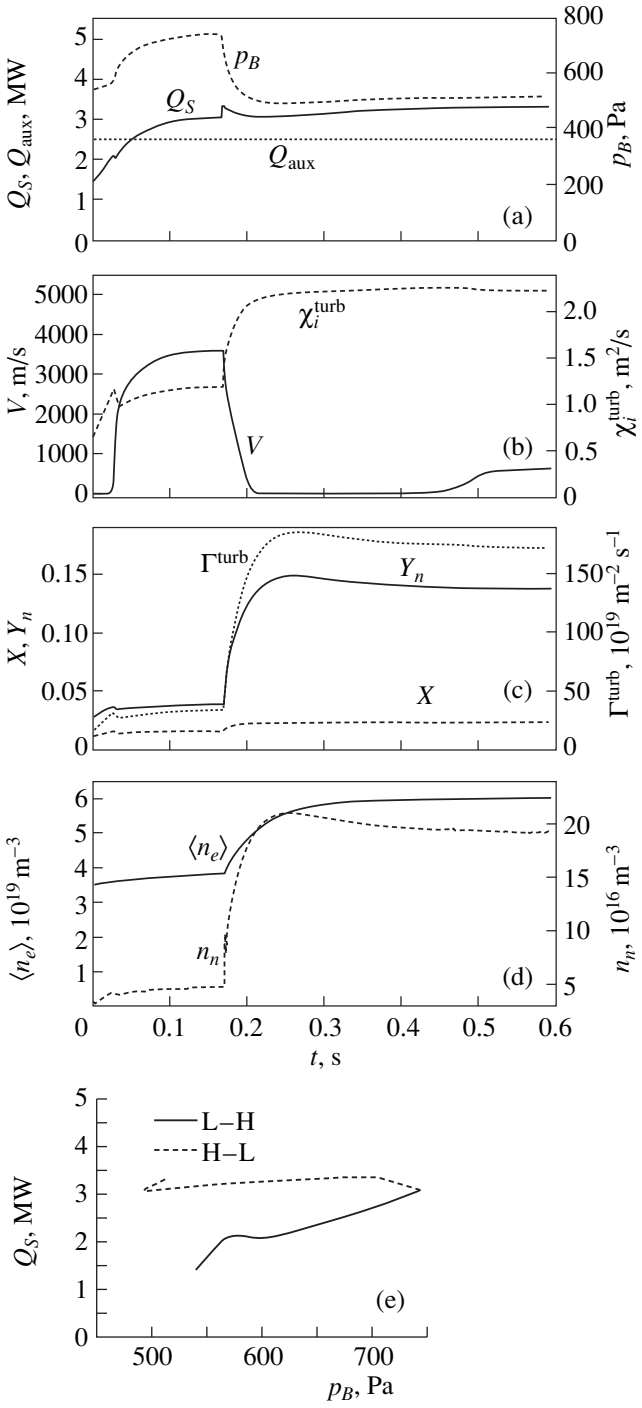

Fig. 10. The same as in Fig. 9 but for the L–H–L transition scenario in which the transition back to the L-mode is driven by an increase in the plasma density via gas puffing through a valve.

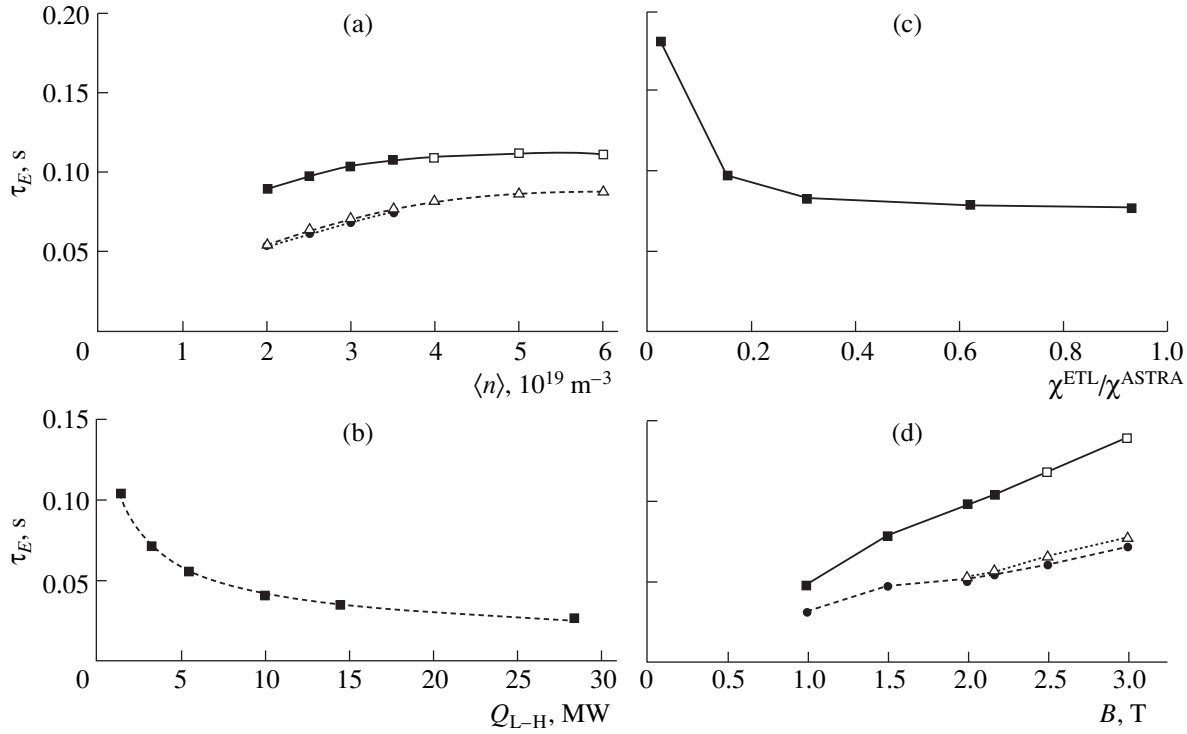

Fig. 11. Dependence of the energy confinement time τ_E on (a) the averaged electron density at $Q_S = 2.5$ MW in the L- and H-modes (the closed squares are for the ohmic mode, the open squares are for the ohmic H-mode, the closed circles are for the L-mode, and the open triangles are for the H-mode); (b) the input power at $\langle n \rangle = 3 \times 10^{19}$ m^{-3}; (c) the ratio of the thermal diffusivity χ^{ETL} inside the transport barrier to the thermal diffusivity χ^{ASTRA} in the main plasma; and (d) the toroidal magnetic field.

9. CONCLUSIONS

We have described the ASTRA transport code supplemented with the four-field ETL model, which serves to impose the boundary conditions of the third kind for the energy balance equations. We have applied the combined ASTRA–ETL model to simulate L–H transition scenarios and to calculate the energy confinement time and the threshold power of the L–H transition as functions of the averaged electron density $\langle n \rangle$; the averaged toroidal magnetic field B; the T_{Se}, T_{Si}, and n_S separatrix parameters; and the neutral density and neutral temperature at the separatrix.

According to the classification proposed by Connor and Wilson in review [15], the ETL model belongs to the class of L–H transition models in which the turbulence is suppressed by either the shear of the radial electric field or the shear of the plasma rotation velocity and the L–H transition itself is described in terms of the phase transition by a set of equations that includes the nonlinearly coupled equations for turbulent fluctuations and a poloidal sheared flow. The power flux $Q_S(\nabla p_B)$ through the separatrix starts to bifurcate when the input power is high enough to achieve the critical pressure gradient at which the convective cells become unstable against the generation of a poloidal sheared flow. Previous models with bifurcated solutions failed to establish the characteristics of the L–H transition as functions of the plasma parameters because the dependence of the transport coefficients on the electric field shear was introduced phenomenologically (see formula (2) in [16]). The ASTRA–ETL model makes it possible to reveal the parametric dependences of the energy confinement time and the threshold power of the L–H transition through self-consistent simulations of the evolution of the averaged profiles; sheared velocity; turbulent fluctuations; and the corresponding transport coefficients, which describe transport processes caused by the drift-resistive ballooning instability in the edge plasma.

When comparing the computed results with the experiment, we focused on the measured quantities. Accordingly, we have presented the calculated values of the sheared poloidal velocity (Figs. 3, 7, 9, 10), which were obtained experimentally in DIII-D, rather than the magnitude of the radial electric field, which is to be evaluated numerically from the measured rotation velocity using the force balance equation (see Fig. 4 in [16]). Since the computed poloidal velocity V and the computed plasma pressure gradient are both close to the experimental ones (see the table in [4]), the depth of the electrostatic well $E_r \approx -14$ kV/m) is also close to the experimental depth (E_r varied from about –11 to about –15 kV/m).

It is of interest to compare our results with the results obtained in [18], in which the identical Braginskii equations were solved, but the problem was treated in a different formulation. Ronglien *et al.* [17] calculated the profiles of the temperature, density, velocity, and radial electric field for prescribed transport coefficients, which were assumed to be constant in the radial direction. Varying the particle diffusivity, they obtained E_r and T_e profiles, which were found to be similar in shape to the experimental profiles in the L- and H-modes. They also concluded that the shear of E_r is due to the shear of the poloidal velocity (see [17, p. 1856]), which agrees with our basic assumption (see (A.3) in [4]), but differs from the accepted views regarding the physics of L–H transitions [16], according to which transport processes are suppressed by the shear of E_r, rather than the suppression of transport processes gives rise to the shear of E_r [17]. The ASTRA–ETL model is aimed at a self-consistent calculation of turbulent transport coefficients during the L–H transition, so that, in the model (as in experiments), the only way to trigger the L–H transition is to raise the input power.

In the four-field ASTRA–ETL model, the evolving density profile plays an important role, in contrast to the two-field ASTRA–ETL model [3], in which this profile was taken from the experiment. Self-consistent calculations of the density profile revealed a significant feedback effect: on the one hand, the threshold power of the L–H transition, the energy confinement time, the amplitude of turbulent fluctuations, and the velocity of the poloidal sheared flow depend substantially on the density, but, on the other hand, they affect the transport coefficients, which, in turn, govern the density profile.

We have shown that the linear dependence of the threshold power on the averaged electron density, $Q_{\text{L–H}} \propto \langle n \rangle$, results exclusively from an increase in n_n. In the range $\nu_{cx} > \nu$, the linear dependence is related to an increase in the viscosity of a poloidally rotating plasma due to charge exchange. In the range of low densities $\langle n \rangle$, in which $\nu_{cx} < \nu$, the dependence becomes nonlinear and the decrease in the density is accompanied by the increase in the threshold power because both the electron and ion temperatures at the separatrix increase. Over the entire range of the averaged electron densities under consideration, the dependence can be approximated by a U-shaped profile:

$$Q_{\text{L–H}} \approx 1.7\langle n \rangle + 15.4/\langle n \rangle - 7.9.$$

The calculated dependence of $Q_{\text{L–H}}$ on the parameter values at the separatrix is well approximated by the analytic estimate (17) and can be described as follows.

(i) For $\nu > \nu_{cx}$, $Q_{\text{L–H}}$ increases with T_{Si} by virtue of $\nu \propto T_{Si}^{5/2}$; for $\nu < \nu_{cx}$, we have $Q_{\text{L–H}} = \text{const}$.

(ii) $Q_{\text{L–H}}$ increases sharply with T_{Se} by virtue of $\sigma \propto T_{Se}^{5/2}$.

(iii) With increasing electron density at the separatrix, $Q_{\text{L–H}}$ decreases as $1/n_S$ by virtue of $\sigma \propto 1/n_S$.

These results indicate that, in deriving a scaling of the form $Q_{\text{L–H}} \propto \langle n \rangle B$ for the threshold power of the L–H transition in terms of the global plasma parameters, we must take into account the "hidden" parameters: T_{Se}, T_{Si}, n_S, T_n, and n_n. If these hidden parameters are neglected, then the uncertainties in the approximation of the experimental points by a statistical approach, which is used, e.g., to make predictions for ITER [18], are so large that the predicted threshold power of the L–H transition lies in the range from 50 to 200 MW. Applying the statistical approach to the samples of data from experiments with close parameter values at the separatrix (at least, with close electron temperatures T_{Se}) makes it possible to significantly reduce the spread in experimental points around the approximated dependences and to increase the accuracy of predictions.

We have shown that the best way to model an increase in the plasma density during the L–H transition is to take into account an increase in the temperature of the warm neutrals. When the temperature and density of the neutral particles are fixed, increasing the input power results in a decrease in the mean plasma density. If the input power is high enough to trigger the L–H transition, then the mean plasma density also decreases, but at a slower rate. In this situation, we failed to observe an increase in the plasma density, because, for the parameter values adopted in our simulations, an improvement in the plasma confinement inside the transport barrier is insufficient to improve confinement of the central plasma by virtue of an increase in the plasma temperature. Taking into account the fact that warm neutrals are produced from the recycling of plasma ions, we assumed that the temperature of neutral particles changes proportionally to the ion temperature at the pedestal, in which case an increase in the ion temperature at the pedestal during the L–H transition leads to an increase in the temperature of neutral particles. As a result, the neutrals penetrate farther into the plasma and the averaged plasma density is observed to increase.

We have modeled the hysteresis effect during an L–H–L transition triggered by increasing the input power.

We have determined the working ranges of the temperatures and densities at the pedestal ($0.05\ \text{keV} < T_{Be} < 0.15\ \text{keV}$ and $0.8 \times 10^{19}\ \text{m}^{-3} < n_{Be} < 3 \times 10^{19}\ \text{m}^{-3}$) that correspond to the onset of the L–H transition in DIII-D plasmas. According to the approximate relationship (Fig. 12a)

$$T_{Be} - T_{Se} \approx 0.1/n_{Be}, \tag{20}$$

with $T_{Se} = 0.03$ keV, the critical parameter for the onset of the L–H transition is the total plasma pressure gradient in the region just inside the separatrix, where a transport barrier forms after the transition. For compar-

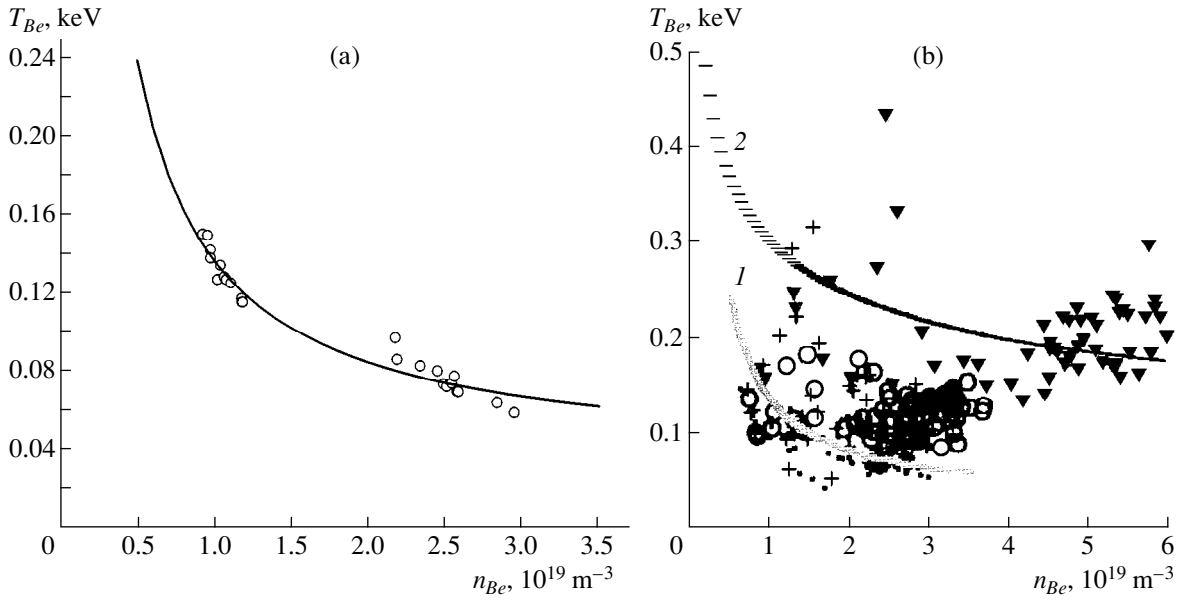

Fig. 12. (a) Range of the parameters T_{Be} and n_{Be} corresponding to the calculated scenarios of the L–H transition (circles); the approximate dependence (20) is shown by the solid curve. (b) Working range of the parameters T_{Be} and n_{Be} measured in a plasma with at the magnetic surface lying at a distance of 2 cm from the separatrix in various DIII-D operating modes (the points are for the ohmic mode, the crosses are for the L-mode, the closed triangles are for the H-mode, and the open circles are for the L–H transition): curves *1* and *2*, calculated with the ASTRA–ETL and ASDEX-Upgrade models, respectively, approximate the lower and upper boundaries of the region in which the L–H transition can occur.

ison with the experimental data, Fig. 12b presents T_{Be} and n_{Be} measured at the magnetic surface lying at a distance of 2 cm from the separatrix in various modes of DIII-D operation (see Figs. 2.2.3–4 in [14, p. 2-46]). Curves *1* and *2*, which were calculated with the ASTRA–ETL and ASDEX-Upgrade models, respectively, approximate the lower and upper boundaries of the parameter range in which the L–H transition can occur.

In the range $\langle n\rangle < 3.6 \times 10^{19}$ m^{-3}, the global energy confinement time τ_E increases linearly with $\langle n\rangle$. In the range of higher electron densities, the energy confinement time in the ohmic, L-, and H-modes obeys the same power law $\tau_E \propto \langle n\rangle^{0.6}$. The confinement saturates because transport via the ion channel dominates over that via the electron channel, in which case transport coefficients are density independent.

The dependence of the energy confinement time on the threshold power was evaluated from the database used in simulations. At fixed values of $\langle n\rangle$, it is found to be $\tau_E = 0.12 Q_{\mathrm{L-H}}^{-0.46}$ (the index of the power law in the measured dependence is –0.5).

For the experimentally observed width of the transport barrier ($L \approx 2$ cm), to achieve a twofold increase in τ_E during the L–H transition requires that the thermal diffusivity inside the barrier be lower than the mean thermal diffusivity in the central plasma by at least a factor of 6. Making the input power profile peaked strongly affects the temperature profile (the ratio $T_i(0)/T_{Bi}$ increases by a factor of 3), but τ_E increases at most by 20%. It is found that the effect of the temperature-profile "stiffness" (T_0/T_B = const) is not observed.

Finally, we recall the following two restrictions of the ASTRA–ETL model. First, the temperatures T_{Se} and T_{Si} at the separatrix are assumed to be fixed; to calculate them requires a simulation of transport processes in the SOL. Second, the seed dissipation coefficients, which stem from the truncation of Fourier expansions of the fluctuating quantities, are assumed to be constant; however, they should depend on the plasma conductivity, which governs the number of unstable modes of turbulent fluctuations.

ACKNOWLEDGMENTS

We are grateful to Yu.N. Dnestrovskij for fruitful discussions of the manuscript and valuable remarks. We also thank S.V. Konovalov, S.E. Lysenko, and K.N. Tarasyan for their interest in this study. This work was supported in part by the Russian Foundation for Basic Research, project no. 96-15-96815 (under the program "Leading Scientific Schools").

REFERENCES

1. T. N. Carlstrom, P. Gohil, J. G. Watkins, *et al.*, Plasma Phys. Controlled Fusion **36**, A147 (1994).

2. R. J. Groebner, T. N. Carlstrom, K. H. Burrell, *et al.*, in *Proceedings of the 16th International Conference on Fusion Energy, Montreal, 1996* (IAEA, Vienna, 1997), Vol. 1, p. 867.
3. Yu. N. Dnestrovskij, M. V. Ossipenko, and S. V. Tsaun, Fiz. Plazmy **24**, 771 (1998) [Plasma Phys. Rep. **24**, 715 (1998)].
4. M. V. Ossipenko and S. V. Tsaun, Fiz. Plazmy **26**, 499 (2000) [Plasma Phys. Rep. **26**, 465 (2000)].
5. G. V. Pereversev, P. N. Yushmanov, A. Yu. Dnestrovskij, *et al.*, Report No. IAE-5358/6 (Kurchatov Institute, Moscow, 1992).
6. T. Ohkawa, Phys. Lett. A **67A**, 35 (1978).
7. M. V. Ossipenko, O. P. Pogutse, and R. V. Shurygin, in *Proceedings of the 12th International Conference on Plasma Physics and Controlled Nuclear Fusion Research, Nice, 1988* [Nucl. Fusion Suppl. **2**, 221 (1989)].
8. P. N. Guzdar, J. F. Drake, D. McCarthy, *et al.*, Phys. Fluids B **5**, 3712 (1993).
9. Yu. N. Dnestrovskij and D. P. Kostomarov, *Numerical Simulation of Plasmas* (Nauka, Moscow, 1993), p.70.
10. R. A. Moyer, J. W. Cuthbertson, T. E. Evans, *et al.*, J. Nucl. Mater. **241**, 633 (1997).
11. S. I. Braginskii, in *Reviews of Plasma Physics*, Ed. by M. A. Leontovich (Gosatomizdat, Moscow, 1963; Consultants Bureau, New York, 1963), Vol. 1.
12. B. A. Carreras, L. W. Owen, R. Maingi, *et al.*, Phys. Plasmas **5**, 2623 (1998).
13. R. J. Groebner, T. N. Carlstrom, K. H. Burrell, *et al.*, in *Proceedings of the 16th International Conference on Fusion Energy, Montreal, 1996* (IAEA, Vienna, 1997), Vol. 1, p. 867.
14. *A Decade of DIII-D Research*, Annual Report of General Atomics, no. GA-A23028 (General Atomics, San Diego, CA, 1999).
15. J. W. Connor and H. R. Wilson, Plasma Phys. Controlled Fusion **42**, R1 (2000).
16. G. M. Staebler, Plasma Phys. Controlled Fusion **40**, 569 (1998).
17. T. D. Ronglien, D. D. Ryutov, N. Mattor, and G. D. Porter, Phys. Plasmas **6**, 1851 (1999).
18. ITER Confinement Database and Modelling Expert Group, in *Proceedings of the 16th International Conference on Fusion Energy, Montreal, 1966* (IAEA, Vienna, 1997), Vol. 2, p. 795.

Translated by I.A. Kalabalyk

Plasma Physics Reports, Vol. 27, No. 1, 2001, pp. 18–29. Translated from Fizika Plazmy, Vol. 27, No. 1, 2001, pp. 19–30.

TOKAMAKS

Numerical Modeling of L–H Transitions in the Presence of a Radial Current at the Edge of a Tokamak Plasma

R. V. Shurygin

Russian Research Centre Kurchatov Institute, pl. Kurchatova 1, Moscow, 123182 Russia

Received April 20, 2000; in final form, June 27, 2000

Abstract—Hydrodynamic equations describing wall plasma turbulence are analyzed numerically using a two-dimensional four-field model. Turbulent transport coefficients are calculated with consideration of the radial current. Numerical analysis revealed a possible scenario for L–H transitions that is associated with the radial current driven by nonambipolar processes. It is shown that the transition of a plasma to an improved confinement mode can also be triggered by other mechanisms. © *2001 MAIK "Nauka/Interperiodica".*

1. INTRODUCTION

It is well known that the confinement of the central plasma in tokamaks is significantly governed by the edge localized electrostatic drift turbulence. Interest in studying turbulent plasma dynamics in the edge regions stems primarily from the following two circumstances. First, most experimental measurements are carried out at the plasma periphery, so that our theoretical results can be conveniently compared with experimental data. Second, the most interesting physical phenomenon—the L–H transition—also occurs near the wall. Accordingly, theoretical efforts have focused mainly on the physical processes at the edge of a tokamak plasma. Most of the theoretical papers in this area are devoted to studying wall plasma turbulence using the Hasegawa–Wakatani (HW) model, which is based on the two-field set of reduced two-fluid hydrodynamic equations for the plasma density n and electric potential Φ [1]. Numerical solutions of the HW equations [2–7] confirmed the theoretical results obtained in papers [8, 9], which suggested that the most important factor governing the amplitude of turbulent fluctuations was the poloidal sheared flow. The numerical results agree well with the measured data, according to which the poloidal rotation velocity increases during the transition to an improved confinement mode (the L–H transition). Note that, although there is a variety of theoretical L–H transition models (see review [10]), present-day two-dimensional nonlinear codes are still not capable of capturing this phenomenon.

Here, we calculate the parameters of the wall plasma turbulence using, instead of the two-field HW equations, a more complete set of the four-field two-fluid nonlinear hydrodynamic equations, which take into account not only fluctuations of the plasma density and electric potential, n and Φ, but also fluctuations of the ion and electron temperatures, T_i, and T_e. This refined theoretical model clearly provides a more adequate description of the physical processes in tokamak wall plasma.

We investigate how the self-consistent radial current J_r affects turbulent transport. We show that the radial current is induced as a result of the response of the plasma to various nonambipolar losses at the periphery of the plasma column in a tokamak. The radial current–driven Lorentz force $[\mathbf{j} \times \mathbf{B}]_\vartheta$ enhances the poloidal sheared flow, thereby suppressing turbulent fluctuations and giving rise to the L–H transition. Our simulations show that the L–H transition occurs in a jumplike manner, regardless of the direction of the radial current. We conclude that many scenarios for triggering transitions to new confinement modes known from experiments may be related to the radial current. However, we present examples in which transitions to new modes of plasma confinement are governed by the change in tokamak plasma parameters that are not associated with the magnitudes of the radial current and poloidal flow velocity, so that there is no indication of a universal mechanism responsible for triggering a wide variety of experimentally observed L–H transitions. Presumably, a unified theoretical model should include all of the mechanisms responsible for transitions to new confinement modes.

2. BASIC EQUATIONS

The general method of deriving the four-field set of equations from the Braginskii reduced two-fluid hydrodynamic equations [11–13] for n, Φ, T_i, and T_e is presented in the Appendix. It is convenient to nondimensionalize the four-field equations by passing over to the new variables

$$t \longrightarrow t/t_0, \quad (x, y) \longrightarrow (x, y)/x_0, \quad \Phi \longrightarrow e\Phi/T_0,$$

$$U \longrightarrow U/V_0, \quad t_0 = 1/(\rho^2\omega_{ci}), \quad \rho = \rho_{0i}/x_0,$$

1063-780X/01/2701-0018$21.00

$$\rho_0 = V_0/\omega_{ci}, \quad V_0^2 = T_0/m_i, \quad D_B = \rho_i V_0,$$

$$\mu \longrightarrow \mu/D_B, \quad D \longrightarrow D/D_B, \quad \omega_0 = 1/t_0,$$

$$n \longrightarrow n/n_0, \quad T \longrightarrow T/T_0, \quad k_y \longrightarrow k_y x_0, \quad g_B = x_0/R,$$

where x_0 is the width of a plane layer in which the four-field equations are solved. The normalizing parameter values are chosen to be $n_0 = 10^{13}$ cm^{-3} and $T_0 = 100$ eV. The nondimensionalization procedure sets Eqs. (A.3), (A.4), and (A.7) in the form

$$\frac{\partial W}{\partial t} + \{\Phi, W\} = C \cdot \nabla_\parallel^2 J - \frac{U}{\rho}\frac{\partial W}{\partial y} + \rho U''\frac{\partial \Phi}{\partial y}$$

$$- g_B\left[(T_{e0} + T_{i0})\frac{\partial n}{N\partial y} + \frac{\partial (T_e + T_i)}{\partial y}\right] + \mu_0 \Delta_\perp W,$$

$$\frac{\partial n}{\partial t} + \{\Phi, n\} = C \cdot \nabla_\parallel^2 J - \frac{U}{\rho}\frac{\partial n}{\partial y} + N'\frac{\partial \Phi}{\partial y}$$

$$+ g_B\left(\frac{\partial \Phi}{\partial y} - T_{e0}\frac{\partial n}{\partial y}\right) + D_0 \Delta_\perp n,$$

$$W = \rho^2 \Delta_\perp \Phi,$$

$$\frac{3}{2}\left[\frac{\partial T_e}{\partial t} + \{\Phi, T_e\}\right] = C_e \cdot \nabla_\parallel^2 J - \frac{U}{\rho}\frac{\partial T_{e0}}{\partial x}$$

$$- g_B K_e + \chi_{e0}\frac{\partial^2 T_e}{\partial x^2},$$

$$K_e = T_e\left[\frac{7}{2}\frac{\partial T_e}{\partial y} + \frac{T_e}{N}\frac{\partial n}{\partial y} - \frac{\partial \Phi}{\partial y}\right], \tag{1}$$

$$\frac{3}{2}\left[\frac{\partial T_i}{\partial t} + \{\Phi, T_i\}\right] = C_i \cdot \nabla_\parallel^2 T_i - \frac{U}{\rho}\frac{\partial T_{i0}}{\partial x}$$

$$+ g_B K_i + \chi_{i0}\frac{\partial^2 T_i}{\partial x^2},$$

$$K_i = T_i\left[\frac{7}{2}\frac{\partial T_i}{\partial y} + \frac{T_i}{N}\frac{\partial n}{\partial y} - \frac{\partial \Phi}{\partial y}\right],$$

$$C = \frac{\omega_{ce}}{\nu_{ei}}, \quad C_e = \alpha_1 T_{e0}\frac{\omega_{ce}}{\nu_{ei}}, \quad C_i = \alpha_2 T_{i0}\frac{\omega_{ci}}{\nu_{ii}},$$

$$J = \alpha_1 T_e + \kappa n - \Phi, \quad \alpha_1 = 1.71,$$

$$\alpha_2 = 3.9, \quad \kappa = T_{e0}/N,$$

where N is the dimensionless background density and the prime denotes the derivative with respect to the minor radius x. Each of the quantities $f = \{n, \Phi, T_i, T_e\}$ is chosen to be a combination of helical waves with the same helicity (k_y = const, k_z = const):

$$f(x, y, z, t) = f_0(x, t) + \sum_{m=1}^{M} f_{Sm}(x, t)\sin(m\chi) + f_{Cm}(x, t)\cos(m\chi), \quad \chi = k_y y - k_z z. \tag{2}$$

Substituting the Fourier expansion (2) into Eqs. (1), we obtain equations for the Fourier coefficients f_{Sm} and f_{Cm} of the modes of the four fluctuating quantities under consideration. For the quantities $f_0 = \{N, U, T_{i0}, T_{e0}\}$, which will be referred to as the background quantities, we arrive at the following equations, averaged over the angle χ:

$$\frac{\partial N}{\partial t} + \frac{\partial \Gamma}{\partial x} + \frac{\partial \Gamma_i^{\text{neo}}}{\partial x} = S_0 N, \tag{3.1}$$

$$\frac{\partial N_a}{\partial t} = -S_0 N + D_a\frac{\partial^2 N_a}{\partial x^2}, \tag{3.2}$$

$$\frac{\partial U}{\partial t} + \frac{\Gamma}{N}\frac{\partial U}{\partial x} + \frac{\partial \Pi}{\partial x} = -\frac{J_x}{\rho^2} - \nu_{\text{neo}}(U - U_{\text{neo}}) - \nu_a U + \mu_{00}\frac{\partial^2 U}{\partial x^2}, \tag{3.3}$$

$$\frac{\partial T_{i0}}{\partial t} + \frac{\Gamma}{N}\frac{\partial T_{i0}}{\partial x} + \frac{\partial Q_i}{\partial x} + \frac{\partial Q_i^{\text{neo}}}{\partial x} = \alpha(T_{e0} - T_{i0}) - \nu_a(T_{i0} - T_a) + P_i, \tag{3.4}$$

$$\frac{\partial T_{e0}}{\partial t} + \frac{\Gamma}{N}\frac{\partial T_{e0}}{\partial x} + \frac{\partial Q_e}{\partial x} = \chi_{00e}\frac{\partial^2 T_{e0}}{\partial x^2} - \alpha(T_{e0} - T_{i0}) + P_e. \tag{3.5}$$

Here,

$$\alpha = \frac{2m_e}{m_i}\frac{\nu_{ei}}{\omega_0}, \quad S_0 = \frac{\langle \sigma V\rangle_{\text{ion}} N_a}{\omega_0},$$

$$\nu_a = S_0 + \frac{\langle \sigma V\rangle_{cx} N_a}{\omega_0};$$

N_a and T_a are the neutral density and temperature; $\Gamma = \langle nV_x\rangle$, $\Pi = \langle V_x V_y\rangle$, and $Q_{e,i} = \langle T_{e,i} V_x\rangle$ are the particle, momentum, and heat turbulent fluxes, respectively; and $U_{\text{neo}} = -k_{\text{neo}}\dfrac{c}{eB}\dfrac{\partial T_i}{\partial x}$ is the neoclassical equilibrium velocity. The expressions for k_{neo}, ν_{neo}, and Γ_i^{neo} will be presented in the next section. The ion heat flux is

described by the following simplified neoclassical relationship, which is valid in the plateau regime:

$$Q_i^{\text{neo}} = -\chi_{i00}\frac{\partial T_i}{\partial x}, \quad \chi_{\text{neo}} = 3\frac{\sqrt{\pi}}{2}\varepsilon^2\left(\frac{q\rho_i}{\varepsilon}\right)\frac{cT_i}{eB},$$

$$\chi_{i00} = \frac{\chi_{\text{neo}}}{D_B}, \quad \chi_{e00} = 0.1\chi_{i00}.$$

The formulas for the ionization and charge exchange cross sections, $\langle\sigma V\rangle_{\text{ion}}$ and $\langle\sigma V\rangle_{cx}$, are taken from [14].

For a thin plane layer ($x_0 \ll a$), the same helicity of the waves allows us to utilize the following expansion at a resonant point such that $k_\parallel(x_{\text{res}}) = 0$:

$$k_\parallel(x) = \frac{\varepsilon}{q(x)}k_y - k_z \approx \frac{k_y(x - x_{\text{res}})}{L_s}, \qquad \frac{1}{L_s} = \frac{s}{qR}, \quad s = \frac{rq'}{q}. \tag{4}$$

With allowance for expression (4), the operator of differentiation in the longitudinal direction, $\nabla_\parallel$, in the above equations for the four fluctuating quantities (for the Fourier coefficients f_{Sm} and f_{Cm}) can be replaced by

$$-\nabla_\parallel^2 = \sigma_0(x - x_0)^2, \quad \sigma_0 = (mk_y x_0)^2\frac{\omega_{ce}}{\nu_{ei}}\left(\frac{x_0}{L_s}\right)^2.$$

In the four-field model based on Eqs. (1), the parameter σ_0 describes the main dissipation channel associated with the escape of electrons along the magnetic field lines.

We solved the sets of nonlinear equations (1) and (3) numerically with the help of an algorithm based on the predictor–corrector method [15], which can be schematically represented as

$$\frac{X^{n+1/2} - X^n}{\tau} = \hat{L}\left[\left(\frac{1}{2} + \frac{\sqrt{3}}{6}\right)X^{n+1/2} + \left(\frac{1}{2} - \frac{\sqrt{3}}{6}\right)X^n\right] + \hat{N}(X^n),$$

$$\frac{X^{n+1} - X^n}{\tau} = \hat{L}\left[\left(\frac{1}{2} + \frac{\sqrt{3}}{6}\right)X^{n+1} - \frac{\sqrt{3}}{6}X^{n+1/2} + \frac{1}{2}X^n\right] + \hat{N}\left(\frac{X^n + X^{n+1/2}}{2}\right),$$

where $\hat{L}$ and $\hat{N}$ are linear and nonlinear operators, respectively. The time step was chosen to satisfy the condition $\tau < 0.3\Delta r/V_0$. This algorithm was found to be more stable than the numerical scheme used in [7].

The fluctuating quantities were assumed to satisfy the boundary conditions

$$W(0) = \Phi(0) = n(0) = T_e(0) = T_i(0) = 0, \qquad W(1) = \Phi(1) = n(1) = T_e(1) = T_i(1) = 0 \tag{5}$$

and the boundary conditions for the background quantities were as follows:

$$N(0) = N_b, \quad N(1) = N_s, \quad N_a(0) = N_{ba}, \quad N_a(1) = N_{sa}, \quad T_{0\alpha}(0) = T_{b\alpha}, \quad T_{0\alpha}(1) = T_{s\alpha}, \quad \alpha = e, i, \quad U(0) = U_{\text{neo}}(1), \quad \left.\frac{dU}{dx}\right|_{x=1} = 0, \tag{6}$$

where the subscripts b and s refer to the left ($x = 0$) and right ($x = 1$) boundaries of the computation region. The resonant point $x_{\text{res}} = 0.5$ was assumed to lie at the center of the computation region $0 < x < 1$. In solving the equations for fluctuations, the dimensionless dissipation coefficients were chosen to lie in the range $D_0 = \mu_0 = \chi_{e0} = \chi_{i0} = 0.0004$–$0.002$, which is far below the D_B value, and the quantity μ_{00} was set to be 0.01. The maximum number of helical waves was $M = 5$, 7, and 9. While the number of helical waves in simulations was increased to $M = 21$, the qualitative behavior of the solution was found to be essentially the same. However, we found that the larger the number M, the more intense the turbulent fluxes ($\Gamma_{21} \sim 2\Gamma_7$). Additionally, with increasing the number of helical waves, we had to use progressively shorter time steps in order to ensure the desired accuracy of the solution.

Some characteristic features of the behavior of the plasma system under discussion can be revealed by analyzing the energy conservation law. We can readily show that the fluctuation energy $W_F = \frac{1}{2}\langle(\nabla\Phi)^2 + n^2\rangle$ satisfies the conservation law

$$\frac{\partial W_F}{\partial t} = S_\Gamma + S_\Pi + S_g + S_N - S_{\text{diss}}, \tag{7}$$

where

$$\langle\ldots\rangle = \int_0^1(\ldots)dx, \quad S_\Gamma = \left\langle -\Gamma\frac{dN}{dx}\right\rangle, \quad S_\Pi = \left\langle -\Pi\frac{dU}{dx}\right\rangle,$$

$$S_{\text{diss}} = \langle\sigma_0(x - x_0)^2J^2\rangle + \frac{\mu_0}{\rho^2}W^2 + D_0(\nabla n)^2,$$

$$S_N = S_0N_aN^2,$$

$$S_g = g_B\left[\Gamma\left(\frac{T_{e0} + T_{i0}}{N} - 1\right] + Q_i + Q_e\right] + \frac{\rho T_{i0}}{N}\left(\frac{d\Pi}{dx}\frac{dN}{dx} + \frac{d\Gamma}{dx}\frac{dU}{dx}\right).$$

An analysis shows that the main contribution to the right-hand side of Eq. (7) comes from the three terms S_Γ, S_Π, and $S_{\text{diss}} \sim \sigma_0 \sim T_{e0}^{3/2}/(NR^2q^2)$. Across the layer,

the time-averaged turbulent flux is positive, $\Gamma > 0$, and the time-averaged density gradient is negative, $dN/dx < 0$. Consequently, we have $S_\Gamma > 0$, which indicates that this quantity plays the role of the source of fluctuations. The sign of the source term S_Π is *a priori* unclear, because it is a product of two alternating-sign quantities. However, numerical calculations show that, on average, this source term is negative, $S_\Pi < 0$. In other words, the poloidal sheared flow acts to suppress fluctuations. The influence of the poloidal flow on the plasma turbulence is one of the most important effects in the physics of tokamak wall plasmas. In the next section, we will show that controlling the poloidal flow velocity via the radial current–driven Lorentz force makes it possible to achieve transitions to improved confinement modes.

The evolution of the background quantities plays an important role in the overall dynamics of the plasma. The gradients of $f_0 = \{N, U, T_{i0}, T_{e0}\}$ depend strongly on the spatial coordinates and time and change substantially under the action of turbulent fluxes, so that the evolution of the background quantities described by Eqs. (3) has the reverse effect on the evolution of the turbulent modes described by Eqs. (1). As a result, the plasma evolves into the self-oscillation regime. The turbulent dynamics of a plasma with spatially and temporally varying gradients of unperturbed quantities is very complicated and differs strongly from the turbulent plasma dynamics simulated in [3–5] under the assumption that the gradients are fixed. Note that, in the regime in which both the background and fluctuating quantities are time-dependent, plasma turbulence is self-sustained (i.e., turbulent fluctuations are sustained by the particle and heat turbulent fluxes, Γ and $Q_{e,i}$), so that the estimates obtained in the traditional theory of plasma turbulence, which deals with the linear growth rate and the width of the linear mode, become inapplicable.

3. RADIAL CURRENT IN A TOKAMAK

In my earlier paper [7], it was shown that the transverse current–driven Lorentz force has a substantial effect on turbulent transport in the wall plasma (near the separatrix in the scrape-off layer). The calculations performed in [7] showed that the radial current should play a key role in triggering L–H transitions, because it can markedly change the velocity of the poloidal flow, which suppresses turbulent fluctuations through the familiar mechanism for the decorrelation of turbulent modes [8, 9]. The effect of the radial current on the turbulent processes in wall plasmas and its possible role in triggering L–H transitions were studied in [16–19].

The mechanism for generating the radial current can be understood using neoclassical theory. With the radial electric field taken into account, the generalized neoclassical fluxes have the form [16]

$$\Gamma_\alpha^{\text{neo}} = -nD_\alpha\left[\frac{N'}{N} + \gamma_\alpha\frac{T_\alpha'}{T_\alpha} - \frac{e_\alpha}{T_\alpha}\left(E_r - \frac{1}{c}B_\theta U_{\alpha\|}\right)\right] \times \exp\left(-\left[\frac{cE_r}{B_\theta V_{T\alpha}}\right]^2\right), \quad \alpha = e, i. \tag{8}$$

Here, the quantity γ_α governs the collisionality regime,

$$D_\alpha = \frac{\sqrt{\pi}}{2}\varepsilon^2\frac{\rho_\alpha}{r}\frac{T_\alpha}{e_\alpha B_\theta}, \quad \varepsilon = r/R,$$

$$\rho_\alpha = V_{T\alpha}/\omega_{c\alpha}, \quad V_{t\alpha} = \sqrt{2T_\alpha/m_\alpha},$$

$U_{\alpha\|}$ is the mean velocity along the magnetic field, and V_T is the thermal velocity.

It is an easy matter to show [20] that, in the absence of additional forces in the time-independent equation for the toroidal angular momentum, the neoclassical transport is automatically ambipolar; i.e.,

$$\Gamma_i^{\text{neo}} = \Gamma_e^{\text{neo}}, \quad J_x^{\text{neo}} = e(\Gamma_i^{\text{neo}} - \Gamma_e^{\text{neo}}) = 0,$$

and no radial current is excited. However, in real physical situations, the presence of neutral particles, turbulent forces, and internal electrodes in the wall region inevitably gives rise to losses of charged particles at the plasma edge and, accordingly, to the radial current associated with these losses. In this case, the neoclassical radial current J_x^{neo} generated in the edge plasma due to violation of the ambipolarity constraint ($\Gamma_i \neq \Gamma_e$) acts to prevent particle losses.

Taking into account the fact that $D_e \ll D_i$, we obtain from formula (8) the following expression for the neoclassical radial ion flux:

$$J_x^{\text{neo}} \approx \frac{KNT_i}{r}\frac{c}{B_\theta V_{Ti}}(E_x - E_a) f\exp(-V^2), \quad K = \frac{c\sqrt{\pi}\varepsilon^2}{B},$$

$$V = \frac{cE_x}{B_\theta V_{Ti}}, \quad E_a = \frac{T_i}{e}\left(\frac{N'}{N} + (1 + k_{\text{neo}})\frac{T_i'}{T}\right) + \frac{B_\theta U_{i\|}}{c}, \tag{9}$$

$$f = 1 + 2V^2 + 4V^4,$$

where the factor f is introduced in order to fit the corresponding formula deduced by Xiao *et al.* [21]. Note that, with the radial electric field taken into account, the most general expressions for the neoclassical ion current in various collisionality regimes were derived by Connor and Stringer [22, 23]. However, in our analysis, it is sufficient to use the simplified expression (9), which is valid in the plateau regime, where we have $\gamma_i = 1 + k_{\text{neo}}$. The quantity k_{neo} is calculated from the formula

$$k_{\text{neo}} = \frac{-1.17 + 0.35\sqrt{\nu_*} + 2.1\nu_*^2\varepsilon^3}{(1 + 0.7\sqrt{\nu_*} + \nu_*^2\varepsilon^3)}, \quad \nu_* = \frac{qR\nu_{ii}}{V_{Ti}\varepsilon^{3/2}}.$$

Since we restrict ourselves to considering the collisional plateau regime, where the neoclassical fluxes depend weakly on the collision frequency, we can apply formula (9) to a turbulent plasma, because, in addition to Coulomb collisions, we only need to take into account turbulence-induced wave–particle collisional interaction. This can be done merely by renormalizing the collision frequency.

The equation for the radial component of the ion momentum yields the following expression for the radial electric field:

$$\frac{cE_x}{B} = -U_y + \frac{\varepsilon}{q}U_z + V_d, \quad V_d = \frac{cP_i'}{eBN}. \tag{10}$$

We neglect the longitudinal velocity, assuming that the condition $(\varepsilon/q)U_z \ll U_y$ holds for the layer in which we solve the four-field equations. We also omit the subscript *y*, assuming that $U_y = U$. In calculating the ion current, we find the field component E_x in Eq. (9) from Eq. (10), in which case the unknown velocity U can be determined from the equation for the poloidal momentum component:

$$mN\left(\frac{\partial U}{\partial t} + \frac{\Gamma}{N}\frac{\partial U}{\partial x} + \frac{\partial \Pi}{\partial x}\right) = -\frac{J_x^{\text{neo}}B}{c} - mN\nu_{\text{neo}}(U - U_{\text{neo}}) - mN_a\nu_a U + mN\mu_0\frac{\partial^2 U}{\partial x^2}, \tag{11}$$

where, for simplicity, the radial profiles of N and T_i are assumed to be prescribed. The expression for the neoclassical viscosity ν_{neo} was taken to be [20]

$$\upsilon_{\text{neo}} = \frac{\sqrt{\pi}}{2}\frac{qV_{Ti}}{R}\exp[-V^2] + \frac{q^2\nu_{ii}}{2(1+V^2)}. \tag{12}$$

Hence, if we calculate the turbulent fluxes Γ and Π, then we arrive at the self-consistent set of equations (9)–(11). Solving this set, we determine the current J_x^{neo}, the field E_x, and the velocity U. Note that, for $\Gamma = \Pi = 0$ and for small values of the viscosity coefficient μ_0, Eq. (11) has the steady-state solution

$$U = U_{\text{neo}} = -k_{\text{neo}}\frac{c}{eB}\frac{T_i'}{T_i}, \quad E_x = E_a = \frac{T_i}{e}\left[\frac{N'}{N} + (1 + k_{\text{neo}})\frac{T_i'}{T}\right], \quad J_x^{\text{neo}} = 0. \tag{13}$$

Clearly, with a nonzero turbulent inertial term $(\Gamma/N)\partial U/\partial x$, a nonzero turbulent force term $\partial\Pi/\partial x$, and a nonzero friction force term associated with neutral particles, Eq. (11) for $U(x, t)$ has a different equilibrium solution, specifically, a solution with $E_x(x, t) \neq E_a$ and $J_x^{\text{neo}}(x, t) \neq 0$. Consequently, according to the equation for the poloidal momentum component, additional forces should give rise to the radial current.

Let us analyze Eq. (11) in order to predict the possible temporal behavior of $U(t)$. Using Eq. (10), we can make the current J_x^{neo} in expression (9) and the viscosity ν_{neo} in formula (12) independent of the field E_x, in which case Eq. (11) becomes

$$mN\frac{\partial U}{\partial t} = G(U) + mN\mu_0\frac{\partial^2 U}{\partial x^2}, \quad G(U) = F_{\text{turb}} - \frac{J_x^{\text{neo}}(U)B}{c} - mN\nu_{\text{neo}}(U)(U - U_{\text{neo}}) - mN_a\nu_a U, \quad F_{\text{turb}} = -\left(\frac{\Gamma}{N}\frac{\partial U}{\partial x} + \frac{\partial \Pi}{\partial x}\right). \tag{14}$$

Equation (14) for the poloidal velocity U is a time-dependent diffusion equation with the nonlinear source term $G(U)$. Examining the characteristic functional dependences of the current and viscosity, $J_x^{\text{neo}}(U)$ and $\nu_{\text{neo}}(U)$, we can see that Eq. (14) can have both jump-like and bifurcated solutions. This conclusion will be validated below by numerical calculations. An analysis of Eq. (14) using bifurcation theory goes beyond the scope of this study and is postponed to a future paper.

Let us consider other physical mechanisms that are responsible for the generation of the radial current and are not associated with additional forces. For simplicity, we write the ion and electron continuity equations in Cartesian coordinates:

$$\frac{\partial(N_iV_{xi})}{\partial x} + \frac{\partial(N_iV_{iz})}{\partial z} = S_i, \quad \frac{\partial(N_eV_{xe})}{\partial x} + \frac{\partial(N_eV_{ez})}{\partial z} = S_e. \tag{15}$$

We take the sum of these equations multiplied by the charge to obtain the relationship

$$\frac{\partial J_x}{\partial x} + \frac{\partial J_z}{\partial z} = e[S_i(x, t) - S_e(x, t)],$$

which gives

$$J_x(x, t) = \int_0^x \left\{e[S_i(x, t) - S_e(x, t)] - \frac{\partial J_z}{\partial z}\right\}dx. \tag{16}$$

Obviously, the transverse nonambipolar current (9) and, accordingly, the radial electric field can stem from two causes: first, the ion and electron sources described by the terms S_i and S_e may differ from one another for some reason and, second, the longitudinal current may be nonuniform. The space charge associated with both the longitudinal current and the difference between the

ion and electron sources is neutralized by the nonzero radial current $J_x = J_x^{\text{neo}}$.

Hence, the above considerations show that the radial current can be generated by external forces and nonambipolar losses of charged particles. In a further analysis, we will take into account the following important circumstance: according to Eq. (11) for the poloidal velocity, the radial current can either intensify or relax the poloidal plasma flow via generation of the Lorentz force.

4. SCENARIOS FOR L–H TRANSITIONS

Based on the above analysis, we can propose the following scenario for L–H transitions in tokamaks. We assume that the turbulent plasma is confined in a tokamak operating in a certain mode. The inevitably present external forces (in the case at hand, these are a turbulence-induced poloidal viscous force and a friction force associated with neutral particles) give rise to a low (but nonzero) radial current in the plasma. An external action on the plasma (heating, beam, polarization, etc.) destroys the balance between oppositely charged particles, thereby violating the ambipolarity constraint for a short time and subsequently giving rise to jumps in the charge density, $\Delta\rho$ (because $S_e \neq S_i$), the radial electric field, ΔE, and the radial current, ΔJ. The neutralizing ion current ΔJ, in turn, gives rise to the jump $\Delta J \cdot B/c$ in the Lorentz force. Recall that the equation for the poloidal velocity has bifurcated solutions. This indicates that the plasma evolves into a qualitatively new equilibrium state in a jumplike manner (the quantity $|U|$ increases rapidly) only when the jump $|\Delta E|$ in the radial electric field is above a certain critical level, $|\Delta E| > |\Delta E_{\text{crit}}|$. If the radial electric field has already undergone such a jump, the poloidal sheared flow becomes more intense, thereby suppressing turbulent fluctuations and triggering an L–H transition. In simulating this process, we self-consistently adjusted the parameters E_r, U, V_d, and J_x^{neo} in accordance with Eqs. (9)–(11), taking into account the turbulent fluxes and background quantities $N(x, t)$ and $T_{i0}(x, t)$ obtained from the solutions to the sets of equations (1) and (3). Note that all these quantities evolve in the unsteady self-oscillation regime.

We checked the above theoretical predictions by calculating the spatial and temporal characteristics of turbulent fluctuations, taking into account the effects of the radial current. In simulations, we used the parameters of the DIII-D tokamak: $R = 167$ cm, $a = 63$ cm, $B = 1.58$ T, $q = 3.5$, $N_b(0) = 1.5$, $N_s(1) = 0.1$, $T_{ib}(0) = T_{eb}(0) = 1$, $T_{is}(1) = T_{es}(1) = 0.3$, $M_i = 2m_{\text{H}}$, and $Z_{\text{eff}} = 1.5$. In order to model the external action on the plasma, we instantaneously violated the ambipolarity constraint and, in the equation for the poloidal velocity, simultaneously switched on the radial electric field ΔE, the additional current ΔJ, and the Lorentz force, all produced by the neoclassical neutralizing current. The jump in the radial electric field was chosen to be

$$\Delta E = \Delta E_0 \exp[-z^2], \quad z = (x - 0.7)/0.2.$$

Figure 1 demonstrates that the L–H transition can be bifurcated in character, depending on the value of the jump ΔE_0: we can clearly see the critical values –35 and +90 V/cm, beyond which the quantity $\langle D \rangle$ falls off sharply.

Figures 2 and 3 illustrate the evolution of the turbulent diffusivity $\langle D \rangle = \langle \Gamma \rangle / (N_b - N_s)$ and kinetic energy $\langle W_0 \rangle$ of the poloidal flow, both averaged according to the prescription

$$\langle F \rangle(t) = \int_0^1 F(x, t)\,dx.$$

The jumps $\Delta E = -50$ and +100 V/cm were switched on at the instant $t = t_0$ and lasted for a time interval of 100 μs. One can see that, after a short relaxation process, the kinetic energy of the poloidal flow increases and the turbulent diffusivity (and, accordingly, the thermal conductivity) decreases. For $\Delta E > 0$, the plasma rotates in the direction of the diamagnetic drift velocity of the ions (the solution with $U < 0$), and, for $\Delta E < 0$, the plasma rotates in the direction of the diamagnetic drift velocity of the electrons (the solution with $U > 0$). After the plasma experiences a bifurcated transition, the poloidal velocity increases from $U \sim U_{\text{neo}} \sim 5$–6 km/s to a level of 20–30 km/s (i.e., by a factor of 4 to 5). Our simulations show that L–H transitions can be triggered in a very simple way, specifically, by creating the conditions for generating the radial electric field and maintaining it at a certain level during a time interval of about 100 μs at the periphery of a tokamak plasma. The technique for producing the radial electric field at the plasma edge has been well developed in experiments on plasma polarization [24, 25].

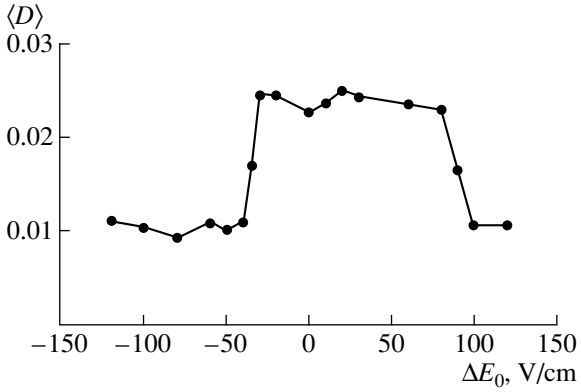

Fig. 1. Turbulent diffusivity $\langle D \rangle$ vs. the jump ΔE_0 in the radial electric field under DIII-D conditions.

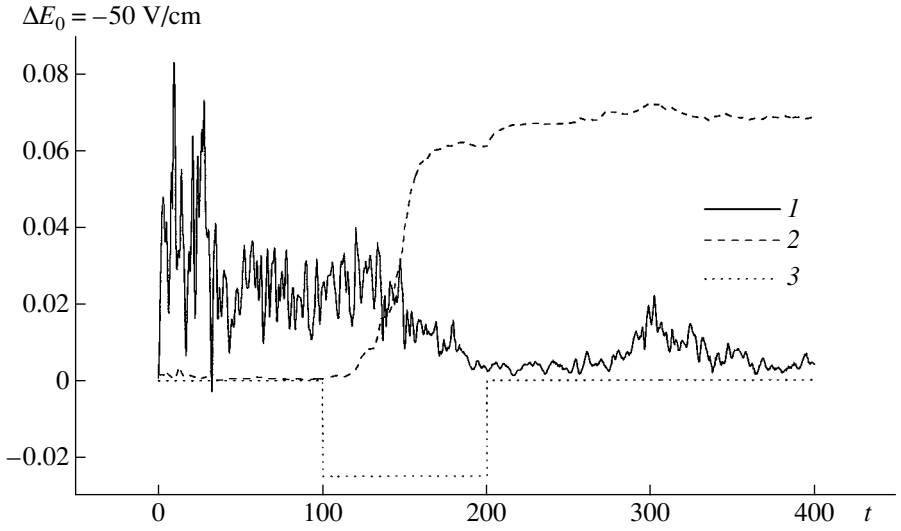

Fig. 2. Evolution of (*1*) the turbulent diffusivity $\langle D \rangle$, (*2*) the kinetic energy $\langle W_0 \rangle$ of the poloidal flow, and $\Delta E(t)$ for the jump $\Delta E_0 = -50$ V/cm in the radial electric field under DIII-D conditions.

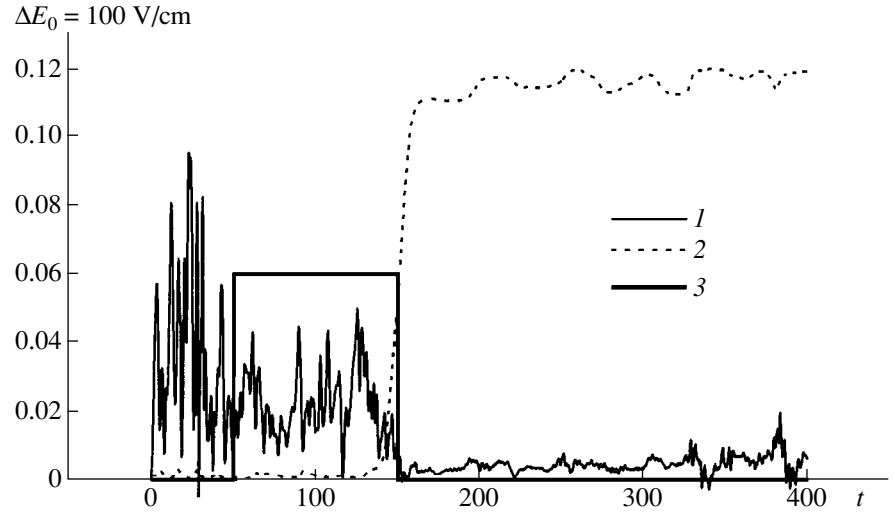

Fig. 3. The same as in Fig. 2 but for the jump $\Delta E_0 = +100$ V/cm in the radial electric field.

Hence, we have shown that the nonambipolar losses of charged particles of any species ($\Delta E > 0$ and $\Delta E < 0$) lead to the triggering of L–H transitions. As a rule, the violation of the ambipolarity constraint at the plasma edge is accompanied by particle losses. Consequently, the L–H transition can be regarded as a self-organization process: in trying to prevent particle losses, the plasma "generates" a neutralizing radial current and poloidal sheared flow in a narrow layer, thereby evolving into a confinement mode with a lower level of turbulent fluctuations.

Another possible scenario of L–H transitions is associated with the fact that, according to expression (9), the radial current J_x^{neo} flowing in the layer depends sensitively on the plasma parameters,

$$J_x^{\text{neo}} = F(N, T_i, q, N', T_i').$$

An external action changes the plasma parameters and, accordingly, the radial current J_x^{neo} and poloidal velocity U, in which case the plasma also evolves into a new confinement mode.

Figure 4 illustrates the time behavior of the averaged turbulent diffusivity $\langle D \rangle$ when the ion temperature increases instantaneously. The calculations were carried out for the following parameter values of the

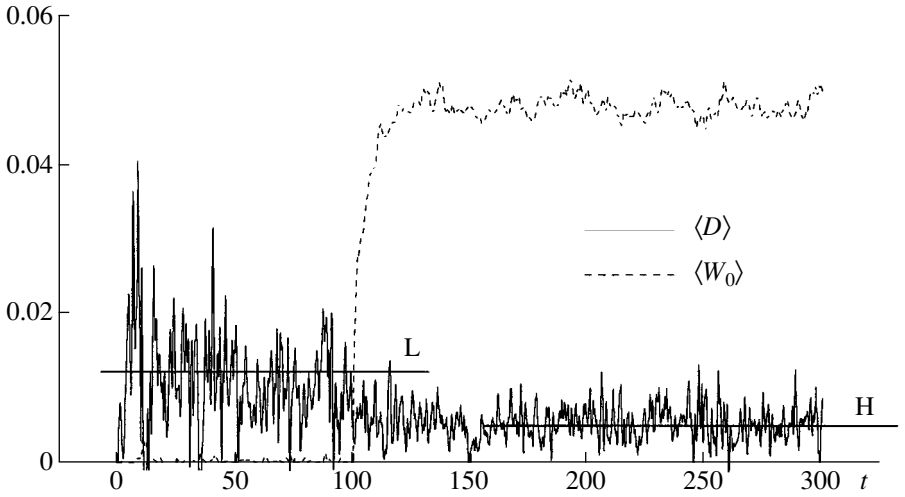

Fig. 4. L–H transition when the ion temperature T_{bi} increases instantaneously from 0.4 to 0.8 and the time evolution of the turbulent diffusivity $\langle D\rangle$ under CASTOR conditions.

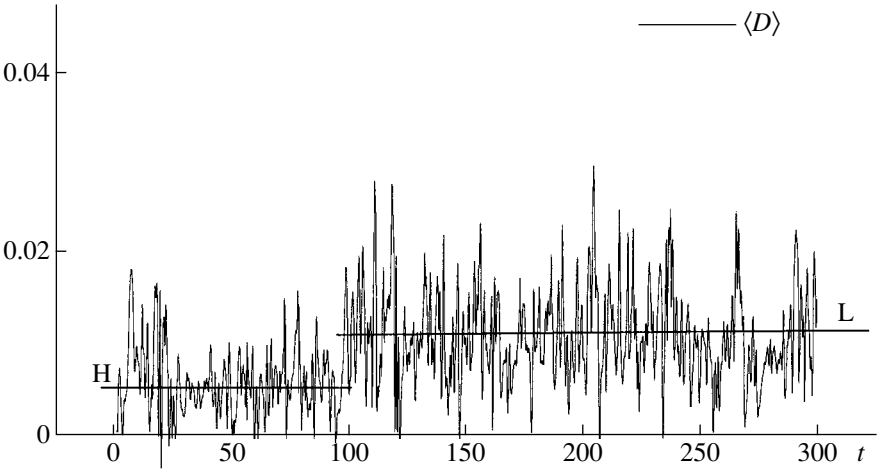

Fig. 5. H–L transition when the safety factor q increases from 3 to 6 and the time evolution of the turbulent diffusivity $\langle D\rangle$ under CASTOR conditions.

CAS-TOR device [26]: $R = 40$ cm, $a = 8.5$ cm, $B = 1$ T, $q = 6$, $N_b = 0.6$, $N_s = 0.1$, $T_{be} = 0.7$, $T_{bi} = 0.4$, $M_i = m_{\rm H}$, $Z_{\rm eff} = 1.5$, and $x_0 = 1.5$ cm. At the instant $t = t_0$, the ion temperature $T_{bi} = 0.4$ at the left boundary $x = 0$ increases to $T_{bi} = 0.8$. We can see that the radial current $J_x^{\rm neo}$ and the poloidal velocity both start to increase and, at the same time, the turbulent flux begins to damp. This example can be interpreted as an L–H transition during auxiliary plasma heating, when the heat wave propagating from the plasma center reaches the plasma periphery.

The transition to a new confinement mode can also be achieved by keeping the radial current $J_x^{\rm neo}$ essentially unchanged while varying the other plasma parameters. Figure 5 displays the time evolution of the turbulent diffusivity when the safety factor is changed instantaneously. Since the layer under analysis is narrow, we can assume that $q = q(a) = \text{const}$. In Eq. (7) for the fluctuation energy, the transition of a plasma to the L-mode is associated with a sharp decrease in the term $S_{\rm diss} \sim 1/q^2$ (an increase in q from 3 to 6). This result correlates well with the following well-known experimental fact: as the total current I decreases (or $q \sim 1/I$ increases), the plasma confinement deteriorates. Note that, in the experiments, the total current usually decreases over a long time interval (of about 1 ms), rather than instantaneously (as is assumed in our model). Of course, a real plasma evolves into a new confinement mode on the same time interval. Since L–H transitions occur usually on time scales of about 30–100 μs, the above experimentally observed transition, which is associated with a decrease in the total current, only reflects how the confinement quality

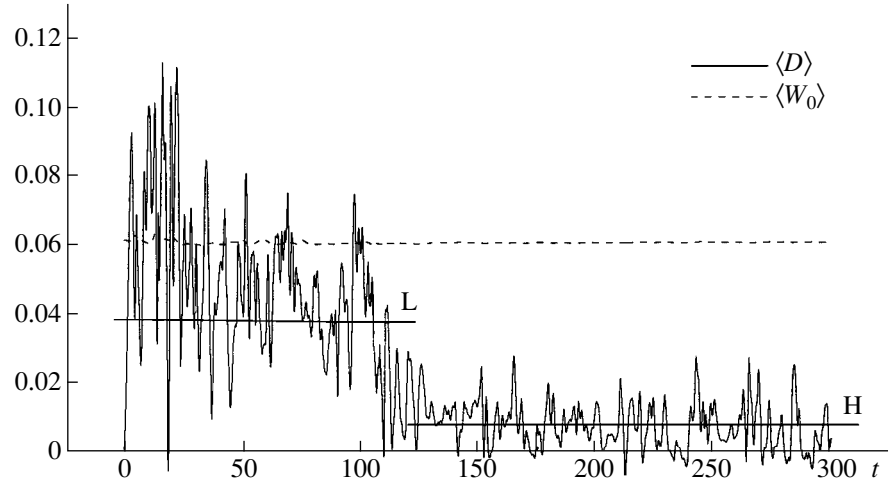

Fig. 6. L–H transition when the neutral density undergoes a jump ($N_{ba} = 0.02 \longrightarrow 0.2$) at the boundary $x = 1$ and the time evolution of the turbulent diffusivity $\langle D \rangle$ under DIII-D conditions.

changes in the same confinement mode and cannot be regarded as an actual L–H transition. In our model, the L–H transition via an instantaneous decrease in the total current stems merely from the assumptions underlying the numerical experiment. In real experiments, this transition is unlikely to be achieved.

Another example of the L–H transition is illustrated in Fig. 6, which shows how the averaged turbulent diffusivity $\langle D \rangle$ evolves when the neutral density at the wall increases instantaneously. In this example, the kinetic energy of the poloidal plasma rotation remains constant, but the density profile $N(r)$ changes radically. From Fig. 7, we can see that $dN/dr > 0$ holds over the greater part of the layer, so that the flux $\Gamma(r)$ in this region intrinsically decreases and can even change sign.

Another possibility of producing the radial current in the tokamak scrape-off layer can be understood from the experiments on plasma polarization, in which the radial electric field is generated by the potential difference between the electrode and the chamber wall and naturally gives rise to the radial current $J_x^{\text{neo}}(E_x)$. Note that, by virtue of Eq. (14), the poloidal velocity should satisfy the boundary condition $U(0) = V_d(0) - c(E_{el}/B)$, which stems from the boundary condition $E(0) = E_{el}$ for the radial electric field at the electrode surface $x = 0$.

For the CASTOR device, we calculated the turbulent diffusion coefficients $\{D, \chi_i, \chi_e\}$ as functions of the radial electric field E_{el} at the electrode surface. From Fig. 8, we can see that, regardless of the polarity of the radial field, the turbulent transport becomes less intense as E_{el} increases. The profiles in Fig. 8 have an important

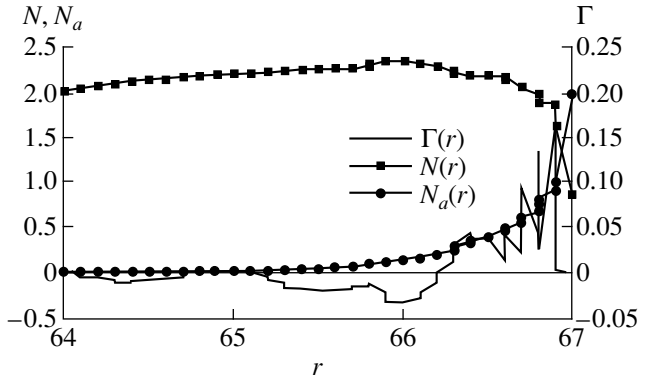

Fig. 7. Radial profiles of the turbulent flux $\Gamma(r)$, plasma density $N(r)$, and neutral density $N_a(r)$ between radial positions of 64 and 67 cm in the DIII-D tokamak (at the time t = 300 μs in Fig. 6).

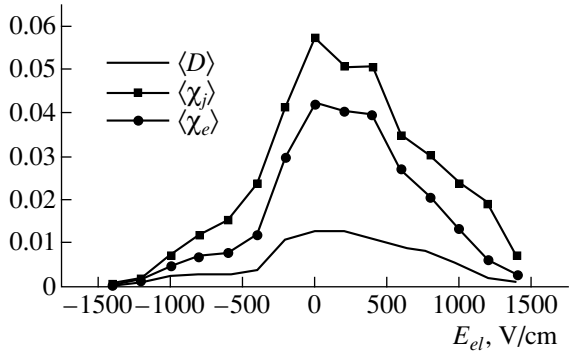

Fig. 8. Turbulent diffusion coefficients $\{D, \chi_i, \chi_e\}$ as functions of the radial electric field at the electrode surface under CASTOR conditions.

characteristic feature: they are asymmetric about the vertical line $E_{el} = 0$. This indicates that, for a radial electric field of negative polarity at the electrode surface (H_--mode), the plasma confinement is better than in the case of positive polarity (H_+-mode). Note that this result agrees with the data from some experiments on plasma polarization [24, 25]. Our calculations show that, for E lying in the range from –400 to –500 V/cm, the dimensionless current is equal to $J_x = j_x/j_0 \sim (0.5–1)\rho^2$, where $j_0 = en_0v_0$, so that, for $\rho \sim 0.05$, $n_0 = 10^{13}$ cm^{-3}, and $v_0 = 10^7$ cm/s, the dimensional (physical) current density is $j_x \sim 80–160$ A/m^2.

5. CONCLUSION

We have investigated the behavior of turbulent fluxes in a tokamak wall plasma by numerical methods. The calculations were carried out with the help of the four-field model constructed from the Braginskii reduced two-fluid hydrodynamic equations [12, 13] by taking into account not only the fluctuations of the plasma density and electric potential but also the fluctuations of the ion and electron temperatures.

In the model proposed here, the radial current plays an important role in triggering transitions to new confinement modes. We have shown that this current, which can be driven by turbulence-induced forces and friction forces associated with neutral particles, is always present in a narrow wall plasma layer in a tokamak. Another possible mechanism for exciting the radial current is associated with the violation of the ambipolarity constraint (or, in other words, the violation of the balance between the distributions of charged particles of different species) for a short time due to an external action (such as microwave heating, neutral beam heating, neutral injection, and plasma polarization). The jumplike violation of the ambipolarity constraint leads to a sequence of jumps:

$$\Delta E \longrightarrow \Delta J \longrightarrow \Delta J \cdot B/c \longrightarrow \Delta U.$$

If the jump in the radial electric field is above a certain critical level, $|\Delta E| > |\Delta E_{\text{crit}}|$, then the plasma can undergo a jumplike transition to a new equilibrium state in which the poloidal velocity is higher and turbulent fluctuations are partially (or even completely) suppressed. The existence of bifurcated solutions stems from the fact that the equation for the poloidal velocity has several equilibrium points, because it contains nonlinear source terms whose specific form is determined by the profiles $J_x^{\text{neo}}(E_x)$ and $\nu_{\text{neo}}(E_x)$. We have shown that even weak radial electric fields $\Delta E \sim \pm 100$ V/cm can give rise to L–H transitions.

We have examined examples in which the transition to a new confinement mode is governed by a change in tokamak parameters that do not affect the poloidal flow velocity. Thus, we can conclude that L–H transitions can occur via different mechanisms. Although the proposed mechanism in which the radial current plays an important role refers to a large number of scenarios for the transition to a new confinement mode, it does not pretend to be universal.

We have also simulated L–H transitions when the radial current at the plasma edge is generated by applying an external voltage to the internal electrode. The calculated dependences of the turbulent diffusion coefficients $\{D, \chi_i, \chi_e\}$ on the radial electric field E_{el} at the electrode surface show that, regardless of the polarity of the field, turbulent transport becomes far less intense as E_{el} increases. In accordance with experimental observations, the turbulent transport in the case of a radial electric field of negative polarity ($E_{el} < 0$, which corresponds to the H_--mode) is somewhat less intense than in the case of a positive polarity ($E_{el} > 0$, which corresponds to the H_+-mode).

ACKNOWLEDGMENTS

This work was supported by the Russian Foundation for Basic Research, project no. 00-15-96526 (under the program “Leading Scientific Schools”).

APPENDIX

Our aim here is to derive nonlinear hydrodynamic equations that describe the evolution of the quantities n, Φ, T_e, and T_i and are valid in a plane wall plasma layer in a tokamak. We assume that the longitudinal tokamak magnetic field is strong enough in order to apply the reduced hydrodynamic approach [11–13]. We consider a plane plasma layer in the tokamak magnetic field $\mathbf{B} = B_0\left(\mathbf{e}_z\left[1 - \frac{x}{R}\right] + \frac{(x - x_0)}{L_s}\mathbf{e}_y\right)$, where x is the radial coordinate and $y = r\theta$ and $z = R\zeta$ are analogues of the periodic coordinates θ and ζ.

The equation for the vorticity can be derived from the current continuity equation

$$\text{div}(\mathbf{j}) = \nabla_\perp(\mathbf{j}_\perp) + \nabla_\parallel(\mathbf{j}_\parallel) = 0, \qquad \text{(A.1)}$$

where $\mathbf{j}_\perp = ne(\mathbf{V}_E + \mathbf{V}_D + \mathbf{V}_P)$, $\mathbf{V}_E = \frac{c}{B}[\mathbf{e}_z \times \nabla\Phi] + \mathbf{e}_y U$, $\mathbf{V}_D = \frac{c[\mathbf{B} \times \nabla P]}{enB^2}$, $P = P_i + P_e$, $\mathbf{V}_P = -\frac{c}{B\omega_{ci}}\frac{d\nabla\Phi}{dt}$, and $\frac{d}{dt} = \frac{\partial}{\partial t} + \mathbf{V}_E \cdot \nabla$.

We substitute the expressions for the transverse velocity components into Eq. (A.1), take into account the magnetic field nonuniformity $B = B_0(1 - x/R)$, and define the dimensional vorticity as [cf. the dimensionless form in Eqs. (1)]

$$W = \frac{c}{B}\Delta_\perp\Phi. \qquad \text{(A.2)}$$

As a result, we arrive at the following equation for the vorticity:

$$\frac{cmn}{B}\left(\frac{\partial W}{\partial t}+\left\{\frac{c}{B}\Phi, W\right\}\right) = \nabla_{\parallel} j_{\parallel} - \frac{c}{RB}\frac{\partial P}{\partial y} + mn\mu\nabla_{\perp}W, \tag{A.3}$$

where $\{A, B\} = \partial A/\partial x \times \partial B/\partial y - \partial A/\partial y \times \partial B/\partial x$.

Using the electron continuity equation

$$\frac{\partial n}{\partial t} + \mathrm{div}[n(\mathbf{V}_{e\perp} + \mathbf{V}_{e\parallel})] = 0$$

and assuming that $V_{e\parallel} \approx -j_{\parallel}/en$, $\mathbf{V}_{\perp e} = \mathbf{V}_E + \mathbf{V}_{De}$, and $\mathbf{V}_{De} = -\dfrac{cT_e[\mathbf{B}\times\nabla n]}{enB^2}$, we obtain

$$\frac{\partial n}{\partial t} + \left\{\frac{c\Phi}{B}, n\right\} = \frac{1}{e}\nabla_{\parallel} j_{\parallel} - \frac{cn}{RB}K_e + D\Delta_{\perp}n_1,$$
$$K_e = \frac{1}{e}\left[\frac{\partial T_e}{\partial y} + T_e\frac{\partial n}{n\partial y}\right] - \frac{\partial \Phi}{\partial y}. \tag{A.4}$$

The longitudinal current can be deduced from the equation for the longitudinal electron velocity by neglecting the inertial terms:

$$j_{\parallel} = \sigma\left[\alpha_1\nabla_{\parallel}\frac{T_e}{e} + \frac{T_e}{e}\frac{\nabla_{\parallel}n}{n} - \nabla_{\parallel}\Phi\right],$$
$$\sigma = \frac{e^2 n}{m_e\nu_{ei}}, \quad \alpha_1 = 1.71. \tag{A.5}$$

The Braginskii two-fluid hydrodynamic equations for the electron and ion temperatures are written as [11]

$$\frac{3n}{2}\frac{dT_e}{dt} = -P_e\,\mathrm{div}\,\mathbf{V}_e - \mathrm{div}\,\mathbf{q}_e + Q_e,$$
$$\frac{3n}{2}\frac{dT_i}{dt} = -P_i\,\mathrm{div}\,\mathbf{V}_i - \mathrm{div}\,\mathbf{q}_i + Q_i, \tag{A.6}$$

where the fluxes $\mathbf{q}_{e,i}$ have the form

$$q_e = -\kappa_{e\parallel}\nabla_{\parallel}T_e - \kappa_{e\perp}\nabla_{\perp}T_e - \frac{5}{2}\frac{cnT_e}{eB}\frac{[\mathbf{B}\times\nabla T_e]}{B} - 0.71\frac{T_e j_{\parallel}}{e},$$
$$\kappa_{e\parallel} = \frac{3.16nT_e}{m_e\nu_{ei}}, \quad \kappa_{e\perp} = \kappa_e^{\mathrm{neo}},$$
$$q_i = -\kappa_{i\parallel}\nabla_{\parallel}T_i - \kappa_{i\perp}\nabla_{\perp}T_i - \frac{5}{2}\frac{cnT_i}{eB}\frac{[\mathbf{B}\times\nabla T_i]}{B},$$
$$\kappa_{i\parallel} = \frac{3.9nT_i}{m_i\nu_{ii}}, \quad \kappa_{i\perp} = \kappa_i^{\mathrm{neo}}, \quad \kappa_{\alpha\perp}^{\mathrm{neo}} = 3\frac{\sqrt{\pi}}{2}\varepsilon^2\frac{q\rho_{\alpha}}{r\varepsilon}\frac{cT_{\alpha}}{eB}.$$

Substituting the electron and ion velocities

$$\mathbf{V}_e = -\frac{\mathbf{j}_{\parallel}}{en} + \mathbf{V}_E + \mathbf{V}_{De}, \quad \mathbf{V}_i = \mathbf{V}_E + \mathbf{V}_{Di}$$

into Eqs. (A.6), we finally arrive at the following nonlinear equations for $T_{e,i}$:

$$\frac{3n}{2}\frac{dT_e}{dt} = \kappa_{e\parallel}\nabla_{\parallel}^2 T_e - \alpha_1\nabla_{\parallel}\frac{j_{\parallel}}{e} + \frac{cnT_e}{RB}\left(\frac{\partial\Phi}{\partial y} - Y_e\right) + Q_e + \kappa_{e\perp}\nabla_{\perp}^2 T_e,$$
$$\frac{3n}{2}\frac{dT_i}{dt} = \kappa_{i\parallel}\nabla_{\parallel}^2 T_i + \frac{cnT_i}{RB}\left(\frac{\partial\Phi}{\partial y} + Y_i\right) + Q_i + \kappa_{i\perp}\nabla_{\perp}^2 T_i,$$
$$Y_{\alpha} = \frac{1}{e}\left[\frac{7}{2}\frac{\partial T_{\alpha}}{\partial y} + T_{\alpha}\frac{\partial n}{n\partial y}\right]. \tag{A.7}$$

The set of equations (A.3), (A.4), and (A.7), supplemented with Eq. (A.2) for the electric potential and Eq. (A.5) for the longitudinal current, describes the nonlinear evolution of the quantities n, Φ, T_e, and T_i and serves as the basis for the four-field two-fluid hydrodynamic model.

REFERENCES

1. A. Hasegawa and M. Wakatani, Phys. Rev. Lett. **50**, 682 (1983).
2. B. A. Carreras, V. E. Lynch, and L. García, Phys. Fluids B **5**, 1795 (1993).
3. B. A. Carreras, V. E. Lynch, L. García, and P. H. Diamond, Phys. Fluids B **5**, 1491 (1993).
4. A. Takayama, M. Wakatani, and H. Sugama, Phys. Plasmas **3**, 3 (1996).
5. S. J. Camagro, D. Biskamp, and B. D. Scott, Phys. Plasmas **2**, 48 (1995).
6. X. N. Su, P. N. Yushmanov, J. Q. Dong, and W. Horton, Phys. Plasmas **1**, 1905 (1994).
7. R. V. Shurygin, Fiz. Plazmy **25**, 739 (1999) [Plasma Phys. Rep. **25**, 677 (1999)].
8. H. Biglari, P. H. Diamond, and P. W. Terry, Phys. Fluids B **2**, 1 (1990).
9. Y. Z. Zhang and S. M. Mahajian, Phys. Fluids B **4**, 1385 (1992).
10. J. W. Connor and H. R. Wilson, Report of UKAEA, no. FUS 421 (EURATOM/UUUKAEA, Culham,1999).
11. S. I. Braginskii, in *Reviews of Plasma Physics*, Ed. by M. A. Leontovich (Gosatomizdat, Moscow, 1963; Consultants Bureau, New York, 1963), Vol. 1.
12. H. R. Strauss, Phys. Fluids **19**, 134 (1976).
13. J. F. Drake and T. M. Antonsen, Phys. Fluids **27**, 898 (1984).
14. V. A. Abramov, V. V. Vikhrev, and O. P. Pogutse, Fiz. Plazmy **3**, 18 (1977) [Sov. J. Plasma Phys. **3**, 288 (1977)].
15. N. V. Nikitin, Zh. Vychisl. Mat. Mat. Fiz. **34**, 909 (1994).

16. T. E. Stringer, Nucl. Fusion **33**, 1249 (1993).
17. F. L. Hinton and Y. B. Kim, Nucl. Fusion **34**, 899 (1994).
18. K. Miaymoto, Nucl. Fusion **36**, 927 (1996).
19. S. I. Itoh and K. Itoh, Phys. Rev. Lett. **67**, 2485 (1991).
20. J. Cornelis, R. Sporken, G. van Oost, and R. R. Weynants, Nucl. Fusion **34**, 655 (1994).
21. H. Xiao, R. D. Hazeltine, and P. M. Valanju, Phys. Plasmas **2**, 1996 (1995).
22. J. W. Connor and T. E. Stringer, Phys. Fluids **14**, 2177 (1971).
23. J. W. Connor and T. E. Stringer, Phys. Fluids **14**, 2184 (1971).
24. R. R. Weynants *et al.*, Nucl. Fusion **32**, 837 (1992).
25. L. G. Askinazi, V. E. Golant, S. V. Lebedev, *et al.*, Nucl. Fusion **32**, 271 (1992).
26. M. Hron, Czech. J. Phys. **49** (12), S1 (1999).

Translated by O.E. Khadin

Plasma Physics Reports, Vol. 27, No. 1, 2001, pp. 30–35. Translated from Fizika Plazmy, Vol. 27, No. 1, 2001, pp. 31–36.

TOKAMAKS

Numerical Analysis of the Near Fields of ICRH Antennas in a Tokamak

V. V. Breev, I. A. Kovan, and N. B. Rodionov

Troitsk Institute for Innovation and Fusion Research, Russian State Science Center, Troitsk, Moscow oblast, 142092 Russia

Received April 4, 2000; in final form, June 27, 2000

Abstract—Results are presented from numerical calculations of the near fields of ICRH antennas in the quasi-steady current approximation in two-dimensional geometry. The distributions of the vacuum electric and magnetic fields as well as of the surface current density in the antenna elements and inside the tokamak chamber are obtained. The electrotechnical characteristics of the antennas are analyzed numerically as functions of their geometric parameters. © *2001 MAIK "Nauka/Interperiodica".*

1. INTRODUCTION

Since the 1970s, in connection to the problem of auxiliary plasma heating in tokamaks, it has become relevant to calculate ICRH antennas, which are aimed at feeding the RF power from external sources into the plasma. Usually, such calculations are based on a Fourier analysis of the antenna spectra, because the plasma dielectric tensor depends on the longitudinal wavenumber $k_\parallel$. For this reason, the wave equation in both the antenna and plasma should be solved by expanding the antenna current in longitudinal harmonics. These calculations are aimed at determining the antenna radiation resistance, which is, as a rule, much lower than the antenna wave resistance, because the wavelength of the emitted wave in vacuum is much longer than that in the plasma. That is why the antenna reactance is affected by the plasma only slightly. On the other hand, constructing antennas requires knowledge of their main parameters in the absence of a plasma: the specific inductance, specific capacitance, wave resistance, loss resistance, etc., which should be calculated for specific geometric configurations, e.g., for antennas in the diagnostic ports of a tokamak or in special cavities in the chamber wall, as well as for antenna arrays in baffled chambers.

Below, we will report the results of numerical calculations aimed at revealing two-dimensional geometric patterns of the near field of an antenna and the self-consistent currents in the antenna conductor and tokamak chamber. The calculations were carried out for an individual antenna and for an antenna system consisting of two radiating elements. The developed numerical code can be generalized to phased-array antennas composed of many individual radiating elements aimed at producing running fields.

2 SOLUTION METHOD

It is well known that the four Maxwell equations can be reduced to two equations for the scalar and vector potentials, φ and $\mathbf{A}$. In order for the potentials to be uniquely determined, they should satisfy the Lorentz gauge. If the parameters of the problem change as harmonic functions of time t according to the law $\exp(i\omega t)$, then the potentials satisfy the d'Alembert equations

$$\Delta\varphi + k^2\varphi + q/\varepsilon_0 = 0, \quad (1)$$

$$\Delta\mathbf{A} + k^2\mathbf{A} + \mu_0\mathbf{j} = 0, \quad (2)$$

where ω is the angular frequency, $i = \sqrt{-1}$ is the imaginary unit, $k = \omega/c$ is the wavenumber, $c = 1/\sqrt{\varepsilon_0\mu_0}$ is the speed of light in vacuum, ε_0 and μ_0 are the permittivity and permeability of free space, q is the space charge, and j is the current density. Using the Lorentz gauge in the form of

$$\operatorname{div}\mathbf{A} = -ik\varphi, \quad (3)$$

we can express the electric and magnetic fields in terms of the potentials:

$$\mathbf{B} = \operatorname{curl}\mathbf{A}, \quad (4)$$

$$\mathbf{E} = -i\omega\mathbf{A} - \operatorname{grad}\varphi, \quad (5)$$

where $\mathbf{B}$ is the magnetic induction and $\mathbf{E}$ is the electric field strength.

First, we determine the antenna parameters in vacuum, in the absence of plasma. Under the operating conditions prevailing in tokamaks, we can assume that the wavelength $\lambda = 2\pi/k$ of radiation emitted by an antenna is much larger than the dimensions of the radiating antenna element, or, in other words, the alternating antenna current is assumed to be quasi-steady [1]. For this reason, in Eqs. (1)–(3), we can drive the wavenumber to zero, $k \longrightarrow 0$. We also assume that the entire

1063-780X/01/2701-0030$21.00

spatial region under analysis is free of external currents and charges. Under these assumptions, Eqs. (1) and (2) can be reduced to two Laplace equations for the scalar and vector potentials.

An individual antenna and antenna system consisting of two radiating elements are represented schematically in Fig. 1, in which the heavy lines show the metal walls of the chamber. The *X*- and *Y*-axes are perpendicular to the minor axis of the torus; the *X*-axis is directed toward the minor axis and the *Y*-axis is oriented in the poloidal direction along the surface of the antenna conductor. The *Z*-axis is aligned with the toroidal magnetic field. In an individual antenna, the central conductor (illustrated by the black rectangle in Fig. 1a) is installed in a cavity in the chamber wall between two conducting surfaces at a distance *d* from the (*y*, *z*) plane. In an antenna system with two radiating elements (Fig. 1b), there is a thin conducting baffle of height *h* between the central conductors. In the figures, the dashed lines represent a continuous electrostatic screen, which is transparent to an alternating magnetic field but is opaque to an electrostatic field. Unlike the Faraday screen, the electrostatic screen is a thin conducting layer, thinner than the skin depth but much thicker than the Debye radius.

As the calculation region, we chose a part of the toroidal chamber with identified ends. Since the antenna conductor is much longer in the *y*-direction than in the (*x*, *z*) plane, we set

$$\mathbf{A} = (0, A_y(x, z), 0),$$

$$\mathbf{B} = \left(-\frac{\partial A_y}{\partial z}, 0, \frac{\partial A_y}{\partial x}\right),$$

in which case the magnetic field lines are described by the equation A_y = const. We thus have to solve a two-dimensional problem in the (*X*, *Z*) plane.

The high-frequency current flows in a skin layer with thickness $\delta_s = 1/\sqrt{\mu_0\sigma\omega}$, where σ is the conductivity of a metal conductor. Since the electromagnetic field does not penetrate into the conductor, we can impose the following boundary conditions on its surface:

$$\mathbf{B}\cdot\mathbf{n} = 0, \tag{6}$$

$$\mu_0\mathbf{j}_{\text{surf}} = \mathbf{n}\times\mathbf{B}, \tag{7}$$

where $\mathbf{j}_{\text{surf}} = \delta_s\mathbf{j}$ is the surface current and $\mathbf{n}$ is the outward-facing unit normal to the surface. The first boundary condition implies that A_y = const at the conductor surface and that the contour of the conductor coincides with a magnetic field line.

For an individual antenna, the problem is formulated as follows. In the entire calculation region, which is bounded by the chamber wall (except for the region occupied by the antenna conductor), we solved the equation

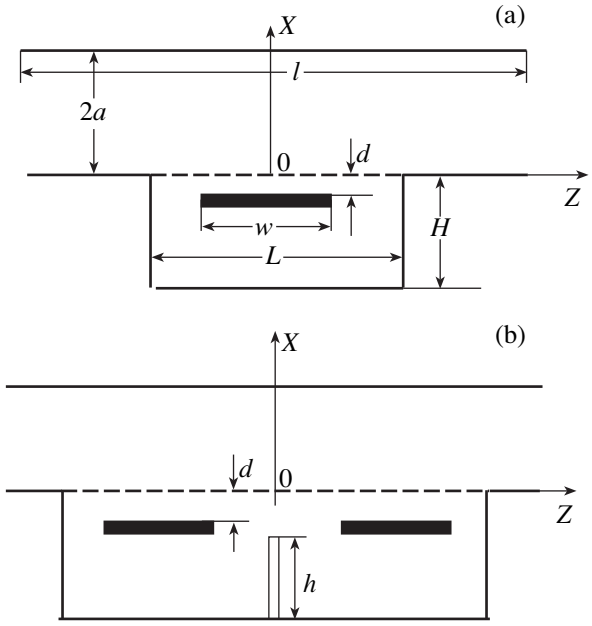

Fig. 1. Schematics of (a) an individual antenna and (b) an antenna system of two radiating elements: *l* is the size of the calculation region in the *z*-direction, 2*a* is the size of the tokamak chamber in the *x*-direction, *L* is the width of the cavity where an antenna is placed, *H* is the height of the cavity, *w* is the width of the antenna conductor, *d* is the distance between the surface of the antenna conductor and the (*y*, *z*) plane, and *h* is the height of the baffle between two radiating elements of the antenna system.

$$\frac{\partial^2 A_y}{\partial x^2} + \frac{\partial^2 A_y}{\partial z^2} = 0 \tag{8}$$

with the boundary conditions $A_y = A_{y1}$ at the contour of the conductor surface and $A_y = A_{y2}$ at the contour of the chamber wall. The constant A_{y1} was set equal to unity. The unknown quantity A_{y2} was determined from the condition that the current J_1 flowing in the antenna conductor is equal to the current J_2 induced in the chamber wall. Taking into account boundary conditions (6) and (7) yields the following expressions for these currents:

$$J_1 = \int_{L_{c1}} (j_{S_z}dx + j_{S_x}dz), \tag{9}$$

$$J_2 = \int_{L_{c2}} (j_{S_z}dx + j_{S_x}dz), \tag{10}$$

where $j_{S_x} = 1/\mu_0\frac{\partial A_y}{\partial x}$ and $j_{S_z} = 1/\mu_0\frac{\partial A_y}{\partial z}$ are the surface current densities along the *x*- and *z*-axes, L_{c1} is the con-

tour of the central conductor, and L_{c2} is the contour of the conducting part of the chamber. The convergence of the iterative procedure for solving Eq. (8) was controlled by means of the condition $J_1 = J_2$. However, after this condition held with the desired accuracy, we additionally checked the difference between the mesh values of the vector potential taken from two successive iteration steps.

The scalar potential was calculated from the equation

$$\frac{\partial^2\varphi}{\partial x} + \frac{\partial^2\varphi}{\partial z} = 0, \tag{11}$$

which was solved in the region bounded by the electrostatic screen, with the boundary conditions

$$\varphi = \varphi_0 = 1 \tag{12}$$

at the surface of the central conductor and

$$\varphi = 0 \tag{13}$$

at the metal side surfaces of the cavity.

The total electrostatic charge induced at the boundaries of the calculation region was obtained from the formula

$$Q = \int_{L_{c1}} q dL, \tag{14}$$

where

$$q = 2\varepsilon_0\left(\frac{\partial\varphi}{\partial x} + \frac{\partial\varphi}{\partial z}\right).$$

Equations (8) and (11) with the boundary conditions (6), (7), (12), and (13) and the periodic boundary conditions at the identified ends of the chamber were solved numerically in finite differences [2] on a two-dimensional uniform grid with a spatial step Δ. The numbers of mesh points in the x- and z-directions were chosen in accordance with the characteristic geometric dimensions of the antenna. We stopped the iterative procedure after the currents J_1 and J_2 became equal to each other. From the calculated total currents and the vector and scalar potentials, we obtained the near field pattern of the antenna and evaluated the antenna parameters, e.g., the line inductance (in H/m)

$$L = \left(\frac{A_{y_1}}{J_1} + \frac{A_{y_2}}{J_2}\right)$$

and the line capacitance $C = (\varphi_0 - \varphi)/Q$ [F/m].

For an antenna system consisting of two phased radiating elements, the problem is formulated as follows. Equation (8) is solved over the entire calculation region shown in Fig. 1b (except for the regions occupied by the antenna conductors), and Eq. (11) is solved in the region bounded by the electrostatic screen, the boundary conditions being the same as in the problem for an individual antenna. The characteristic feature of the antenna system under consideration is that the radiating elements are mutually coupled to one another: the radiating elements were treated as two symmetric coupled oscillatory circuits with the frequency

$$\omega_C = \frac{1}{\sqrt{((L_1 \pm L_{12})l_y + 2L_n)C_{\text{eff}}}}. \tag{15}$$

Here, L_1 is the line inductance of the central conductor, L_n is the inductance of the supply line, and the capacitance of a circuit has the form

$$C_{\text{eff}} = (\alpha C l_y + C_n + C_{\text{ext}})/2,$$

where the numerical coefficient $\alpha \approx 1/2$ is determined from the potential distribution at the surface of the antenna conductor, C is the capacitance per unit length of the central conductor with respect to the electrostatic screen and the chamber wall, C_n is the capacitance of the supply line, C_{ext} is the external capacitance of the supply line, L_{12} is the mutual inductance of the radiating elements, and l_y is the antenna conductor length. The plus and minus signs refer to the cases when the currents flowing in radiating elements are inphase and antiphase, respectively. Ensuring the electric strength of an antenna usually requires that the conditions $2L_n \ll L_1 l_y$ and $C_{\text{ext}} \gg C l_y$ be satisfied.

Depending on the value of the coupling coefficient (see, e.g., [3])

$$A = k_C Q,$$

where $k_C = L_{12}/L_1$ is the inductive coupling coefficient, $Q = \omega L_\Sigma/r$ is the Q-factor of an oscillatory circuit, $L_\Sigma = (L_1 \pm L_{12})l_y + 2L_n$, and r is the active resistance of an oscillatory circuit, we can distinguish the following two regimes.

The range $A < 1$ corresponds to weakly coupled oscillatory circuits, whose amplitude–frequency characteristic has a single maximum. The range $A \geq 1$ corresponds to strongly coupled oscillatory circuits (the amplitude–frequency characteristic is double-humped), which are thus mismatched with one another.

3. NUMERICAL RESULTS

In calculations, we used the following geometric parameters of the antennas shown in Fig. 1:

The length of the part of the chamber in the z-direction was	l = 78 cm
The distance between the side surfaces of the cavity along the x-axis was	$2a$ = 100 cm
The depth of the cavity for an antenna in the chamber wall was	H = 40 cm
The width of the cavity was	L = 28 cm
The width of the antenna conductor was	w = 10 cm

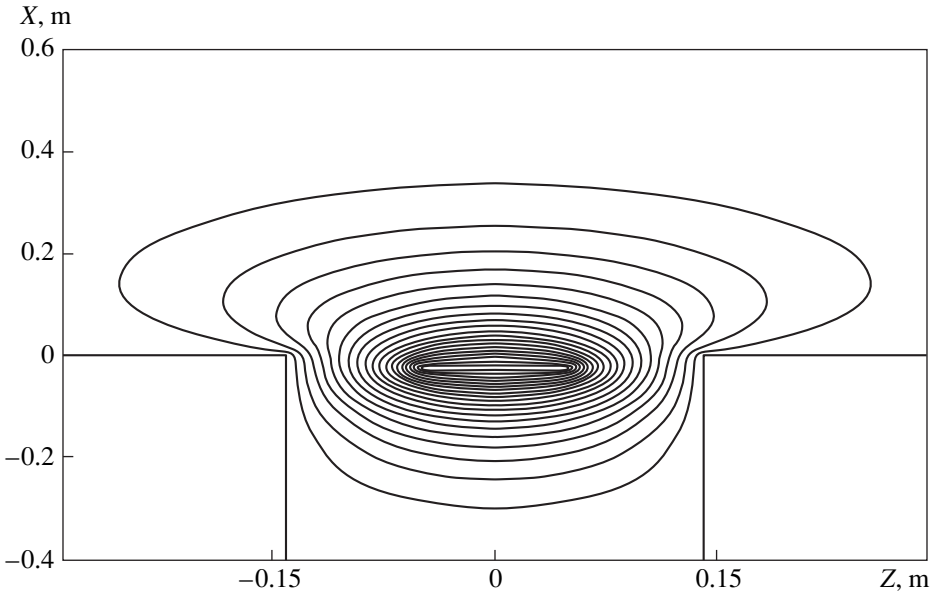

Fig. 2. Magnetic field distribution of an individual antenna for l = 78 cm, $2a$ = 100 cm, L = 28 cm, H = 40 cm, w = 10 cm, and d = 2 cm.

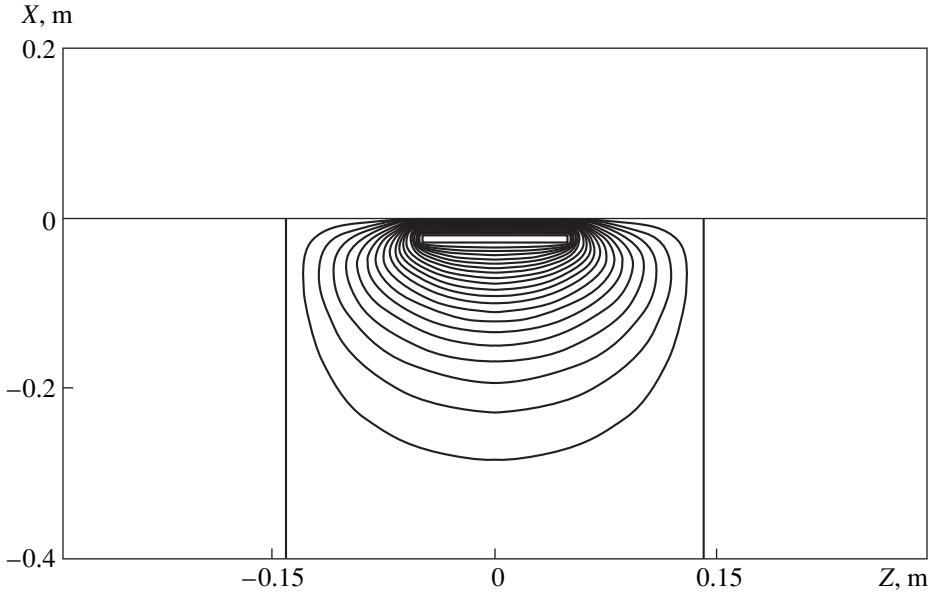

Fig. 3. Equipotential surfaces of the electric field of an individual antenna for l = 78 cm, $2a$ = 100 cm, L = 28 cm, H = 40 cm, w = 10 cm, and d = 2 cm.

We varied the distance d from the antenna conductor to the (y, z) plane and the baffle height h. The thickness of both the antenna conductor and the baffle was 1 cm, and the conductor length in the y-direction was set to be 50 cm.

In Fig. 2, we display a portion of the pattern of the magnetic field lines calculated for d = 2 cm. We can see that the magnetic field is primarily concentrated near the central conductor, the penetration depth of the magnetic field into the chamber being about one-third of the chamber radius.

Figure 3 shows the equipotential surfaces of the electric field for the same case as in Fig. 2. One can see that the equipotentials are concentrated between the central conductor and the screen, without penetrating into the working volume.

The current calculated at the surface of the antenna conductor was found to be rather high at the conductor

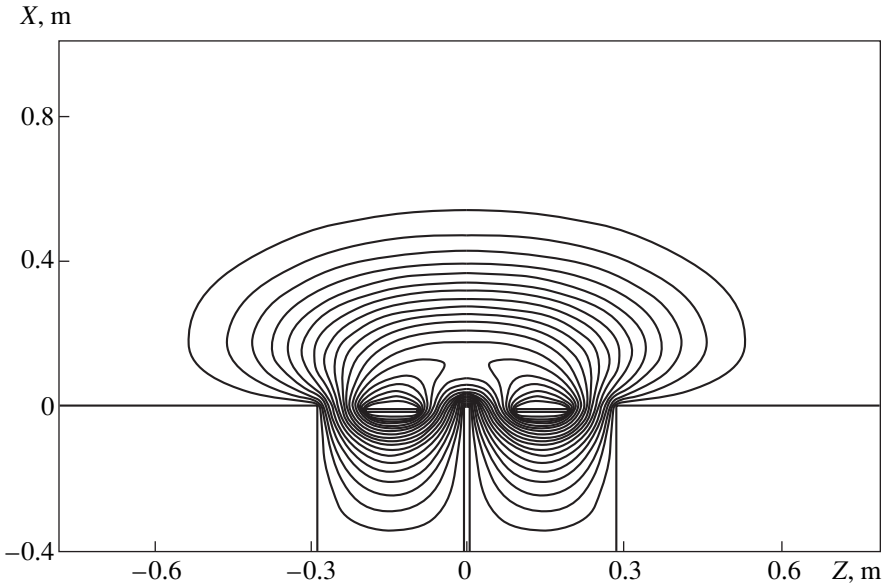

Fig. 4. Magnetic field lines of two radiating elements in which the currents are inphase for l = 156 cm, $2a$ = 100 cm, L = 28 cm, H = 40 cm, w = 10 cm, d = 2 cm, and h = 40 cm.

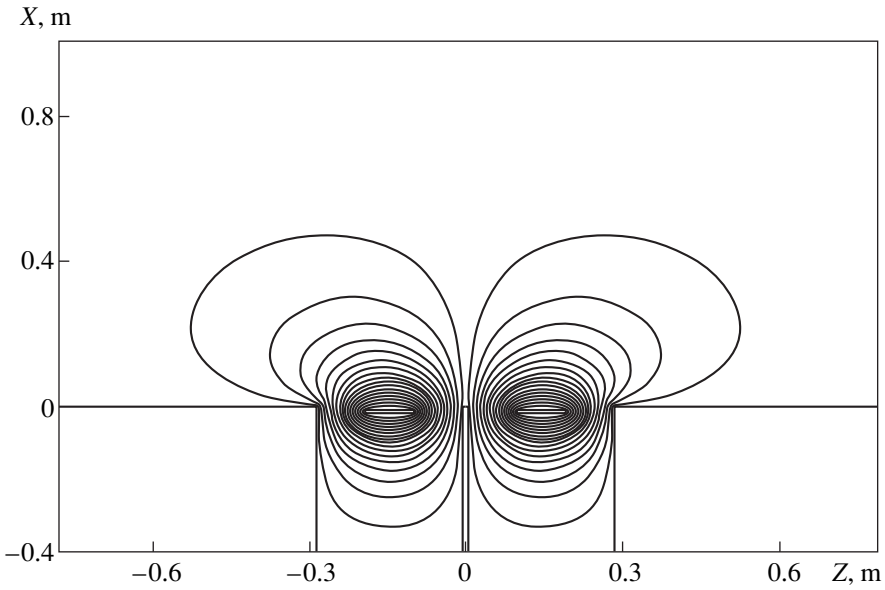

Fig. 5. Magnetic field lines of two radiating elements in which the currents are antiphase for the same parameters of the antenna system as in Fig. 4.

edges (it is higher than the current at the side surfaces of the conductor by a factor of more than 2). Over the surface of the cavity, the current was found to be distributed in an analogous manner: it was concentrated at the corners of the cavity near the (y, z) plane.

We also present two electrotechnical parameters of an individual antenna:

The specific inductance is L_1 = 0.44 μH/m

The specific capacitance is C = 68.0 pF/m

Figures 4 and 5 show the magnetic field lines for an antenna system consisting of two radiating elements in which the currents are inphase (0°) and antiphase (180°), respectively. The geometry of the antenna system corresponds to that in Fig. 1b at d = 1 cm. We can see a significant coupling between the magnetic fluxes when the currents in the radiating elements are inphase.

The calculated mutual inductance of the radiating elements was found to depend strongly on the baffle

height h. Thus, for h = 40 cm, we have L_{12} = 0.048 μH/m, while, for h = 36 cm, we have L_{12} = 0.101 μH/m. For $L_{12}l_y \geq 2L_n$, the inductive coupling coefficient is about 0.1–0.2, which corresponds to the regime of strong coupling, resulting in a frequency mismatch between the oscillatory circuits even when the Q-factors of the loaded oscillatory circuits lie in the range $Q \geq 10$.

3. CONCLUSION

We have developed an algorithm for calculating the two-dimensional vacuum near field of an ICRH antenna. We have computed the distributions of the magnetic field lines, electrostatic fields, and current densities at the surface of the current-carrying antenna conductor and at the metal wall of the tokamak chamber. We have used these distributions to evaluate the main electrotechnical parameters of the antennas. We have revealed that the effect of the baffles in antenna systems on their frequency characteristic is strong. The developed numerical code makes it possible to calculate the pattern of the running field for an antenna system composed of appropriately phased radiating elements.

ACKNOWLEDGMENTS

We thank A.P. Popryadukhin for his useful remarks and L.G. Kurkina for her help in the preliminary stages of this work.

REFERENCES

1. I. E. Tamm, *The Principles of Electricity Theory* (Nauka, Moscow, 1976).
2. A. A. Samarskiĭ, *The Theory of Difference Schemes* (Nauka, Moscow, 1977).
3. S. I. Baskakov, *Lectures on Circuit Theory* (Mosk. Énerg. Inst., Moscow, 1991).

Translated by G.V. Shepekina

Plasma Physics Reports, Vol. 27, No. 1, 2001, pp. 36–43. Translated from Fizika Plazmy, Vol. 27, No. 1, 2001, pp. 37–44.

DUSTY PLASMA

Ordered Dusty Structures in Nuclear-Track Neon and Argon Plasmas

V. I. Vladimirov*, L. V. Deputatova*, V. I. Molotkov*, A. P. Nefedov*, V. A. Rykov, V. S. Filinov*, V. E. Fortov*, and A. V. Khudyakov****

**Institute for High Energy Densities, Russian Academy of Sciences, Moscow, 127412 Russia*

***Leipunskii Research Institute for Physics and Power Engineering, Russian State Scientific Center, Obninsk, Kaluga oblast, 249020 Russia*

E-mail: rykov@ippe.obninsk.ru

Received March 27, 2000; in final form, June 20, 2000

Abstract—Ordered dusty structures formed of spherical monodisperse and polydisperse grains are obtained for the first time in a nuclear-track plasma produced by α-particles and fission fragments of ^{252}Cf nuclei passing through neon or argon. A theoretical model of such a plasma is proposed. Monte Carlo computer simulations based on this model are carried out to explain the formation of such structures. *© 2001 MAIK "Nauka/Interperiodica".*

1. INTRODUCTION

So far, dusty structures with far and near orders have been obtained in plasmas of a stratified gas discharge [1, 2], thermal plasmas [3], and RF discharge plasmas [4]. Ordered dusty structures have also been obtained in a nuclear-track plasma [5, 6] produced in air by α-particles and fission fragments of ^{252}Cf. The levitation of dust grains is achieved by applying an electric field that balances the gravity force. Because of the high percentage of oxygen in air, the mean lifetime of an electron in a track at atmospheric pressure is equal to ~0.3 μs, whereas the time of its drift to the electrodes separated by a distance of several centimeters attains several microseconds for typical values of the reduced field E/p in the ionization chamber (here, E is the field strength and p is the gas pressure). Therefore, the electric charge of dust grains is generated primarily due to the action of negative and positive ions. Since the temperatures of negative and positive ions differ slightly and are rather low, this charge cannot be too high.

Of particular interest is the charging of dust grains in nuclear-track plasmas of inert gases, in which the electrons play a dominant role and can impart a substantial negative charge to the dust grains if the electron temperature is much higher than the ion temperature. In terms of physical characteristics, the nuclear-track plasma of inert gases differs significantly from both thermal and gas-discharge plasmas. Therefore, experiments with a nuclear-track dusty plasma provide new information on the ability of the dust component to self-organize. At relatively low intensities of radioactive sources typical of laboratory conditions, this plasma has a distinct track structure [7], the lifetime of the tracks produced by nuclear-reaction products being much shorter than the time interval between the tracks. In addition to sharp time variations, the nuclear-track plasma has a strongly nonuniform spatial distribution because the length of the track is much longer than its diameter. The Debye length in the track plasma is much shorter than the track length; however, it is often comparable with the track cross size.

The aim of this study is to produce dusty ordered structures in a nuclear-track plasma created by nuclear-reaction products in inert gases and perform computer simulations of the processes resulting in the formation of such structures.

2. EXPERIMENTAL SETUP

The experimental setup consisted of a hermetically sealed glass cell in which the physical processes under study occurred, facilities for evacuating the cell and filling it with a gas, a facility for injecting dust grains into a nuclear-track plasma, a diagnostic system for observing the behavior of macroscopic objects in the experimental cells, and a computerized system for data acquisition and processing. Inside the experimental cell (Fig. 1), two electrodes were situated at a distance that could be varied from 17 to 35 mm. The lower electrode was grounded through a sensitive electrometer, and the upper electrode was at a potential of 0 to 2500 V of either positive or negative polarity. A planar ^{252}Cf source of ionizing particles with an intensity of 10^5 fission/s was placed at the lower electrode. Along with fission fragments, the source emitted α-particles. The source diameter was 7 mm. The solid angle within which the ionizing particles were emitted was close to 2π.

Dust grains were injected into the chamber through a metal grid serving as the bottom of a container placed

1063-780X/01/2701-0036$21.00 © 2001 MAIK "Nauka/Interperiodica"

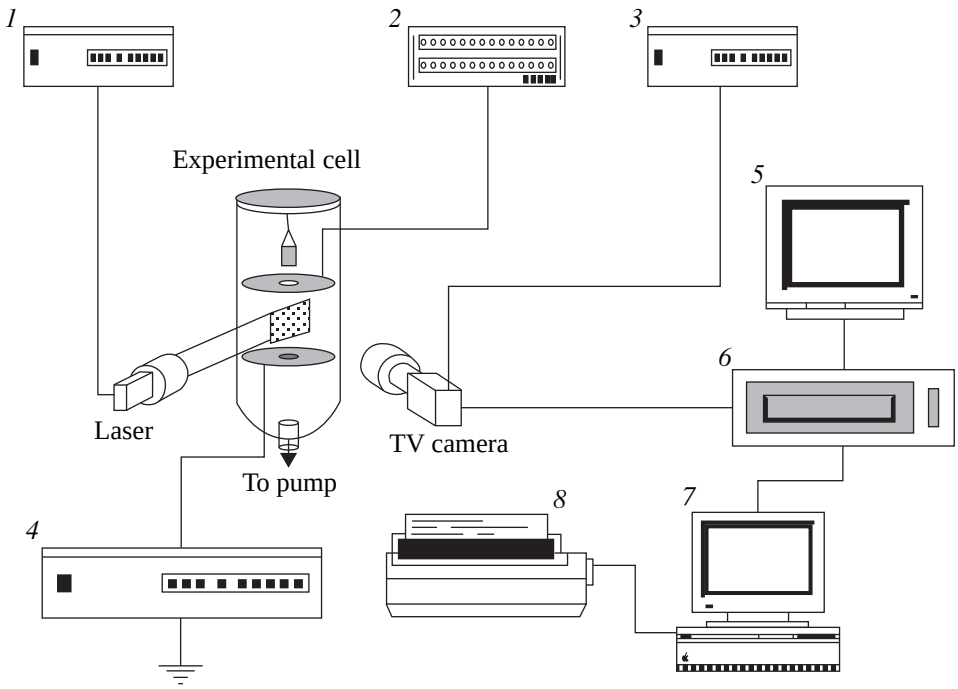

Fig. 1. Schematic of the experimental setup: (*1*, *3*), power supply units, (*2*) high-voltage power supply, (*4*) V7-30 electrometer, (*5*) Panasonic TV set, (*6*) Panasonic VCR, (*7*) computer with videocapture, and (*8*) printer.

behind the aperture in the upper electrode; they could also be injected with a gas jet. The container was shaken with the help of a vibrator. For the visual observation of the grains, we used a diode laser with a cylindrical lens producing a focused light beam with the thickness and width of the waist in the center of the ionization chamber equal to 150 μm and 30 mm, respectively. The light scattered by grains was recorded by a CCD-camera; its output signal was shown on a TV screen and could be recorded on videotape or on computer in order to process individual frames. The electron and ion densities in the nuclear-track plasma were deduced from the value of the ionization current between the electrodes.

3. EXPERIMENTAL RESULTS

We studied the behavior of spherical monodisperse melamineformaldehyde grains 1.87 and 4.82 μm in diameter and polydisperse CeO_2 grains with a mean diameter of 1 μm. Experiments were carried out in neon and argon at pressures of 0.25×10^5, 0.5×10^5, 0.75×10^5, and 1×10^5 Pa. When the upper electrode was at a positive potential, we observed the formation of conical structures of CeO_2 grains near the electrode aperture (Fig. 2) after the grains were injected into the chamber with a gas jet. In some cases, we observed linear structures (Fig. 3). The conical structures were observed both in neon and argon. The structures were situated near the axis of the electrode system and their cross size in the upper part was about 5 mm. As the electric field levitating the dust grains decreased, the dusty structure, gradually shifting toward the lower electrode, took the shape of a drop (Fig. 4). Unfortunately, the spread in the sizes of CeO_2 grains presents a severe problem in processing the experimental results. In experiments with melamineformaldehyde grains with a mass density of 1.5 g/cm^3 and diameter of 1.87 ± 0.13 μm, the grains were injected either from a container or with a gas jet. Conical structures were also observed (Fig. 5). Figure 6 shows the results of calculations of the pair distribution function [8] of melamineformaldehyde grains. The pair distribution function has a maximum when the distance between grains is 130 ± 30 μm. The charges of levitating grains observed in the experiments were estimated as 300 electron charges. For T_p = 300 K and an intergrain distance of 130 μm, the coupling parameter Γ characterizing the degree to which the plasma is nonideal is equal to 40, which results in the ordering of dust grains.

As is known, the electron temperature depends almost linearly on the reduced field *E*/*p*. In a quasineutral plasma with the electron and ion diffusivities D_- and D_+ and electron and ion temperatures T_- and T_+, the mean equilibrium grain charge $\langle Q \rangle$ is equal to [9]

$$\langle Q \rangle = -\frac{R_p k_B T_-}{e} \ln\left(1 + \frac{D_- T_+}{D_+ T_-}\right), \quad (1)$$

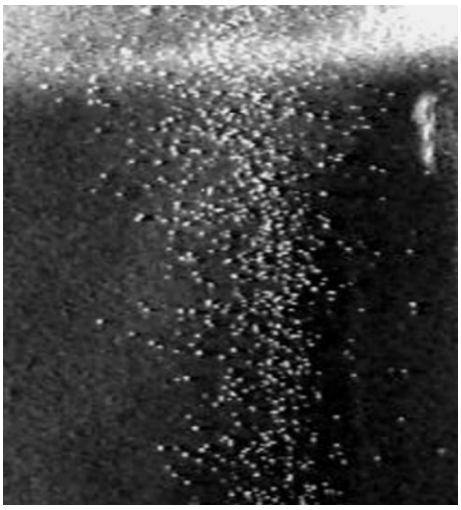

Fig. 2. General view of the structure of polydisperse CeO_2 grains. The Ne pressure is 0.25×10^5 Pa, the voltage between the electrodes is 80 V, and the distance between the electrodes is 17 mm. The flares from the glass walls and the electrode are also seen. The actual dimensions of the fragment are 3.5×4 mm.

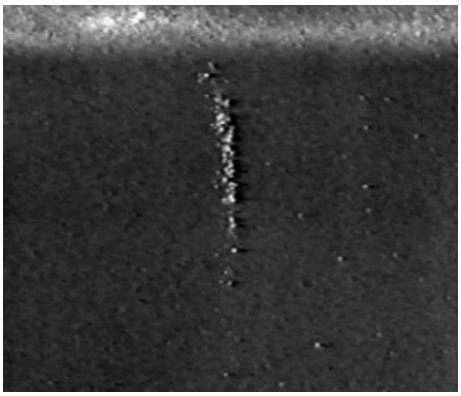

Fig. 3. Linear structure formed of CeO_2 grains in neon at a pressure of 0.5×10^5 Pa. The voltage between the electrodes is 805 V, and the interelectrode distance is 17 mm. The actual dimensions of the fragment are 7×8 mm.

where k_B is the Boltzmann constant and R_p is the grain radius. The charge $\langle Q \rangle$ depends strongly on R_p and T_-.

The equilibrium condition for spherical grains reduces to

$$\langle Q \rangle E = mg = \frac{4}{3}\pi\rho R_p^3, \tag{2}$$

where m is the grain mass and ρ is the grain material mass density (7.3 g/cm^3 for cerium oxide). For intermediate values of the electric field, the typical value of the grain charge calculated from relation (2) lies in the range from 200 to 400 electron charges. An additional spread in the calculated charge values is caused by the field inhomogeneity.

4. NUCLEAR-TRACK PLASMA WITH DUST GRAINS

One fission fragment produces several millions of electron–ion pairs in the track, whereas one α-particle produces up to several hundreds of thousands of pairs. For several nanoseconds after the passage of an ionizing particle, the track strongly broadens, the electron density decreases by one order of magnitude, and the quasineutrality condition is violated. In an external electric field, in a time of several tens of nanoseconds, the plasma bunch transforms into drift flows of electrons and ions, which affect the grains that fall into the nuclear-track plasma. Since the masses and characteristic energies of electrons and ions differ substantially, the electron flow arriving at the grain significantly exceeds the ion flow and the grain is negatively charged. In most cases, the energy of nuclear-reaction particles is high enough so that they can penetrate through a grain with radius of several microns. As a result of secondary electron emission, the grain charge can change sharply not only in magnitude, but also in sign, because the secondary emission coefficient attains several hundreds of electrons per fission fragment. Hence, the grain charge is governed by complicated physical processes with characteristic times of several nanoseconds to several tens of nanoseconds, which allows us to use constant values of the mean grain charge for characteristic experimental times on the order of several tens to several hundreds of milliseconds.

In order to simplify the modeling, the dependence of the energy of an ionizing particle on the distance that it had covered was approximated by the following formulas:

$$E(r) = \begin{cases} E_0\left(1 - \dfrac{r}{R_f}\right)^{\lambda}, & r < R_f \\ 0, & r \geq R_f \end{cases} \tag{3}$$

for fission fragments,

$$E(r) = \begin{cases} E_1\left(1 - \dfrac{r}{2R_\alpha} - \dfrac{r^2}{2R_\alpha^2}\right)^{\delta}, & r < R_\alpha \\ 0, & r \geq R_\alpha \end{cases} \tag{4}$$

for α-particles,

where E_0 and E_1 are the initial particle energies, r is the distance from the ionizing source, R_f is the full range of the fission fragment in a gas, R_α is the full range of an α-particle in a gas, and λ and δ are the approximation parameters. For neon at a pressure of 10^5 Pa, we have

R_f = 4 cm, R_α = 8 cm, λ = 1.7, and δ = 1.1; for argon, we have R_f = 3 cm, R_α = 6 cm, λ =1.6, and δ = 1.2. The full range was calculated by analytical formulas from [10, 11].

The number of electron–ion pairs produced per second in a unit volume of a charged-particle track at a distance r from the point source can be written in the form

$$W(r) = \sum_i \frac{I_i}{2\pi r^2 \varepsilon_i}\left|\frac{dE_i}{dr}\right|, \quad (5)$$

where dE_i/dr is the specific energy loss, ε_i is the energy cost of the production of one electron–ion pair (for gases, $\varepsilon \sim 30$ eV), and I_i is the intensity of emission of the ith nuclear-particle species. Note that the ^{252}Cf source emits α-particles and fission fragments in the ratio 32 : 2 and only one-half of the total number of particles fall into the volume under study, while the other particles are lost in the substrate.

In this paper, an attempt to describe the phenomenon of dust-grain levitation in a nuclear-track plasma is made for the first time; thus, the theoretical approach used does not claim to completely describe the behavior of grains under our experimental conditions. The prime objective of this paper is to choose an appropriate model for describing the most typical features of the behavior of dust grains in a plasma and reveal the physical factors forming the potential well in which dust grains levitate. Therefore, for numerical modeling, we should choose experimental conditions under which stable steady-state structures were observed. From this standpoint, the neon pressure range from 2.5×10^4 to 7.5×10^4 Pa and the structures shown in Figs. 2–5 are the most appropriate. The levitation of monodisperse grains was observed only in the central region of the device. To investigate the levitation and the interaction between dust grains, it is necessary to determine the mechanism responsible for charging these grains and clarify the character of the forces acting on them. In the present-day literature, several physical processes have been discussed that affect both the interaction between the dust grains and the balance between the gravity and electric forces acting on the levitating grains. To determine the electric forces acting on a grain, it is necessary to solve Poisson's equation taking into account the intensity of the generation of electrons and ions by a radioactive source; their diffusion; and the location of dust grains whose charge, in turn, depends on the local floating potential. It is unlikely that this problem can be solved self-consistently; consequently, it is convenient to separate out the force caused by the interaction between grains and regard the plasma as a background. Since the electron and ion plasma densities are several orders of magnitude higher than the grain number density, the interaction between the plasma and dust grains can be modeled by introducing an effective potential for the interaction between grains. This effective potential can be calculated by averaging over the positions of electrons and ions [2]. As a result, the subsystem of dust grains turns out to be unclosed and can exchange the charge and energy with the plasma.

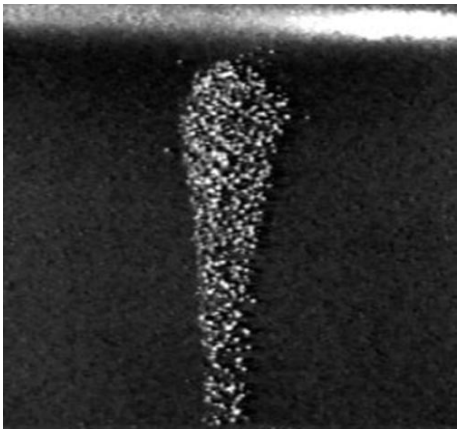

Fig. 4. Structure formed of polydisperse CeO_2 grains with a mean diameter of 1 μm in neon at a pressure of 0.825×10^5 Pa. The voltage between the electrodes is 195 V, and the interelectrode distance is 17 mm. The actual dimensions of the fragment are 7×8 mm.

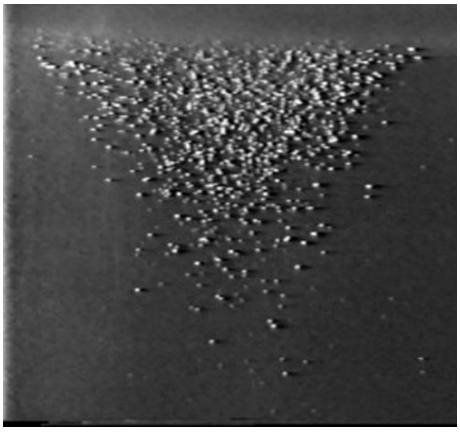

Fig. 5. Structure formed of monodisperse melamineformaldehyde grains with a mean diameter of 1.87 μm in neon at a pressure of 0.5×10^5 Pa. The voltage between the electrodes is 162 V, and the interelectrode distance is 30 mm. The actual dimensions of the fragment are 9.5×10 mm.

Along with the partial screening of the dust-grain charge by plasma electrons and ions strongly interacting with grains, of significant importance is the fact that regions with higher densities of free ions appear in the plasma because of the focusing action of a large negative grain charge on the drift ion current. It was shown in [12] that the equivalent positive charge can reach

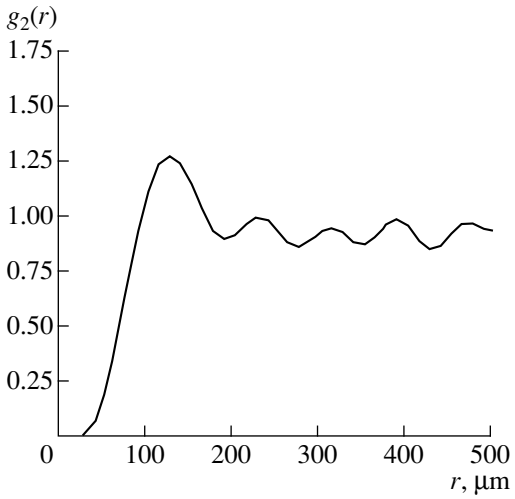

Fig. 6. Pair distribution function for the central region of the structure shown in Fig. 4.

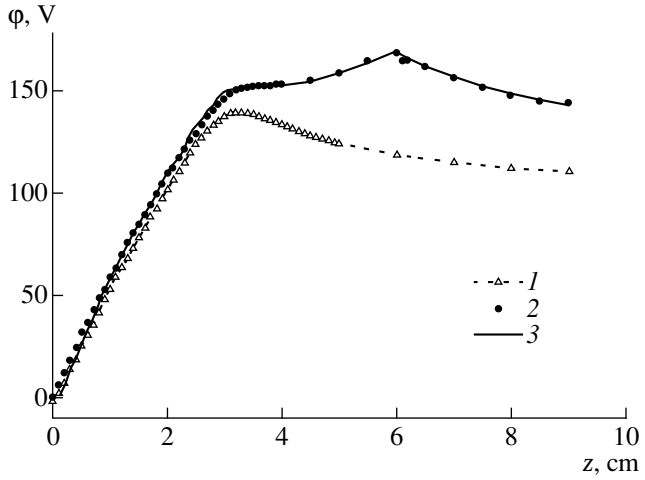

Fig. 7. The measured profiles of the electric potential along the cell axis in (*1*) the disk–ring and (*2*) disk–ring–disk configurations; curve *3* shows the results of calculations.

one-third of the dust-grain charge and its distance from the grain *d* is shorter than or on the order of the Debye radius. This anisotropic polarization of the background plasma can influence many processes. For example, the polarization of a plasma containing dust grains can lead to the trapping of other dust grains if their mean kinetic energy is not too high. It is the interaction anisotropy that may be responsible for ordering the grains into crystal-like three-dimensional and linear structures [1, 2].

The plasma screening of dust grains, the influence of the electron and ion flows, and recombination on the grain surface were considered, e.g., in [13], where it was shown that, at short distances, the pair interaction potential is negligibly small due to Debye screening and, at distances on the order of several radii, approaches the asymptote inversely proportional to the square of the distance between the grains.

The effective potential of the interaction between two grains $U(r_1, r_2)$ takes into account the spatial dependence of the grain charge on the floating potential and includes both the terms describing the screening of dust grains by plasma electrons and ions and the terms related to the contribution from the anisotropic interaction between dust grains. The form of the potential $U(r_1, r_2)$ approximating the results of numerical simulations [12–16] is given in [2] and, thus, is omitted in this paper.

5. ELECTROSTATIC WELL

The levitation of dust grains trapped in an electrostatic well is possible if the grain weight is compensated by the electrostatic force, which acts on both the negatively charged grain and the equivalent positive charge of an ion cloud accompanying this grain. The electrostatic field is determined by both the volume processes occurring in the plasma and the processes of recombination and absorption of charged particles on the wall. In this experiment, the electrostatic well was produced by the electric field created by the negative surface charge on the wall of the experimental device, the electric field of the electrodes, and the steady-state positive space charge arising in the plasma near the radioactive source due to the higher mobility of electrons compared to that of ions. For numerical simulations of charged-grain structures in an electrostatic well, it is necessary to have convenient analytical expressions for the well potential that will correctly reflect its physical nature.

The electrostatic field produced by the wall charge resulted in the grains being concentrated near the cell axis. The electric field near the axis was modeled in an electrolytic bath by a set of electrodes including a grounded disk, a hollow disk, and a second disk. The second disk modeled the upper flange situated on the end of a glass bulb (Fig. 1). Since, in experiments with dust grains, the upper flange and the hollow electrode were at the same potential, the corresponding model electrodes were connected by a conductor. The measurements were also carried out in the absence of the second disk. The results of modeling are shown in Fig. 7. In the same figure, we present the results from calculations of the field potential $\varphi_{el}(z)$ along the *z*-axis by the formula

$$\varphi_{el}(z) = A\varphi_d(a, z) + B\varphi_r(a, b - z) + C\varphi_d(a, 2b - z) + D, \quad (6)$$

where the indices *d* and *r* stand for the disk and ring potentials; *a* is the disk radius (equal to the ring radius); and *b* is the distance between the disk and the ring, the second disk being situated at double the distance from

the lower disk. The disk and ring potentials on the axis are expressed by analytical formulas [17]. The factors *A*, *B*, *C*, and *D* are chosen so as to obtain the voltage applied to the electrodes in the experiment and reproduce the experimental data when varying the coordinate *z*. The sharp maximum (both in the experiment and calculations) corresponds to the potential of the upper disk (the data represented in Fig. 7 refer to a specific experiment with dust grains in which the voltage was equal to 162 V). The larger values of *z* correspond to the points at the axis that lie beyond the upper disk. It is seen from the figure that, for the set of electrodes consisting of only a disk and a ring, the electric field differs strongly from the experimental one; hence, it is necessary to take into account the field created by the upper flange.

Figure 8 shows the axial electric field calculated from the data in Fig. 7. It is seen that the field near the axis decreases and almost vanishes above the ring. In the region where the conical structure is observed (between 2 and 3 cm from the lower disk), both the field and the ratio *E*/*p* affecting the value of the grain charge decreases almost two times. Expression (6) was used in numerical simulations of the levitation of dust grains near the cell axis. The radial dependence of the electric field in this region was calculated by the formula [18]

$$\varphi_{el}(z, r) = \varphi_{el}(z) - \frac{1}{4}\frac{d^2\varphi_{el}(z)}{dz^2}r^2,$$

where r is the distance from the axis and $\varphi(z)$ is given by expression (6). The electric field far from the axis was calculated by formulas from [17, 19].

The region near the radioactive source where plasma quasineutrality is violated can be modeled by a positively charged object whose shape is similar to a weakly elongated ellipsoid of revolution and whose space charge is maximum near the source. The problem of determining the three-dimensional potential field created by the conducting charged ellipsoid of revolution can be solved in elementary functions [20].

Hence, the electric filed of the electrostatic well is the sum of the electric field produced by the negative surface charge on the wall of the experimental device, the electric field of the electrodes, and the steady-state positive space charge arising near the radioactive source.

6. NUMERICAL SIMULATIONS

A plasma with a disperse phase was simulated numerically by the standard Monte Carlo method [21]. When simulating by this method, an ensemble of a finite number N of particles in a cell of size L is usually considered. It is convenient to measure the cell size L in units of the Debye radius r_D, which was chosen to be equal to 200 μm in modeling the experiment. In our calculations, taking into account the operating speed of available computers and a reasonable computation

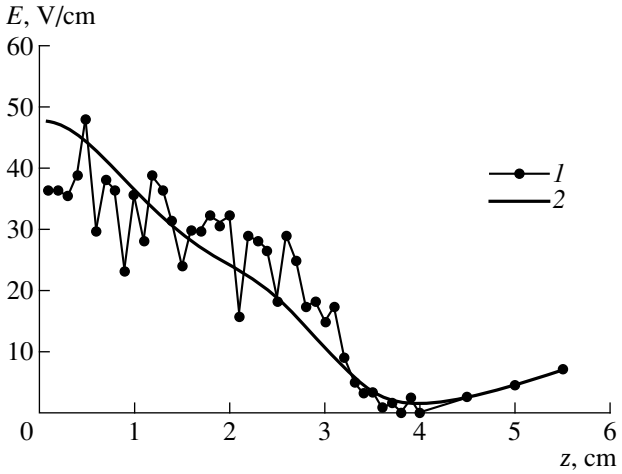

Fig. 8. The profile of the electric field along the cell axis: (*1*) experiment and (*2*) calculation.

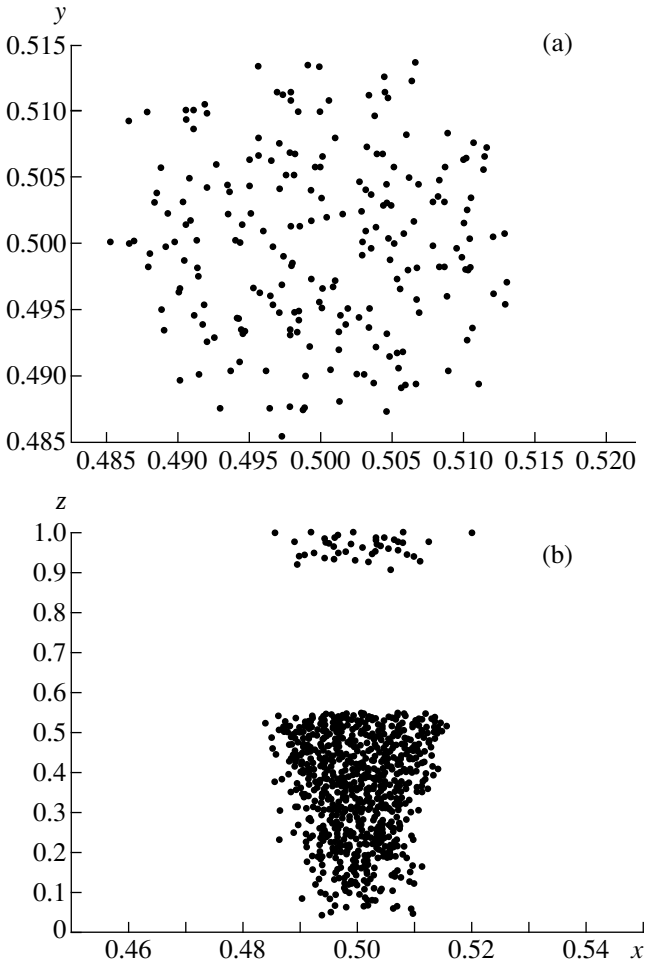

Fig. 9. Calculated (a) horizontal and (b) vertical cross sections of dusty structures.

time, we restricted ourselves to $N = 1000–2000$. The size of the Monte Carlo cell containing the characteristic grain structure was chosen to be equal to $L = 150r_D \approx 3$ cm, which approximately corresponded to the experimental conditions. Note, however, that the decrease in the cell dimensions and the number of dust grains in simulations as compared to the experiment made it possible to substantially reduce the calculation resources; in our case, the characteristic computation time was about 10 h.

Figure 9 shows the horizontal and axial vertical cross sections of the calculated dusty structure. The horizontal cross section is given for a height of $0.45L$. The coordinate along the tube diameter is plotted on the horizontal axis; the point $0.5L$ corresponds to the axis, and an interval of 0.1 corresponds to $\sim 15r_D$ (or 3 mm).

Let us consider the results of Monte Carlo simulations. It is important that the radial component of the electric field inside the cell increases as the distance from the radiation source decreases. Indeed, the stronger radial field in the lower part of the cell leads to a stronger compression of the cloud of grains that are repulsed from each other due to the interaction between them. In addition, as follows from the data obtained, when the grains are displaced randomly toward or away from the source, they return to the region where the levitation conditions are satisfied, i.e., where the gravity force is balanced by the electrostatic force. Therefore, the equilibrium in the levitation region is stable. Simulations show that the structure only slightly depends on the pressure, which agrees with the experiment.

As was already noted in [2], the physical reason for the appearance of linear dusty structures is the focusing action of negatively charged dust grains on the ion current, which leads to the formation of clouds with a higher ion density between the grains and gives rise to the dipole interaction between them. In a nuclear-track plasma, the value of the dipole moment of the dust grain–screening cloud system is substantially lower than that in a gas-discharge plasma; consequently, linear ordered structures do not form in a nuclear-track plasma. However, the mean value of the repulsive force between dust grains is high enough for the near order to occur.

The shape of a cloud of levitating dust grains depends on the field of the electrostatic well, the electric field of the electrodes, and the gravity force. However, the physical situation is significantly complicated by the dependence of the grain charge on spatial coordinates and, as a consequence, by the appearance of a non-Coulomb addition to the Coulomb force, as was discussed in [2]. The non-Coulomb addition is opposite in direction to the gradient of the grain-charge magnitude and displaces the dust-grain cloud into the region of the electrostatic well where the grain charges and, consequently, the repulsion energy are minimum. In our experimental device, the cloud of levitating dust grains resembles a "jigger."

7. CONCLUSION

Stable dusty structures in a nuclear-track plasma in neon and argon in an external electric field have been obtained experimentally, and a theoretical model of this plasma has been developed. With a great number of injected grains, we observed stable liquidlike structures, whereas with a smaller number of grains, we observed linear structures of different configurations. The physical mechanisms governing the levitation of 1.87-μm melamineformaldehyde grains and the formation of their ordered structures in a nuclear-track neon plasma at a pressure of 2.5×10^4 Pa are investigated both experimentally and theoretically. The ordered structures arising in a dusty plasma are studied numerically by the Monte Carlo method. The calculations give a deeper insight into the formation of dusty structures under the experimental conditions. The results of calculations agree qualitatively with experimental data.

ACKNOWLEDGMENTS

We thank A.I. Chusov for his help in preparing the experimental device and his assistance in experiments. This work was supported by the Russian Foundation for Basic Research, project nos. 97-02-16572 and 00-02-17620.

REFERENCES

1. V. E. Fortov, A. P. Nefedov, V. M. Torchinskiĭ, *et al.*, Pis'ma Zh. Éksp. Teor. Fiz. **64**, 86 (1996) [JETP Lett. **64**, 92 (1996)].
2. O. M. Belotserkovskiĭ, I. E. Zakharov, A. P. Nefedov, *et al.*, Zh. Éksp. Teor. Fiz. **115**, 819 (1999) [JETP **88**, 449 (1999)].
3. V. E. Fortov, V. S. Filinov, A. P. Nefedov, *et al.*, Zh. Éksp. Teor. Fiz. **111**, 889 (1997) [JETP **84**, 489 (1997)].
4. Yu. V. Gerasimov, A. P. Nefedov, V. A. Sinel'shchikov, and V. E. Fortov, Pis'ma Zh. Tekh. Fiz. **24** (19), 62 (1998) [Tech. Phys. Lett. **24**, 774 (1998)].
5. V. E. Fortov, V. I. Vladimirov, L. V. Deputatova, *et al.*, Dokl. Akad. Nauk **366**, 184 (1999) [Dokl. Phys. **44**, 279 (1999)].
6. V. E. Fortov, A. P. Nefedov, V. V. Vladimirov, *et al.*, Phys. Lett. A **258**, 305 (1999).
7. A. P. Budnik, Yu. V. Sokolov, and A. S. Vakulovskiy, Hyperfine Interact. **88**, 185 (1994).
8. F. M. Kuni, *Statistical Physics and Thermodynamics* (Nauka, Moscow, 1981).
9. B. M. Smirnov, *Aerosols in Gases and Plasmas* (IVTAN, Moscow, 1990).
10. J. Lindhard, V. Nielsen, M. Scharff, and P. V. Thomsen, Mat. Fys. Medd. K. Dan. Vidensk. Selsk. **33** (10) (1963).
11. H. Bethe, Ann. Phys. (Leipzig) **5**, 325 (1930).
12. V. A. Schweigert, I. V. Schweigert, A. Melzer, *et al.*, Phys. Rev. E **54**, 4155 (1996).
13. J. E. Daugherty, M. D. Kilgore, R. K. Porteous, and D. B. Graves, J. Appl. Phys. **72**, 3934 (1992).

14. I. V. Schweigert, V. A. Schweigert, V. M. Bedanov, *et al.*, Zh. Éksp. Teor. Fiz. **114**, 1672 (1998) [JETP **87**, 905 (1998)].
15. F. Melandso and J. Goree, Phys. Rev. E **52**, 5312 (1995).
16. F. Melandso and J. Goree, J. Vac. Sci. Technol. A **14**, 511 (1996).
17. W. R. Smythe, *Static and Dynamic Electricity* (McGraw-Hill, New York, 1950; Inostrannaya Literatura, Moscow, 1954).
18. A. A. Zhigarev and G. G. Shamaeva, *Electron-Beam and Photoelectronic Devices* (Vysshaya Shkola, Moscow, 1982).
19. V. V. Batygin and I. N. Toptygin, *Problems in Electrodynamics* (Fizmatgiz, Moscow, 1962; Academic, London, 1964).
20. L. D. Landau and E. M. Lifshitz, *Electrodynamics of Continuous Media* (Nauka, Moscow, 1982; Pergamon, New York, 1984).
21. V. M. Zamalin, G. É. Norman, and V. S. Filinov, *Monte Carlo Method in Statistical Thermodynamics* (Nauka, Moscow, 1977).

Translated by N.F. Larionova

Plasma Physics Reports, Vol. 27, No. 1, 2001, pp. 44–55. Translated from Fizika Plazmy, Vol. 27, No. 1, 2001, pp. 45–57.

NONIDEAL PLASMA

Comparative Analysis of the Theoretical Models of a Hot Dense Plasma and the Density Functional Theory

N. Yu. Orlov and V. E. Fortov

Institute for High Energy Densities, Associated Institute for High Temperatures, Russian Academy of Sciences, Izhorskaya ul. 13/19, Moscow, 127412 Russia

Received June 21, 2000

Abstract—A general set of self-consistent field equations that describes the state of the whole ensemble of atoms and ions in a hot dense plasma is derived using the density functional theory. The set of equations is used to obtain equations of the Thomas–Fermi model, the Hartree–Fock–Slater model, the detail configuration account method, and the ion model. This approach makes it possible to identify the physical approximations underlying the theoretical models and to analyze their applicability ranges. Some of the results obtained from the Hartree–Fock–Slater model, the detail configuration account method, and the ion model are compared with the experimental data. *© 2001 MAIK "Nauka/Interperiodica".*

1. INTRODUCTION

In order to solve important scientific and technological problems in controlled thermonuclear fusion research, it is necessary to know the physical parameters of plasmas at ultrahigh temperatures and at densities close to the density of solids. Experiments aimed at achieving such extremely high plasma temperatures and densities are very expensive. The important plasma parameters include thermal conductivity, light-absorption spectral coefficients, and Planck or Rosseland mean free paths. These characteristics can be calculated using the following theoretical models of a hot dense plasma, which have been developed over the last fifty years: the Thomas–Fermi (TF) model [1], the Hartree–Fock–Slater (HFS) model [2, 3], the detail configuration account (DCA) method [4], and the ion model [5]. The calculation accuracy is governed by the physical approximations that underlie a particular model. Clearly, a theoretical model ensures reliable results only in the temperature and density ranges in which the physical assumptions made in deriving the relevant model equations are valid.

The model equations are usually derived by constructing approximate analytic approaches that increasingly satisfy more exact formulations based on fairly general physical principles. However, to derive equations for problems that are very difficult to analyze theoretically (such as the problem of describing the optical properties of a plasma) requires physical assumptions that do not follow directly from the basic physical principles described by exact formulas. Of course, the physical assumptions involved can be validated indirectly by comparing the theoretical results with the experimental data, but doing so is fairly complicated because of the large number of assumptions that are to be verified simultaneously. A discussion of the underlying physical assumptions seems to be of no less importance than performing formal manipulations with equations.

Hence, in order to determine the applicability ranges of different theoretical models, it is necessary to examine each step in the derivation of the corresponding basic equations, formulate the problem in the most precise way, and analyze the underlying physical assumptions and the equations themselves. It is also necessary to compare the theoretical results with the experimental data.

The applicability ranges are difficult to establish, because the above four models were formulated based on different initial assumptions and the basic sets of equations were derived in different ways. To some extent, this circumstance complicates a comparison between the physical approximations and, accordingly, between the corresponding applicability ranges. In this paper, we apply one of the most recent methods—the density functional theory—in order to develop a unified approach to analyzing both the basic equations used in particular theoretical models and the underlying physical assumptions. We also compare some of the theoretical results obtained from the HFS model, the DCA method, and the ion model with the experimental data.

2. SET OF SELF-CONSISTENT FIELD EQUATIONS FOR A STATISTICAL ENSEMBLE OF PLASMA ATOMS AND IONS

In the density functional theory [6, 7], it is shown that the grand thermodynamic potential Ω, which is defined as

$$\Omega = \mathrm{Sp}\{\hat{W}(\hat{H} - \mu\hat{N} + \Theta\ln\hat{W})\}, \qquad (1)$$

1063-780X/01/2701-0044$21.00

and is regarded as a functional of the electron density, reaches a maximum in a state of thermodynamic equilibrium. Here, $\hat{H}$ is the Hamiltonian of the system, Θ is the temperature of matter, μ is the chemical potential, $\hat{N}$ is the particle number operator, and $\hat{W}$ is the density matrix. In equilibrium, the density matrix has the form

$$\hat{W} = \exp\left[-\frac{\hat{H}-\mu\hat{N}}{\Theta}\right]/\mathrm{Sp}\exp\left[-\frac{\hat{H}-\mu\hat{N}}{\Theta}\right]. \quad (2)$$

We consider a system of interacting atoms and ions in the ground and excited states and adopt spherical atomic cells of radius r_0 (with a nucleus of charge Z at the center) as subsystems. The radius of the cell can be defined as

$$r_0 = \left[\frac{3}{4\pi N_A}\right]^{1/3}\frac{1}{a_0}\left[\frac{A}{\rho}\right]^{1/3}, \quad (3)$$

where A [g] is the atomic weight, ρ [g/cm^3] is the plasma density, $a_0 = 5.292 \times 10^{-9}$ cm, and $N_A = 6.02 \times 10^{23}$ is Avogadro's number. Here and below, we use atomic units. The subsystems differ from each other by the sets of occupation numbers of the bound (discrete) electronic states. Each subsystem also contains unbound (continuum) electrons. The states of subsystems are regarded as the states of plasma atoms and ions. It is assumed that each subsystem, defined by specifying the set of occupation numbers of the bound and unbound electronic states, can be described by a wave function in terms of the occupation numbers [8]:

$$|\Phi_A\rangle = |n_1^A, n_2^A, \ldots, n_k^A, \ldots\rangle, \quad (4)$$

where n_k^A is the number of electrons in the kth quantum state in subsystem A. We also assume that the interaction of subsystem A with other plasma subsystems can be approximately taken into account by introducing the effective potential $V_{\mathrm{ext}}^A(r)$. This approach is referred to as the local density approximation [6]. In [6, 7], it was proved that, in a multicomponent plasma, the set of the effective potentials is uniquely determined by the set of exact electron densities, in which case we have

$$\hat{H} = \sum_A \hat{H}_A, \quad (5)$$

$$\hat{H}_A = \sum_i\left[-\frac{1}{2}\Delta_i - \frac{Z}{r} + V_{\mathrm{ext}}^A(\mathbf{r})\right] + \sum_{i<j}\nu(\mathbf{r}_i, \mathbf{r}_j), \quad (6)$$

where the terms $\nu(\mathbf{r}_i, \mathbf{r}_j)$ describe the interaction between the electrons of subsystem A. It is convenient to represent the Hamiltonian $\hat{H}_A$ as

$$\hat{H}_A = \sum_i \hat{T}_i + \sum_{i<j}\nu(\mathbf{r}_i, \mathbf{r}_j), \quad (7)$$

where

$$\hat{T}_i = -\frac{1}{2}\Delta_i - \frac{Z}{r_i} + V_{\mathrm{ext}}^A(\mathbf{r}_i). \quad (8)$$

In the second quantization description [8], the operator $\hat{H}_A$ has the form

$$\hat{H}_A = \sum_{m,n}\langle m|\hat{T}|n\rangle a_m^+ a_n + \frac{1}{2}\sum_{k_1,k_2,k_3,k_4}\langle k_1k_2|\nu|k_4k_3\rangle a_{k_1}^+ a_{k_2}^+ a_{k_3} a_{k_4}. \quad (9)$$

Here, we use Dirac's notation

$$\langle i|\hat{T}|j\rangle = \int \Psi_i^*(\mathbf{r})\hat{T}\Psi_j(\mathbf{r})d\mathbf{r}, \quad (10)$$

$$\langle ij|\nu|lk\rangle = \iint \Psi_i^*(\mathbf{r}_1)\Psi_j^*(\mathbf{r}_2)\nu\Psi_l(\mathbf{r}_1)\Psi_k(\mathbf{r}_2)d\mathbf{r}_1 d\mathbf{r}_2, \quad (11)$$

where $\Psi_\alpha(\mathbf{r})$ is the wave function of an electron in the αth quantum state. Under the assumption that the occupation numbers n_i^A in expression (4) refer to the bound states at $i \le K$ and to the unbound states at $i > K$, formula (1) takes the form

$$\Omega = \sum_A W_A E_A - \mu\sum_A W_A N_A + \Theta\sum_A W_A \ln W_A, \quad (12)$$

where

$$E_A = \langle\Phi_A|\hat{H}_A|\Phi_A\rangle. \quad (13)$$

Expression (13) can be represented as

$$\langle\Phi_A|\hat{H}_A|\Phi_A\rangle = I_0 + I_1 + I_2, \quad (14)$$

where

$$I_0 = \langle\Phi_A|\hat{T}|\Phi_A\rangle = \sum_{m\le K}\langle m|\hat{T}|m\rangle a_m^+ a_m + \sum_{m>K}\langle m|\hat{T}|m\rangle a_m^+ a_m. \quad (15)$$

The terms I_1 and I_2 can be found by substituting the second term in operator (9) into expression (13). The term I_1 corresponds to the case with $k_1 = k_3$ and $k_2 = k_4$, and the term I_2 corresponds to the case with $k_1 = k_4$ and $k_2 = k_3$. Then, we have

$$I_2 = \frac{1}{2}\sum_{k_1,k_2}\langle\Phi_A|a_{k_1}^+ a_{k_2}^+ a_{k_2} a_{k_1}|\Phi_A\rangle\langle k_1k_2|\nu|k_1k_2\rangle = I_{21} + I_{22} + I_{23} + I_{24}, \quad (16)$$

$$I_{21} = \frac{1}{2}\sum_{k_1 \le K}\sum_{k_2 \le K} n_{k_1} n_{k_2} \langle k_1 k_2 | \nu | k_1 k_2 \rangle, \quad (17)$$

$$I_{22} = \frac{1}{2}\sum_{k_1 \le K}\sum_{k_2 > K} n_{k_1} n_{k_2} \langle k_1 k_2 | \nu | k_1 k_2 \rangle, \quad (18)$$

$$I_{23} = \frac{1}{2}\sum_{k_1 > K}\sum_{k_2 \le K} n_{k_1} n_{k_2} \langle k_1 k_2 | \nu | k_1 k_2 \rangle, \quad (19)$$

$$I_{24} = \frac{1}{2}\sum_{k_1 > K}\sum_{k_2 > K} n_{k_1} n_{k_2} \langle k_1 k_2 | \nu | k_1 k_2 \rangle, \quad (20)$$

and, analogously,

$$I_1 = -\frac{1}{2}\sum_{k_1, k_2} \langle \Phi_A | a^+_{k_1} a_{k_1} a^+_{k_2} a_{k_2} | \Phi_A \rangle \langle k_1 k_2 | \nu | k_2 k_1 \rangle = I_{11} + I_{12} + I_{13} + I_{14}, \quad (21)$$

$$I_{11} = -\frac{1}{2}\sum_{k_1 \le K}\sum_{k_2 \le K} n_{k_1} n_{k_2} \langle k_1 k_2 | \nu | k_2 k_1 \rangle, \quad (22)$$

$$I_{12} = -\frac{1}{2}\sum_{k_1 \le K}\sum_{k_2 > K} n_{k_1} n_{k_2} \langle k_1 k_2 | \nu | k_2 k_1 \rangle, \quad (23)$$

$$I_{13} = -\frac{1}{2}\sum_{k_1 > K}\sum_{k_2 \le K} n_{k_1} n_{k_2} \langle k_1 k_2 | \nu | k_2 k_1 \rangle, \quad (24)$$

$$I_{14} = -\frac{1}{2}\sum_{k_1 > K}\sum_{k_2 > K} n_{k_1} n_{k_2} \langle k_1 k_2 | \nu | k_2 k_1 \rangle. \quad (25)$$

Here, the term I_2 refers to the so-called "direct" interaction and I_1 refers to the "exchange" interaction. The term I_{11} corresponds to the exchange interaction between the bound electrons, the terms I_{12} and I_{13} describe the exchange interaction between the bound and unbound electrons, and the term I_{14} accounts exclusively for the unbound states. Since the exchange interaction between the bound and unbound electrons is, as a rule, very weak, the terms I_{12} and I_{13} are usually neglected. If the unbound states are described in the quasiclassical approximation, then the term I_{14} is set to zero.

Let us determine additional conditions under which the functional in formula (12) should be minimized. First, we rewrite formula (12) as

$$\Omega = \sum_{A^c}\sum_{f} \{ W_A(n^c_A, n^f_A) E_A - \mu W_A(n^c_A, n^f_A) N_A + \Theta W_A(n^c_A, n^f_A) \ln W_A(n^c_A, n^f_A), \quad (26)$$

with summations over the states of the "core" of subsystem A^c and over the unbound states. The "core" states are defined by the sets $\{n^c_A\}$ of occupation numbers of the bound states, in which case the number of electrons in the kth bound state of subsystem A is denoted by n^c_{Ak}. The bound states are characterized by specifying the electron density $n^f_A(\mathbf{r}, \mathbf{p})$ in phase space (where $\mathbf{r}$ and $\mathbf{p}$ are the coordinate and momentum of an electron). Additionally, the wave functions of the bound electrons should be orthonormal:

$$\int \Psi^*_i(\mathbf{r}) \Psi_j(\mathbf{r}) d\mathbf{r} = \delta_{ij}, \quad (27)$$

where the superscript A in the wave functions is omitted for brevity. In order to use the method of Lagrange multipliers, we must supplement expression (26) with the term

$$\Omega_\lambda = \sum_{A^c}\sum_{i \le K}\sum_{j \le K} \lambda^A_{ij} \langle i \| j \rangle. \quad (28)$$

Since the system as a whole is electrically neutral,

$$\sum_A W_A N_A = Z, \quad (29)$$

we must supplement expression (26) with the term

$$\Omega_B = B\left[\sum_A W_A N_A - Z\right]. \quad (30)$$

To take into account this term, we can simply replace μ by $\mu - B$, because the variation of Z vanishes. And finally, we use the normalization condition

$$\sum_A W_A = 1, \quad (31)$$

which gives rise to the additional term

$$\Omega_R = R\left[\sum_A W_A - 1\right]. \quad (32)$$

Hence, we must search for the extremum of the functional

$$\Omega_t = \Omega + \Omega_\lambda + \Omega_R. \quad (33)$$

In the expression

$$\Omega + \Omega_R = \sum_{A^c}\sum_{f} [W_A(n^c_A, n^f_A)(E_A + R) - \mu W_A(n^c_A, n^f_A) N_A + \Theta W_A(n^c_A, n^f_A) \ln W_A(n^c_A, n^f_A)] \quad (34)$$

summation is implied over all sets $n_A^f(\mathbf{r}, \mathbf{p})$. Since the system contains a macroscopically large number of particles (in the case at hand, these are unbound electrons) and the number of their quantum states is also macroscopically large, the probability $W_A(n_A^c, n_A^f)$ is nearly zero except when $n_A^f(\mathbf{r}, \mathbf{p})$ is equal to its mean (equilibrium) value [9], in which case we obtain

$$\Omega + \Omega_R = \sum_{A^c} [W_A(n_A^c, \bar{n}_A^f)E_A - \mu W_A(n_A^c, \bar{n}_A^f)N_A + \Theta W_A(n_A^c, \bar{n}_A^f)\ln W_A(n_A^c, \bar{n}_A^f)]\Delta\Gamma_A^f, \quad (35)$$

where $\Delta\Gamma_A^f$ is the total number of unbound electronic states in subsystem A. This enables us to represent W_A as [10]

$$W_A(n_A^c, \bar{n}_A^f) = W_A^c(n_A^c)W_A^f(\bar{n}_A^f). \quad (36)$$

The normalization condition gives [11]

$$W_A^f(\bar{n}_A^f)\Delta\Gamma_A^f = 1, \quad (37)$$

so that we have

$$\Omega + \Omega_R = \sum_{A^c} [W_A^c E_A - \mu W_A^c N_A + \Theta W_A^c \ln W_A^c W_A^f(\bar{n}_A^f) + RW_A^c]. \quad (38)$$

Hence, the final expression for Ω_t has the form

$$\Omega_t = \sum_{A^c}\left\{[W_A^c E_A - \mu W_A^c N_A + \Theta W_A^c \ln W_A^c W_A^f(\bar{n}_A^f) + RW_A^c] + \sum_{i,j\le K}\lambda_{ij}^A\langle i \| j\rangle\right\}. \quad (39)$$

The set of self-consistent field equations describing the state of the statistical ensemble of interacting plasma atoms and ions can be derived from expression (39). Thus, varying Ω_t with respect to δW_A^c and taking into account normalization condition (31) yields the Gibbs distribution

$$W_A = Cg_A\exp\left\{-\frac{E_A - \mu N_A}{\Theta}\right\}, \quad (40)$$

where g_A is the statistical weight, μ is the chemical potential, E_A is the total energy, and N_A is the total number of particles in subsystem A. Varying Ω_t with respect to $\delta\Psi_i^{*A}$ leads to the Hartree–Fock equation for all unbound states of subsystem A:

$$\hat{T}_A\Psi_i(\mathbf{r}_1) + V_A(\mathbf{r}_1)\Psi_i(\mathbf{r}_1) - \sum_{j\le K} n_{Aj}^c\int\Psi_j^*(\mathbf{r}_2)\frac{1}{|\mathbf{r}_1 - \mathbf{r}_2|}\Psi_i(\mathbf{r}_2)d\mathbf{r}_2\Psi_j(\mathbf{r}_1) = \sum_j\lambda_{ij}^A\Psi_j(\mathbf{r}_1). \quad (41)$$

The set of one-electron wave functions $\Psi_\alpha(\mathbf{r})$ can be chosen so as to diagonalize the Hamiltonian operator [8], in which case Eq. (41) can be written as

$$T_A\Psi_i(\mathbf{r}_1) + V_A(\mathbf{r}_1)\Psi_i(\mathbf{r}_1) - \sum_{j\le K} n_{Aj}^c\int\Psi_j^*(\mathbf{r}_2)\frac{1}{|\mathbf{r}_1 - \mathbf{r}_2|}\Psi_i(\mathbf{r}_2)d\mathbf{r}_2\Psi_j(\mathbf{r}_1) = \varepsilon_{ii}^A\Psi_i(\mathbf{r}_1), \quad (42)$$

where

$$V_A(\mathbf{r}_1) = \int\frac{\rho_A(\mathbf{r}_2)}{|\mathbf{r}_1 - \mathbf{r}_2|}d\mathbf{r}_2, \quad (43)$$

$$\rho_A(\mathbf{r}) = \rho_A^c(\mathbf{r}) + \rho_A^f(\mathbf{r}), \quad (44)$$

$$\rho_A^c(\mathbf{r}) = \sum_{i\le K} n_{Ai}^c|\Psi_i(\mathbf{r})|^2, \quad (45)$$

$$\rho_A^f(\mathbf{r}) = \int\bar{n}_A^f(\mathbf{r}, \mathbf{p})\frac{2d\mathbf{p}}{(2\pi)^3}, \quad (46)$$

and the diagonal Lagrange multipliers ε_{ii}^A are the one-electron energy levels. For brevity, we omit the superscript A in the wave functions $\Psi_i(\mathbf{r})$.

Finally, we can vary Ω_t with respect to $\delta\bar{n}_A^f$, using formulas (17)–(25) and treating $\Delta\Gamma_A^f$ in the quasiclassical approximation,

$$\ln\Delta\Gamma_A^f = \int\left[\ln\frac{1}{1 - \bar{n}_A^f} - \bar{n}_A^f\ln\frac{\bar{n}_A^f}{1 - \bar{n}_A^f}\right]\frac{2d\mathbf{r}d\mathbf{p}}{(2\pi)^3} \quad (47)$$

to arrive at

$$\bar{n}_A^f(\mathbf{r}, \mathbf{p}) = \left\{\exp\left[\frac{1}{\Theta}\left(\frac{p^2}{2} - \frac{Z}{r} + V_A(\mathbf{r}) + V_{\text{ext}}^A(\mathbf{r}) - \mu\right)\right]\right\}^{-1}. \quad (48)$$

Let us summarize the physical assumptions made to derive the above set of equations.

(i) The exchange interaction between the bound and unbound electrons is neglected.

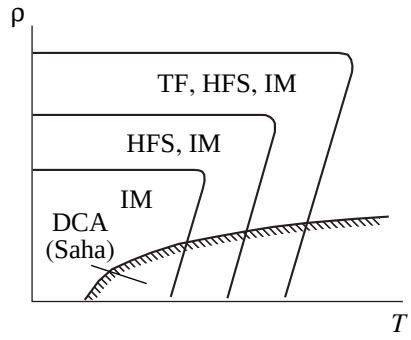

Fig. 1. Applicability ranges of different theoretical models in the variables T (plasma temperature) and ρ (plasma density).

(ii) The unbound states are described in the quasiclassical approximation.

(iii) The external interaction is taken into account in the local density approximation.

The basic equations of the TF, HFS, and ion models as well as the DCA method can be derived from the above set of equations by making additional physical assumptions. Figure 1 schematically shows the applicability ranges of different theoretical models in the "plasma temperature–plasma density" coordinates. Since the boundaries of the applicability ranges differ between different chemical elements, Fig. 1 is merely a qualitative illustration of the applicability of the physical models. If the plasma temperature and/or density extends out of the applicability range of the TF model in Fig. 1, then one must use the model of a homogeneous electron gas. However, the analysis of this model goes beyond the scope of our study.

3. THOMAS–FERMI MODEL

The TF model can be applied when the plasma temperature is very high, so that the plasma is almost completely ionized. The basic equations for the TF model can be derived from the set of equations presented in the previous section by assuming that the occupation numbers of the bound electronic states equal zero. Under this additional assumption, all subsystems A have the same structure: each subsystem contains a central core with charge Z and the unbound electrons, which move in the field of the core and interact with each other. Each of the plasma subsystems is affected by the remaining subsystems. The electron densities inside each spherical atomic cell of radius r_0 is described by formulas (46) and (48). If we assume that the electron density inside the cell depends only on r and is independent of the angular variables and if we neglect $V_{\text{ext}}^{A}(\mathbf{r})$ in comparison with $V_A(\mathbf{r})$, then we can expand the integrand in expression (43) in spherical functions [12] to obtain

$$V_A(r_1) = \frac{4\pi}{r_1}\int_0^{r_1} r_2^2 \rho_A(r_2)dr_2 + 4\pi\int_{r_1}^{r_0} r_2\rho_A(r_2)dr_2.$$

We can readily show that the function $U_A(\mathbf{r}) = Z/r - V_A(\mathbf{r})$ satisfies the equation

$$\frac{1}{r}\frac{d^2}{dr^2}[rU_A(r)] = 4\pi\rho_A(r).$$

We use expression (48), omit the index A in formulas, and introduce the notation

$$\rho(r) = \frac{(2\Theta)^{3/2}}{2\pi^2} I_{1/2}\left(\frac{U(r)+\mu}{\Theta}\right),$$

$$I_k(x) = \int \frac{y^k}{1+\exp(y-x)}dy,$$

to arrive at the TF equation

$$\frac{1}{r}\frac{d^2}{dr^2}[rU(r)] = \frac{2}{\pi}(2\Theta)^{3/2} I_{1/2}\left(\frac{U(r)+\mu}{\Theta}\right) \qquad (49)$$

supplemented with the boundary conditions

$$rU(r) = Z \quad \text{for} \quad r = 0,$$
$$\frac{dU}{dr} = 0 \quad \text{for} \quad r = r_0, \qquad (50)$$
$$U(r_0) = 0$$

and with the electroneutrality condition

$$4\pi\int_0^{r_0} \rho(r) r^2 dr = Z. \qquad (51)$$

Conditions (50) and (51) were discussed in detail by Nikiforov [13].

The TF equation was derived using the assumptions made in Section 2 and the following two additional assumptions:

(i) The occupation numbers of the bound electronic states equal zero.

(ii) The external interaction potential $V_{\text{ext}}^{A}(\mathbf{r})$ is low in comparison with $V_A(\mathbf{r})$.

4. HARTREE–FOCK–SLATER MODEL

The HFS model [2, 3] is based on the so-called "average-atom" (or "average-ion") approximation, in which an enormous number of plasma atoms and ions in the ground and excited states are modeled by a fictitious electron configuration where the occupation numbers of the bound electronic states are calculated from the Fermi–Dirac formula. In this approach, the occupation numbers may turn out to be noninteger. Another

important characteristic feature of the HFS model is that it approximately takes into account the exchange interaction through the introduction of an approximate formula for the effective exchange interaction potential.

Let us derive the HFS equations from the general equations given in Section 2. First, we derive a set of equations in the Hartree approximation. We ignore the exchange interaction in Eq. (42) and neglect $V_{\text{ext}}^{A}(\mathbf{r})$ in comparison with $V_A(\mathbf{r})$ to apply the central-field approximation [13], which implies the use of the spherically symmetric potential $U_A(\mathbf{r})$ in place of $V_A(\mathbf{r})$:

$$U_A(r) = \frac{1}{4\pi}\int V_A(\mathbf{r})d\Omega.$$

In the central-field approximation, the one-electron wave function for the bound states can be written as

$$\Psi_\alpha(\mathbf{r}) = \Psi_{nlm}(\mathbf{r}) = \frac{1}{r}R_{nl}(r)Y_{lm}(\theta, \varphi),$$

in which case, instead of the Hartree–Fock equation (42), we arrive at the Schrödinger equation

$$-\frac{1}{2}(R_{nl})'' + \left[-U_A(r) + \frac{l(l+1)}{2r^2}\right]R_{nl}(r) = \varepsilon_{nl}^{A}R_{nl}(r), \quad (52)$$

where we introduced the notation $\varepsilon_{nl}^{A} = \varepsilon_{ii}^{A}$. The so-called multipole expansion [12] puts the above expression for $U_A(r)$ in the form

$$U_A(r) = \frac{Z}{r} - \frac{4\pi}{r}\int_0^r r_1^2\rho^A(r_1)dr_1 - 4\pi\int_r^{r_0} r_1\rho^A(r_1). \quad (53)$$

The electron density is described by the formulas

$$\rho^A(r) = \rho_1^A(r) + \rho_2^A(r),$$

$$\rho_1^A(r) = \frac{1}{4\pi r^2}\sum_{n,l} n_{Anl}^c R_{nl}^2(r), \quad (54)$$

$$\rho_2^A(r) = \frac{\sqrt{2}\Theta^{3/2}}{\pi^2}$$

$$\times \int_P \sqrt{y}\left\{1 + \exp\left[y - \frac{U_A(r)}{\Theta} - \frac{\mu}{\Theta}\right]\right\}^{-1} dy,$$

where the domain of integration P is determined by the condition $y > U_A(r)/\Theta$. Here, in place of n_{Ak}^c, we introduce the notation n_{Anl}^c, because, in the case at hand, the bound states are specified by the principal (n) and orbital (l) quantum numbers.

Formally, the average-atom approximation implies that the sum $\sum_{A^c}$ in expression (38) should be calculated in the same way as the sum $\sum_f$ in formula (34). To do this, in place of relationship (36), we must use the expression

$$W_A(\bar{n}_A^c, \bar{n}_A^f) = W_A^c(\bar{n}_A^c)W_A^f(\bar{n}_A^f). \quad (55)$$

In other words, we pass over from an enormous number of different subsystems labeled by the index A to a single subsystem, which is characterized by the "mean" occupation numbers $\bar{n}_k^c$ of the bound states k. If we omit the index A in (52)–(55) and use the expression [11, 13]

$$\ln\Delta\Gamma^c = \sum_{k\le K}\left[\ln\frac{1}{1-\bar{n}_k^c} - \bar{n}_k^c\ln\frac{\bar{n}_k^c}{1-\bar{n}_k^c}\right] \quad (56)$$

for the total number $\Delta\Gamma^c$ of bound electronic states, then we can vary $\delta\bar{n}_k^c$ to obtain

$$\bar{n}_{nl}^c = 2(2l+1)\left\{1 + \exp\left[\frac{1}{\Theta}(\bar{\varepsilon}_{nl} - \mu)\right]\right\}^{-1}. \quad (57)$$

The superscript c can also be omitted, because the quantum numbers (n, l) refer to the bound states. Then, the HFS equations reduce to

$$-\frac{1}{2}(R_{nl})'' + \left[-U(r) + \frac{l(l+1)}{2r^2}\right]R_{nl}(r) = \bar{\varepsilon}_{nl}R_{nl}(r),$$

$$U(r) = \frac{Z}{r} - \frac{4\pi}{r}\int_0^r r_1^2\rho(r_1)dr_1 - 4\pi\int_r^{r_0} r_1\rho(r_1),$$

$$\rho(r) = \rho_1(r) + \rho_2(r),$$

$$\rho_1(r) = \frac{1}{4\pi r^2}\sum_{n,l}\bar{n}_{nl}R_{nl}^2(r), \quad (58)$$

$$\rho_2(r) = \frac{\sqrt{2}\Theta^{3/2}}{\pi^2}\int_P \sqrt{y}\left\{1 + \exp\left[y - \frac{U(r)}{\Theta} - \frac{\mu}{\Theta}\right]\right\}^{-1} dy,$$

$$P: y > \frac{U(r)}{\Theta},$$

$$\bar{n}_{nl} = 2(2l+1)\left\{1 + \exp\left[\frac{1}{\Theta}(\bar{\varepsilon}_{nl} - \mu)\right]\right\}^{-1},$$

and the electroneutrality condition (29) can be written as

$$4\pi\int_0^{r_0}\rho(r)r^2dr = Z. \quad (59)$$

Table 1. Beryllium plasma at a temperature of 100 eV

Density, g/cm^3	M	S
1.85	3	34
0.9	3	34
0.185	4	69

Table 2. Aluminum plasma at a temperature of 100 eV

Density, g/cm^3	M	S
2.7	6	27131
0.27	12	5200299
0.1	17	1.19×10^8
0.027	28	1.76×10^{10}

To arrive at the final set of equations used in the HFS model, we must replace the potential $U(r)$ in formulas (58) by $\tilde{U}(r)$ defined as

$$\tilde{U}(r) = U(r) + U_{\text{exc}}(r),$$

where the potential $U_{\text{exc}}(r)$ is introduced artificially in order to approximately take into account the exchange interaction. Note that neither the introduction of $U_{\text{exc}}(r)$ nor its specific form stem from the general set of equations derived in Section 2. Different approximate formulas for $U_{\text{exc}}(r)$ were proposed in [2, 3]. For example, Nikiforov and Uvarov [3] used the approximate expression

$$U_{\text{exc}}(r) = \frac{\pi\rho(r)}{\Theta}\left[1 + 6\frac{\rho(r)}{\Theta^{3/2}} + \frac{\pi^4}{3}\left(\frac{\rho(r)}{\Theta^{3/2}}\right)^2\right]^{-1/3}. \quad (60)$$

The wave functions satisfy the normalization condition

$$\int_0^{r_0} R_{nl}^2(r)dr = 1. \quad (61)$$

The boundary conditions required to determine the eigenfunctions $R_{nl}(r)$ and the eigenvalues ε_{nl} of the energy can be imposed as follows:

$$R_{nl}(0) = 0, \quad R_{nl}(r_0) = 0. \quad (62)$$

Other ways to impose the boundary conditions were proposed in [2, 13]. However, a discussion of this topic is beyond the scope of our paper.

The HFS model equations were derived using the physical assumptions presented in Section 2 and the following additional assumptions:

(i) The average-atom (or average-ion) approximation is adopted.

(ii) The external interaction potential $V_{\text{ext}}^A(\mathbf{r})$ is low in comparison with $V_A(\mathbf{r})$.

We emphasize that we can pass over to the mean occupation numbers only when the number of bound electronic states is very large [9]. For a strongly nonideal plasma, this requirement fails to hold. Let N be the number of different states 1s of atoms and ions with different electron configurations. The upper bound S on this number ($N < S$) can be found from the simple formula

$$S = \sum_{n=1}^{Z} C_{M+n-1}^n,$$

where $C_{M+n-1}^n = \frac{(M+n-1)!}{n!(M-1)!}$ is the number of different arrangements of n identical objects in M different cells. The letter M denotes the maximum possible number of shells (n, l) of plasma atoms and ions for a given plasma temperature and density. This number was calculated using the ion model, which will be described in Section 6. Since we do not take into account the Pauli principle, the number S represents an upper bound on the actual number of different electron configurations. Clearly, each electron configuration is characterized by its own energy level 1s. The results calculated for beryllium and aluminum plasmas are presented in Tables 1 and 2, respectively.

From these tables, we can see that the number of different energy levels 1s is insufficiently large to introduce the mean occupation numbers, at least at normal densities of beryllium and aluminum plasmas.

An attempt to calculate the optical parameters of the plasma using only the average-atom approximation is known to be unsuccessful: the results obtained in this way disagree with the experimental data [14]. Agreement can be established perturbatively, with the wave functions $R_{nl}(r)$ in formulas (58) being the basic wave functions and the eigenvalues $\bar{\varepsilon}_{nl}$ of the energy being the unperturbed energy levels [15]. The applicability conditions for perturbation theory restrict the applicability range of the HFS model [5, 15]: the results obtained at too low temperatures turn out to be incorrect.

5. DETAIL CONFIGURATION ACCOUNT METHOD

The DCA method [4] makes it possible to calculate the quantum states of both the bound and unbound electrons for atoms and ions at plasma temperatures and densities for which the HFS model is already inapplicable. This method deals with the actual (rather than fictitious) plasma atoms and ions, in which the occupation numbers of the electronic states (i.e., the number of electrons at any bound state) are integer (unlike in the HFS model). The DCA method implies that the quan-

tum states should be calculated from the Hartree–Fock equations and that the densities of plasma atoms and ions should be evaluated in the Saha approximation.

The basic equations of the DCA method can be derived from the general set of equations presented in Section 2. If, in formula (48), we neglect the quantity $\tilde{V}_A(\mathbf{r}) = -Z/r + V_A(\mathbf{r}) + V_{\text{ext}}^A(\mathbf{r})$ in comparison with $p^2/2$, then we can see that $\bar{n}_A^f(\mathbf{r}, \mathbf{p})$ is independent of $\mathbf{r}$. This approach is known as the approximation of a constant density of unbound electrons. The density n_e of these electrons is related to the chemical potential μ by $\exp\left(-\frac{\mu}{\Theta}\right) = \frac{1}{n_e}\left(\frac{\Theta}{2\pi}\right)^{3/2}$ if $\exp\left(-\frac{\mu}{\Theta}\right) \gg 1$.

Let j be the ion charge number, s be the number of the energy state of an ion at a fixed j, $E_{j,s}$ be the energy of this ion, and $X_{j,s}$ be the density of the ions with the charge number j at the energy state s. Without consideration of the interaction between the unbound electrons and an ion, the Gibbs distribution yields the Saha–Boltzmann formula

$$n_e \frac{X_{j+1,p}}{X_{j,s}} = \frac{g_{j+1,p}}{g_{j,s}} 2\left(\frac{\Theta}{2\pi}\right)^{3/2} \exp\left[-\frac{1}{\Theta}(E_{j+1,p} - E_{j,s})\right], \quad (63)$$

where $g_{j,s}$ is the statistical weight of an ion. Equations (29) are solved under the additional conditions $\sum_{j,k} X_{j,k} = 1$ (the normalization condition) and $n\sum_{j,k} jX_{j,k} = n_e$ (the electroneutrality condition), where n is the density of atomic nuclei expressed in cm^{-3}. Note that, in the DCA method, the set of self-consistent field equations can be solved separately for each atom and ion in both the ground and excited states. This circumstance greatly simplifies the calculations. The structure of the basic equations for the DCA method was analyzed in [15].

Along with the physical approximations presented in Section 2, the following additional assumptions were made to derive equations of the DCA method:

(i) The density of the unbound electrons is assumed to be constant. This approximation is constructed by neglecting the quantity $\tilde{V}_A(\mathbf{r}) = -Z/r + V_A(\mathbf{r}) + V_{\text{ext}}^A(\mathbf{r})$ in comparison with $p^2/2$ in formula (48).

(ii) The energy of the interaction between the unbound electrons and an ion is negligible in comparison with the energy of the ion.

(iii) The external interaction potential $V_{\text{ext}}^A(\mathbf{r})$ is low in comparison with $V_A(\mathbf{r})$.

The first and second assumptions, which lead to the Saha approximation (63), substantially simplify the general set of equations, which describes the state of an ensemble of plasma atoms and ions. It turns out that the Hartree–Fock equations for subsystems with electron configurations $A = \alpha$ and $A = \beta$ are independent of each other, so that the Hartree–Fock equations can be solved separately for each electron configuration. On the other hand, the same two assumptions make the DCA method inapplicable to strongly nonideal plasmas.

As for the third assumption, we note that the DCA method makes it possible to approximately describe the effect of $V_{\text{ext}}^A(\mathbf{r})$ by introducing the required corrections.

6. ION MODEL

The ion model was developed in order to provide the possibility of calculating the optical parameters of the plasma over wider temperature and density ranges in comparison with the models described above. For this purpose, it is necessary to solve the set of self-consistent field equations (40)–(48) for an ensemble of plasma atoms and ions (this set cannot be divided into subsystems, each describing the state of only one atom or ion). Mathematically, this problem seems to be extremely difficult. It is well known that solving self-consistent field equations even for an individual atom is a very complicated task. In the ion model as formulated, the mathematical difficulties are even more serious, because of the much greater number of integrodifferential equations to be solved. The solution method was originally developed for monatomic substances and then for plasmas with a complicated chemical composition [16]. However, the ion model was developed successfully only after studies in which the role of relativistic effects was investigated [17], the proposed approach was justified based on the density functional theory [18], and the analytic results were systematically compared with the experimental data [5]. At the initial development stage, the ion model was based on the set of Schrödinger equations in which the exchange interaction was taken into account only approximately. The next stage resulted in the solution of the Hartree–Fock equations [19]. Here, we analyze a version of the ion model that is based on the Schrödinger equation.

We consider subsystem j with the set $\{N_{nl}^j\}$ of occupation numbers of the bound electronic states (here, the index j plays the same role as the index A in Section 2). If we incorporate the exchange interaction into the equations derived in Section 2 in the same way as was done in Section 4, then we arrive at the following equation for the bound electrons:

$$-\frac{1}{2}(R_{nl}^j)'' + \left[-V_j(r) + \frac{l(l+1)}{2r^2}\right]R_{nl}^j(r) = E_{nl}^j R_{nl}^j(r). \quad (64)$$

The boundary conditions and the normalization condition for the wave functions are the same as in Section 4.

The potential $V_j(r)$ is written as

$$V_j(r) = V_1^j(r) + V_2^j(r), \quad (65)$$

where

$$V_1^j(r) = \frac{Z}{r} - \frac{4\pi}{r}\int_0^r r_1^2 \rho_j(r_1)dr_1 - 4\pi\int_r^{r_0} r_1\rho_j(r_1), \quad (66)$$

$$V_2^j(r) = \frac{\pi\rho_j(r)}{\Theta}\left[1 + 6\frac{\rho_j(r)}{\Theta^{3/2}} + \frac{\pi^4}{3}\left(\frac{\rho_j(r)}{\Theta^{3/2}}\right)^2\right]^{-1/3}. \quad (67)$$

The electron density has the form

$$\rho_j(r) = \rho_1^j(r) + \rho_2^j(r). \quad (68)$$

Here, the density of the bound electrons is equal to

$$\rho_1^j(r) = \frac{1}{4\pi r^2}\sum_{n,l} N_{nl}^j (R_{nl}^j(r))^2, \quad (69)$$

and the density of the unbound electrons is described in the quasiclassical approximation:

$$\rho_2^j(r) = \frac{\sqrt{2}\Theta^{3/2}}{\pi^2}\int_A \sqrt{y}\left\{1 + \exp\left[y - \frac{V_j(r)}{\Theta} - \frac{\mu}{\Theta}\right]\right\}^{-1} dy, \quad (70)$$

where the domain of integration A is determined by the condition $y > \frac{V_j(r)}{\Theta}$. The chemical potential μ can be deduced from the electroneutrality condition, $\sum_j W_j N_j = Z$, where $N_j = \sum_{nl} N_{nl}^j + 4\pi\int_0^{r_0}\rho_2^j(r)r^2dr$ is the total number of electrons in the subsystem carrying a j subscript and W_j is the Gibbs distribution,

$$W_j = Cg_j\exp\left\{-\frac{E_j - \mu N_j}{\Theta}\right\} \quad (71)$$

with E_j being the total energy and $g_j = \prod_{nl} C_{2(2l+1)}^{N_{nl}^j}$ being the statistical weight.

The set of equations (64)–(71) describes the state of the statistical ensemble of plasma ions. Obviously, the groups of equations describing the states of subsystems denoted by subscripts $j = 1, 2$, etc. are coupled through the electroneutrality condition. Such equations are impossible to solve for all plasma ions even with the most advanced computers. However, these equations can be solved for the subsystem of main (or "reference") ions, which obey the Gibbs distribution W_j and have the highest density. Having solved Eqs. (64)–(71) for this ion subsystem, we can apply the perturbation theory to determine the quantum parameters of the remaining plasma ions with lower densities.

7. PERTURBATION THEORY IN THE ION MODEL

Solving Eqs. (64)–(71) leads to several sets of wave functions and electron energy levels (the number of sets is equal to the number of reference ions), in contrast to the DCA method, which assumes only one set (see Section 4). Consequently, in the ion model, we can construct several versions of the perturbation theory. For instance, if we need to calculate the parameters of an ion with the set $\{\tilde{N}_{nl}\}$ of occupation numbers (assuming that the density $\tilde{W}$ of such ions is low), we can find a reference ion whose electron configuration $\{N_{nl}^k\}$ is the closest to $\{\tilde{N}_{nl}\}$. Let W_k be the density of such reference ions and $\{E_{nl}^k\}$ be the set of electron energy levels. Then, the density $\tilde{W}$ can be obtained from the formulas

$$\tilde{W} = W_k P[\tilde{N}_{n_1l_1}]/P[N_{n_1l_1}^k],$$

$$P[N_{nl}] = C_{g_l}^{N_{nl}} p_{nl}^{N_{nl}}(1 - p_{nl})^{g_l - N_{nl}},$$

$$p_{nl} = \left[1 + \exp\left(\frac{E_{nl}^k - \mu}{\Theta}\right)\right]^{-1}, \quad g_l = 2(2l+1),$$

$$C_m^n = \frac{m!}{n!(m-n)!},$$

which are written for a simple case in which the electron configuration $\{N_{nl}^k\}$ differs from $\{\tilde{N}_{nl}\}$ by only the occupation numbers n_1 and l_1 of one electron shell. These formulas can be generalized to more complicated cases.

The electron energy levels for an ion with the occupation numbers $\{\tilde{N}_{nl}\}$ can be evaluated from the following formula of the perturbation theory:

$$\tilde{E}_{nl} = E_{nl}^k + \sum_{n_1,l_1}(\tilde{N}_{n_1l_1} - N_{n_1l_1}^k)R_{nln_1l_1},$$

where

$$R_{nln_1l_1} = \iint R_{nl}^2(r)\frac{1}{r_>}R_{n_1l_1}^2(r_1)drdr_1,$$

$r_> = \max(r, r_1)$, and $R_{nl}(r)$ are the wave functions calculated for the electron configuration $\{N_{nl}^k\}$. In this case, the change in the potential caused by a change in the occupation numbers is described by the formula

$$\delta V_1(r) = \tilde{V}_1(r) - V_1^k(r) = -\int\frac{1}{r_>}\sum_{nl}\delta N_{nl}R_{nl}^2(r_1)dr_1,$$

Table 3. Occupation numbers of the electronic states and the densities of aluminum ions at $T = 10$ eV and $\rho = 10^{-2}$ g/cm^3

Quantum state	1*s*	2*s*	2*p*	3*s*	3*p*	3*d*	Density W_j, g/cm^3
mean occupation number N_{nl}	2.00	1.99	5.95	5.7×10^{-2}	8.5×10^{-2}	5.9×10^{-2}	
$j = 1$	2	2	6	0	0	0	7.8×10^{-1}
$j = 2$	2	2	6	0	1	0	6.7×10^{-2}
$j = 3$	2	2	6	0	0	1	4.7×10^{-2}
$j = 4$	2	2	6	1	0	0	4.6×10^{-2}
$j = 5$	2	2	5	0	0	0	3.5×10^{-2}
$j = 6$	2	2	6	0	1	1	4.0×10^{-3}
$j = 7$	2	2	6	1	1	0	3.9×10^{-3}
$j = 8$	2	2	5	0	1	0	3.0×10^{-3}
$j = 9$	2	2	6	1	0	1	2.7×10^{-3}
$j = 10$	2	2	5	0	0	1	2.1×10^{-3}
$j = 11$	2	2	5	1	0	0	2.0×10^{-3}
$j = 12$	2	2	6	1	1	1	2.4×10^{-4}
$j = 13$	2	2	5	0	1	1	1.8×10^{-4}
$j = 14$	2	2	5	1	1	0	1.7×10^{-4}

where $\delta N_{nl} = \tilde{N}_{nl} - N_{nl}^k$. Obviously, this change is the smallest if the configuration $\{N_{nl}^k\}$ is the closest to $\{\tilde{N}_{nl}\}$. Consequently, the perturbation theory constructed in the ion model yields more exact results in comparison with the perturbation theory used in the HFS model [5].

Note that the total number of spectral lines can sometimes exceed 10^8, in which case it is impossible to perform the corresponding calculations even with modern computers [20]. Such a large number of spectral lines is related to ions with very low densities and, accordingly, with an extremely large number of electron configurations. It is practically impossible to systematically take into account the actual shape of each spectral line emitted by such ions. One way of solving this problem is to introduce a so-called "additional" spectral line broadening. The whole ion ensemble is divided into three groups. The first group consists of ions with densities above 10^{-3}, i.e., the reference ions for which Eqs. (64)–(71) should be solved. The second group consists of ions with densities from 10^{-6} to 10^{-3}; the parameters of these ions are evaluated perturbatively in the ion model. The third group consists of ions with densities below 10^{-6}. The absorption coefficients are calculated from the detailed shapes of the spectral lines from the ions of the first two groups. The spectral lines from the ions of the third group are, as a rule, close to the corresponding lines from the ions of the first two groups; therefore, they can be taken into account by introducing additional broadening of the spectral lines from the ions of the first two groups. This approach substantially improves the efficiency of computations and yields results that agree well with the experimental data [21].

Recall that the set of equations of the ion model can be solved for a group of the main (reference) ions, whose densities are the highest for a given plasma temperature and density. The question naturally arises of how to single out the group of reference ions. This can be done in the following way. First, the problem can be solved in the average-atom approximation in order to determine the mean occupation numbers N_{nl} of the electronic states. The ions whose electron configurations are closest to the configuration of an average atom (with the occupation numbers N_{nl}) have the highest density. The densities of the ions with the same electron configurations as those of the highest density ions but with a single excited electron are somewhat lower. In other words, the larger the number of excited electrons in the ions, the lower the density of these ions. The results of the corresponding calculations for an aluminum plasma are presented in Table 3.

In this table, the electron configuration of the ion marked with the index $j = 1$ is the closest to that of an average atom (the density of such ions is the highest); the ions denoted by the indices $j = 2$, 3, 4, and 5 are similar in configuration to the highest density ions with one excited electron; the ions labeled by the indices $j = 6$, 7, 8, 9, 10, and 11 are similar in configuration to the highest density ions with two excited electrons; and so on. This approach makes it possible to select the group of main (reference) ions.

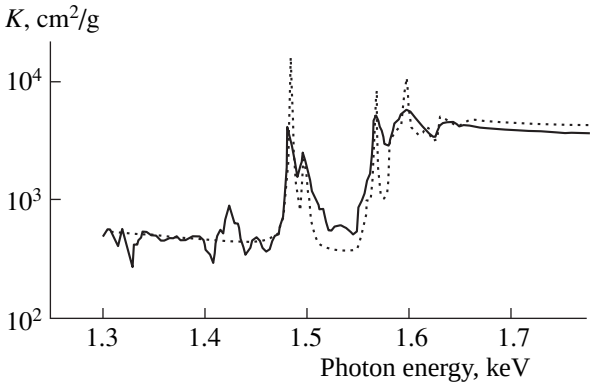

Fig. 2. Comparison between the spectral absorption coefficients measured experimentally (solid curve) [22] and calculated theoretically from the ion model (dashed curve) for an aluminum plasma at $T = 18$ eV and $\rho = 0.05$ g/cm^3.

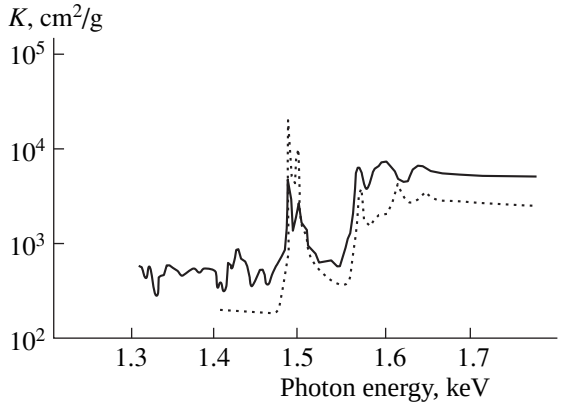

Fig. 3. Comparison between the spectral absorption coefficients measured experimentally (solid curve) [22] and calculated theoretically from the DCA method (dashed curve) for an aluminum plasma at $T = 18$ eV and $\rho = 0.05$ g/cm^3.

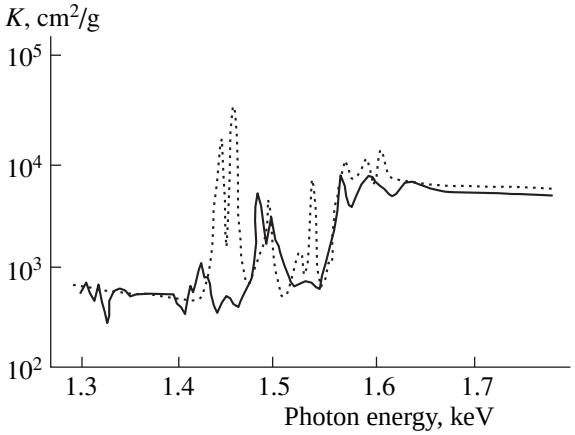

Fig. 4. Comparison between the spectral absorption coefficients measured experimentally (solid curve) [22] and calculated theoretically from the HFS model (dashed curve) for an aluminum plasma at $T = 18$ eV and $\rho = 0.05$ g/cm^3.

The equations of the ion model were derived using the assumptions made in Section 2 and the following two additional assumptions:

(i) The exchange interaction is taken into account approximately.

(ii) The external interaction potential $V_{\text{ext}}^{A}(\mathbf{r})$ is low in comparison with $V_A(\mathbf{r})$.

A refined version of the ion model was developed by Denisov and Orlov [19] on the basis of the relativistic Hartree–Fock equations without the first additional assumption. As for the second additional assumption, the external interaction can be described perturbatively in the conventional ion model.

Let us again turn to Fig. 1. Note that the ion model is valid over the entire applicability range of the TF model; i.e., it applies to plasmas with such high temperatures and/or densities that there are essentially no bound electrons. This circumstance is very important for solving the problems of radiative gas dynamics. Recall that the boundaries of applicability of the HFS model and DCA method differ between different chemical elements and have not yet been determined exactly. For this reason, even monatomic substances are difficult to analyze numerically, to say nothing about plasmas with a complicated chemical composition.

8. RESULTS OF CALCULATIONS

It is of interest to compare the spectral absorption coefficients calculated from different theoretical models with the experimental data. For the ion model, DCA method, and HFS model, a comparison with the data from experiments reported by Davidson [22] is illustrated in Figs. 2, 3, and 4, respectively. In those experiments, the spectral absorption coefficient was determined under conditions typical of a nonideal plasma, the nonideality parameter $\Gamma = Z_0/(r_0\Theta)$ (where Z_0 is the mean ion charge number) being approximately equal to 0.45. We can see that the ion model better fits the experiments than the DCA method and HFS model. This can be explained by the fact that the ion model equations were derived under more general physical assumptions than the equations of the DCA method and HFS model. Accordingly, the ion model can have wider application than the other models under discussion.

In Fig. 5, we compare the experimental and theoretical profiles of the function

$$T(E) = \exp[-K(E)\rho d],$$

where $K(E)$ is the spectral absorption coefficient, which depends on the photon energy. The theoretical profile was obtained from the ion model by taking into account additional broadening of the spectral lines. The experimental profile was measured by Springer *et al.* [23] in a mixture consisting of 65% niobium atoms and 35% aluminum atoms. We can see that the introduction of

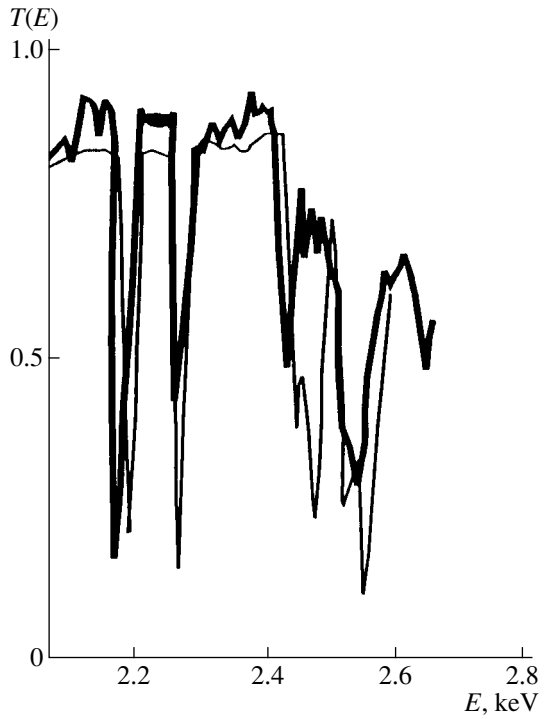

Fig. 5. Comparison between the functions $T(E)$ measured experimentally (heavy curve) [23] and calculated theoretically from the ion model (light curve) for a plasma with a complicated chemical composition at T = 47 eV, ρ = 0.0257 g/cm^3, and $\rho d = 2.57 \times 10^{-4}$ g/cm^2.

additional broadening of the spectral lines ensures good agreement between the theory and experiment.

9. CONCLUSION

An analysis based on the density functional theory shows that the physical assumptions used in deriving equations of a particular theoretical model restrict its applicability range (Fig. 1). Thus, the applicability range of the ion model is wider than those of the HFS model and DCA method, because the latter were constructed using additional physical assumptions.

We restricted our analysis to hot dense plasmas. The methods for calculating the optical parameters of a plasma with a lower density and temperature are presented in [24, 25].

REFERENCES

1. R. Feynman, M. Metropolis, and E. Teller, Phys. Rev. **75**, 1561 (1949).
2. B. F. Roznyai, Phys. Rev. A **5**, 1137 (1972).
3. A. F. Nikiforov and V. B. Uvarov, Chislennye Metody Mekh. Sploshnoĭ Sredy **4**, 114 (1973).
4. D. Salzman and A. Krumbein, Phys. Rev. A **32**, 3627 (1985).
5. N. Y. Orlov, Laser Part. Beams **15**, 627 (1997).
6. N. March, V. Kon, Vashita, *et al.*, *Theory of Inhomogeneous Electron Gas* (Mir, Moscow, 1987).
7. A. K. Radjagopal, Adv. Chem. Phys. **41**, 59 (1980).
8. N. H. March, W. H. Young, and S. Sampanthar, *The Many-Body Problem in Quantum Mechanics* (Cambridge Univ. Press, Cambridge, 1967; Mir, Moscow, 1969).
9. K. Huang, *Statistical Mechanics* (Wiley, New York, 1963; Mir, Moscow, 1966).
10. C. Kittel, *Thermal Physics* (Wiley, New York, 1973; Nauka, Moscow, 1977).
11. L. D. Landau and E. M. Lifshitz, *Statistical Physics* (Nauka, Moscow, 1964; Pergamon, Oxford, 1980).
12. A. F. Nikiforov and V. B. Uvarov, *Special Functions of Mathematical Physics: a Unified Introduction with Applications* (Nauka, Moscow, 1978; Birkhauser, Basel, 1987).
13. A. F. Nikiforov, *Numerical Methods of Solution of Quantum Mechanics Problems* (Mosk. Gos. Univ., Moscow, 1981).
14. T. R. Carson, D. F. Mayers, and D. W. N. Stibbs, Mon. Not. R. Astron. Soc. **140**, 483 (1968).
15. N. Yu. Orlov, in *Encyclopedia of Low-Temperature Plasma*, Ed. by V. E. Fortov (Nauka, Moscow, 2000).
16. N. Yu. Orlov, Zh. Vychisl. Mat. Mat. Fiz. **27**, 1058 (1987).
17. N. Yu. Orlov, Differ. Uravn. **20**, 1253 (1984).
18. N. Yu. Orlov, Mat. Model. **6**, 3 (1994).
19. O. B. Denisov and N. Yu. Orlov, Mat. Model. **5**, 3 (1993).
20. S. Rose, J. Phys. B **25**, 1667 (1992).
21. N. Yu. Orlov and V. E. Fortov, Dokl. Akad. Nauk **370** (1), 34 (2000) [Dokl. Phys. **45**, 1 (2000)].
22. S. J. Davidson, J. M. Foster, C. C. Smith, and K. A. Warburton, Appl. Phys. Lett. **52**, 847 (1988).
23. P. T. Springer, T. S. Perry, D. F. Fields, *et al.*, in *Atomic Processes in Plasmas*, Ed. by E. S. Marmar and J. I. Terry (AIP, New York, 1992) [AIP Conf. Proc. **257**, 78 (1992)].
24. L. M. Biberman and G. É. Norman, Usp. Fiz. Nauk **91**, 193 (1967) [Sov. Phys. Usp. **10**, 52 (1967)].
25. V. A. Kamenshchikov, Yu. A. Plastinin, V. M. Nikolaev, and L. A. Novitskiĭ, *Radiation Properties of Gases at High Temperatures* (Mashinostroenie, Moscow, 1971).

Translated by O.E. Khadin

Plasma Physics Reports, Vol. 27, No. 1, 2001, pp. 56–61. Translated from Fizika Plazmy, Vol. 27, No. 1, 2001, pp. 58–63.

NONLINEAR PHENOMENA

Observation of Nonlinear Coupling between Drift and Ion-Acoustic Oscillations in Low-Frequency Plasma Turbulence

A. E. Petrov, K. A. Sarksyan, N. N. Skvortsova, and N. K. Kharchev

Institute of General Physics, Russian Academy of Sciences, ul. Vavilova 38, Moscow, 117942 Russia

Received June 1, 2000; in final form, July 6, 2000

Abstract—It is shown experimentally that the characteristics of structural ion-acoustic turbulence in a plasma are governed primarily by the development of density gradient–driven drift oscillations. The cyclicity of appearance and disappearance of drift wave packets and ensembles of ion-acoustic solitons in a steady-state turbulent plasma, as well as the correlation between them, is determined. © *2001 MAIK "Nauka/Interperiodica".*

One of the interesting, but poorly studied, problems of nonlinear plasma physics is the combined effect of different instabilities simultaneously existing in a plasma on the formation of steady-state plasma turbulence. The TAU-1 device was designed for studying nonlinear plasma processes. In this device, the frequency spectrum of low-frequency plasma turbulence is closely related to two instabilities, namely, the drift dissipative instability and ion-acoustic current-driven instability. Experiments carried out in the TAU-1 device demonstrated the nonlinear interaction between the drift (driven by the former instability) oscillations and ion-acoustic (driven by the latter instability) oscillations in steady-state low-frequency turbulence.

The TAU-1 device is described in detail in [1]. A cylindrical argon plasma column, 4 cm in diameter and 100 cm in length, was produced in a uniform magnetic field of ≤800 Oe by a steady low-energy (E_b = 60–150 eV) electron beam. The argon pressure was $p = (2–4) \times 10^{-4}$ torr. The plasma density was maintained at a level of $n = (0.9–1.2) \times 10^{10}$ cm^{-3}. The electron temperature was T_e = 5–7 eV, and the ion temperature was $T_i \approx 0.1T_e$. The characteristic plasma frequencies ranged as follows: $\nu < \Omega_i < \omega_{dr} < \omega_s \leq \omega_{Li} \ll \Omega_e$, ω_{Le}, where Ω_i and Ω_e are the electron and ion gyrofrequencies, respectively; ω_{Li} and ω_{Le} are the ion and electron plasma frequencies; and ω_{dr} and ω_s are the drift and ion-acoustic frequencies. All data presented in this paper were obtained for steady-state values of the macroscopic parameters of the TAU-1 plasma. The steady-state plasma conditions could be maintained for 3–5 h without any change in the magnetic field, argon pressure, beam current, mean plasma density, electron temperature, etc.

Fluctuations of the plasma floating potential were measured by a Langmuir probe. The probe was a rod 0.3 mm in diameter and 3 mm in length. The signal was divided into two channels; after necessary amplification and filtering in both channels, the drift signal was discriminated in the first channel and the ion-acoustic signal was discriminated in the second channel. Since the amplitude of the ion-acoustic signal was one order of magnitude lower than that of the drift signal, a high-pass filter and an amplifier were used in the second channel to match the signal amplitude to the operating range of an analog-to-digital converter (ADC). The filter had a cutoff at 300 kHz and an attenuation of 20 dB. Both channels were connected to the inputs of an OS-2 ADC card (the record length was up to 2×128 kB, and the sampling frequency was 10 MHz). Then, the digitized signals were analyzed by various numerical methods of spectral analysis. In studying the signals, we used the spectral methods of Fourier analysis, wavelet analysis, and correlation analysis; a detailed description of these methods is presented in [2, 3]. Note that, in contrast to Fourier analysis, in wavelet analysis, the signals are expanded in series using the so-called wavelets as the basis functions. The functions describing the wavelets have the shapes of wave packets: they oscillate in time and decrease at infinity. Using wavelet analysis, it is possible to detect the appearance and disappearance of local coherent structures in the time signals under study. In our study, we used wavelets similar to those used in our previous studies of ion-acoustic turbulence [2]: $\Psi_a(t) = a^{-1/2} \times \exp[i2\pi t/a - (t/a)^2/2]$. Such a wavelet is the convolution of a Gaussian function and harmonic oscillations; its half-width is $\Delta t = a$. The characteristic time scale of the wavelet can be interpreted as a reciprocal of the corresponding frequency $\omega = 2\pi/a \pm \Delta\omega/2$. In the figures presented below, we use this frequency, rather than the wavelet time scale.

Drift oscillations in a plasma arise due to drift dissipative instability caused by the plasma-density gradient. The frequency Fourier spectrum of drift oscillations lies in the range below 100 kHz and consists of quasi-harmonics ($\Delta\omega_{dr} < \omega_{dr}$). A typical drift spectrum

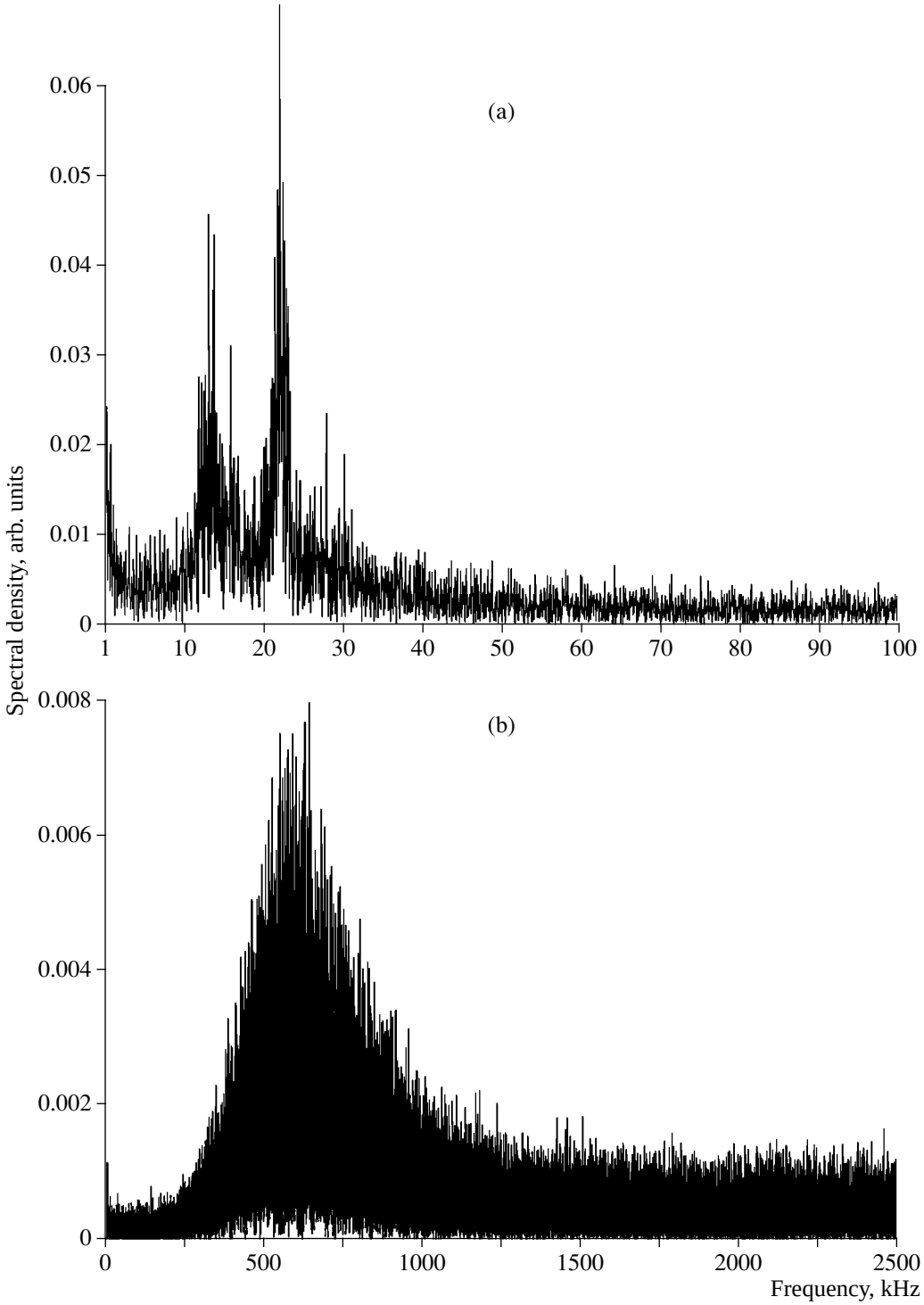

Fig. 1. Fourier spectra of (a) drift and (b) ion-acoustic signals measured at the plasma axis. The time window is 26 ms, $H = 500$ G, $p = 3 \times 10^{-4}$ torr, $I_b = 250$ mA, and $U_b = 120$ V.

is shown in Fig. 1a. The aperiodic buildup of drift oscillations was studied in [4]. A continuous spectrum between the drift and ion plasma frequencies corresponds to structural ion-acoustic turbulence. The source of this turbulence is associated with the ion-acoustic current-driven instability. The structural ion-acoustic turbulence may be regarded as a strong turbulence that is in dynamic equilibrium with ion-acoustic solitons [2, 5]. This kind of turbulence exists over a wide range of macroscopic plasma parameters; a struc-

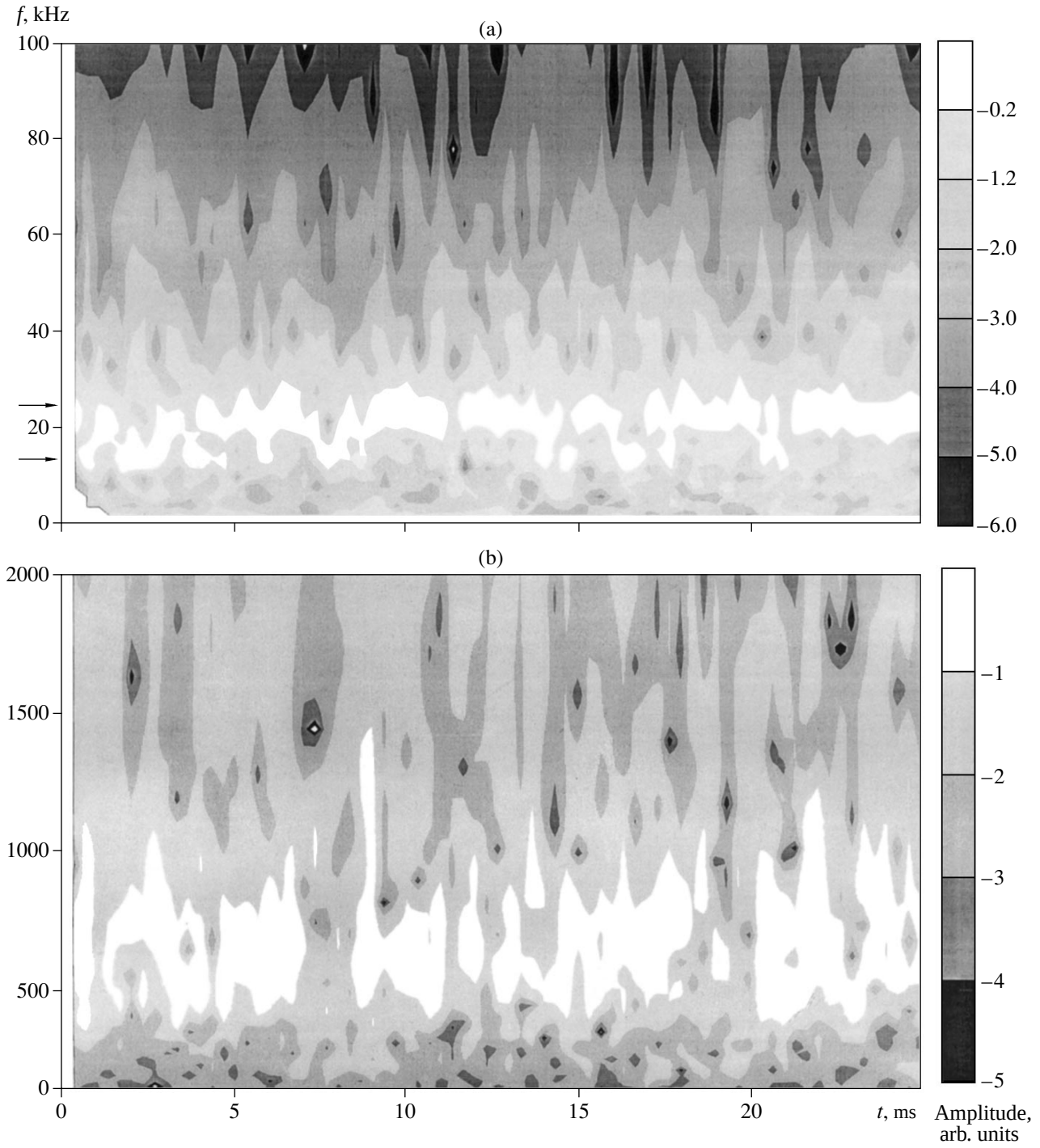

Fig. 2. Wavelet time spectra of (a) drift and (b) ion-acoustic signals measured at the plasma axis. The time window is 26 ms, H= 500 G, $p = 3 \times 10^{-4}$ torr, $I_b = 250$ mA, and $U_b = 120$ V.

tural nature of the turbulent state persists both near and far from the instability threshold. The solitons comprise up to 20–30% of the total energy of turbulence. The solitons can nonlinearly interact with each other according to "decay" and "coupling" scenarios to form a stable steady state. In [6], it was shown that the structural ion-acoustic plasma turbulence is a self-similar probability process rather than a Gaussian (normal) process. Figure 1b shows a typical broadband Fourier spectrum of structural ion-acoustic turbulence measured with a long time window (the frequencies below 500 kHz are cut off here).

Figure 2 shows how two wavelet spectra of potential fluctuations vary with time in (a) the drift and (b) ion-acoustic frequency ranges. These spectra were mea-

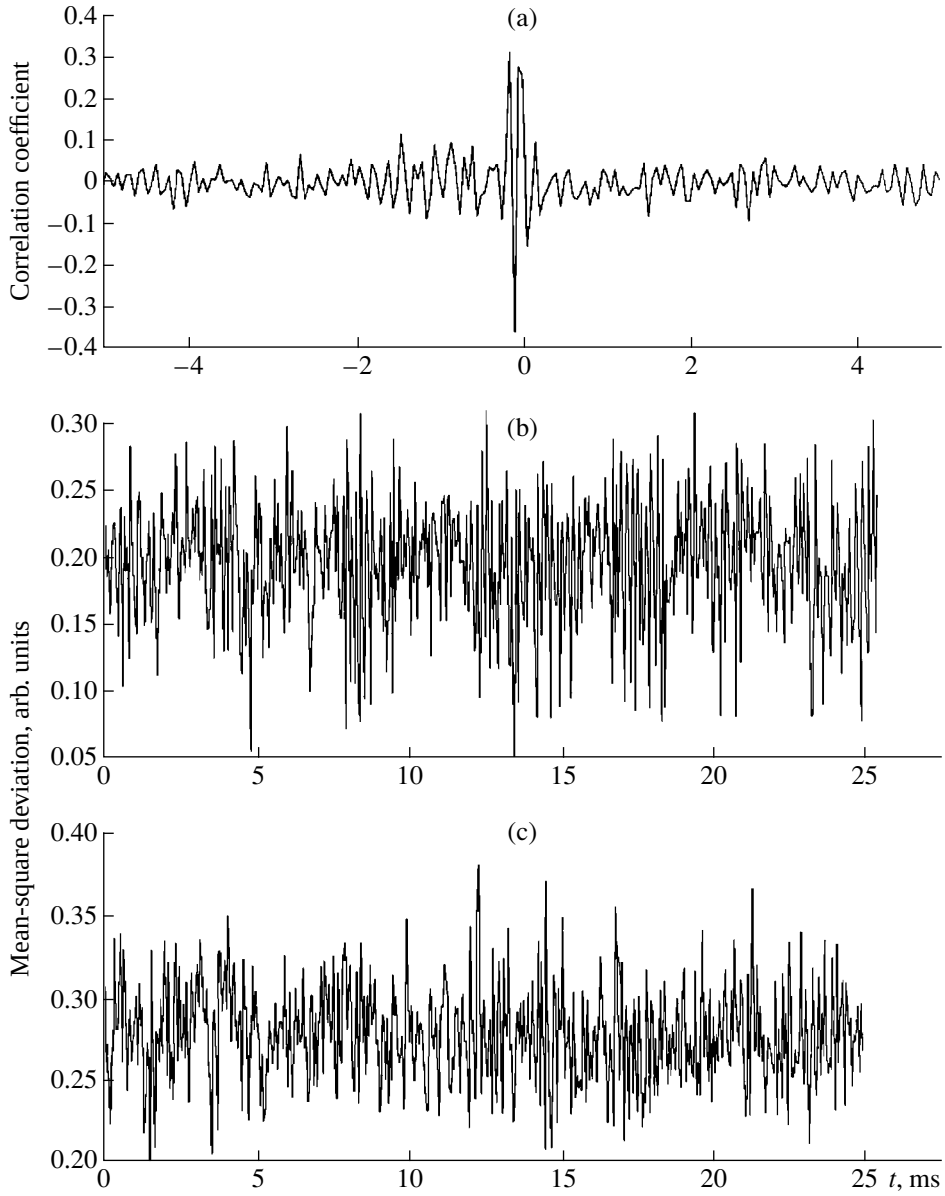

Fig. 3. (a) Cross-correlation function of the dispersion (mean-square deviation) of drift and ion-acoustic signals measured at the plasma axis and the dispersion of (b) the drift signal and (c) the ion-acoustic signal for $H = 500$ G, $p = 3 \times 10^{-4}$ torr, $I_b = 250$ mA, and $U_b = 120$ V.

sured at a beam current of $I_b = 250$ mA corresponding to the maximum turbulent and drift levels. The spectra were obtained by interpolating through 75 individual spectra calculated for successive 0.35-ms time intervals. The amplitude of spectral components (in arbitrary units) is shown in the plot by gray shading. The running time (the initial time is chosen arbitrarily) is plotted on the abscissa, and the frequency is plotted on the ordinate. The spectra of both the drift fluctuations and structural ion-acoustic turbulence vary markedly with time at the constant values of the macroscopic plasma parameters. Within this time window, we can see the appearance and disappearance of quasi-harmonics in the drift frequency range and time structures in the acoustic frequency range. It is seen (Fig. 2a) that two quasi-harmonics with definite frequencies (~14 and 22 kHz, indicated by the arrows on the ordinate) appear in the drift spectrum in successive time intervals. The spectra with quasi-harmonics are separated by a noise spectrum; i.e., there is no gradual transformation of one quasi-harmonic into another. The same two quasi-harmonics are seen in the Fourier spectrum of the drift signal in Fig. 1a. In the given time realization, two drift quasi-harmonics exist in the form of finite-duration wave packets. Such behavior, when one

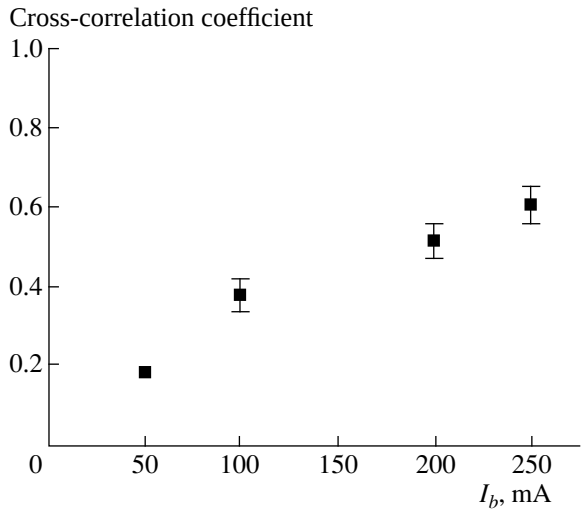

Fig. 4. The cross-correlation coefficient of the dispersion of the drift and ion-acoustic signals measured at the middle of the plasma radius as a function of the electron beam current for $H = 500$ G, $p = 3 \times 10^{-4}$ torr, and $U_b = 120$ V.

to three quasi-harmonics appear successively, was observed in all of the realizations. However, we cannot say what is the nature of the recorded drift wave packets. In the same figure, one can see the spectrum of the structural ion-acoustic turbulence for the same realization. In [2], such a shape of the spectrum of the structural ion-acoustic turbulence was attributed to the appearance and disappearance of an ensemble of solitons of different dimensions and durations. We recall that the Fourier spectrum of this state is broadband (Fig. 1b). The duration of quasi-harmonics in the drift spectrum is determined by the drift-oscillation wave packet and attains several milliseconds; such a wave packet includes from several tens of oscillations to one hundred oscillations; the pauses between the wave packets last several hundreds of microseconds. The duration of the time structure in the acoustic spectrum also reaches several milliseconds and is determined by the lifetime of the soliton ensemble. The duration of pauses between wave packets attains one millisecond (at high beam currents, e.g., at $I_b = 250$ mA). The question arises as to whether the appearance of intense drift wave packets is related to the appearance of an ensemble of ion-acoustic solitons.

To answer this question, it is necessary to compare the two time realizations with the characteristic times that differ by more than two orders of magnitude, because the characteristic drift frequencies are lower than the acoustic frequencies by a factor of 10^2–10^3 (see Fig. 1). In order to apply the correlation analysis, it is desirable to bring these time realizations to a comparable time (or frequency) scale. Such a time scale is presented in Fig. 2; this is a fraction of the pauses between the instants of the appearance of wave packets or ensembles of ion-acoustic solitons. This time scale ranges from several tens of microseconds to one hundred microseconds. Formally, this time scale can be found by calculating time variations in the dispersion of temporal signals. Figures 3b and 3c show the mean-square deviations (dispersion) of drift and ion-acoustic signals for the chosen time realizations. The dispersion of the time signals characterizes the energy of signal fluctuations. Each point in these curves is calculated using 250 points of the original signal or over a time interval of 50 μs. Figure 3a shows the cross-correlation function between the variations in the dispersion of the drift and acoustic signals. The cross-correlation coefficient between the time realizations of the dispersion of the drift and acoustic signals attains 30–40% for the same measurement conditions in the plasma center as for Fig. 2 (at a beam current of $I_b = 250$ mA). The cross-correlation time between these realizations is about several milliseconds. Hence, the appearance of drift wave packets is correlated with the appearance of ensembles of acoustic solitons. The correlation between these plasma phenomena exists during the total lifetime of a drift wave packet or an ensemble of solitons (both times are about several milliseconds). For this reason, when we increase the time interval used in calculations of the dispersion of drift and acoustic signals to 250–500 μs, so that the pauses between the wave packets (ensembles of solitons) or even several wave packets (ensembles of solitons) fall within this time interval, the cross-correlation coefficient decreases.

The correlation coefficient between drift wave packets and ensembles of ion-acoustic solitons increases when the probes are displaced into the region where the drift velocity is maximum. Under our experimental conditions, this region lies at the middle of the plasma radius. In contrast to the data presented in Fig. 3a, the correlation coefficient in this region can attain 60% under the same conditions (at a beam current of $I_b = 250$ mA). Figure 4 shows the cross-correlation coefficient of the dispersion of drift and ion-acoustic signals versus the current at the middle of the plasma radius (the time interval used in calculating the dispersion is the same for all values of the current and is equal to 50 μs). It is seen that, as the current decreases from 250 to 50 mA, the correlation coefficient falls by a factor of 3. It was shown previously that an increase in the beam current results in an increase in the intensity of both the drift signal [7] and ion-acoustic signal [2]. Moreover, it was shown that, as the beam current increases, the frequency of the appearance of ensembles of solitons decreases, whereas the intervals between these events increase, which is confirmed by recent measurements. As the beam current decreases, the cross-correlation coefficient between drift wave packets and ensembles of solitons decreases significantly.

Therefore, the measured high values of the correlation coefficient indicate that the appearance of a drift

wave packet is related to the formation of an ensemble of ion-acoustic solitons. Before discussing the mechanism for this relation, it is necessary to explain why drift oscillations in our experiment exist in the form of finite-duration wave packets. Previously, it was shown [8] that the onset of the drift-dissipative instability is accompanied by a buildup of drift oscillations of ion-acoustic nature in the frequency range below 100 kHz. The nonlinear saturation of such drift oscillations was explained by the diffusion loss of oscillations, because the transverse diffusion of ions increases as their energy increases in the field of drift waves. It was taken into account that the ions acquire energy due to their stochastic acceleration in the field of waves that have a finite-width spectrum. Apparently, the broadband structural ion-acoustic turbulence can also contribute to such ion heating. The increase in the ion energy and the transport of oscillations into low-density plasma layers with subsequent ion cooling can result in the disruption of the drift-dissipative instability and the disappearance of drift wave packets. This, in turn, is accompanied by fast ion cooling, so that the initial conditions (or conditions close to them) are restored for the onset of the drift-dissipative instability, and the next drift wave packet appears. Then, the whole cycle of the evolution, saturation, and disappearance of drift wave packets and the associated ensemble of ion-acoustic solitons repeats. A question also arises conceming the mechanism responsible for the observed relation between drift wave packets and ion-acoustic solitons. The fact is that, under our conditions, the drift oscillations are mainly azimuthal with a wavenumber of $k_\phi \sim 1$–2 cm^{-1} [9]. It is known [10] that, in this case, drift oscillations can give rise to an ion-acoustic instability. Therefore, the evolution of the structural ion-acoustic turbulence can simultaneously be governed by two processes—the longitudinal current and drift oscillations with a large azimuthal wavenumber. As was shown above, the latter process is intermittent in time; consequently, the existence of ensembles of solitons and structural ion-acoustic turbulence will also be intermittent.

ACKNOWLEDGMENTS

We thank G.M. Batanov and A.A. Rukhadze for fruitful discussions. This work was supported by the Russian Foundation for Basic Research, project nos. 98-02-16345 and 00-02-17507.

REFERENCES

1. G. M. Batanov, L. M. Kovrizhnykh, L. V. Kolik, *et al.*, Tr. Fiz. Inst. Akad. Nauk SSSR **160**, 122 (1985).
2. K. A. Sarksyan, N. N. Skvortsova, N. K. Kharchev, and B. Ph. Milligen, Fiz. Plazmy **25**, 362 (1999) [Plasma Phys. Rep. **25**, 312 (1999)].
3. B. Ph. van Milligen, E. Sánchez, T. Estrada, *et al.*, Phys. Plasmas **2**, 3017 (1995).
4. V. V. Abrakov, A. E. Petrov, K. A. Sarksyan, and N. N. Skvortsova, Fiz. Plazmy **20**, 1069 (1994) [Plasma Phys. Rep. **20**, 959 (1994)].
5. A. A. Rukhadze, K. A. Sarksyan, and N. N. Skvortsova, J. Phys. IV **5**, 6 (1995).
6. N. N. Skvortsova, K. A. Sarksyan, and N. K. Kharchev, Pis'ma Zh. Éksp. Teor. Fiz. **70**, 203 (1999) [JETP Lett. **70**, 201 (1999)].
7. F. F. Asadullin, G. M. Batanov, K. A. Sarksyan, and A. V. Sapozhnikov, Fiz. Plazmy **4**, 1104 (1978) [Sov. J. Plasma Phys. **4**, 618 (1978)].
8. F. F. Asadullin, G. M. Batanov, L. V. Kolik, *et al.*, Fiz. Plazmy **7**, 414 (1981) [Sov. J. Plasma Phys. **7**, 226 (1981)].
9. V. V. Abrakov, A. E. Petrov, K. A. Sarksyan, *et al.*, Plasma Phys. Controlled Fusion **39**, 367 (1997).
10. A. V. Timofeev and B. N. Shvilkin, Usp. Fiz. Nauk **118**, 273 (1976) [Sov. Phys. Usp. **19**, 149 (1976)].

Translated by N.F. Larionova

Plasma Physics Reports, Vol. 27, No. 1, 2001, pp. 62–67. Translated from Fizika Plazmy, Vol. 27, No. 1, 2001, pp. 64–70.

PLASMA DYNAMICS

Dynamics of the Current Front in a Current-Carrying Plasma Bridge

G. I. Dolgachev, A. S. Kingsep, and A. G. Ushakov

Russian Research Centre Kurchatov Institute, pl. Kurchatova 1, Moscow, 123182 Russia

Received December 23, 1999; in final form, June 1, 2000

Abstract—At the RRC Kurchatov Institute, high-impedance plasma opening switches have recently been developed that enable efficient pulse sharpening and are capable of operating in a repetitive mode. This paper presents the results of studying the conduction phase preceding the current break. In this stage, the magnetic-field and current waves propagate in the plasma from the switch to the load. The magnetic-field and current detectors placed along the plasma axis are used to measure the velocity and acceleration of the current front near the cathode and anode. At the end of the conduction phase, the characteristic velocities near the cathode and anode attain 100 and 50 cm/μs, respectively. During the current front propagation, the width of the front nearly triples. The acceleration and widening of the front are reasonably explained within electron magnetohydrodynamics. It is shown that the voltage during the current break depends on the length of the coaxial cathode of the switch. When the cathode length is shorter than the distance covered by the current front, the generated voltage decreases substantially. *© 2001 MAIK "Nauka/Interperiodica".*

1. INTRODUCTION

The penetration of a nonlinear magnetic-field wave into the plasma bridge of a plasma opening switch (POS) is a well-known effect that has been studied both theoretically [1, 2] and experimentally [3–8].

The effect was first observed in [3]. The penetration velocity of $(2–3) \times 10^8$ cm/s was first measured in the so-called "nanosecond switches" with a duration of the conduction phase of less than 100 ns (the conduction time was 20–40 ns, and the amplitude of the current of the inductive energy storage was 500–850 kA) [4]. In the experiments carried out in the DUBL generator with a microsecond conduction time (0.9 μs, 300 kA), the penetration of the current into the plasma bridge was studied [5]. It was found that the penetration velocity in the cathode region was equal to 2×10^7 cm/s; during the last 50 ns before the current break, the current channel quickly accelerated up to 10^8 cm/s. In the experiments of [6], in which the conduction time was 1 μs and the current amplitude was 500 kA, the current distribution at different times and, correspondingly, the current penetration velocity ($(2–3) \times 10^7$ cm/s) were measured with loops placed in the anode–cathode gap. In nanosecond switches (100 ns, 135 kA), the Zeeman effect was used to estimate the penetration velocity of the magnetic field. Spectroscopic measurements of the Zeeman broadening of the BaII line indicated the onset of the magnetic field in the plasma at a distance of 5 mm from the anode 30 ns after the start of the generator current, which corresponded to a penetration velocity of 10^8 cm/s [7]. For microsecond POSs with a planar configuration of the plasma-filled diode (a conduction time of ~1.6 μs and current of 80 kA), the measurements of the delay between the signal from an ion detector and the start of the generator current yielded a penetration velocity of the current front of $\geq 10^8$ cm/s [8]. All of the above measurements show the importance of nonlinear processes determining the high penetration velocity of the magnetic field (from 2×10^7 to more than 10^8 cm/s).

This paper is devoted to studying the dynamics of the magnetic-field penetration and its influence on the parameters of a POS. We studied relatively low-current (100–200 kA) high-impedance switches with a microsecond conduction phase. Such switches enable efficient pulse sharpening (in particular, in the repetitive mode [9–11]) and are characterized by a relatively high impedance (10–30 Ω) in the breaking stage. In the conduction phase, which lasts for 1–1.5 μs, the impedance can reach several ohms. In a coaxial configuration, the large distance covered by the plasma during the current pulse (several tens of cm) allows several magnetic field detectors to be set at the cathode and anode and more accurate measurements of the parameters of the current front.

2. PARAMETERS OF THE POS

For experiments, we chose a typical generator with a high-impedance POS [12] operating in the single-pulse mode. Originally, the accelerator was intended to generate repetitive electron-beam pulses (500 kV, 100 ns, 10 kA) emerging into atmospheric air. The parameters of the device were as follows: the capacitance of a Marx generator, which served as an energy storage bank, was 0.4 μF; the output voltage was 170 kV; the free oscillation period of the Marx–POS

1063-780X/01/2701-0062$21.00

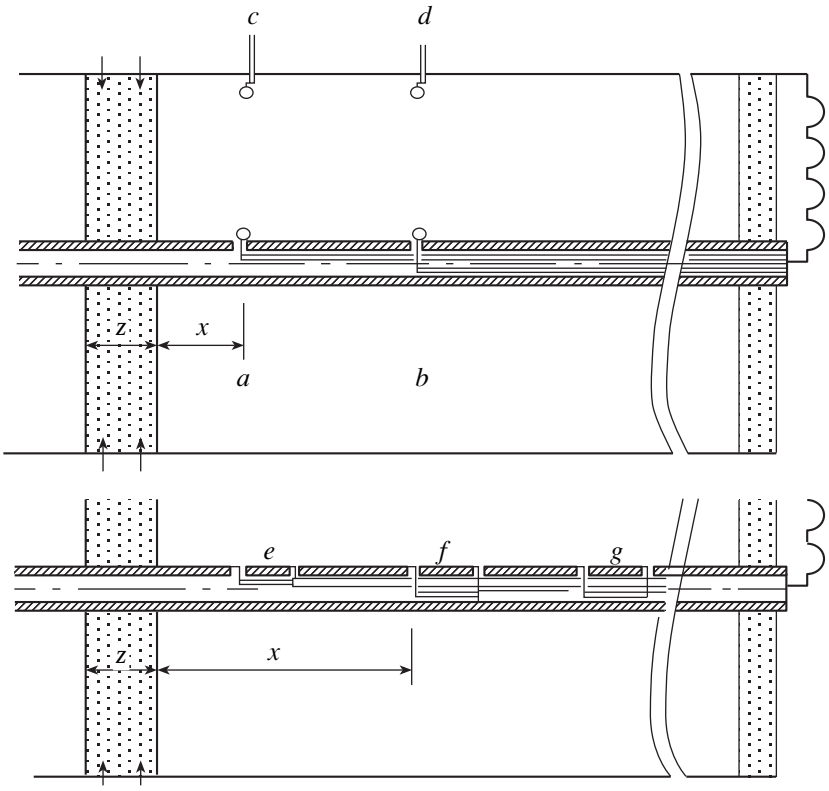

Fig. 1. Arrangement of the detectors in the region between the POS (on the left) and the load (on the right): (*a–d*) *dB*/*dt* loops placed at the central and outer electrodes, 15 and 30 cm away from plasma guns, and (*e–g*) central-electrode shunts placed at a distances of 15, 30, and 45 cm, respectively, from the plane in which the plasma guns are positioned.

circuit was 4 μs; and the current amplitude was 120 kA. The diameters of the POS electrodes were 14 and 160 mm. To fill the interelectrode gap with a plasma, we used 24 plasma guns placed at the outer electrode. The schematic of the region between the POS and load is shown in Fig. 1.

When operating with a high-impedance load, the voltage multiplication factor was equal to 3–5, which allowed us to obtain an electric pulse with a voltage of 500–600 kV, current of 10 kA, and duration of 100 ns in the electron diode load. Figure 2 presents the typical waveforms demonstrating the parameters of the device loaded with a high-resistance diode (Fig. 2a) or a 0.4- to 0.7-μH inductance coil (Fig. 2b). In the latter case, the voltage multiplication factor was equal to 1.5–2; thus, the voltage at the POS did not exceed 350 kV.

3. DIAGNOSTICS

The current and voltage were measured with standard electric diagnostics. A loop placed in the vacuum chamber in front of the plasma guns was used to measure the voltage. In the conduction phase, a signal from the loop $U = -LdI/dt$ represents the voltage from the Marx generator, which decreases as $\cos(\omega t)$ (Fig. 2). The amplitude of the signal gives the characteristic scale of the voltage. The break of current occurs when the Marx generator is nearly discharged and $LdI/dt = 0$. In the phase of the current break, the signal from the loop reverses its sign and represents the voltage at the POS accurate to the voltage remaining at the Marx generator. Both the total current in the Marx–POS circuit and the current in the load were measured with ohmic coaxial 0.03-Ω shunts placed in the breaks of the outer electrode of the vacuum coaxial line. To measure the parameters of the current front in the POS conduction phase, we used loops measuring the *dB*/*dt* signal that were placed on the cathode and anode surfaces at different distances from the POS: 15 cm for loops *a* and *c* and 30 cm for loops *b* and *d* (see Fig. 1). We also used current shunts embedded into the cathode that were placed at a distances (*e*) 15, (*f*) 30, and (*g*) 45 cm from the right edges of the plasma guns. The shunts were made of thin-walled (0.1 mm) 20-mm-long stainless steel tubes with a diameter of 14 mm (the same as the cathode diameter). Thus, the presence of shunts did not affect the electrode configuration. The measurements carried out with the detectors of the electric and magnetic fields were performed in the regime in which an inductance coil was used as a load. All of the experiments (unless otherwise stated) were carried out at the negative polarity of the central electrode.

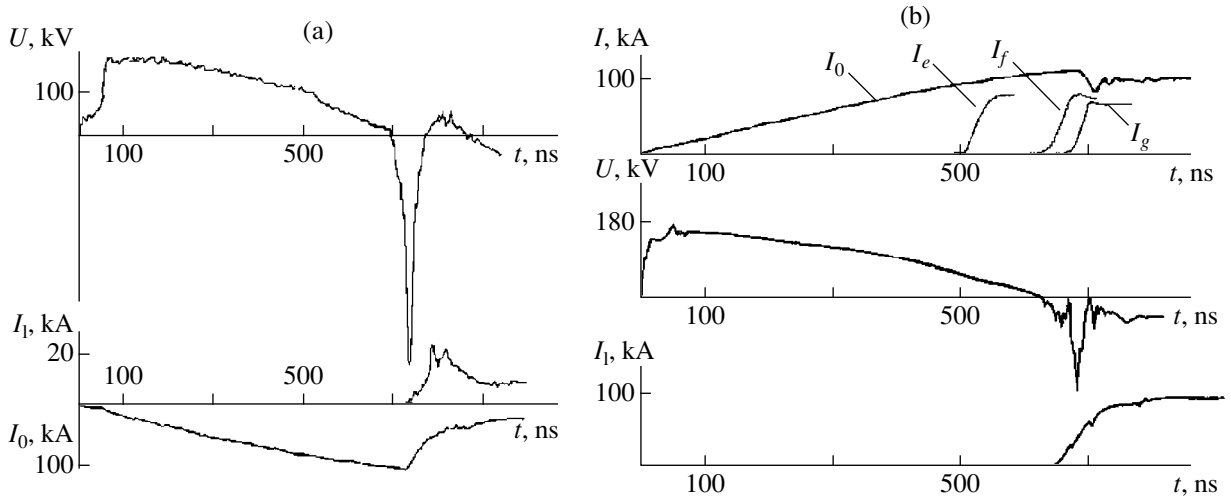

Fig. 2. Typical waveforms of (a) the voltage $U = LdI/dt$ at the inductance coil of the Marx–POS circuit, the diode current I_l, and the generator current I_0 for a POS loaded with a diode and (b) the generator current I_0; the currents I_e, I_f, and I_g from shunts *e*, *f*, and *g*, respectively; the loop voltage *U*; and the load current I_l for a POS loaded with an inductance coil.

4. EXPERIMENTAL RESULTS

The velocity of the current channel was determined from the instants at which the shunt signals reached 0.5 of their amplitude values (see Fig. 2b). As the current channel passed near shunts *e*, *f*, and *g*, its velocity was measured to be $\sim 3 \times 10^7$, 10^8, and 5×10^8 cm/s, respectively. By the instant of the current break, this velocity exceeded 5×10^8 cm/s. Note that the current recorded with these shunts is about 80% of the total current. The remaining 20% of the current flows through the plasma. Comparing the shapes of the shunt signals with each other, we can see that, when passing from shunt *e* to shunt *g*, the steepness of the current front increases slightly, whereas its velocity increases from 30 to 500 cm/μs. This fact evidences that the spatial width of the front increases; by the end of the conduction phase, it increases nearly threefold.

Figure 3 presents the waveforms of the generator current and the signals from four *dB*/*dt* detectors (denoted as *a*–*d* in Fig.1), one pair of which is placed at the cathode (central electrode) and the other one is placed at the anode. The propagation velocity of the magnetic field along the cathode, which was estimated from the instants corresponding to the maximums of the signals from detectors *a* and *b*, is nearly the same as the current-channel velocity measured with shunts. The propagation velocity along the anode, which was determined with the help of detectors *c* and *d*, is somewhat less. The fact that these velocities are different indicates that the current front is tilted, assuming that the current flows along straight lines between the corresponding points at the cathode and anode. Thus, the current front looks like a fragment of a cone; by the instant of the current break, the cone angle is about ~100°.

It is worth noting that the signals from the anode loops start nearly simultaneously with the generator current I_0 and, when the main *dB*/*dt* signals appear, these fast signals have reached 20–30% of the amplitude value. The origin of the fast signals may be attributed to one or both of two effects: (i) the penetration of the magnetic field into the gaps among the plasma flows near the anode surface, where the plasma guns are placed [9], and (ii) fast penetration into the anode region [13]. At the reversed polarity, when the central electrode is an anode, the effect of fast penetration into the anode region is also observed, although to a lesser extent. This is illustrated in Fig. 4, where the signals from shunt *f* (Fig. 1) are presented for both the negative and positive polarities of the central electrode. The operating regimes were chosen such that, in both cases, the current breaks occurred at the same instants (500 ns). The shapes of the signals are quite different; when the central electrode is positive, a prepulse with a duration of about 50 ns appears before the onset of the main current. The prepulse current amplitude is about 10% of the main current. The propagation velocity of the main current along the central electrode does not depend on the electrode polarity.

5. INFLUENCE OF THE POS CATHODE LENGTH

The position of the detector (the signal from which is detected just before the break) determines the farthest point reached by the current wave during the conduction phase and, therefore, the effective POS length, which, in our case, does not exceed 45 cm.

This effective length is nearly the same as the length of the cathode fragment exposed to ion bombardment. The bombardment results in the appearance of a distinct polished area on the cathode with a 10-cm-wide

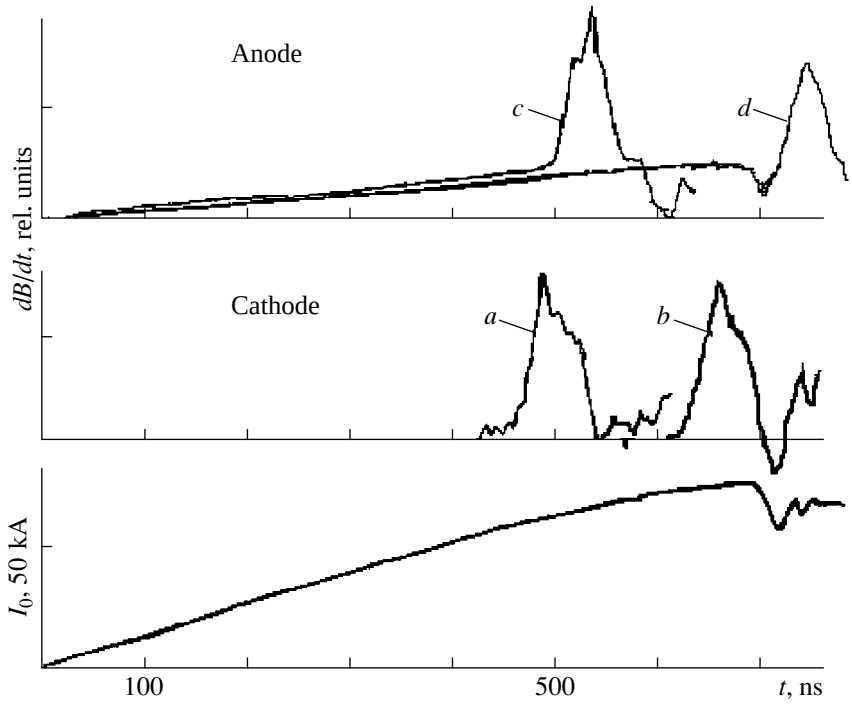

Fig. 3. Waveforms of the dB/dt signals from detectors *a–d* (see Fig. 1) and the generator current I_0.

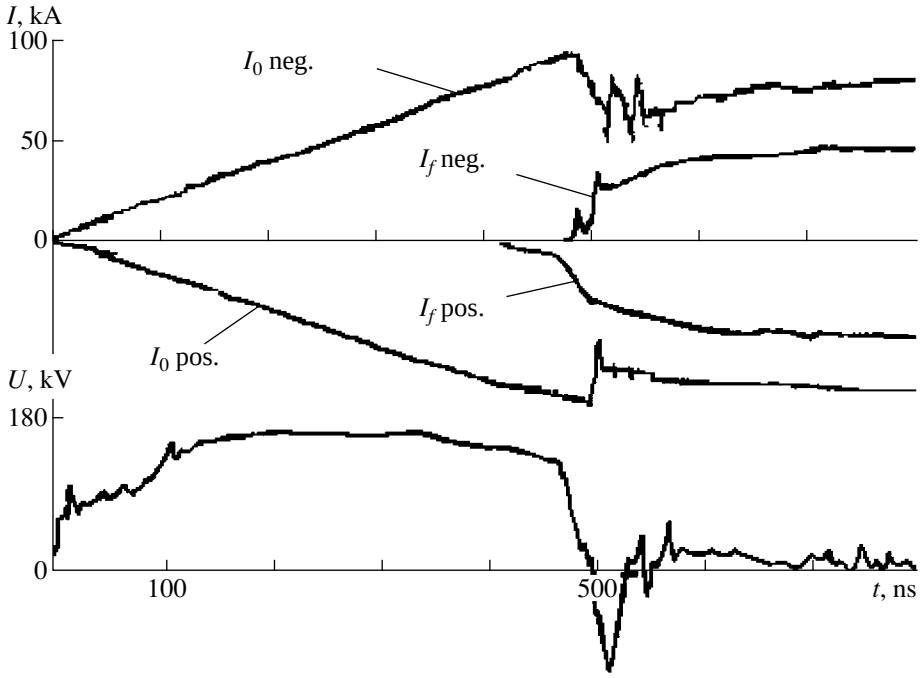

Fig. 4. Waveforms of the generator current I_0 and shunt current I_f at negative and positive polarities of the central electrode and the loop voltage U.

blurred border on the load side. The length of the polished area is 35–45 cm and is almost independent of the type of load (high-impedance diode or inductance coil).

Does the POS effective length in question have a real physical meaning? To answer this question, we have studied the influence of the cathode length on the POS operation. The dependence of the voltage at the POS on the cathode (central electrode) length is shown in Fig. 5. It is seen that the fastest current break and the highest voltage amplitude occur at cathode lengths not

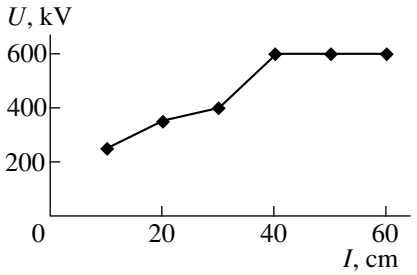

Fig. 5. Amplitude of the POS voltage vs. the length of the central electrode (cathode).

shorter than 40 cm, e.g., at lengths longer than the POS effective length. As soon as the cathode length becomes less than the effective length of the region exposed to the ion flux, the voltage at the POS decreases. Unfortunately, the experimental data obtained do not provide an unambiguous explanation of this fact, which is of great practical importance.

6. DISCUSSION OF THE RESULTS

Undoubtedly, the propagation of the magnetic field (or current) from the diode toward the load in the form of a wave with a fairly steep front is worthy of discussion. The front accelerates during the propagation and has the highest velocity just before the break. Simultaneously, the front width also increases, however, not in proportion to the acceleration, but to a lesser extent. Certainly, no diffusion mechanisms can be responsible for such penetration of the field into a conducting medium.

Therefore, in contrast to common opinion, switching the current to the load cannot only be reduced to the dynamics of the plasma-filled diode. The processes in the rarefied plasma that expands from the diode towards the load seem to be important for the POS operation. This conclusion is in good agreement with the recent work covered in [14]. The existence of the optimum length of a coaxial POS found by us is also evidence in favor of this conclusion. We will give a detailed explanation of this effect in a subsequent paper.

The effect of the field penetration into a conducting (even a perfectly conducting) medium via a strongly nonlinear wave is well known and can be explained within electron magnetohydrodynamics (EMHD) [1, 2]. This effect was first observed in the POS experiments [3]. The POS parameters in the conduction phase always lie within the EMHD applicability range:

$$V_{Te}, V_{Ae} \gg j/ne \gg c_S, V_A,$$

$$\omega_{Be} \gg \tau \gg \omega_{Bi},$$

$$c/\omega_{pe} \ll a \ll c/\omega_{pi}.$$

Here, a and τ are the characteristic space and time scales of the problem, respectively, other notations being standard. It follows from the last inequality that, if the plasma parameters in the interelectrode gap of the diode are within the EMHD applicability range, then the same is certainly true for the parameters of a rarefied plasma outside the diode. The nonlinear wave responsible for the convective transport of the magnetic field [1], often referred to as a Kingsep–Mokhov–Chukbar (KMC) wave, can be derived from one of the basic EMHD equations,

$$\partial \mathbf{B}/\partial t = \frac{1}{8\pi e}\nabla \ln n \times \nabla B^2 + \frac{c^2}{4\pi\sigma}\nabla^2 \mathbf{B}.$$

This wave is caused by the transverse density gradient. In the case of axial symmetry, the quantity $\nabla(nr^2)$ serves as such a gradient; hence, the characteristic spatial scale $\delta \sim |\nabla \ln(nr^2)|^{-1}$ enters all the basic relations. The characteristic solution is

$$B = \frac{B_0}{2}\left\{1 - \tanh\frac{x - V_{\mathrm{KMC}}t}{\Delta}\right\},$$

where $V_{\mathrm{KMC}} \approx V_{\mathrm{A}}\dfrac{c}{\omega_{pi}\delta} \gg V_{\mathrm{A}}$ and $\Delta \approx \dfrac{ne\delta c^2}{\sigma}$.

Thus, according to this approach, the front of the magnetic-field wave propagates with a velocity much higher than the velocity of the preceding expansion of the substance (the front velocity greatly exceeds the Alfvén velocity); therefore, the profile of the plasma density can be considered time-independent. Since the density certainly decreases along the direction of expansion and $V_{\mathrm{KMC}} \propto n^{-1}$, one of the effects in question, namely, the front acceleration, can be explained quite reasonably.

There is not such a clear explanation for the effect of the front widening. In the case of Coulomb conductivity, which depends only on the temperature, the shrinking of the front should occur because $\Delta \propto n$. A self-consistent account of plasma heating at the front of the KMC wave can only enhance the effect.

However, it should be noted that the first row of the inequalities that determine the EMHD applicability range also determines the range of plasma parameters in which the effects of anomalous resistance and turbulent plasma heating are of importance (see, e.g., [15]). Moreover, it is this regime in which our POS operated, which was confirmed experimentally in [16] (see also [17]). A peculiarity of the regime of anomalous resistance is that the momentum exchange between electrons and ions, which are accelerated by the electric field in opposite directions, occurs via emission and absorption of one or another type of plasma waves, rather than via Coulomb collisions. When the plasma is incompletely magnetized,

$$B^2 \ll 4\pi nmc^2,$$

which is certainly true in our case, ion-acoustic fluctuations act as momentum carriers. If the current in a system is determined by an external electric circuit, then only the strongly nonlinear regime of the ion-acoustic instability is possible [15]; in this case, the conductivity is determined by the Sagdeev formula

$$\sigma = \omega_{pe}\frac{neV_{Te}}{j},$$

or, analogously,

$$\mathbf{j} \approx n^{3/4}eT^{1/4}m^{-1/2}\mathbf{E}.$$

Let us substitute this dependence into the expression for Δ, taking into account that the current density at the wave front is inversely proportional to the front width, $j \propto I/\Delta$, where I is the total current in the plasma. Then, we have

$$\Delta \approx \frac{ne\delta c^2}{\sigma} \propto \frac{nI}{n^{3/2}\Delta} \Rightarrow \Delta \propto n^{-1/4},$$

which means that the acceleration of the front of the KMC wave should be accompanied by the front widening, which, however, should be less pronounced than the acceleration. In our opinion, such an explanation seems to be reasonable and self-consistent.

7. CONCLUSION

Based on the above measurements, we can draw the following preliminary conclusions about the plasma dynamics in the conduction phase of a high-impedance POS. A specific feature of the magnetic-field propagation along the anode surface is the existence of a fast prepulse; the propagation velocity of the main magnetic-field wave at the anode is less than that at the cathode. Both the current channel and the front of the magnetic-field wave accelerate along the POS axis; their propagation velocity increases from 0.3×10^8 to 5×10^8 cm/s. This acceleration is fairly well described by the EMHD formula for the penetration velocity of the magnetic-field wave (KMC wave). The widening of the current front during the acceleration toward the load can be estimated as $\Delta \propto n^{-1/4}$.

The propagation of the current channel toward the load determines the minimum length of the cathode (40 cm for our POS) that serves as an ion current collector; at shorter lengths, the voltage induced at the POS during the current break significantly decreases.

ACKNOWLEDGMENTS

This work was supported by INTAS (grant no. 97-0021 CRDF RP1-2113) and the Russian Foundation for Basic Research (project no. 99-02-16659).

REFERENCES

1. A. S. Kingsep, Yu. V. Mokhov, and K. V. Chukbar, Fiz. Plazmy **10**, 854 (1984) [Sov. J. Plasma Phys. **10**, 495 (1984)].
2. A. S. Kingsep, K. V. Chukbar, and V. V. Yan'kov, in *Reviews of Plasma Physics*, Ed. by V. V. Kadomtsev (Énergoizdat, Moscow, 1987; Consultants Bureau, New York, 1990), Vol. 16.
3. R. A. Meger, R. J. Commisso, G. Cooperstein, and S. A. Goldstein, Appl. Phys. Lett. **42**, 943 (1983).
4. S. S. Payne, T. W. Hussey, R. W. Stinnett, and N. F. Roderick, IEEE Trans. Plasma Sci. **PS-15**, 824 (1987).
5. V. M. Bystritskiĭ, Ya. E. Krasik, I. V. Lisitsin, *et al.*, in *Proceedings of the 8th All-Union Symposium on High-Current Elecronics, Sverdlovsk, 1990*, Part 3, p. 112; P. S. Anan'in, V. B. An, Ya. E. Krasik, *et al.*, *ibid*, p. 115.
6. J. Commisso, P. J. Goodrich, J. M. Grossmann, *et al.*, Phys. Fluids B **4**, 2368 (1992).
7. M. Sarfaty, R. Shpitalnik, B. Arad, *et al.*, Phys. Plasmas **2**, 2583 (1995).
8. G. S. Belen'kiĭ, Yu. P. Golovanov, G. I. Dolgachev, *et al.*, Fiz. Plazmy **21**, 897 (1995).
9. G. I. Dolgachev, L. P. Zakatov, and A. G. Ushakov, Fiz. Plazmy **17**, 1171 (1991) [Sov. J. Plasma Phys. **17**, 679 (1991)].
10. N. U. Barinov, G. S. Belen'ki, G. I. Dolgachev, *et al.*, IEEE Trans. Plasma Sci. **23**, 945 (1995).
11. G. I. Dolgachev, L. P. Zakatov, and A. G. Ushakov, IEEE Trans. Plasma Sci. **26**, 1410 (1998).
12. G. I. Dolgachev, M. S. Nitishinsky, and A. G. Ushakov, in *Proceedings of the 11th IEEE International Pulsed Power Conference, Baltimore, Maryland, 1997*, Vol. 1, p. 281.
13. A. V. Gordeev, A. V. Grechikha, and Ya. L. Kalda, Fiz. Plazmy **16**, 95 (1990) [Sov. J. Plasma Phys. **16**, 55 (1990)].
14. Ya. Krasik, A. Dunaevsky, J. Felsteiner, and J. R. Gouer, J. Appl. Phys. **85**, 686 (1999).
15. A. S. Kingsep, Fiz. Plazmy **17**, 582 (1991).
16. G. I. Dolgachev, L. P. Zakatov, Yu. G. Kalinin, *et al.*, Fiz. Plazmy **22**, 1017 (1996) [Plasma Phys. Rep. **22**, 921 (1996)].
17. A. Weingarten, S. Alexiou, Y. Maron, *et al.*, Phys. Rev. E **59**, 1096 (1999).

Translated by N.N. Ustinovskiĭ

Plasma Physics Reports, Vol. 27, No. 1, 2001, pp. 68–75. Translated from Fizika Plazmy, Vol. 27, No. 1, 2001, pp. 71–78.

LOW-TEMPERATURE PLASMA

Generation of Plasma Oscillations in a Low-Pressure Microwave Discharge

A. M. Bystrov and V. B. Gildenburg

Institute of Applied Physics, Russian Academy of Sciences, ul. Ul'yanova 46, Nizhni Novgorod, 603600 Russia

Received May 12, 2000; in final form, June 20, 2000

Abstract—The resonant excitation of plasma (Langmuir) oscillations during the microwave breakdown of a low-pressure gas is studied both analytically and numerically using the simplest uniform model. It is shown that, because of a significant delay in electron heating and cooling, this effect ensures that the plasma density increases at a high (resonant) rate, even after exceeding a critical value, and can reach a very high (overcritical) level. © *2001 MAIK "Nauka/Interperiodica".*

In the dynamics of a low-pressure microwave discharge, an important role is played by the plasma resonance phenomenon, which implies that the electric field amplitude becomes very large as the plasma density approaches a critical value. In particular, this phenomenon significantly increases the propagation velocity of the ionization fronts [1, 2] and gives rise to the so-called plasma-resonance ionization instability in both microwave and optical discharges [3, 4].

Previously, the dynamics of ionization processes under plasma resonance conditions was studied theoretically by taking into account the fact that the amplitude of the forced oscillations increases resonantly at the frequency of the external source, but without consideration of the accompanying "transient" excitation of natural plasma oscillations at the plasma (Langmuir) frequency at the instant when it passes through the critical value equal to the frequency of the external field. The time scales on which the natural plasma oscillations are damped (in a collisional or collisionless regime) after their excitation in low-pressure discharges may be fairly long. For this reason, the electric field in the excitation region remains at a high (resonant) level over much longer time scales than the forced oscillations, which are rapidly damped after the plasma density exceeds a certain critical value. As a result, the overall dynamic picture of the discharge changes markedly: in particular, after exceeding the critical (resonant) value, the plasma density continues to grow at a high rate to a level well above the critical level, in which case the spectrum of the excited Langmuir fields significantly changes in an adiabatic fashion as time elapses.

Our purpose here is to qualitatively analyze and numerically model the generation of Langmuir fields and their effect on the discharge dynamics using the simplest uniform model, which takes into account the delays of both the polarization response and the Joule heating of electrons under the plasma resonance conditions but neglects the spatially nonlocal character of the latter two processes. This model actually describes how the electric field and the plasma evolve in a thin (compared to the wavelength of the electromagnetic wave) isolated layer oriented perpendicular to the external electric field. Such layers appear during gas breakdown in an electromagnetic field in the nonlinear stage of ionization instability. It is in these layers that the plasma density increases above the critical level. At this stage of investigation, we disregard the following circumstance, which complicates a theoretical analysis: in these layers, the profiles of the field amplitude and plasma density may become strongly peaked during the breakdown [4–6], so that the nonlocal effects, which we neglect here, will become important. Qualitative estimates and preliminary results from simulations of the dynamics of a nonuniform breakdown [7] (with consideration of nonlocal effects due to spatial dispersion, diffusion, and heat conduction) show that, in the range of discharge parameters under consideration (see below), the uniform model provides a fairly good description of the discharge dynamics in regions where the plasma density is the highest.

The main physical factors governing the evolution of the electromagnetic field and plasma are assumed to be the electron-impact ionization of gas molecules, electron attachment to neutral molecules, electron–molecule collisions, and the effect of the produced plasma on the microwave field. The basic set of equations consists of the equations for the longitudinal electric field $\mathbf{E} = \mathbf{x}_0 E(t)$ and longitudinal electron current density $\mathbf{j} = \mathbf{x}_0 j(t)$,

$$j + \frac{1}{4\pi}\frac{dE}{dt} = J = J_0 \cos\omega t, \tag{1}$$

$$\frac{dj}{dt} = \frac{e^2 N}{m} E - \nu j \tag{2}$$

1063-780X/01/2701-0068$21.00 © 2001 MAIK "Nauka/Interperiodica"

and the balance equations for the electron density (plasma density) $N(t)$ and electron temperature (mean energy) $T_e(t)$,

$$\frac{dN}{dt} = (\nu_i - \nu_a)N, \tag{3}$$

$$\frac{dT_e}{dt} = \frac{2}{3N}\langle jE\rangle - \delta_T\nu(T_e - T_g). \tag{4}$$

Here, ν is the effective collision frequency, ν_i is the electron-impact ionization rate, ν_a is the electron attachment rate, e and m are the charge and mass of an electron, δ_T is the mean fraction of energy lost by an electron in (mainly, inelastic) collisions with an atom or a molecule, T_g is the gas temperature, and the angular brackets stand for averaging over the period of the alternating electric field.

In the uniform quasistatic model (the model of a "plane capacitor"), Eq. (1) determines the total current density J, which is regarded as a prescribed harmonic function of time t with a constant amplitude J_0 and constant frequency ω. The local constitutive equation (2) is valid for any arbitrary time function $N(t)$ changes, provided that the electrons originate at a zero velocity or obey an isotropic distribution over initial velocities. In the balance equations (3) and (4), the difference between the electron-impact ionization rate and the electron loss rate, $\nu_i - \nu_a$, and the factor δ_T are regarded as prescribed functions of temperature and are approximated by the expressions

$$\nu_i - \nu_a = \nu_a\left(\frac{(T_e/T_{cr})^\beta}{1 + [(T_e - T_{cr})/T_s]^\beta} - 1\right), \tag{5}$$

$$T_s = T_{cr}(\nu/\nu_a)^{1/\beta},$$

$$\delta_T = \delta_{T0} + \frac{T_e - T_{cr}}{T_e + T_s} \quad \text{for} \quad T_e > T_{cr}, \tag{6}$$

$$\delta_T = \delta_{T0} \quad \text{for} \quad T_e < T_{cr}.$$

The parameters ν_a, δ_T, T_{cr}, and β and the electron–molecule collision frequency ν are assumed to be constant. Since the electron velocity distribution function in a discharge plasma is usually far from being Maxwellian, the notion of "temperature" is here rather conditional. Equation (4) should in fact be treated as the simplest phenomenological equation for a functional of the electron energy distribution T_e, which determines the rates of the main processes in the balance equation (3). The approximate expressions (5) and (6) correctly describe the most important issues in our problem: the existence of a threshold temperature for the breakdown, T_{cr} ($\nu_i(T_{cr}) = \nu_a$); a sharp increase in ν_i (determined by the power-law index β) as T_e increases to $T_e \sim T_{cr}$ with the related saturation level $\nu_i \simeq \nu$ in the range $T_e > T_s$; and an increase in the inelastic losses δ_T with the related saturation level $\delta_T \simeq 1$ in the range $T_e > T_s$. We also assume that the following conditions are satisfied: $\nu \gg \nu_a$ (and, accordingly, $T_s \gg T_{cr}$), $T_{cr} \gg T_g$, and $\nu \ll \omega$.

Eliminating the current density j in Eqs. (1) and (2), we can see that the electric field E satisfies the following oscillator equation with a friction coefficient ν, time-dependent frequency $\omega_p = \sqrt{4\pi e^2 N(t)/m}$ of the natural plasma oscillations, and prescribed time-dependent harmonic function $F = 4\pi(\partial J/\partial t + \nu J) = 4\pi J_0(-\omega\sin\omega t + \nu\cos\omega t) = F_0\cos(\omega t + \varphi_0)$ on the right-hand side:

$$\frac{d^2E}{dt^2} + \nu\frac{dE}{dt} + \omega_p^2(t)E = F_0\cos(\omega t + \varphi_0). \tag{7}$$

Equation (7) describes the well-known phenomenon of the resonant excitation of natural oscillations. This phenomenon was previously analyzed in the context of various physical oscillators under the assumption that the natural frequency changes according to a prescribed (linear) law [8, 9]. Here, we are interested in solving the differential equations (1)–(4) [or, equivalently, Eqs. (3), (4), and (7)] in the case where the plasma frequency changes sufficiently slowly ($d\omega_p^2/dt \ll \omega^3$) and the initial conditions correspond to the initial stage of breakdown. We assume that, at the initial instant $t = 0$, the electron density is far below the critical level, $N(0) = N_0 \ll N_{cr} = m(\omega^2 + \nu^2)/4\pi e^2$, the plasma frequency being $\omega_p(0) \ll \omega$; the electron current $j(0)$ is low in comparison with the displacement current $dE/4\pi dt$; the electron temperature is equal to the equilibrium temperature T_{eq}, which satisfies Eq. (4) with $dT_e/dt = 0$ (provided that the field and current are harmonic functions of time); and the electric field amplitude $E(0)$ and related electron temperature $T_e(0) = T_{eq}(0)$ slightly exceed the threshold for breakdown, E_{cr}, $T_{cr} = E_{cr}^2/[3\delta_{T0}m(\omega^2 + \nu^2]$.

The above equations enable us to analyze how the field and plasma will evolve. The entire evolution process can be divided into three main stages, which correspond to different ranges of the plasma density $N(t)$.

(i) The preresonance stage ($N_0 < N < N_{cr} - \Delta N$), in which the solution to Eq. (7) describes forced oscillations at the frequency ω of the external source; the oscillation amplitude gradually increases as the plasma density approaches a resonant value.

(ii) The stage of generation of natural plasma oscillations when the plasma density increases from just below to just above the critical value ($N_{cr} - \Delta N < N < N_{cr} + \Delta N$). We will show that, under conditions corresponding to the breakdown of a low-pressure gas, $\Delta N \ll N_{cr}$ holds; i.e., the natural plasma oscillations are excited in a narrow density range in the vicinity of the critical density.

(iii) The stage of adiabatic evolution of the amplitude and frequency of the excited plasma oscillations accompanied by their collisional damping (in the density range $N > N_{cr} + \Delta N$). This stage is characterized by a fast explosive ionization process, which, however, occurs on a time interval long enough for the plasma density to increase far above the critical level ($N \gg N_{cr}$). After the ionization process, the plasma density N slowly decreases to approximately the critical steady-state value, $N_s \sim N_{cr}$.

In the first two stages, the electric field in the plasma can be assumed to be quasi-harmonic, $E = \mathrm{Re}(\tilde{E}(t)\exp(-i\omega t))$. Under this assumption, we can switch to a description of the evolution of the complex amplitude $\tilde{E}$ (a "slowly varying envelope") by using the following first-order reduced equation, which is a consequence of Eq. (7):

$$\left(\frac{2i}{\omega} + \frac{\nu}{\omega}\right)\frac{d\tilde{E}}{dt} + \varepsilon\tilde{E} = \tilde{D}, \tag{8}$$

where $\varepsilon = 1 - (N/N_{cr})(1 + i\nu/\omega)^{-1}$ is the time-dependent complex plasma dielectric function and $\tilde{D} = 4\pi i J_0/\omega$ is a given amplitude of the electric induction $D = \mathrm{Re}(\tilde{D}\exp(-i\omega t))$, which is related to the total current density J by $dD/dt = 4\pi J$. In the range of validity of Eq. (8), the mean power of the field energy losses [the power of the external source in the energy balance equation (4)] is equal to

$$\langle jE\rangle = (e^2 N\nu/2m\omega^2)|\tilde{E}|^2. \tag{9}$$

We introduce the dimensionless variables $\tau = \nu_a t$, $\mathrm{E} = \tilde{E}/E_{cr}$, $n = N/N_{cr}$, and $T = T_e/T_{cr}$ and the parameters $D_0 = \tilde{D}/E_{cr}$, $\delta_a = \nu_a/\omega$, $\delta = \nu/\omega$, and $\mu = \nu_a/\nu$ in order to rewrite the density and temperature balance equations, the reduced equation for the electric field amplitude, and the initial conditions as

$$2i\delta_a\frac{d\mathrm{E}}{d\tau} + \varepsilon\mathrm{E} = D_0, \quad \varepsilon = 1 - n(1 - i\delta), \tag{10}$$

$$\frac{dn}{d\tau} = (f(T) - 1)n, \quad f(T) = \frac{T^\beta}{1 + \mu(T-1)^\beta}, \tag{11}$$

$$\frac{dT}{d\tau} = \frac{1}{\mu}(\delta_{T0}|\mathrm{E}|^2 - \delta_T(T)T),$$
$$\delta_T = \delta_{T0} + \frac{T-1}{T + \mu^{-1/\beta}}, \tag{12}$$

$$n(0) = n_0 \ll 1, \quad \mathrm{E}(0) = \mathrm{E}_0 = D_0/\varepsilon(0),$$
$$T(0) = T_0 \approx |\mathrm{E}_0|^2 > 1. \tag{13}$$

For estimates and calculations, we adopt the reference parameter values

$$\delta = 1.5\times10^{-2}, \quad \mu = \delta_a/\delta = 10^{-5}, \quad \beta = 2.7,$$
$$D_0 = 1.5, \quad \delta_{T0} = 0.05. \tag{14}$$

According to the reference data presented, e.g., in [10, 11], these values correspond to air breakdown at a pressure of $p \approx 0.4$ torr in an electric field with a frequency of $\omega \approx 1.9\times10^{11}$ s^{-1} (the wavelength being $\lambda = 1$ cm) and an initial amplitude of $1.5E_{cr}$ (with $E_{cr} \approx 1.8$ kV/cm, which corresponds to $T_{cr} \approx 1$ eV). These parameter values allow the basic equations to be somewhat simplified (see below). In particular, in the first two stages of the process under discussion, we can assume that the dielectric function in the field equation is purely real, setting $\varepsilon = 1 - n$. Also, in these stages, the dimensionless electron temperature T remains at least two times lower than the value $T_s/T_{cr} = \mu^{-1/\beta} \approx 72$, at which the dependences $\nu_i(T)$ and $\delta_T(T)$ start to saturate. In this case, the parameter μT^β in the expression for ν_i is much smaller than unity and the density balance equation becomes

$$\frac{dn}{d\tau} = (T^\beta - 1)n. \tag{15}$$

Let us describe the entire evolution process at different stages and estimate the characteristic values of ε related to the transitions from one stage to another.

1. Preresonance Stage

In the reduced field equation (10), we can also omit the term with the first time derivative and describe the adiabatic evolution of the field amplitude by the simple relationship

$$\mathrm{E} = D_0/\varepsilon. \tag{16}$$

This stage is characterized by three successive electron heating regimes in which the plasma density and field amplitude change according to different laws.

When $n \ll 1$, the field amplitude and electron temperature are constant and are close to their prescribed initial values. The gas is ionized in an avalanche fashion: the plasma density increases according to the exponential law $n = n_0\exp(\gamma_0 t)$ at a rate equal to $\gamma_0 = T_0^\beta - 1$.

Then, because of a decrease in $\varepsilon = 1 - n$, the field amplitude and plasma temperature and density all increase at a progressively higher rate. However, during a certain time interval, the temperature at each instant remains close to its equilibrium level $T_q = T_{eq}/T_{cr}$, which follows from the equation $T_q\delta_T(T_q) = |\mathrm{E}|^2\delta_{T0}$. In the temperature range $T \gg \delta_{T0}/\mu^{1/\beta} \approx 3.14$, the functions

$\delta_T(T)$ and $T_q(|E|)$ are almost linear, $\delta_T(T) \approx \mu^{1/\beta}T$ and $T_q = |E|\sqrt{\delta_{T0}/\mu^{1/\beta}} \approx 1.9|E|$, and the discharge evolution is described by the equation

$$\frac{d\varepsilon}{d\tau} = -\frac{q}{\varepsilon^\beta}, \quad q = \delta_{T0}^{\beta/2}\mu^{1/2}D_0. \tag{17}$$

This equilibrium heating regime occurs under the condition

$$\frac{dT_q}{d\tau} \ll \frac{\delta_{T0}}{\mu}|E|^2. \tag{18}$$

According to Eqs. (15) and (16), condition (18) holds until the dielectric function ε remains sufficiently large in comparison with a certain characteristic value ε_q:

$$\varepsilon^\beta \gg \varepsilon_q^\beta = (D_0^2\delta_{T0}\mu^{1/\beta})^q, \quad q = (\beta - 1)/2. \tag{19}$$

Finally, in the range $\varepsilon < \varepsilon_q$, the electron heating becomes nonequilibrium and the temperature increases at a much slower rate than the field amplitude and satisfies the following approximate equation in the range of validity of relationship (16):

$$\frac{dT}{d\tau} = \frac{\delta_{T0}}{\mu}\frac{D_0^2}{|\varepsilon|^2}. \tag{20}$$

This equation and the equation

$$\frac{d\varepsilon}{d\tau} = -T^\beta, \tag{21}$$

which follows from Eq. (15) in the range $|\varepsilon| \ll 1$, constitute the full set of equations describing the discharge dynamics at the end of the preresonance stage. Let $\varepsilon = \varepsilon_q$ be the conventional boundary between the ranges corresponding to the equilibrium and nonequilibrium electron heating regimes (for the parameter values at hand, we have $\varepsilon_q = 0.15$). Then, it is a simple matter to qualitatively describe the behavior of the functions $\varepsilon(t)$ and $T(t)$ in each of these ranges. In particular, over a certain finite time interval ($\tau < \tau_0 = \text{const}$) in the nonequilibrium heating regime, the solution to Eqs. (20) and (21) in the range $\mathrm{Re}\,\varepsilon \gg \delta$ can be represented as

$$\varepsilon = \frac{(\beta + 1)\delta_{T0}D_0^2}{\mu T^{\beta+1}}, \quad T(\tau) = \frac{1}{[A(\tau_0 - \tau)]^p},$$
$$p = \frac{1}{2\beta + 1}, \quad A = \frac{\mu(2\beta + 1)}{\delta_{T0}D_0^2(\beta + 1)^2}. \tag{22}$$

Hence, within the above approximation, in which the electric field is described by the simplest expression (16) and the dielectric function ε is assumed to be purely real (in other words, the collisional losses and the generation of Langmuir waves are both neglected), the electron heating, even when delayed, is explosive in character: at a certain time τ_0, the dielectric function ε vanishes and the field amplitude and electron temperature become infinite.

2. Stage of the Generation of Langmuir Oscillations

In the preresonance stage, we omitted the first term $2i\delta_a dE/d\tau$ in Eq. (10). We can estimate this term using relationships (16) and (22) and find that it can be neglected under the condition

$$|\varepsilon|^p \gg \varepsilon_r^p = [2(1 + \beta)\delta_{T0}D_0^2(2\delta_a)^{1/\beta}\delta]^{\beta/(\beta+1)}, \quad p = (3\beta + 2)/(\beta + 1). \tag{23}$$

Knowing the parameter ε_r (which in the numerical example at hand is equal to 5×10^{-2}), we can estimate the maximum field amplitude $|E_r|$ and maximum electron temperature T_r in the resonant range $\mathrm{Re}\,\varepsilon < \varepsilon_r$. From (20)–(23), we obtain

$$|E_r| \approx \frac{D_0}{\varepsilon_r} = 30,$$
$$T_r \approx \left[\frac{(\beta + 1)\delta_{T0}D_0^2}{\mu\varepsilon_r}\right]^{1/(\beta+1)} = 33. \tag{24}$$

Note that, when the collisionality parameter $\delta = \nu/\omega$ is larger than ε_r, inequality (23) holds for any plasma density by virtue of the obvious relationship $|\varepsilon| > \delta$, in which case the simplest expression (16) for the steady-state amplitude of the forced oscillations of the electric field remains valid during the discharge evolution and the excitation of natural plasma oscillations can be ignored. Taking into account the fact that, in our model of gas breakdown, the quantity $\delta_a/\delta = \mu = 10^{-5}$ is a pressure-independent constant, we turn to inequality (23) to find the quantity ε_r as a function of the parameter δ. From the condition $\delta \gg \varepsilon_r(\delta)$, we determine the range of δ values in which essentially no plasma oscillations are excited:

$$\delta^s \gg \delta_{\min}^s = 2\mu[2(\beta + 1)\delta_{T0}D_0^2]^\beta, \quad s = 2\beta + 1. \tag{25}$$

For the parameter values (14), we obtain $\delta_{\min} = 0.17$, which corresponds to an air pressure of about $P \approx 7$ torr at the wavelength $\lambda = 1$ cm.

Now, we examine the field evolution in the density range from just below to just above the critical value. In this range, inequality (23) fails to hold (i.e., the quantity $|N_c - N|$ is comparable with or smaller than $\Delta N \equiv \varepsilon_r N_c$), and both terms should be kept on the left-hand side of the field equation (10), which is valid in the limit $|\varepsilon| \ll 1$. The general solution to Eq. (10) for the complex amplitude of the electric field has the form

$$E = \exp(-f(\tau))\left[-\frac{iD_0}{2\delta_a}\int_0^\tau \exp(f(\tau'))d\tau' + C_1\right], \tag{26}$$

where $f(\tau) = \frac{i}{2\delta_a}\int_0^\tau (n - 1 - i\delta n)d\tau'$, $C_1 = \mathrm{E}(0)$ is a complex constant equal to the field amplitude at the resonant point, and the initial time is chosen to satisfy the condition $n(\tau = 0) = 1$. In the immediate vicinity of the resonant point $n = 1$, we can approximate the function $n(\tau)$ by the linear dependence

$$n(\tau) = 1 + \dot{n}(0)\tau, \tag{27}$$

where $\dot{n}(0) = dn/d\tau(0)$. We also introduce the new variable $\tau' = \sqrt{\dot{n}(0)/(4\delta_a)}\,\tau$ and the notation

$$\psi(\tau') = \exp[-i(\tau')^2 - \gamma\tau'], \quad \gamma = \delta/\sqrt{\delta_a\dot{n}(0)}, \tag{28}$$

in order to write solution (26) as

$$\mathrm{E}(\tau') = \psi(\tau')\left[-\frac{iD_0}{\sqrt{\delta_a\dot{n}(0)}}\int_0^{\tau'}\frac{dt'}{\psi(t')} + C_1\right], \tag{29}$$

which can be expressed in terms of Fresnel integrals. For $|\tau'| \gg 1$ with $\tau' < 0$ ($n < 1$), solution (29) obeys the asymptotic expression

$$\mathrm{E}(-\tau' \gg 1) = -\frac{D_0}{\sqrt{4\delta_a\dot{n}(0)}\tau' - i\delta} + \left(\frac{-iD_0}{\sqrt{\delta_a\dot{n}(0)}}I + C_1\right)\exp[-i(\tau')^2 - \gamma\tau'], \tag{30}$$

where

$$I = \int_0^{-\infty}\exp(ix^2 + \gamma x)dx = \sqrt{\frac{\pi}{2}}\exp(i\gamma^2/4)\left(-\frac{1+i}{2} + S(\gamma/\sqrt{2\pi}) + iC(\gamma/\sqrt{2\pi})\right), \tag{31}$$

and S and C are Fresnel integrals.

The constant C_1 can be found by matching the asymptotic expression (30) with the solution $\mathrm{E} = D_0/\varepsilon$, which refers to the preresonance stage and coincides with the first term in (30) in the region where the linear dependence (27) is valid:

$$C_1 = \mathrm{E}(0) = iD_0 I/\sqrt{\delta_a\dot{n}(0)}. \tag{32}$$

Substituting the derivative $\dot{n}(0) \approx T_r^\beta$ into expression (32), we find the field amplitude at the instant when the plasma density passes through the critical value: $|\mathrm{E}(0)| \approx 38$, which is comparable in magnitude to the amplitude of the resonant field estimated in expression (24).

In the range of large positive τ' values ($n > 1$), the asymptotic form of solution (29) differs from (30) in that it contains the nonzero factor $2C_1$ in front of the exponential function in the second term (in the range $\tau' < 0$, this factor vanishes):

$$\mathrm{E}(\tau' \gg 1) = -\frac{D_0}{\sqrt{4\delta_a\dot{n}(0)}\tau' - i\delta} + 2C_1\exp(-i(\tau')^2 - \gamma\tau'). \tag{33}$$

This expression implies that, for $\mathrm{Re}\,\varepsilon < 0$ with $\varepsilon_r < |\mathrm{Re}\,\varepsilon| \ll 1$, the electric field can be represented as a superposition of the field of forced oscillations with amplitude D_0/ε at the frequency ω of the external source [the first term in (30)] and the field of natural plasma oscillations with the maximum amplitude $2C_1$ and adiabatically varying frequency [the second term in (30)].

Hence, in the range of τ' values from $\tau' \sim -1$ to $\tau' \sim +1$ (in which case $\mathrm{Re}\,\varepsilon = 1 - n$ lies between ε_r and $-\varepsilon_r$), natural plasma oscillations with the maximum amplitude $|\mathrm{E}_{p0}| \approx 2C_1 = 2|\mathrm{E}(0)| = D_0\sqrt{\pi/(\delta_a\dot{n}(0))} \approx 76$ are generated. According to the reduced equation (10), the amplitude of the natural plasma oscillations decreases only because of the wave damping due to electron collisions. In the numerical example at hand, the damping rate is fairly low ($\gamma = 0.27$) and, in the range $\tau' \sim 1$, it is still insignificant. As a result, the field amplitude remains at a high (resonant) level over a substantially longer time interval; this is also true for the rate at which the electron temperature and density increase.

3. Discharge Dynamics in the Range of Overcritical Plasma Densities

In the range $n > 1$, in which $|\varepsilon| \sim 1$, the field evolution should be described by the complete (rather than reduced) equation (7). Even for plasma densities slightly above the critical level ($-\mathrm{Re}\,\varepsilon \gg \varepsilon_r$ or $\tau' \gg 1$), the complete equation admits a solution in the adiabatic (Wentzel–Kramers–Brillouin) approximation; under the above condition $\delta = \nu/\omega \ll 1$, the dimensional solution has the form

$$E = \mathrm{Re}\left[\frac{\tilde{D}}{\varepsilon(t)}\exp(-i\omega t) + A\sqrt{\frac{\omega}{\omega_p(t)}}\exp\left(-i\int_0^t\omega_p(t')dt' - \nu t/2\right)\right], \tag{34}$$

where the initial time corresponds to the time at which the plasma density equals the critical value (as is the case in the previous stage). The constant A is found by matching the asymptotic solutions (33) and (34) in the range $\varepsilon_r \ll |\mathrm{Re}\,\varepsilon| \ll 1$, in which they are both valid: $A = 2C_1E_{cr}$.

In the range where the difference between the frequencies ω and ω_p is not small, the mean power of the

external source of electron heating in the energy balance equation (4) can be calculated approximately as the sum of the partial power losses associated with the fields of oscillations at these frequencies in expression (34). This can be done by averaging over the periods of both of these fields and over the frequency difference $\omega_p - \omega$:

$$\langle jE\rangle = (e^2 N\nu/2m\omega^2)|E_{cr}|^2 \times\left(\frac{D_0^2}{|\varepsilon|^2} + \frac{4|C_1|^2\omega^3}{\omega_p^3}\exp(-\nu t)\right). \quad (35)$$

An analysis of the approximate expression (33) for the field amplitude and the balance equation (12) shows that, for $|\varepsilon|$ of about ε_r and higher, the amplitude of the total electric field and the temperature initially increase by a factor of about 2. In the range $\varepsilon \sim (3–5)\varepsilon_r \sim -(0.15–0.3)$, they reach their maximum (throughout the discharge) values: $|E|_{max} \approx |E_{p0}| \approx 76$ and $T_{max} \approx 80$. In this range, the mechanism for electron heating changes markedly. First, since T_{max} is approximately equal to T_s, it is necessary to take into account the saturation of the functions $\nu_i(T)$ and $\delta_T(T)$. Second, the field amplitude and, accordingly, the equilibrium temperature T_q initially increase at a progressively lower rate and then begin to decrease (because of collisional absorption and an increase in $|\varepsilon|$). Due to this circumstance and the delayed heat exchange, the electron temperature becomes larger than the equilibrium one and, then, decreases at a comparatively low rate. In dimensional units, the time scale on which the electron temperature decreases is estimated as $\Delta t_1 \sim (5–10)\nu^{-1}$, which is about one order of magnitude longer than the time scale ν^{-1} on which the natural plasma oscillations are damped. As a result, the plasma density continues to increase at a fairly high rate even after it exceeds a critical value. In this case, the ionization process is explosive in character: on the time scale Δt_1, which is very short in comparison with the duration of the other breakdown stages, the plasma density N increases from the critical density to the value N_{max}, which is several times larger than the critical density.

Hence, we can conclude that both of the inertial effects under consideration—the delayed polarization response, described by the inertial term $(2i/\omega)dE/dt$ in the field equation, and the delayed heating and cooling of the electrons—ensure the explosive character of the ionization process on a time scale long enough for the formation of a very dense (overdense) plasma.

By the time when the plasma density reaches its maximum value, the natural plasma oscillations in the discharge are essentially completely damped and the electric field is again described by the simplest expression $E = D_0/\varepsilon$. Also, the field amplitude and the temperature both drop below the critical level ($|E| < 1$, $T < 1$). As a result, in the final stage of the discharge, the plasma density slowly decreases (on a characteristic time scale of about $\Delta t_2 \sim \nu_a^{-1}$) and approaches the steady-state density $N_s = N_c(1 + D_0)$, which is determined by the condition $|E| = 1$.

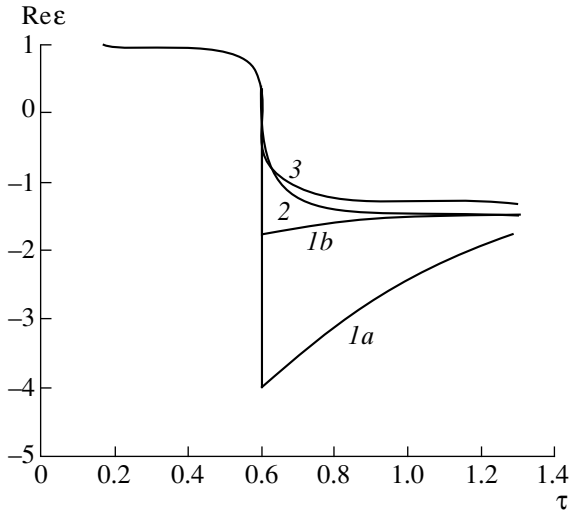

Fig. 1. Time evolution of $Re\varepsilon(\tau)$ for different values of the parameter $\delta = \nu/\omega$. Curves *1a*, *2*, and *3* are calculated for $\delta = 0.01$, 0.1, and 0.3, respectively. Curve *1b* is obtained for $\delta = 0.01$ without allowance for the excitation of plasma oscillations (under the assumption $E = D_0/\varepsilon$).

In order to quantitatively illustrate the breakdown scenario and the role of plasma oscillations at different gas pressures, we solved Eqs. (10)–(13) numerically for the following three values of the parameter $\delta = \nu/\omega$: $\delta = 10^{-2}$, $\delta = 10^{-1}$, and $\delta = 3 \times 10^{-1}$. The first is the value used to obtain the above estimates. The remaining two values refer to higher air pressures of 4 and 12 torr (at the same frequency $\omega \approx 1.9 \times 10^{11}$ s^{-1}). The initial plasma density was set to be $n(0) = N(0)/N_{cr} = 10^{-2}$. The remaining input parameters for simulations were taken from (14). In the density range $n \geq 1.3$, in which the adiabatic solution (34) to Eq. (4) is undoubtedly valid, instead of solving the field equation (10), we used this solution because it is better suited for a description of the two-frequency regime. For this reason, in place of expression (9) for the Joule power loss, we used expression (35) with an appropriately transformed heating source term on the right-hand side of the temperature balance equation (13).

The calculated results are illustrated in Figs. 1–3. For the above three values of δ, Fig. 1 shows the plots of the function $Re\varepsilon(\tau) = 1 - N(\tau)/N_{cr}$, which describe the evolution of the plasma density $N(\tau)$ (in terms of the dimensionless time $\tau = \nu_a t$) during the discharge: from the onset of breakdown to the final steady state. The value $\tau = 0.6$ corresponds roughly to the instant at which the plasma density reaches its resonant value. For $\delta = 10^{-2}$ (which is small in comparison with the

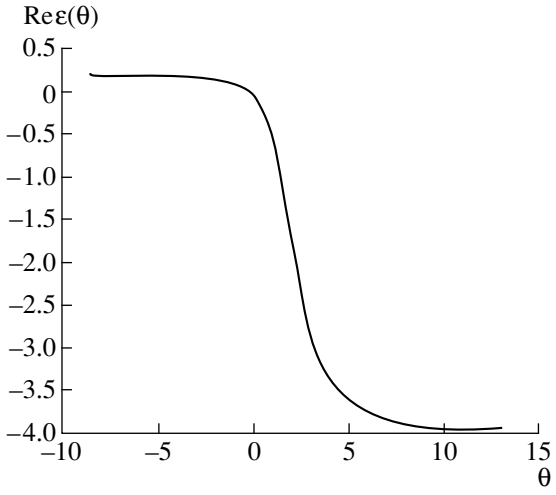

Fig. 2. Time evolution of $\mathrm{Re}\varepsilon(\theta)$ for $\delta = 0.01$; $\theta = (\tau - \tau_0) \times 10^{-5}$. The critical density is reached at the time $\tau_0 \approx 0.6$.

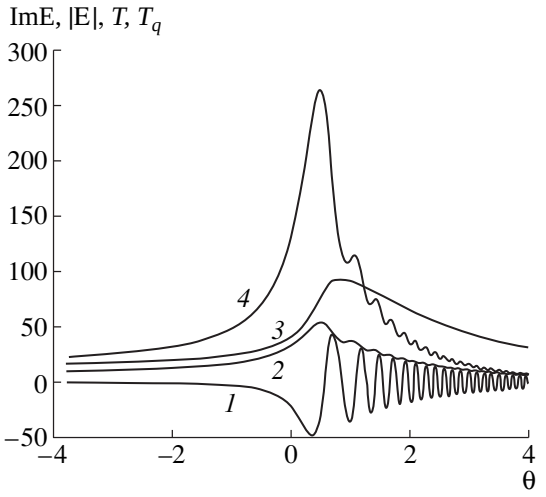

Fig. 3. Time evolutions of (*1*) the imaginary part ImE of the complex field amplitude; (*2*) the absolute value |E| of the complex field amplitude; (*3*) the electron temperature T; and (*4*) the equilibrium temperature T_q for $\delta = 0.01$; $\theta = (\tau - \tau_0) \times 10^{-5}$ and $\tau_0 \approx 0.6$.

above estimate $\varepsilon_r = 0.15$ for the characteristic width of the transient range), intense excitation of plasma oscillations in the vicinity of the resonant point gives rise to an explosive increase in the plasma density (from $N = N_{cr}$ to $N = N_{\max} \approx 5N_{cr}$). On the time scale adopted in Fig. 1, the plasma density is seen to undergo the largest jump (curve *1a*) when passing through the resonant point. For the remaining two δ values, which are comparable to ε_r, the plasma oscillations are generated at lower rates and the jumps at the resonant point are far less pronounced (curves *2*, *3*). In Fig. 1, the role of plasma oscillations in the breakdown process is also illustrated by curve *1b*, which shows the time evolution of $\mathrm{Re}\varepsilon(\tau)$ calculated from the steady-state electric field $E = D_0/\varepsilon$ at $\delta = 10^{-2}$ (i.e., without allowance for the excitation of plasma oscillations). In this case, the maximum plasma density is seen to be lower by a factor of about 2.

For $\delta = 10^{-2}$, the evolution of the field and plasma under the conditions of intense generation of plasma oscillations in the second stage and at the beginning of the third stage is illustrated in Figs. 2 and 3 on shorter time scales. From a more detailed plot of $\mathrm{Re}\varepsilon(\tau)$ in Fig. 2, we can see that the jump in the plasma density occurs on a time scale of about $\Delta\tau \approx 10^{-4}$ or, in dimensional units, $\Delta t \approx 10/\nu \approx 5 \times 10^{-9}$ s. In Fig. 3, the time evolutions of $\mathrm{Im}E(\tau)$ (curve *1*), $|E|(\tau)$ (curve *2*), and the electron temperature $T(\tau)$ (curve *3*) are displayed in the immediate vicinity of the plasma resonance, where the plasma oscillations are generated most intensively and the delay of electron heating is most significant. In order to illustrate the delayed heating, Fig. 3 also presents the time evolution of the equilibrium temperature $T_q(\tau)$ (curve *4*). The numerical results justify the validity of a qualitative analysis of the main stages of the discharge. The field amplitude and electron temperature calculated at the resonant point $n = 1$ ($|E_r| = 35$ and $T_r = 40$) agree well with the qualitative predictions (38 and 33, respectively).

CONCLUSIONS

The numerical results as well as the results of a qualitative analysis, which are shown to be in satisfactory agreement, provide evidence that inertial effects play an important role during the stage in which the plasma density passes through the critical value in a low-pressure discharge. We have considered two types of inertial effects: the delay of the polarization response (this effect is described by the inertial term $(2i/\omega)dE/dt$ in the field equation and is responsible for the generation of natural plasma oscillations) and the delay of heat exchange between electrons, on the one hand, and an alternating electric field and neutral gas molecules, on the other hand. Due to both of these effects, the plasma density continues to increase at a fairly high (resonant) rate even after it exceeds a critical value and the ionization process acquires an explosive character.

The effects considered result in the jumplike increase in the plasma density, which grows from the critical value to highly overcritical values in several nanoseconds. This phenomenon is of interest due to its possible applications in solving technological problems associated with the conversion and transmission of high-power microwave radiation; in particular, it can be used to create fast shutters and switches for antenna transmission lines and storage devices for high-power radar systems.

ACKNOWLEDGMENTS

This work was supported by the Russian Foundation for Basic Research, project no. 99-02-16238.

REFERENCES

1. V. B. Gildenburg, A. A. Zalezskiĭ, and V. E. Semenov, Izv. Vyssh. Uchebn. Zaved., Radiofiz. **38**, 991 (1995).
2. Yu. A. Brodskiĭ, S. V. Golubev, V. G. Zorin, and G. M. Fraĭman, Zh. Éksp. Teor. Fiz. **88**, 771 (1985) [Sov. Phys. JETP **61**, 453 (1985)].
3. V. B. Gildenburg and A. V. Kim, Zh. Éksp. Teor. Fiz. **74**, 141 (1978) [Sov. Phys. JETP **47**, 72 (1978)].
4. V. B. Gildenburg, A. G. Litvak, and N. A. Zharova, Phys. Rev. Lett. **78**, 2968 (1997).
5. V. B. Gildenburg and A. A. Solodov, Pis'ma Zh. Éksp. Teor. Fiz. **62**, 535 (1995) [JETP Lett. **62**, 551 (1995)].
6. N. V. Vvedenskiĭ, N. K. Vdovicheva, V. B. Gildenburg, *et al.*, Izv. Vyssh. Uchebn. Zaved., Radiofiz. **40**, 991 (1997).
7. V. B. Gildenburg and N. V. Vvedenskii, in *Proceedings of the International Workshop on Strong Microwaves in Plasma, Nizhni Novgorod, 2000*, Ed. by A. G. Litvak (Institute of Applied Physics, Nizhni Novgorod, 2000), Vol. 2, p. 575.
8. A. F. Kuckes, Plasma Phys. **10**, 367 (1968).
9. S. V. Bulanov, L. M. Kovrizhnykh, and A. S. Sakharov, Zh. Éksp. Teor. Fiz. **72**, 1810 (1977) [Sov. Phys. JETP **45**, 949 (1977)].
10. N. D. Borisov, A. V. Gurevich, and G. M. Milikh, *Artificial Ionized Region in Atmosphere* (IZMIRAN, Moscow, 1985).
11. A. D. MacDonald, *Microwave Breakdown in Gases* (Wiley, New York, 1966; Mir, Moscow, 1969).

Translated by O.E. Khadin

Plasma Physics Reports, Vol. 27, No. 1, 2001, pp. 76–81. Translated from Fizika Plazmy, Vol. 27, No. 1, 2001, pp. 79–84.

LOW-TEMPERATURE PLASMA

Calculation of Transport Coefficients with Allowance for the Chemical Composition of a Low-Temperature High-Density Metal Plasma

E. M. Apfelbaum and M. F. Ivanov

Institute for High Energy Densities, Associated Institute for High Temperatures, Russian Academy of Sciences, Izhorskaya ul. 13/19, Moscow, 127412 Russia

Received April 3, 2000; in final form, June 8, 2000

Abstract—The model proposed by Ichimaru for calculating transport coefficients is generalized to describe a plasma containing neutral atoms and ions with different charges. Ichimaru's model was developed for a fully ionized two-component (electrons and a single ion species) plasma with a temperature above 10^5 K. Taking into account several species of positive ions and neutral atoms makes it possible to extend Ichimaru's model to a partially ionized plasma. Transport coefficients calculated from different models are compared with the experimental data. © *2001 MAIK "Nauka/Interperiodica".*

1. INTRODUCTION

Information on plasma transport coefficients (among which we will consider only electric and thermal conductivities) is needed to solve both fundamental and applied problems. Although many papers have been devoted to the calculation of transport coefficients (see, e.g., [1–6]), at present, reliable results have been obtained only for a classical two-component (electron–ion) plasma with a relatively high temperature ($T >$ 100 eV) and an electron density $n_e < 10^{20}$ cm^{-3} [1–4]. For lower temperature higher density plasmas, the transport coefficients are more difficult to calculate, because it is necessary to take into account quantum-mechanical corrections and the more complex charge composition of the ions. For $T > 10$ eV, the quantum-mechanical corrections were included in the calculations that were carried out in [1, 2, 4] in the effective mean ion charge approximation. The presence of ions of different charges and neutral atoms in a plasma with $T < 10$ eV and a moderate density was incorporated by Pavlov [5], who treated noble gases and alkali metals in the classical approximation.

Lee and More [6] attempted to take into account the effect of both the charge composition of the plasma ions and the degeneration of the electron plasma component on the kinetic coefficients in xenon and aluminum plasmas in the temperature range $T \leq 10$ eV, but their calculations differed from those carried out by Pavlov only in that they modeled the degenerate electron component by replacing the classical Boltzmann distribution function with the Fermi–Dirac function.

Note that, in [3, 5, 6], the nonideal nature of the plasma was taken into account only via the screening of the two-body interaction potential in the Debye approximation. This approach is only valid for weakly ionized rarefied plasmas and does not apply to higher density plasmas. In [1, 2, 4], the nonideal nature of a plasma was taken into account more accurately; moreover, Ichimaru *et al.* [1] also considered how to pass over from a nonideal plasma to the limiting case of an ideal plasma as the plasma temperature and density change (this passage to the limit will be discussed below).

For a low-temperature high-density plasma of metals such as aluminum and copper (which are very important for practical applications), the transport coefficients are even more difficult to calculate, because the experimental data on these metals (in contrast to the data on noble gases and alkali metals) have been obtained only recently and are not as complete as could be desired [7, 8]. As was noted in [7], the first theoretical results obtained for aluminum and copper plasmas from some of the cited models [1, 3, 4, 6] disagree with these experimental data. This disagreement is not surprising in view of the above drawbacks of the models.

Hence, the question of how to correctly incorporate the effect of both the degeneration of the electron plasma component and the charge composition of the plasma ions on transport coefficient remains open. Our purpose here is to generalize the physically correct and relatively simple model developed by Ichimaru *et al.* [1] for a two-component nonideal plasma with a degenerate electron component to a partially ionized plasma with a complex charge composition of the ions.

2. DESCRIPTION OF THE MODEL

It is well known that the electron component makes a major contribution to the electric and thermal conduction processes [5]. The fluxes of the electrons that carry the heat and electric current can be expressed as functionals of the electron distribution function. Accord-

1063-780X/01/2701-0076$21.00

ingly, in order to calculate the thermal and electric conductivities, we need to determine the electron distribution function. Since the macroscopic electron fluxes can be represented, on the one hand, as linear functionals of the electron distribution function and, on the other hand, as linear functions of the external field and plasma temperature gradient, we can immediately linearize the electron distribution function in the latter two parameters.

In [1], the electron distribution function in a high-density plasma is determined based on the Wigner distribution function, which is an analogue of the classical distribution function in a quantum-mechanical description of the system.

Following [1], we consider the Heisenberg equation

$$i\hbar\frac{\partial}{\partial t}\xi = [\hat{H}, \xi], \tag{1}$$

where

$$\xi(\mathbf{p}, \mathbf{k}) = 2\hat{a}_{\mathbf{p}}^{+}\hat{a}_{\mathbf{p}+\hbar\mathbf{k}}, \tag{2}$$

and the Hamiltonian has the form

$$\hat{H} = 2\sum_{p}\frac{p^2}{2m}\hat{a}_{\mathbf{p}}^{+}\hat{a}_{\mathbf{p}}$$
$$-|e|\sum_{\mathbf{p},\mathbf{k}}\int\frac{d\omega}{2\pi}\phi_t(\mathbf{k}, \omega)\xi(\mathbf{p}, -\mathbf{k})\exp(-i\omega t), \tag{3}$$
$$\phi_t(\mathbf{r}, t) = \sum_{\mathbf{k}}\int_{-\infty}^{\infty}\frac{d\omega}{2\pi}\phi_t(\mathbf{k}, \omega)\exp[i(\mathbf{kr} - \omega t)].$$

Here, $a_{\mathbf{p}}$ and $a_{\mathbf{p}}^{+}$ are, respectively, the creation and annihilation operators of the electrons. In expression (2), the doubled product of these operators is the number of electrons in state p at $k = 0$ (the factor 2 corresponds to degeneration in the spin quantum number). The first term in Hamiltonian (3) corresponds to the operator of the electron kinetic energy, and the second term describes the electron potential energy in the field with the potential ϕ produced by the remaining plasma particles.

We represent the potential ϕ as the sum of two components referring to the external field E and the self-field of the plasma:

$$\phi_t(\mathbf{k}, \omega) = \langle\phi\rangle + \varphi(\mathbf{k}, \omega)$$
$$= 2\pi i\frac{\mathbf{k}}{k^2}\mathbf{E}\delta_{\mathbf{k},0}\delta(\omega) + \varphi(\mathbf{k}, \omega). \tag{4}$$

Using expressions (3) and (4), we average Eq. (1) over an ensemble of particles. The resulting Fourier transformed equation is the desired kinetic equation for the Wigner distribution function,

$$\frac{\partial F}{\partial t} = -\frac{\mathbf{p}}{m}\nabla F(\mathbf{p}, \mathbf{r}) + |e|\mathbf{E}\frac{\partial F}{\partial \mathbf{p}}$$
$$-i\frac{e}{2}\sum_{\mathbf{k}}\int\frac{d\omega}{2\pi}\Delta_{\mathbf{p}}^{\mathbf{k}}\langle\xi(\mathbf{p}, -\mathbf{k})\varphi(\mathbf{k}, \omega)\rangle e^{-i\omega t}, \tag{5}$$

where

$$\Delta_{\mathbf{p}}^{\mathbf{k}} f(\mathbf{p}) = \frac{1}{\hbar}[f(\mathbf{p} + \hbar\mathbf{k}) - f(\mathbf{p})],$$

the Wigner distribution function F is defined as

$$F(\mathbf{p}, \mathbf{r}) = \sum_{\mathbf{k}}\langle\xi(\mathbf{p}, \mathbf{k})\rangle e^{i\mathbf{kr}}$$
$$= \sum_{\mathbf{k}}\mathrm{Tr}(\hat{\rho}\xi(\mathbf{p}, \mathbf{k}))e^{i\mathbf{kr}}, \tag{6}$$

the angular brackets denote averaging over the statistical ensemble, and ρ is the density matrix. The last term in Eq. (5) plays the role of the collision integral, thereby determining all transport properties of the plasma.

We introduce the electron density fluctuations in phase space,

$$\delta N(\mathbf{k}, \omega, \mathbf{p}) = \int_{-\infty}^{\infty} dt\xi(\mathbf{p}, \mathbf{k})\exp(i\omega t), \tag{7}$$

in which case distribution function (6) reduces to

$$\frac{\partial F}{\partial t} = -\frac{\mathbf{p}}{m}\nabla F(\mathbf{p}, \mathbf{r}) + |e|\mathbf{E}\frac{\partial F}{\partial \mathbf{p}}$$
$$-i\frac{e}{2}\sum_{\mathbf{k}}\int\frac{d\omega}{2\pi}\Delta_{\mathbf{p}}^{\mathbf{k}}\langle\delta N\varphi^*(\mathbf{k}, \omega, \mathbf{p})\rangle, \tag{8}$$

where the correlator in the integrand has the form [7]

$$(2\pi)^2\langle\delta N\varphi^*(\mathbf{k}, \omega, \mathbf{p})\rangle\delta(\omega + \omega')$$
$$= \langle\delta N(\mathbf{k}, \omega, \mathbf{p})\varphi(-\mathbf{k}, \omega')\rangle. \tag{9}$$

According to [1], we must express the electron density fluctuations δN in terms of the equilibrium distribution function $F(p)$. The general description of this procedure, which was developed by Klimontovich for the classical case, can be found in, e.g., [9, 10]. Then, we have

$$\delta N = \frac{\Delta_{\mathbf{p}}^{\mathbf{k}}F(\mathbf{p})}{\omega - \omega_{pk} + i0}|e|\varphi(\mathbf{k}, \omega),$$
$$F(\mathbf{p}) = \langle\xi(\mathbf{p}, 0)\rangle, \tag{10}$$
$$\omega_{pk} = \Delta_{\mathbf{p}}^{\mathbf{k}}\frac{p^2}{2m_e}.$$

Hence, the integral term in Eq. (8) is expressed in terms of the correlator of the squared absolute value of the

potential, so that the final kinetic equation takes the form

$$\frac{\partial F}{\partial t} + \frac{\mathbf{p}}{m}\nabla F(\mathbf{p}, \mathbf{r}) - |e|\mathbf{E}\frac{\partial F}{\partial \mathbf{p}} = ie^2\int\frac{d\mathbf{k}}{(2\pi)^3}\int d\omega\Delta_{\mathbf{p}}^{\mathbf{k}}\left[\frac{\Delta_{\mathbf{p}}^{\mathbf{k}}F(\mathbf{p})}{\omega - \omega_{pk} + i0}\right]\langle|\varphi(\omega, \mathbf{k})|^2\rangle. \quad (11)$$

In this equation, we replace the sum over the wave vector **k** by a corresponding integral. Further, in order to determine the transport coefficients, we represent the distribution function as a sum of the equilibrium and nonequilibrium functions and adopt the Fermi–Dirac distribution $F_0(\mathbf{p})$ as the equilibrium function. With this representation of the distribution function, we linearize Eq. (11) about the steady state in a standard way. As a result, the equilibrium distribution function enters only the left-hand side of the final kinetic equation and the collision integral is a functional of the nonequilibrium distribution function.

In order to derive the transport coefficients, we first evaluate the static electric conductivity. To do this, we retain only the term with the electrostatic field on the right-hand side of Eq. (11). In [1], the nonequilibrium distribution in the collision integral was described by the Fermi–Dirac function with a shifted argument, $F = F_0(|\mathbf{p} - m_e\mathbf{u}|)$, where **u** is the mean electron flow velocity. In this case, the electric current density is equal to $\mathbf{J} = -n_e|e|\mathbf{u}$, so that we can evaluate the electric conductivity as the limit of the ratio of the current density to the electric field strength, as $\mathbf{u} \longrightarrow 0$ (we assume that the plasma is isotropic, in which case the electric conductivity tensor is a scalar). Integrating Eq. (10) over momentum **p** yields the following expression for the reciprocal of the desired electric conductivity:

$$\frac{1}{\sigma} = \lim_{u\to 0}\frac{1}{(en_e u)^2}\int\frac{d\mathbf{k}}{(2\pi)^3} \times \int d\omega\mathbf{k}\mathbf{u}\langle|\varphi(\mathbf{k}, \omega)^2|\rangle\,\mathrm{Im}\,\chi_0(\mathbf{k}, \breve{\omega}), \quad \breve{\omega} = \omega - \mathbf{k}\mathbf{u}, \quad \chi_0(\mathbf{k}, \omega) = -\int d\mathbf{p}\frac{\Delta_{\mathbf{p}}^{\mathbf{k}}F_0(\mathbf{p})}{\omega - \omega_{pk} + i0}. \quad (12)$$

In calculating static transport coefficients, the expression for χ_0 can only be treated in the low-frequency limit, in which the integral over momentum in (12) is taken by expanding in powers of a small frequency:

$$\mathrm{Im}\,\chi_0 \longrightarrow -2\pi^2 m^2\frac{\omega}{k}F_0\left[\left(\frac{\hbar k}{2}\right)^2\right]. \quad (13)$$

In [1], the correlator $\langle|\varphi|^2\rangle$ in Eq. (12) was determined under the assumptions that an electron is much lighter than an ion and a completely ionized plasma consists exclusively of electrons (*e*) and ions (*i*):

$$\langle|\varphi(\mathbf{k}, \omega)^2|\rangle = n_i\left|\frac{4\pi Z_i e^2}{\varepsilon(\mathbf{k})k^2}\right|^2 S_{ii}(\mathbf{k})\delta(\omega). \quad (14)$$

Here, the numerator is the Fourier-transformed electron–ion interaction energy, the denominator contains the dielectric function, S_{ii} is the ion structure factor (see below for details), $\delta(\omega)$ is the Dirac delta-function of frequency, n_i is the ion density, and Z_i is the ion charge number. Note that this representation of the correlator corresponds to the first Born approximation in scattering theory. It is well known that this approximation limits the magnitude of the two-body interaction potential. However, expression (14) contains the cross section for the screened (rather than unscreened) Coulomb scattering; consequently, with the dielectric function evaluated correctly, this expression yields fairly reliable results [2]. We will use this representation of the correlator in further analysis.

Now, we consider a plasma with several ion species and neutral atoms. This situation is typical of a low-temperature plasma whose temperature is close to or lower than the ionization potential. Such a plasma cannot be described in the Ichimaru approximation, which assumes a single heavy ion species. Expression (14) generalized to the case of a multispecies plasma has the form

$$\langle|\varphi(\mathbf{k}, \omega)^2|\rangle = \sum_i n_i\delta(\omega)\sum_r S_{i,r}\left|\frac{w_{re}(\mathbf{k})}{\varepsilon(\mathbf{k})}\right|^2. \quad (15)$$

Here, the subscripts *i* and *r* denote atoms and all ion species, and w_{er} is the Fourier transformed potential energy of the interaction of electrons with ions of species *r* or atoms. For the terms from expression (15) that describe the electron–ion interaction, this energy has the form $w_{er} = 4\pi Z_r e^2/k^2$ and refers exclusively to the unscreened Coulomb interaction, while the dielectric function ε allows for screening. The potential of the interaction of electrons with ions and atoms will be analyzed below.

Substituting formulas (13) and (15) into Eq. (11) yields the following expression for the electric conductivity σ:

$$\frac{1}{\sigma} = \frac{m^2}{12\pi^3\hbar^3 e^2 n_e^2}\int_0^\infty dk k^3 f_0(k/2) \times \sum_{ir} S_{ir}(k)A_i^\sigma n_i\left|\frac{w_{er}(k)}{\varepsilon(k)}\right|^2, \quad (16)$$

where

$$f_0(k) = \left[\exp\left(\frac{\hbar^2 k^2}{2m_e k_B T} - \alpha\right) + 1\right]^{-1},$$

and $\alpha = \mu/(k_B T)$, with μ being the chemical potential of the electrons. Electron–electron collisions are incorporated into expression (16) via the coefficients $\mathbf{A}^\sigma$, which were obtained by Spitzer [3] and, more recently, were refined by Van Odenhoven and Schram [11]. These coefficients depend on the ion charge number and approach unity as $Z_i \longrightarrow \infty$.

Generalizing the results obtained by Ichimaru *et al.* [1] to the case of a multispecies plasma, we can evaluate the thermal conductivity in a similar way:

$$\frac{1}{\kappa} = \frac{(T/T_F)^{9/2}}{16\sqrt{2}\pi\Sigma^2}\frac{\sqrt{m}}{k_B(k_B T)^{5/2} n_e}$$

$$\times \int_0^\infty dk k^3 \sum_{i,r} A_i^\kappa n_i S_{ir}(k)\left|\frac{w_{er}(k)}{\varepsilon(k)}\right|^2 \qquad (17)$$

$$\times \int_{k/2k_F}^\infty dx x(x^2-\lambda^2)\frac{\partial f_0(k_F x)}{\partial \alpha},$$

where f_0 is defined in the same way as in formula (16) and the coefficient $\mathbf{A}^\kappa$, which is analogous to $\mathbf{A}^\sigma$ in (16), was calculated in [11].

For a two-component plasma, formula (16) passes over to the corresponding formula obtained in [1, 2]:

$$\frac{1}{\sigma} = 4\left(\frac{2\pi}{3}\right)^{1/2}\frac{\Gamma^{3/2}}{\omega_p}L_E,$$

where Γ is the coupling parameter, characterizing the degree to which the plasma is nonideal; ω_p is the plasma frequency; and L_E is the Γ-dependent generalized Coulomb logarithm. A similar formula was also derived in [3, 6], but with a Coulomb logarithm in a different form. However, in accordance with [1, 2], the Coulomb logarithm derived from formula (16) is better suited for describing a nonideal plasma than the logarithms obtained in [3, 6] using the Debye approximation.

Hence, in order to calculate the desired transport coefficients for a nonideal plasma, we have to determine the electron–atom interaction potential, the ion structure factors, the dielectric function, the chemical composition of the plasma, and the electron chemical potential μ. The chemical composition and chemical potential at a given plasma temperature and density were calculated by solving the equations of the generalized chemical model (specifically, the Saha equations for a multispecies plasma consisting of electrons, neutral atoms, and a mixture of ion species) with allowance for corrections introduced by the interaction between plasma particles [12].

3. CALCULATION OF THE STRUCTURE FACTORS, DIELECTRIC FUNCTION, AND ELECTRON–ATOM INTERACTION POTENTIAL

In formulas (14) and (15), the ion structure factor is the Fourier transformed two-body correlation function $g_{pq}(r)$:

$$S_{pq}(\mathbf{k}) = \delta_{pq} + \sqrt{n_p n_q}\int g_{pq}(\mathbf{r})e^{i\mathbf{kr}}d\mathbf{r}. \qquad (18)$$

The structure factor $S_{pq}(r)$ and dielectric function can be deduced from the so-called hypernetted chain equations. This method is equivalent to a virial expansion of free energy and was described in detail by Balescu [10], who showed that the hypernetted chain equations correspond to a four-term virial expansion. We used the classical method of hypernetted equations, because Ichimaru *et al.* [2] showed that, when the temperatures under consideration are still sufficiently high ($T \geq 1$ eV), the correlation functions obtained by the classical method and its quantum analogue are close to each other.

The first of the hypernetted equations is that for the ion–ion correlation function $g(r)$ [10]:

$$g_{it}(r) = \exp\{-\Phi_{it}(\mathbf{r})/(k_B T) + g_{it}(r) - 1 - c_{it}(r)\}, \qquad (19)$$

where $c(r)$ is the so-called direct correlation function and $\hat{\Phi}(\mathbf{r})$ is the energy of interaction between two particles of the indicated species. We introduce the new function

$$h_{it}(r) = g_{it}(r) - 1$$

and close the chain by the Ornstein–Zernike relationship

$$h_{it}(r) = c_{it}(r) + \sum_\lambda n_\lambda \int c_{\lambda t}(\mathbf{r}-\mathbf{r}_1)\mathbf{h}_{i\lambda}(\mathbf{r}_1)d\mathbf{r}_1. \qquad (20)$$

From Eqs. (19) and (20), we can find the functions $h(r)$ and $g(r)$. In our study, we solved Eqs. (19) and (20) numerically for a multispecies plasma.

Having found the structure factor, we can calculate the dielectric function by applying the linear response theory [1, 10]. Let the plasma be affected by an external field, and let the plasma–field system be described by the Hamiltonian

$$H = \sum_p \int \rho_p(\mathbf{r})V(\mathbf{r}, t)d\mathbf{r}, \qquad (21)$$

where the subscript p stands for the particle species, V is the external field, and ρ is the electric charge density. Taking the Fourier transformation of the charge density perturbed by the external field gives

$$\delta\rho_p(\mathbf{k}, \omega) = \sum_d \chi_{pd}(\mathbf{k}, \omega)V_d(\mathbf{k}, \omega), \qquad (22)$$

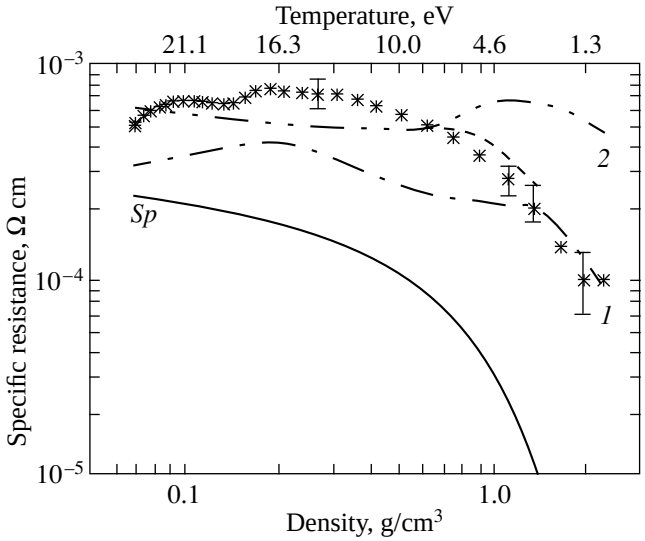

Fig. 1. Specific resistance of aluminum vs. the plasma density. The upper horizontal axis represents the temperature, which corresponds to the density plotted on the lower horizontal axis and was calculated in [8] from the equation of state. The experimental results of [8] and [7] are shown by asterisks and triangles, respectively. The calculated results of [3], [6], and [1] are depicted as curves *Sp*, *1*, and *2*, respectively. The dashed curve illustrates the results of our calculations.

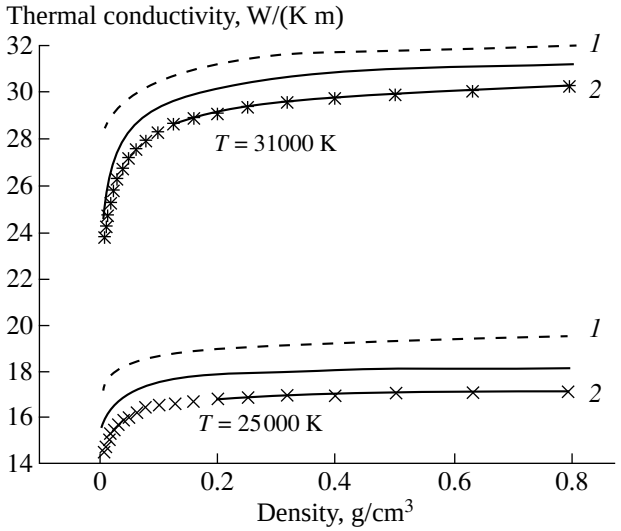

Fig. 2. Thermal conductivity of aluminum vs. the plasma density at different temperatures. Curves *1* and *2* correspond to the calculated results of [6] and [1], respectively. The solid curve illustrates the results of our calculations.

where $\hat{\chi}$ is the response function.

The Fourier transformed reciprocal of the dielectric function is determined as

$$\frac{1}{\varepsilon(\mathbf{k}, \omega)} = 1 + \sum_{pd} w_{pd}(\mathbf{k})\chi_{pd}(\mathbf{k}, \omega), \qquad (23)$$

where, as in formula (15), w_{pd} is again the Fourier transformed potential energy of the interaction between two particles.

According to the fluctuation dissipation theorem, we have

$$S_{pd} = -\frac{\hbar}{2\pi}\coth\left[\frac{\hbar\omega}{2k_{\mathrm{B}}T}\right]\mathrm{Im}\,\chi_{pd}. \qquad (24)$$

Hence, knowing the structure factors, we can find the Fourier transformed reciprocal of the dielectric function from expressions (23) and (24).

Now, we solve for the electron–atom interaction potential, which depends on the sort of atom under consideration. Thus, Pavlov [5] calculated the cross sections for electron–atom collisions using the Moliére–Glauber approximation and assuming that the atoms of noble gases are hydrogen-like. However, we are dealing with aluminum atoms, which do not possess the properties of hydrogen-like atoms. For this reason, we employ a combination of the variational and Hartree–Fock methods, which are described in [13, 14]. First, we assume that all of the atoms are in the ground state, in which case, according to [14], the electron wave function can be represented as a sum of the coordinate-dependent and spin-dependent functions, the latter being an eigenfunction of the total spin angular momentum operator for the electron system of an atom. (Since an aluminum atom contains thirteen electrons, the total spin of the aluminum atoms in the ground state is equal to $S = 1/2$.) In accordance with the Hartree–Fock method, the coordinate-dependent wave function can be chosen to be a combination of one-particle wave functions that is symmetrized in a proper manner (see [13]) and depends on one or several parameters α_i. We determine these parameters variationally, i.e., by minimizing the averaged Hamiltonian for an atom. For an N-particle electron wave function $\Psi_N = \Psi_N(r_1 \ldots r_N, \alpha_1 \ldots \alpha_N)$ (with $N = 13$ for aluminum), the minimization procedure yields

$$E = \langle\Psi_N|H|\Psi_N\rangle, \quad \frac{\partial E}{\partial\alpha_i} = 0, \quad i = 1, \ldots, N. \qquad (25)$$

We average the electron–atom interaction energy over the resulting wave function to obtain the desired potential $\Phi(r)$:

$$U_{ea} = -\frac{Z|e|^2}{R} + \sum_{k=1}^{N}\frac{|e|^2}{|\mathbf{R} - \mathbf{r}_k|}, \qquad (26)$$
$$\Phi(R) = \langle\Psi|U_{ea}|\Psi\rangle.$$

Note that, in deriving the electron–atom interaction potential (26), we again used the Born approximation. Although doing so is not quite correct, in the situation under discussion, the positive-ion density is close to the neutral-atom density or even higher [12] and the cross section for electron scattering by ions is known to be

much larger than that for electron scattering by atoms [14], so that we can neglect corrections to the Born approximation without any serious loss of accuracy. The electron–atom interaction potential (26) was used to calculate the kinetic coefficients.

4. RESULTS OF CALCULATIONS OF THE ELECTRIC AND THERMAL CONDUCTIVITIES

The transport coefficients calculated from formulas (16) and (17) are shown in Figs. 1 and 2, respectively. In Fig. 1, we also depict the experimental data obtained in [7, 8] when measuring the electric conductivity of aluminum and illustrate the results calculated by Benage *et al.* [8] from other models. Figure 1 presents the specific resistance as a function of the density, plotted on the lower horizontal axis. The upper horizontal axis represents the temperature, which corresponds to the density plotted on the lower horizontal axis and was calculated by Benage *et al.* [8] from the equation of state.

According to [8], Ichimaru's model [1] applies to plasmas with high temperatures and low densities, whereas Lee and More's model [6] gives better results for plasmas with low temperatures and high densities. Recall that the latter model is well suited for a classical high-temperature plasma. That this model is in better agreement with the experimental data stems from the fact that, although Lee and More did not systematically incorporate quantum-mechanical effects in a low-temperature high-density plasma, they included electron–atom interaction in addition to electron–ion interaction. In contrast, Ichimaru *et al.* [1] treated the plasma as a two-component medium with the effective ion charge. In [8], the ion charge number was calculated in the so-called average-ion approximation, which is based on the Thomas–Fermi model. However, the results obtained in this approximation differ from the experimental data both quantitatively and qualitatively. Consequently, in calculating the transport coefficients, it is of fundamental importance to take into account the charge composition of a low-temperature high-density plasma. This conclusion is confirmed by our calculations of the electric conductivity of aluminum for $0.01 < \rho < 1.2$ g/cm^3 and $10000 < T < 100000$ K, as is evident from Fig. 1. In Fig. 2, we compare the thermal conductivities obtained from our model and the models developed in [1, 6].

ACKNOWLEDGMENTS

We are grateful to V.K. Gryaznov for providing us with the results of calculations of the chemical composition of the plasma in the temperature and density ranges under consideration.

REFERENCES

1. S. Ichimaru, S. Mitake, S. Tanaka, and X.-Z. Yan, Phys. Rev. A **32**, 1768 (1985).
2. S. Ichimaru, S. Tanaka, and X.-Z. Yan, Phys. Rev. A **41**, 5616 (1990).
3. L. Spitzer, *Physics of Fully Ionized Gases* (Interscience, New York, 1956; Mir, Moscow, 1962).
4. M. W. C. Dharma-Wardana and F. Perrot, Phys. Rev. A **36**, 238 (1987).
5. G. A. Pavlov, *Heat Transfer in Plasma with Strong Coulomb Interaction* (Énergoatomizdat, Moscow, 1995).
6. Y. T. Lee and R. M. More, Phys. Fluids **27**, 1273 (1984).
7. I. Krisch and H.-J. Kunze, Phys. Rev. E **58** (5), 6557 (1998).
8. J. F. Benage, W. R. Shanahan, and M. S. Murillo, Phys. Rev. Lett. **83** (15), 2953 (1999).
9. E. M. Lifshitz and L. P. Pitaevskiĭ, *Physical Kinetics* (Nauka, Moscow, 1979; Pergamon, Oxford, 1981).
10. R. Balescu, *Equilibrium and Nonequilibrium Statistical Mechanics* (Wiley, New York, 1975; Mir, Moscow, 1978).
11. E. J. F. van Odenhoven and P. P. J. Schram, Physica A (Amsterdam) **133**, 74 (1985).
12. I. L. Iosilevskiĭ, V. K. Gryaznov, É. E. Son, *et al.*, *Thermophysical Properties of the Working Media of Gas-Phase Nuclear Reactors* (Énergoatomizdat, Moscow, 1980).
13. G. F. Drukarev, *Theory of Collisions of Electrons with Atoms and Molecules* (Fizmatgiz, Moscow, 1963).
14. L. D. Landau and E. M. Lifshitz, *Quantum Mechanics: Non-Relativistic Theory* (Nauka, Moscow, 1989; Pergamon, Oxford, 1977).

Translated by O.E. Khadin

Plasma Physics Reports, Vol. 27, No. 1, 2001, pp. 82–85. Translated from Fizika Plazmy, Vol. 27, No. 1, 2001, pp. 85–88.

LOW-TEMPERATURE PLASMA

Optical Characteristics of a Gallium Laser Plasma

A. K. Shuaibov, L. L. Shimon, A. I. Dashchenko, I. V. Shevera, and M. P. Chuchman

Uzhgorod State University, Pidgirna str. 46, Uzhgorod, 88000 Ukraine

Received April 19, 2000; in final form, May 20, 2000

Abstract—Results are presented from studies of the emission from an erosion gallium laser plasma at a moderate intensity ($W = (1–5) \times 10^8$ W/cm^2) of a 1.06-μm laser radiation. It is shown that, under these conditions, the lower excited states of gallium atoms are populated most efficiently. Among the ions, only the most intense GaII lines are observed in the emission spectrum. The populations of GaI and GaII excited states are not related to direct electron excitation, but are determined by the recombination of gallium ions with slow electrons. The recombination times of GaIII and GaII ions in the core of the plasma jet are determined from the waveforms of emission in the GaII and GaI spectral lines and are equal to 10 and 140 ns, respectively. The results obtained are of interest for spectroscopic diagnostics of an erosion plasma produced from gallium-containing layered crystals during the laser deposition of thin films. © *2001 MAIK "Nauka/Interperiodica".*

Emission from an erosion plasma produced on the surface of metals, alloys, and crystals under laser irradiation at an intensity of 10^8–10^{12} W/cm^2 at the focus was studied for the purpose of obtaining a stimulated emission of radiation via ion transitions [1], direct spectral analysis [2], development of ion sources, and diagnostics of laser deposition of thin films [3]. Along with laser mass spectrometry, spectral methods for diagnosing a laser plasma provide important information about the plasma parameters. Carbon [4], aluminum [5, 6], and magnesium [7] plasmas were studied in detail using emission spectroscopy in the UV and visible spectral regions. In order to optimize the process of laser deposition of thin films produced, e.g., from $PbGa_2S_4$ or $CdGa_2Se_4$ layered crystals at a moderate intensity of a neodymium laser, it is necessary to have information about the spectral and temporal emission characteristics of individual constituents of such crystals in a laser plasma. For a gallium laser plasma, this information is not available. The emission-intensity distribution over the GaI and GaII levels and mechanisms for populating the excited states in a gallium laser plasma at a moderate laser intensity have been poorly studied.

In this paper, we present the results of studying the time-averaged spectra and time behavior of the emission from excited atoms and ions of gallium in different spatial regions of a plasma jet produced under irradiation by a YAG:Nd^{3+} laser at a moderate pulse energy.

Experiments were carried out with a repetitive neodymium Q-switched laser. The pulse duration was 20 ns and the repetition rate was 12 Hz. The laser beam was focused by a lens ($F = 50$ cm) to a spot 0.4–0.5 mm in diameter, which allowed us to obtain an intensity of $(3–5) \times 10^8$ W/cm^2 on the gallium surface. A plate of especially pure gallium was positioned inside a vacuum chamber with a residual gas pressure of 3–12 Pa. The emission in the 210- to 600-nm spectral region was analyzed with the help of an MDR-2 monochromator with a 1200 line/mm grating. Radiation emitted from different spatial regions of the plasma jet was collected by a lens. Most attention was given to the emission from the core of the plasma jet, whose center was located 1 mm from the metal surface, and from the jet region located 7 mm from the surface. Time-averaged spectra were detected by an FEU-106 photomultiplier and recorded by a KSP-4 recorder. The FEU-106 + MDR-2 system was calibrated with hydrogen and tungsten band lamps, which allowed us to measure the relative intensities of emission lines (I/k_λ, where k_λ is the relative spectral response of the recording system). The measurements of pulsed radiation with a time resolution of 2–3 ns and duration shorter than 1 μs were conducted with an ELU-14FS electron linear multiplier and a 6LOR-04 oscillograph. Longer radiation pulses were recorded with a FOTON pulsed photomultiplier connected to a C1-99 oscillograph. The best time resolution in this case was 20 ns. The system for recording plasma emission is described in more detail in [8, 9]. Emission spectra were identified using the tables in [10] and paper [11].

Figure 1 shows the time-averaged emission spectrum from the core of the erosion gallium plasma jet, without taking k_λ into account. The emission spectrum consists of GaI and GaII spectral lines against the continuum background extended over the entire wavelength range under investigation. The emission from higher ionization states of gallium ions was not detected. The identified emission lines, relative intensities of GaI and GaII lines, and the distribution of radiation fluxes $\Delta I/k_\lambda$ over GaI and GaII transitions in the 210- to 600-nm spectral range are given in the table. The value $\Delta I/k_\lambda$ is expressed in percent and presents the ratio of the intensity of each line to the total emission

1063-780X/01/2701-0082$21.00 © 2001 MAIK "Nauka/Interperiodica"

intensity of all of the lines (without the continuum intensity) over the entire wavelength range under investigation. As is seen from the table, the most efficiently populated levels are the lower states of GaI, namely, the $5^2S_{1/2}$ (E_{up} = 3.07 eV) and $4^2D_{5/2,\,3/2}$ (E_{up} = 4.31 eV) states. The four most intense lines of gallium atoms comprise 90% of the total line-emission intensity of the plasma jet in the 210- to 600-nm wavelength range. A comparison of the distribution of the emission intensity from the plasma produced at a distance of 1–7 mm from the metal surface with the excitation cross sections of GaI and GaII lines show that they, as a whole, are not correlated. Hence, even in the core of the plasma jet, the maximum electron temperature is much lower than the excitation energy of the lowest GaI states (E_{up} = 3.07 eV). As in aluminum laser plasmas [2], the main mechanism for populating the GaI and GaII excited states is associated with the recombination of slow electrons with gallium ions. In this case, electrons are more efficiently captured into the upper GaI** states. Further, due to collisions between GaI** atoms and thermal electrons, the energy of the populated levels of GaI atoms decreases to a certain excited state corresponding to the bottleneck of the recombination flux; then, the emission of spectral lines occurs from this state. In our case, the bottleneck of the recombination flux is the GaI $5^2D_{5/2,\,3/2}$ states with an energy of 5.01 eV. For the GaII ions, the bottleneck is the 4^1D_5 level with the energy E_{up} = 23 eV.

To study the mechanism for populating the excited states of gallium atoms in more detail, we investigated the time behavior of the radiation emitted via GaI and GaII transitions. The waveforms of the intensity of the most intense GaI and GaII lines from the core of the plasma jet are shown in Fig. 2. The starting time in all of the waveforms corresponds to the leading edge of the neodymium laser pulse. The duration of the continuum was 20 ns, which coincided with the duration of the laser pulse. The emission from GaII ions and the GaI

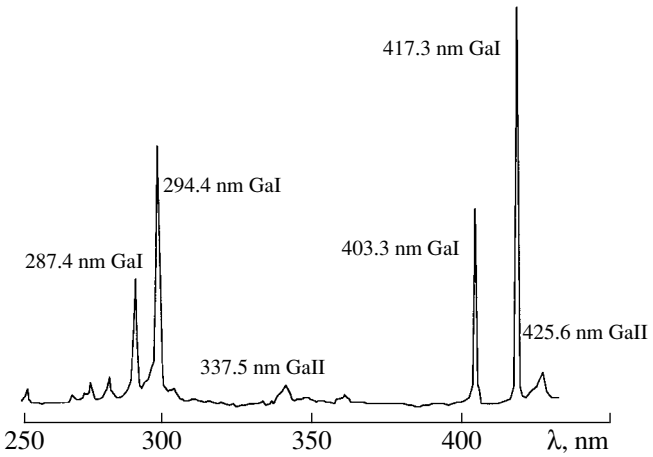

Fig. 1. Emission spectrum from the core of an erosion gallium laser plasma.

287.4-nm resonance line was the shortest ($t \le 50$ ns). The duration of emission via the other intense GaI transitions attained 300–400 ns. A longer duration is typical for the emission from lower GaI levels (except for the resonance line, which may be attributed to a substantial self-absorption). The radiation lifetimes of GaI excited states were less than 6.6–6.8 ns [12]. Therefore, the duration of emission via an individual GaI transition is determined by the recombination time of GaII ions and the duration of line emission of excited singly charged ions is determined by the recombination time of GaIII ions.

In [2], the expression $\ln[I(t)/I(0)] = -t/\tau_p$ was deduced for the decay of the intensity of spectral lines $I(t)$ for ions with charge z as a function of time t, which allows one to determine the recombination time (τ_p) for ions with the charge $z + 1$ (for atoms, we have $z = 0$). Such logarithmic dependences for the GaI and GaII spectral lines are shown in Fig. 3. From the tangent of the slope of lines *1* and *2* (Fig. 3), we determined the

Intensity distribution in the emission spectrum of the gallium plasma jet

λ, nm	Atom (ion)	Transition	E_{up}, eV	I/k_λ, rel. units	$\Delta I/k_\lambda$, %	Q_m, $\times 10^{-18}$ cm^2 [11]
403.3	GaI	$4^2P_{3/2}$–$5^2S_{1/2}$	3.07	0.45	15	71.2
294.4	GaI	$4^2P_{1/2}$–$4^2D_{5/2,\,3/2}$	4.31	1.00	30	72.7
417.3	GaI	$4^2P_{3/2}$–$5^2S_{1/2}$	3.07	0.95	30	134.00
287.5	GaI	$4^2P_{1/2}$–$5^2D_{3/2}$	4.31	0.45	15	55.2
278.1	GaII	4^1P_1–5^1S_0	19.21	0.05	<5	3.4
272.0	GaI	$4^2P_{3/2}$–$6^2S_{1/2}$	4.66	0.10	<5	18.1
266.5	GaI	$4^2P_{3/2}$–$4s4p^2\ ^4P_{3/2}$	4.75	0.05	<5	13.0
250.1	GaI	$4^2P_{3/2}$–$5^2D_{5/2}$	5.01	0.20	5	20.2
245.0	GaI	$4^2P_{1/2}$–$5^2D_{3/2}$	5.01	0.05	<5	10.8

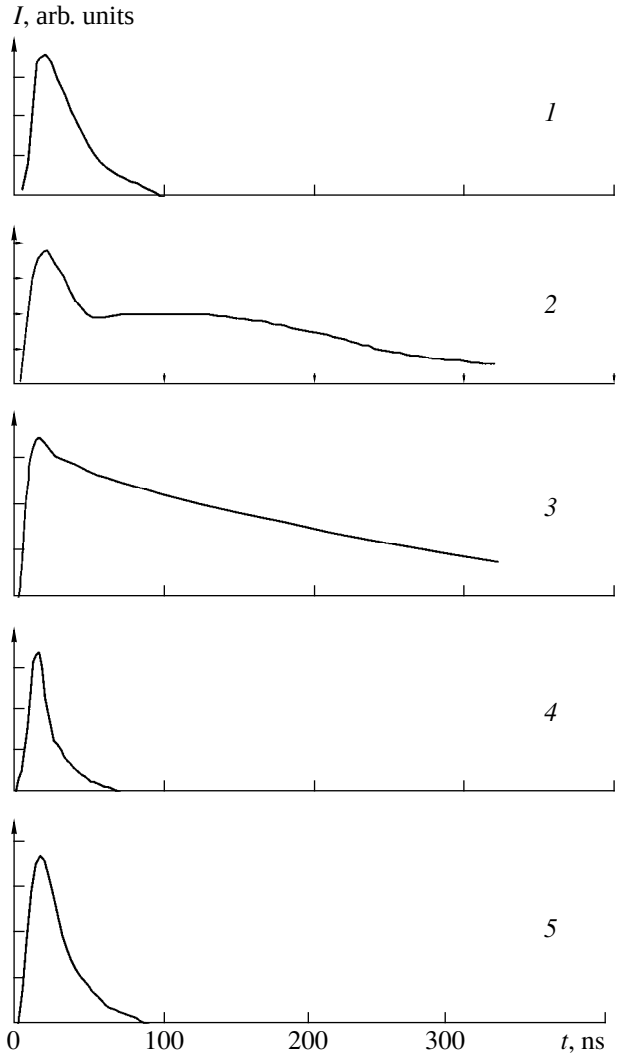

Fig. 2. Waveforms of the intensity of radiation emitted from the core of the laser plasma via the transitions of gallium atoms and ions: (*1*) GaII 278.0-nm, (*2*) GaI 417.3-nm, (*3*) GaI 403.3-nm, (*4*) GaII 337.5-nm, and (*5*) GaI 287.4-nm lines.

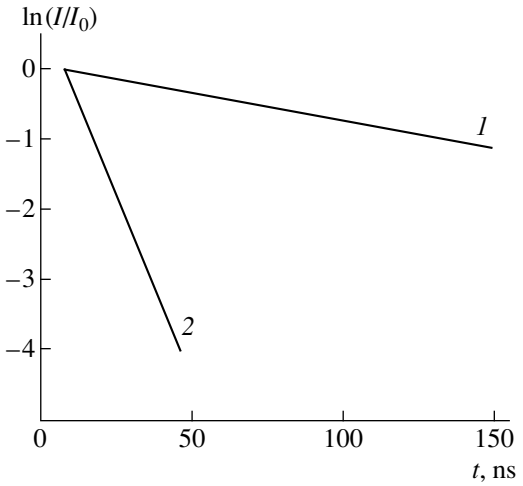

Fig. 3. Logarithmic time dependences of the normalized emission intensity of (*1*) GaI 403.3-nm and (*2*) GaII 278.0-nm lines.

recombination times of GaIII and GaII ions. The recombination of these ions results in populating the upper excited states from which GaI 403.3-nm and GaII 278.1-nm lines are emitted. In the core of the laser plasma (d = 1 mm), the value of τ_p for GaIII ions is 10 ns and it is τ_p = 140 ns for GaII ions. The τ_p values obtained for GaIII and GaII ions (at a residual pressure of 10 Pa) are much shorter than the recombination times for AlIV, AlIII, and AlII ions (350, 500, and 1000 ns, respectively) obtained in [2]. This difference is explained by a higher residual air pressure and a larger distance of the observation point from the aluminum surface (d = 5 mm) in experiment [2]. Nevertheless, the hierarchy of the recombination times for different ionization states is qualitatively the same in this case.

When measuring the emission from a point lying on the axis of the plasma jet at a distance of 7 mm from the surface, the full duration of the GaI and GaII line emission increased to 2–4 μs (Fig. 4). The time behavior of emission via the transitions of Ga atoms and ions agrees qualitatively with the analogous data for the AlI and AlII lines [2]. The average propagation velocity of the gallium plasma jet (for d = 1–7 mm) estimated from the waveforms of the GaI emission line (Fig. 4) is 12.6 km/s.

In summary, it is shown that, if a gallium surface is irradiated by a 1.06-μm laser at an intensity of (3–5) × 10^8 W/cm^2, the main contribution to the laser plasma emission comes from four lines of gallium atoms with the upper levels $5^2S_{1/2}$ and $4^2D_{5/2, 3/2}$. The GaI $5^2D_{5/2, 3/2}$ GaI (E_{up} = 5.01 eV) levels are the bottleneck in the recombination population of GaI excited states; for

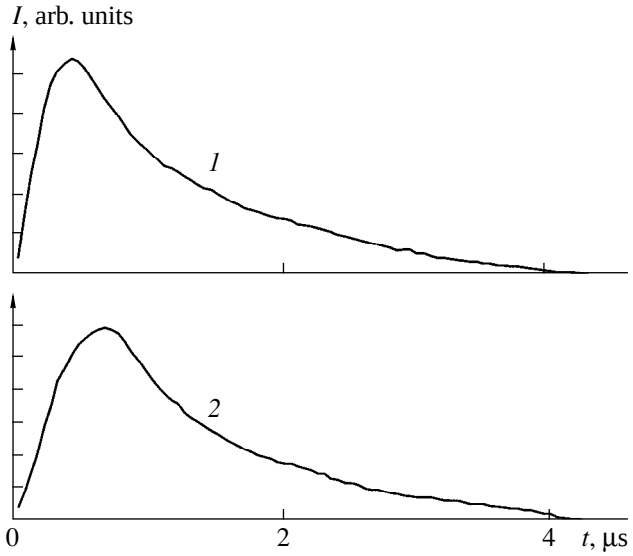

Fig. 4. Waveforms of the intensity of emission in (*1*) GaI 417.3-nm and (*2*) GaII 425.6-nm lines from the laser plasma jet.

GaII ions, such a bottleneck is the GaII $4D^5$ (E_{up} = 23 eV) level. The recombination times of GaIII and GaII in the core of the plasma jet are equal to 10 and 140 ns, respectively. The GaI 417.3- and 403.3-nm spectral lines can be used as diagnostic lines during laser deposition of thin films produced from gallium-containing compounds.

REFERENCES

1. V. A. Boĭko, B. A. Bryunetkin, F. V. Bunkin, *et al.*, Kvantovaya Élektron. (Moscow) **10**, 901 (1983).
2. L. T. Sukhov, *Laser Spectral Analysis: Physical Principles* (Nauka, Novosibirsk, 1990).
3. B. K. Kotlyarchuk, D. I. Popovich, and V. Ya. Pentko, Zh. Tekh. Fiz. **57** (9), 1824 (1987) [Sov. Phys. Tech. Phys. **32**, 1091 (1987)].
4. O. B. Anan'in, Yu. A. Bykovskiĭ, B. V. Zamyshlyaev, *et al.*, Fiz. Plazmy **9**, 319 (1983) [Sov. J. Plasma Phys. **9**, 186 (1983)].
5. O. B. Anan'in, Yu. A. Bykovskiĭ, V. V. Mlynskiĭ, and E. L. Stupitskiĭ, Kvantovaya Élektron. (Moscow) **16**, 2267 (1989).
6. D. V. Gaĭdarenko, A. G. Leonov, and D. I. Chekhov, Fiz. Plazmy **17**, 918 (1991) [Sov. J. Plasma Phys. **17**, 534 (1991)].
7. A. F. Golovin, Kvantovaya Élektron. (Moscow) **21**, 175 (1994).
8. A. K. Shuaibov, A. I. Dashchenko, I. V. Shevera, and A. I. Minya, Fiz. Plazmy **23**, 960 (1997) [Plasma Phys. Rep. **23**, 886 (1997)].
9. A. K. Shuaibov, L. L. Shimon, A. I. Dashchenko, and A. I. Minya, Fiz. Plazmy **25**, 201 (1999) [Plasma Phys. Rep. **25**, 179 (1999)].
10. A. N. Zaĭdel', V. K. Prokof'ev, S. M. Raĭskiĭ, *et al.*, *Tables of Spectral Lines* (Nauka, Moscow, 1969).
11. L. L. Shimon, É. I. Nepiĭpov, V. L. Goldovskiĭ, and N. V. Golovchak, Ukr. Fiz. Zh. (Russ. Ed.) **20** (2), 232 (1975).
12. N. M. Érdevdi and L. L. Shimon, Opt. Spektrosk. **41**, 1084 (1976) [Opt. Spectrosc. **41**, 640 (1976)].

Translated by N.F. Larionova